STUDIES OF LONGITUDINAL AND TRANSVERSE ELECTRON BEAM PARAMETERS OF THE INDUS ACCELERATOR

By

AKASH DEEP

PHYS03201204003

Raja Ramanna Centre for Advanced Technology, Indore

A thesis submitted to the

Board of Studies in Physical Sciences

in partial fulfillment of requirements

for the Degree of

DOCTOR OF PHILOSOPHY

of

HOMI BHABHA NATIONAL INSTITUTE

October, 2018

Homi Bhabha National Institute[1]

Recommendations of the Viva Voce Committee

As members of the Viva Voce Committee, we certify that we have read the dissertation prepared by **Akash Deep** entitled "**Studies of longitudinal and transverse electron beam parameters of the Indus accelerator**" and recommend that it may be accepted as fulfilling the thesis requirement for the award of Degree of Doctor of Philosophy.

Chairman - Prof. Arup Banerjee	Arup Banerjee	**Date:** 30/08/2019
Guide / Convener - Prof. Mohammed H. Modi		**Date:** 30.8.19
Examiner - Prof. M. Boland	M J Boland	**Date:** 2019-08-30
Member 1- Prof. A. Chakrabarti	Aparna Chakrabarti	**Date:** 30.8.19
Member 1- Prof. Vinit Kumar		**Date:** 30.8.19
Member 2- Prof. M. P. Singh		**Date:** 30.8.19
Member 3- Prof. Haranath Ghosh	Haranath Ghosh	**Date:** 30/08/2019
Member 4- Prof. Sataya Bulusu		**Date:** 30/08/19
Technology Advisor - Shri T. A. Puntambekar		**Date:** 30/8/2019
**Member 5- Prof. A. K. Gupta (BARC, Mumbai)		**Date:** 09-09-2019

Final approval and acceptance of this thesis is contingent upon the candidate's submission of the final copies of the thesis to HBNI.

I/We hereby certify that I/we have read this thesis prepared under my/our direction and recommend that it may be accepted as fulfilling the thesis requirement.

Date: 30.8.19
Place: **RRCAT, Indore**

(Guide, Prof. M. H. Modi)

[1] This page is to be included only for final submission after successful completion of viva voce.

** I could not attend the meeting, however, I have gone through the thesis and agree with the decision of Doctoral committee

STATEMENT BY AUTHOR

This dissertation has been submitted in partial fulfillment of requirements for an advanced degree at Homi Bhabha National Institute (HBNI) and is deposited in the Library to be made available to borrowers under rules of the HBNI.

Brief quotations from this dissertation are allowable without special permission, provided that accurate acknowledgement of source is made. Requests for permission for extended quotation from or reproduction of this manuscript in whole or in part may be granted by the Competent Authority of HBNI when in his or her judgment the proposed use of the material is in the interests of scholarship. In all other instances, however, permission must be obtained from the author.

Akash Deep

DECLARATION

I, hereby declare that the investigation presented in the thesis has been carried out by me. The work is original and has not been submitted earlier as a whole or in part for a degree / diploma at this or any other Institution / University.

Akash Deep

LIST OF PUBLICATIONS ARISING FROM THE THESIS

Journals

1. "Design of synchrotron radiation interferometer for beam size measurement at visible diagnostic beamline in Indus-2 SRS", **Akash Deep Garg**, M.H. Modi, and T.A. Puntambekar, *Nucl. Instrum. Methods Phys. Res. A,* **2018**, *902*, p 164-172.
2. "Studies of longitudinal profile of electron bunches and impedance measurements at Indus-2 synchrotron radiation source", **Akash Deep Garg**, S. Yadav, M. Kumar, B.B. Shrivastava, A. Ojha, and T.A. Puntambekar, *Nucl. Instrum. Methods Phys. Res. A,* **2016**, *814*, *p* 66-72.
3. "Design of X-ray diagnostic beamline for a synchrotron radiation source and measurement results", **Akash Deep Garg**, A.K. Karnewar, A. Ojha, B.B. Shrivastava, A.C. Holikatti, T.A. Puntambekar, and C.P. Navathe, *Nucl. Instrum. Methods Phys. Res. A,* **2014**, *15*, p 15-23.
4. "Measurement of bunch length in Indus-1 storage ring using fast photodiode", **Akash Deep Garg,** R.K. Nathwani, A.C. Holikatti, A.K. Karnewar, Y. Tyagi, S. Yadav, T.A. Puntambekar, and C.P. Navathe, *Rev. Sci. Instrum,* **2012**, *83*, pp 113304-113306.

Conferences

1. "Design of synchrotron radiation interferometer for beam size measurement in Indus-2 synchrotron radiation source", **Akash Deep Garg,** T.A. Puntambekar, *Indian Particle Accelerator Conference (**InPAC-2018**), RRCAT, Indore, India* (2018).

2. "Measurement of transverse beam parameters at X-ray diagnostic beamline in Indus-2 synchrotron radiation source", **Akash Deep Garg**, A. Ojha, A.K. Karnewar, B.B.

Shrivastava, A.C. Holikatti, T.A. Puntambekar, *Indian Particle Accelerator Conference (**InPAC-2015**), TIFR, Mumbai, India* (2015).

3. "Design of X-ray diagnostic beamline for Indus-2 synchrotron radiation source", **Akash Deep Garg,** A.K. Karnewar, D.K. Joshi, T.A. Puntambekar, *Indian Particle Accelerator Conference (**InPAC-2011**), IUAC, New Delhi, India* (2011).

4. "Measurement of longitudinal electron beam parameters using indigenously developed streak camera system at Indus-1 SRS", J. Upadhyay, **Akash Deep Garg**, Monika Jain, A. Ojha, Y. Tyagi, M.L. Sharma, T.A. Puntambekar, C.P. Navathe, and H.S. Vora, *Indian Particle Accelerator Conference (**InPAC-2015**), TIFR, Mumbai, India* (2015).

5. "Development of LabVIEW based image processing algorithm for online measurement of beam parameters at X-ray diagnostic beamline of Indus-2", A. Ojha, **Akash Deep Garg**, A.K. Karnewar, A.C. Holikatti, B.B. Shrivastava, T.A. Puntambekar , and C.P. Navathe, *Indian Particle Accelerator Conference (**InPAC-2013**), VECC, Kolkata, India* (2013).

6. "Development of data acquisition and control system for diagnostic beamlines of Indus-2", B.B. Shrivastava, A.C. Holikatti, A. Ojha, **Akash Deep Garg**, A.K. Karnewar, B.B. Sonawane, M. Chauhan, H.T. Satyawan, T.A. Puntambekar, C.P. Navathe, *Indian Particle Accelerator Conference (**InPAC-2013**), VECC, Kolkata, India* (2013).

Akash Deep

I dedicate this dissertation to my family…

ACKNOWLEDGEMENTS

It is my pleasure to acknowledge here the efforts of many colleagues who have made it possible for me to complete the research work described in this dissertation. Foremost among them is Shri **T.A. Puntambekar**, Head, Beam Diagnostics and Coolant Systems Division (BDCSD), RRCAT. He encouraged and guided me to pursue this research work. He has provided full support in various activities during the course of this work.

I would like to express my sincere gratitude to my Ph.D. guide Prof. **M.H. Modi**, Head, Soft X-ray Applications Lab., RRCAT, for his conscientious support, patience, motivation and knowledge sharing. His guidance helped me in all the time of research and writing of this thesis. I could not have imagined having a better advisor and mentor for my Ph.D. study.

Besides my guide, I would like to thank the rest of doctoral committee members: Prof. **Arup Banerjee**, Prof. **A. Chakrabarti**, Prof. **Vinit Kumar**, Prof. **M.P. Singh**, Prof. **H. Ghosh**, Prof. **Sataya Bulusu** (IIT, Indore) and Dr **Anit Gupta** (BARC-TIFR, Mumbai) for their insightful comments, encouragement, valuable guidance and support.

I am extremely grateful to Prof. **P.A. Naik**, Director RRCAT, who motivated, encouraged and extended full support to pursue the Ph.D. work. He guided me at many important technical points when he was the chairman of Doctoral committee.

It is also my pleasure to thank Prof. **P.D. Gupta**, former Director RRCAT, who granted me the permission and also encouraged to pursue the Ph.D. work. I am also very thankful to Prof. **S.M. Oak,** Prof. **G.S. Lodha,** Prof. **S.K. Gupta** (BARC, Mumbai) former doctoral committee members who have retired during this course for their guidance and support.

I am extremely thankful Dr. **Rohn Dowd** (Australian Synchrotron, Melbourne); Dr. **V. Simulak** and Dr. **G. Rehm** (DIAMOND Light Source, UK); Dr. **F. Sannibale** (Advanced Light Source, Lawrence Berkeley National Laboratory, US); and Dr. **L. Torino** (ALBA, Spain) for their technical guidance through e-mails in the beamline design, software simulations and data analysis of these measurements.

I want to thank my Ph.D. thesis examiners for their very insightful comments about my research work. Their comments have contributed significantly in the improvement of this thesis. On the same note, I would like to thank the members of my oral examination committee (Ph.D. Defense) especially Dr. **M.J. Boland** (Canadian Light Source, Saskatoon) for raising a number of interesting points of discussion and possible future research directions.

I would like to express my special appreciation and thanks to my Beam Diagnostics Section (BDS) colleagues Shri **Yogendra M. Sheth**, Shri **A.K. Karnewar**, Shri **Y. Tyagi**, Shri **S. Yadav**, Shri **Mukesh Kumar**, Shri **A. Ojha**, Shri **A.C. Holikatti**, Shri **B.B. Shrivastava**, Shri **R. Jain**, Shri **L.K. Babbar** for their continuous encouragement and support in our lab.

I am thankful to Shri **Gurnam Singh**, Dr **Tapas Ganguly**, Shri **A.D. Ghodke**, Dr **Anil Sinha**, Dr G. **Haridas**, Dr. **Amalendu Sharma**, Dr. **Pradeep Kumar Sharma**, Dr. **A.A. Fakhri** and Shri **R. Husain** for their technical guidance and urgent inputs in the beamline design and development work. I am also very thankful to our Indus operation crew for their always ready to help mode during various experimental studies at Indus.

Last but not the least, I would like to thank my family for their love, support and encouragement at each stage.

Akash Deep

CONTENTS

SYNOPSIS

Synchrotron radiation (SR) is the electromagnetic radiation emitted by relativistic charged particles when accelerated radially. It has many special characteristics which makes it attractive for various research applications, viz. high flux, high brightness, wavelength tunability, high stability, highly collimated beam and pulsed time structure. Any desired wavelength from IR to hard x-rays can be selected by using a monochromator. It has tremendous applications in the basic research. Initially SR was an inconvenient energy loss in particle accelerators made for high energy nuclear physics experiments. Later on dedicated electron accelerators known as Synchrotron Radiation Sources (SRSs) were built for obtaining SR, and to utilize the full potential of this radiation. Third generation SRS facilities are designed to provide high brightness by incorporating insertion devices (i.e. wiggler magnets, undulator magnets) [1][2]. Indus-2 is a third generation SRS with 2.5 GeV energy and 200 mA beam current operating at RRCAT, Indore, India [3]. Measurement and control of this highly intense, low emittance electron beam through narrow vacuum chambers poses a lot of challenges [4][5].

The motion of electrons in a SRS is guided by an external magnetic field lattice created by periodic arrangement of dipoles (DP), quadrupoles (QP), sextupoles (SP) and steering magnets. The electrons confined within the bunch execute betatron oscillations about the closed orbit in transverse planes and synchrotron oscillations

about the synchronous phase in longitudinal plane. The electrons within a bunch are continuously scattered due to elastic and inelastic scattering within the same bunch (Touschek effect), and also with the residual atoms present in the vacuum chamber [6]. The quality of the stored beam also depends upon the electromagnetic interactions of the beam with its surroundings, such as radio frequency (RF) cavities, narrow gap insertion devices (IDs) and various discontinuities along the vacuum chamber. These interactions can also deteriorate the quality of stored beam or may make the beam unstable [7]. Further the demand to get high brightness SR has led to the production of beams with low emittance. However particles confined in the smaller phase space are more prone to instability or beam loss. Therefore in modern SRS facilities producing smaller and smaller beam (for higher SR brightness) puts more and more stringent requirements on the performance of the beam diagnostics [2]. The measurement and analysis of beam parameters is very important and it provides the key information for improving the performance of the SRS.

Although various types of diagnostic devices are installed in the ring, but there are certain beam parameters which can be better measured and analysed by optical methods such as synchrotron radiation [8][9], optical transition radiation [10][11] and diffraction radiation [12]. These are based on the principle that the emitted radiation has inherited information of the particle distribution from the electron beam. SR is a very versatile, efficient and non-destructive tool for characterization of the relativistic charged particle beam.

Precise measurement of the particle beam emittance is a very important input to characterize the performance of any accelerator or SRS. In most of the accelerators, beam emittance is monitored through the measurement of transverse beam size [13]. In modern low-emittance rings, it has become possible to reduce the vertical emittance to a few pm.rad [14][15]. The corresponding vertical beam size reduces to

few microns level in the bending magnet sections. Precise measurement of such a small transverse beam size is a very challenging task in these rings or SRSs. Measurement of transverse beam size by visible SR imaging is limited by diffraction. X-ray imaging optics using Fresnel zone plates (FZP) [16], compound refractive lenses (CRL) [17], Kirkpatrick and Baez optics [18][19], and pinhole camera [20][21][22], are commonly used for the transverse measurements. Each method has its own advantages and limitations. FZP and CRL have better resolution, but to avoid large chromatic aberrations both require monochromatic light [23]. Resultantly, the photon flux arriving at the detector becomes very low and difficult to measure at low beam currents. An x-ray pinhole camera is widely used because of its simple setup, moderate resolution and high practical reliability [9]. The SR interferometer method developed by T. Mitsuhashi [24] has better spatial resolution than imaging method. Its vertical resolution is also limited by the natural opening angle of SR. π-polarization is another useful method for measuring vertical beam size with a resolution of few microns [25]. Although both are suitable for small beam sizes, but π-polarisation is confined only to the vertical measurements. The longitudinal information of the beam is measured from visible SR by using fast photo detectors [8].

The main motivations for pursuing this work are

i. Design and development of diagnostic beamlines at the Indus-2 SRS.
ii. Studies of the longitudinal and transverse beam parameters of Indus-2 by using diagnostic beamlines.
iii. Design study of the SR interferometer for measurements of transverse beam sizes with a spatial resolution of few microns in Indus-2 and future high brightness SRSs in India.

In view of the first objective, two diagnostic beamlines, viz. visible diagnostic beamline (V-DBL, BL-23) and X-ray diagnostic beamline (X-DBL, BL-24) have been designed and developed at Indus-2 [26][27][28]. X-DBL is used to perform transverse measurements by using pinhole array system. It can measure beam size, beam emittance, beam position and beam divergence. The pinhole system provides good spatial resolution (~ 15 μm) for wide range of beam movements and beam currents, which was very much required at the initial stages of operation and optimization in any SRS. V-DBL uses the visible portion from wide SR spectrum for longitudinal measurements. Measurement of beam parameters such as bunch length, bunch separation and bunch filling pattern are performed by using streak camera [29], fast photo receiver and avalanche photodiode. These beamlines are used regularly for the online monitoring (at 1 Hz) of beam parameters, and also for the dedicated beam physics experiments.

In view of the second objective, studies of the longitudinal profile of electron bunch and impedance measurement of Indus-2 SRS were carried out by using dual sweep synchroscan streak camera at V-DBL. Transverse measurements related to beam size, beam emittance, beam position, SR beam position and dispersion were performed at X-DBL.

In view of the third objective, design study of SRI was carried out for the beam diagnostics of Indus-2 SRS. SRI technique is being used in a few advanced SRS facilities to measure the beam size through the analysis of the spatial coherence of the SR [30][31]. It can measure transversal beam sizes down to a few microns with visible SR. This method also provides the possibility of bunch resolved measurements with gating techniques. It will be useful for measurement and studies during low emittance operation of Indus-2 and future high brightness SRSs in India.

The thesis work reported here comprises six chapters. Chapter 1 gives a brief introduction about Indus SRS, SR based diagnostics and motivation for the present work. The next three chapters provide detailed description of work related to design of two diagnostic beamlines at Indus-2 SRS [26] and measurement of important transverse and longitudinal parameters of electron beam [32][33]. Optical design of SRI based diagnostics for Indus-2 is presented in Chapter 5 [34]. Finally summary of the research work pursued for the thesis is presented in Chapter 6. Brief description of the each chapter is given below.

Chapter 1 highlights the motivation and importance of the work done in this thesis. A brief introduction of Indus-2 SRS, beam parameters and measurement techniques are presented. Optical techniques used to measure the transverse beam size are discussed in detail. Literature survey of the existing diagnostic beamlines with an aim to develop diagnostic beamlines at Indus-2 and measure its important beam parameters is presented. A brief classification of x-ray diagnostic techniques based on focusing methods, viz. reflection, refraction and diffraction is presented. The choice of technique depends upon the requirement of spatial resolution and system dynamic range for beam movements and beam currents. As most of detectors are available in the visible spectral range, so it has immense scope for fast measurements. A brief introduction to visible diagnostics is also discussed here.

In **Chapter 2**, details of the design and development of diagnostic beamlines at Indus-2 is discussed. X-ray diagnostic beamline is based on pinhole array system which can measure the beam size and beam emittance. Size of the pinhole and pitch are optimized based on the minimization of spread function, and the requirement of divergence measurements under various dynamic conditions. A staggered pair blade monitor (SPM) is also installed in parallel to pinhole array for the measurement of

photon beam position at 8 m from the source point [26]. V-DBL design is based on a water cooled primary mirror, which is used to extract visible light from the wide SR spectrum [35]. In this beamline, the visible light is focused on different detectors such as a streak camera system, fast photo receiver and other instruments kept in a dark room. Optimization results of the angular acceptance and spread function of the visible beamline are also presented. Beamline provides online information of the beam parameters which is very useful for longitudinal beam dynamic studies even during the beam injection.

In **Chapter 3**, studies of the longitudinal profile of electron bunch and impedance measurements of Indus-2 SRS are presented. The longitudinal profile of electron bunch is analyzed in a single bunch mode. Measurements carried at injection energy (550 MeV) and at final beam energy (2.5 GeV) by using dual sweep synchroscan streak camera at V-DBL are discussed. The effects of wakefield generated interactions between the circulating electrons and the surrounding vacuum chamber are analyzed in terms of the measured effects on longitudinal beam distribution. The equilibrium charge distribution of a bunch is analysed by using solutions of the Haissinski equation [36]. The major factors influencing the bunch lengthening, potential-well distortion and microwave instability are also discussed. Longitudinal distribution fitted with analytical solutions for different longitudinal coupling impedances is also discussed [37][38]. The impedance of the storage ring is obtained from the measured bunch lengthening with different impedance models [31]. The impedance of storage ring obtained by a series R+L impedance model predicts the values of resistance and inductance as 1350 ± 125 Ω and 180 ± 25 nH respectively. These results are also compared with the values obtained from the measured synchronous phase advancing and scaling laws. These studies provide very useful inputs in calculation of various thresholds for beam instabilities by beam physicists. Before doing these studies at Indus-2, we have learnt a lot by measurement

of bunch length in Indus-1 SRS by using a fast photo receiver system. Results of these measurements are also discussed briefly at the end of this chapter.

In **Chapter 4,** the analysis of transverse beam parameters is presented. Modified theoretical equations for online measurements of source position and emission angle with pinhole array optics are also presented. Results of online measurement are compared with the measurements at an independent x-ray beam position monitor (SPM) installed in the X-DBL. Measured values from both systems found to be within ± 12 μm (or $\pm$ 1.5 μrad) for sufficiently wide range of beam movement [26]. Results of experimental measurement of beam dispersion by changing frequency of RF cavity are discussed. X-DBL is used regularly for online measurements of transverse beam parameters. Measurement results of beam position, beam size and beam emittance with natural decay of beam current in Indus-2 are presented. For Indus-2, natural horizontal and vertical beam sizes obtained at the BL-24 source point are 357.2 μm and 47.6 μm respectively at 2.5 GeV. Measurement results of the beam sizes during low emittance trial operations of Indus-2 (~45 nm. rad) are also discussed [5].

Chapter 5 describes the physics design of SRI for beam diagnostics in the Indus-2 SRS. A quad slit system is optimized to measure the beam sizes in both planes. The theoretical background of this method is described in the framework of wave-optics. SRI was applied for the first time at the KEK-PF to measure small beam sizes with a superior resolution than beam imaging [39]. Nowadays, SRI is being used in many advanced SRSs. It is based on Van Cittert-Zernike theorem relating transverse source profile to spatial coherence, and the particle beam size can be inferred from the fringe contrast [40][41]. Results of simulations of this SRI system using the Synchrotron Radiation Workshop (SRW) code [42] and the visibility

analysis of interferogram by horizontal and vertical curve fitting are also presented. By using SRI, transverse beam sizes down to few microns can be measured. Transverse emittance can also be evaluated from the measured beam size by using known optics (Twiss) parameters at the source point. This work will be useful for measuring very small beam sizes during low emittance operations of Indus-2 SRS, and for future high brightness SRSs in India. Even full reconstruction of beam profile under different beam couplings is possible by rotating double-pinhole mask [30].

In **Chapter 6**, the summary of the thesis work and the future scope are discussed.

LIST OF FIGURES

LIST OF TABLES

NOMENCLATURE

SR	Synchrotron Radiation
SRS	Synchrotron Radiation Source
X-DBL	X-ray Diagnostic Beamline
V-DBL	Visible Diagnostic Beamline
FE	Front-end (of beamlines)
BPM	Beam Position Monitor
FZP	Fresnel Zone Plate
CRL	Compound Refractive Lens
SPM	Staggered Pair blade Monitor
SC	Streak Camera
OTR	Optical Transition Radiation
DR	Diffraction Radiation
BR	Bremsstrahlung Radiation
PWD	Potential Well Distortion
MWI	Microwave Instability
SRI	Synchrotron Radiation Interferometer

SRW	Synchrotron Radiation Workshop
ID	Insertion Device
SOFB	Slow Orbit Feedback (System)
FOFB	Fast Orbit Feedback (System)
BS	Booster Synchrotron
TLs	Transfer Lines
DP	Dipole Magnet
QP	Quadrupole Magnet
SP	Sextupole Magnet
RF	Radio-Frequency
SBE	Single Bunch Effects
MBE	Multi Bunch Effects
TCSPC	Time Correlated Single Photon Counting

Chapter 1 Introduction

1.1 Synchrotron radiation source

Synchrotron radiation is produced when a charged particle moving at a relativistic speed is forced to change its direction by applying magnetic field. The combination of Lorentz contraction and the Doppler shift for a relativistic particle turns the wavelength of cm length scale into nm length scale, thus making SR the best possible x-ray source [43]. SR has many special characteristics which makes it powerful diagnostics tool in material science, viz. high photon flux, high brightness [44] (many orders of magnitude brighter than conventional sources), wavelength tunability, highly collimated beam, pulse structure and polarisation [45][46].

Initially the experiments with SR were parasitic to the high energy nuclear physics experiments, and SR loss was an inconvenient energy loss in particle accelerators. Later on dedicated electron accelerators known as *synchrotron radiation sources* were built for obtaining SR and to utilize the full potential of these radiations. SR has tremendous applications in basic research. With recent advances in technology and quality control of the emitted SR, SRSs are divided into four categories [47][48].

a) **First generation:** These accelerators were mainly built for high-energy nuclear physics experiments, and SR experiments were parasitic. These machines were not optimized for

brightness, and were typical accelerators where the electron beams were constantly injected, accelerated, and extracted (rather than storing i.e. storage rings).

b) Second generation: These were the dedicated SRSs and SR from bending magnets was used for basic research. The numbers of straight sections in the accelerator were limited and the SR brightness was also less than 10^{12} photons /s /mm^2 /mrad^2 /0.1 % bandwidth (the standard units of the spectral brightness of an x-ray source).

c) Third generation: In order to increase the source brightness, the emittance of the particle beam must be decreased. So, third generation SRSs were designed to provide high brightness SR (typically 10^{18} photons /s /mm^2 /mrad^2 /0.1 % bandwidth [49]), and a large number of straight sections were provided for incorporating insertion devices (i.e. wiggler and undulator magnets) [1][2]. Insertion devices act like a sequence of bending magnets with alternating polarities. In undulator beam deflections are very small, and it results in coherent interference of the emitted light.

d) Fourth generation: These SRSs are based on what is called *multiparticle coherent emission,* in which coherence along the path of the electrons (or longitudinal coherence) plays a major role [47][50]. This is achieved by micro bunching of the electrons on a length scale that is comparable to or smaller than the scale of the wavelengths (λ) emitted. SR emission becomes proportional to the square of the number of electrons (N), and there is very large enhancement in light emission (typically $N \sim 10^{12}$). These sources are designed to reach the theoretical diffraction limit of source emittance $\left(\varepsilon_x \leq \lambda/_{4\pi}\right)$, i.e. typically less than 80 pm.rad for soft x-rays of $\lambda \approx 1$ nm) [50]. Energy recovery linac (ERL) [51] and free electron laser (FEL) [1][52] are the present generation SRSs.

1.2 Indus-1 and Indus-2 synchrotron radiation source

1.2.1 Injector system

Indus-1 and Indus-2 are the two SRS facilities operating at RRCAT, Indore, INDIA [53]. These share a common injector system consisting of Microtron, Booster Synchrotron (BS) and transfer lines (TL) [54][55]. A schematic view of the Indus accelerator facility is shown in Figure 1.1. The electrons are generated and accelerated to 20 MeV in the Microtron (20 mA, 500 ns pulse width and rep rate of 1 Hz). These electron pulses are injected into the BS through a transfer line TL-1. Beam acceleration takes place in BS, and its energy is increased from 20 MeV to 450 MeV / 550 MeV. The electron beam (at 450 MeV) is extracted from the BS and then transported to the Indus-1 storage ring through the transfer line TL-2. This process of production, acceleration and injection is repeated at 1 Hz till the beam current of 125 mA is accumulated in the Indus-1 storage ring.

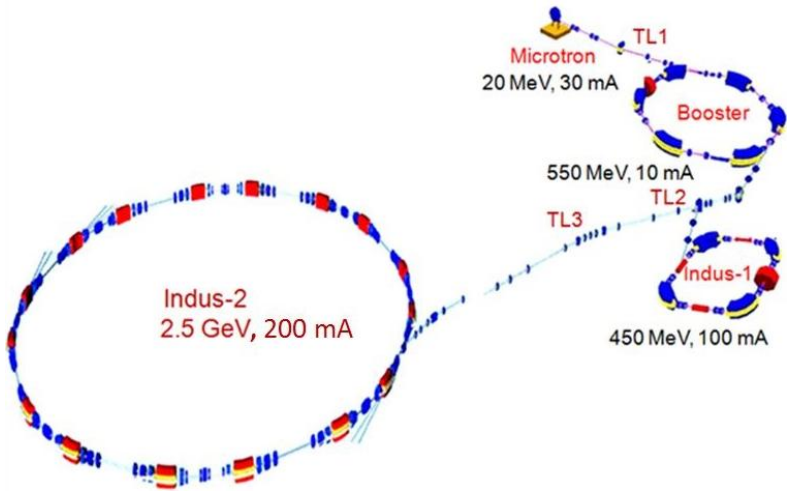

Figure 1.1: *Schematic view of the Indus accelerator facility at RRCAT.*

For the injection into Indus-2, a 550 MeV beam is extracted from the BS and transported to Indus-2 through the transfer lines TL-2 and TL-3. Injection process continues till the beam current reaches a desired level of 200 mA. Once beam current is filled, its beam energy is ramped from 550 MeV to 2.5 GeV.

1.2.2 Indus-1 and Indus-2

Indus-1 is a 450 MeV electron storage ring designed to satisfy the SR user's requirement in the wavelength range of 10-1000 Å. The magnetic lattice of the ring has four superperiods with a total circumference of 18.96 m. Each superperiod consists of a combined function 90° bending magnets (with a field index of 0.5), two pairs of quadrupoles, one pair of sextupoles (for chromaticity correction) and a 1.3 m long straight section. The injection septum, the injection kicker and the RF cavity (31.613 MHz) are installed in straight section S1, S3 and S4 respectively. The SR flux is tapped from 3 bending magnets, and each bending magnet vacuum chamber has two ports (10° and 50°). Indus-1 provides a broad SR spectrum extending from far infrared to soft x-ray region with a critical wavelength of 61 Å from its four bending magnets (1.5 T). This spectrum covers absorption thresholds of many important elements for basic research. Presently six SR user beamlines are operational at Indus-1 [56]. There is also a provision to incorporate a 3 T wiggler (ID) in its straight section S2, which will provide SR with critical wavelength of 31 Å. The magnetic lattices of Indus-1 and Indus-2 SRSs are shown in Figure 1.2.

Indus-2 is a third generation SRS with 2.5 GeV electron beam energy and 200 mA beam current. It is a booster cum storage ring, where the electrons injected at 550 MeV are

accelerated to 2.5 GeV, and beam is kept stored for several hours. Indus-2 storage ring has a circumference of ~172 m, and magnets are arranged in a periodic fashion forming 8 unit cells of an expanded Chasman Green lattice. In Indus-2, five long straight sections (~ 4.6 m) are kept for incorporating five insertion devices (IDs).

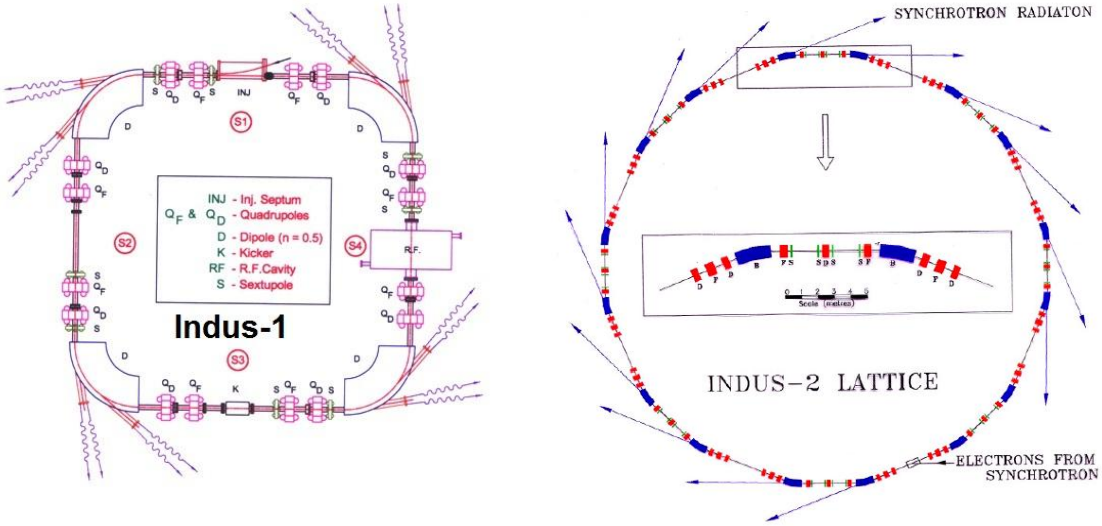

Figure 1.2: *Magnetic lattices of Indus-1 and Indus-2 synchrotron radiation source.*

Each unit cell has two 22.5˚ dipole magnets (DP), four focusing and five defocusing quadrupoles (QP), and four sextupoles (SP). A triplet of QPs controls the dispersion in the achromat section; two QP triplets are used for beam sizes adjustment in the long straight sections and four SPs are used for the correction of chromaticities in the achromat section [57]. Closed orbit distortion (COD) correction is carried out by horizontal (48 Nos.) and vertical (40 Nos.) steering magnets distributed over the ring. A set of 6 RF cavities operating at frequency of 505.812 MHz provides the required energy for beam acceleration (from 550

MeV to 2.5 GeV) and SR loss compensation. The critical wavelength from 1.5 T dipole magnets is ~2 Å. Important design parameters of the Indus-2 are shown in Table 1.1.

Table 1.1: *Various design parameters of the Indus-2 SRS.*

Electron energy (*GeV*)	2.5
Maximum current (*mA*)	200
Number of super periods	8
Circumference (*m*)	172.47
Harmonic number	291
Dipole field (*T*)	1.502
Bending radius (*m*)	5.552
Bending angle (*degree*)	22.5
Tune points	9.2, 5.2
$\epsilon_x\ (nm.rad)$ /$\epsilon_y\ (nm.rad)$	58 / 5.8
σ_z (*mm*)	16
Energy spread	0.0001
γ^{-1} (μrad)	204.4
RF frequency (*MHz*)	505.812
Momentum compaction factor	0.0071
Natural energy spread (*RMS*)	0.0009
Synchrotron tune at 550 *MeV* / 2.5 *GeV*	0.0212/ 0.0123
Natural bunch length (*ps*) at 550 *MeV* / 2.5 *GeV*	17.7 / 43
Average beam size (RMS) (μm)	250
Magnets DP/QP/SP	16/72/32
Critical energy (*keV*)	6.242
Total power/revolution (*kW*)	125
Linear power density (*W/mrad*)	20

Indus-2 can accommodate 21 bending magnet (BM) and 5 insertion device (ID) beamlines. Presently, sixteen BM beamlines have been commissioned and are being used by the researchers from different laboratories, universities and national institutes [58] [59]. These beamlines can be used for basic studies related to Protein crystallography, Angle dispersive XRD (ADXRD), Energy dispersive XRD (EDXRD) [60], Extreme conditions AD/ED XRD, EXAFS, X-ray fluorescence micro-probe [61], X-ray photoelectron spectroscopy, Grazing incidence x-ray scattering, soft x-ray reflectivity [62], X-ray imaging, lithography [63][64] and various engineering applications [65]. A number of material science related problems have been investigated using these beamlines and several papers have already been published.

Three undulators (two planar and one APPLE type) have been commissioned for 3 ID based beamlines, viz. Atomic, Molecular and Optical Science (AMOS), Angle resolved PES, and X-ray Magnetic Circular Dichroism (MCD) [66]. Two wigglers, a 3.5 Tesla superconducting multipole wiggler (SMPW) and a 5 Tesla superconducting wavelength shifter (SWLS) will be installed in Indus-2 during the next few years.

1.3 Beam parameters

The motion of electrons in an accelerator is guided by the magnetic lattice created by periodic arrangement of dipoles, quadrupoles, sextupoles and various steering magnets. Magnetic lattice of a SRS is designed to focus the electron beam. The combination of high intensity and low emittance (i.e. small beam size and small divergence) results in increase of the source

brightness. The electrons confined within the bunch execute betatron oscillations about the closed orbit in transverse planes and synchrotron oscillations with respect to synchronous phase in longitudinal plane. The electrons within a bunch are continuously scattered due to elastic and inelastic scattering within the same bunch (Touschek effect) and with the residual atoms present in the vacuum chamber [67]. Therefore it is important to understand the dynamics of charge particles in a magnetic lattice for controlling the quality of emitted SR.

1.3.1 Transverse beam dynamics

1.3.1.1 Equation of motion (Hill's equation)

The equation of motion of charged particles can be derived by using Lorentz force, *hard edge model* for magnetic field (i.e. magnetic field takes the step change along the length of the magnet) and by keeping only linear terms (for DPs and QPs). Let ρ_0 be the radius of curvature for the ideal (or design) orbit and a particle is displaced with respect to this design orbit as shown in Figure 1.3. The position vector $\vec{R}$ of any point (say *P*), and the force exerted on the charge particle can be written as

$$\vec{R} = r\,\hat{x} + y\,\hat{y} \tag{1.1}$$

and

$$e\left(\vec{v} \times \vec{B}\right) = e\left[-v_S B_y\,\hat{x} + v_S B_x\,\hat{y} + \left(v_x B_y - v_y B_x\right)\hat{s}\right] \tag{1.2}$$

Generally velocity and acceleration is obtained from time derivative of $\vec{R}$. But in accelerators main interest is in the particle motion along the design trajectory i.e. how the motion evolves with respect to the design trajectory instead of time. So time parameter (*t*) is replaced with

parameter (s), and by taking the component of B as zero in the direction of motion, the equation of motion in x-direction becomes [68]

$$\frac{d^2x}{ds^2} - \frac{\rho_0 + x}{{\rho_0}^2} = -\frac{B_y}{B\rho_0}\left(1 + \frac{x}{\rho_0}\right)^2 \tag{1.3}$$

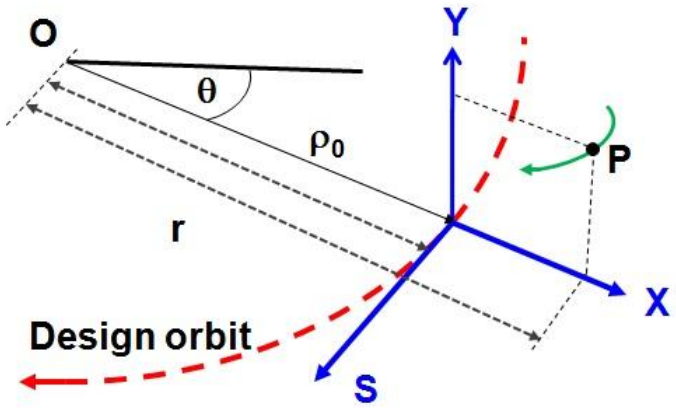

Figure 1.3: *Motion of the charged particle on a displaced orbit with respect to ideal orbit.*

This is a nonlinear equation for particle motion in the horizontal plane. With substitution of $B_y = B_{y0} + \frac{\partial B_y}{\partial x}x$ and retaining the terms only up to first order in x (i.e. close to design orbit or in paraxial region) final equation becomes

$$\frac{\partial^2 x}{\partial s^2} + \left(\frac{1}{{\rho_0}^2} + \frac{1}{B\rho_0}\frac{\partial B_y}{\partial x}\right)x = 0 \tag{1.4}$$

This equation is valid in the bending magnet as well as in QP (linear terms). The second term in the bracket is the QP strength i.e. a focusing term, $k = \frac{{\partial B_y}/{\partial x}}{B\rho_0} = \frac{g}{B\rho_0}$ where g is the field gradient. The first term $(1/{\rho_0}^2)$ is a dipolar term and is on the same footing as of the QP strength k. Similarly the equation of motion in vertical plane can also be derived as

$$\frac{d^2y}{ds^2} - \frac{1}{B\rho_0}\frac{\partial B_y}{\partial x}y = 0 \tag{1.5}$$

Eq. (1.4) and Eq. (1.5) can be written in general form as

$$\frac{d^2x}{ds^2} + K(s)\,x = 0 \tag{1.6}$$

where $K = \frac{1}{{\rho_0}^2} + k$ is the strength of applied magnetic field. In the vertical plane, the form of equation is same but K = -*k* (as there is no bending in the vertical plane). The negative sign of *k* shows focusing/ defocusing action is opposite to the horizontal plane.

This equation is similar to equation of simple harmonic motion and is known as Hill's equation (i.e. equation of motion of charge particle in linear approximation). However, the coefficient *K* here is not a constant; but a function of the independent parameter s. Therefore this equation shows that there is some kind of oscillatory motion (not SHM) and the oscillations are called betatron oscillations. In accelerator optics, *K* is a constant in each element i.e. *K* is a *piecewise constant*. Therefore equation of motion is solved in each magnetic element separately and then all the solutions are combined to get overall behaviour of the magnetic lattice.

1.3.1.2 Courant Snyder invariant, Twiss parameters and beam emittance

As discussed earlier, the Hill's equation $x'' + K(s)x = 0$ has coefficient K which is a function of s. Important beam dynamics information can be obtained by assuming initial solution of Hill's equation as

$$x = A\sqrt{\beta(s)}\ \cos\{\,\phi(s) + \phi_0\,\} \tag{1.7}$$

where the amplitude term $A\sqrt{\beta(s)}$ has two components, constant A and $\beta(s)$ as a function of s. This equation shows the betatron oscillations with initial phase ϕ_0. By taking derivative of Eq. (1.7), and substituting for *sine* and *cosine* values we get an important equation as

$$\gamma\, x^2 + 2\alpha\, xx' + \beta\, x'^2 = A^2 \tag{1.8}$$

where three parameters $\alpha = -\frac{1}{2}\frac{d\beta}{ds}$, $\beta = \left(\frac{d\phi}{ds}\right)^{-1}$ and $\gamma = \frac{1+\alpha^2}{\beta}$ are known as *Twiss Parameter or lattice parameter*, which are the function of *s* and decided by magnetic lattice. This equation represents an ellipse, with position dependent terms on left side and a constant term on right side [69]. Therefore, for any particular particle with initial conditions (x, x'), this expression shows the motion invariant known as *Courant Snyder invariant.* Thus as the particle passes through the magnetic channel, its position (x) and slope of the trajectory (x') changes but the combination: $\gamma\, x^2 + 2\alpha\, xx' + \beta\, x'^2$ will remain a constant.

1.3.1.3 Beam size and beam emittance

Various charge particles travelling around the accelerator ring are performing betatron oscillations, and individual particles moves in phase space along the contour of an ellipse (*Courant Snyder invariant*). The area of the ellipse traced by outermost particle in the beam (i.e. largest ellipse) is known as the *beam emittance* ($\varepsilon = \pi A^2$). The size of beam envelope (or *beam size*) is given by $\sigma(s) = \sqrt{\epsilon\,\beta(s)}$, which is a function of s i.e. location. Therefore

beam emittance is the phase space area of the beam, and it represents the information of both beam size as well as beam divergence.

In accelerator although beam emittance remains a constant but beam ellipse keeps on changing its orientation and aspect ratio (shape) during its propagation through the various accelerator components as shown in Figure 1.4.

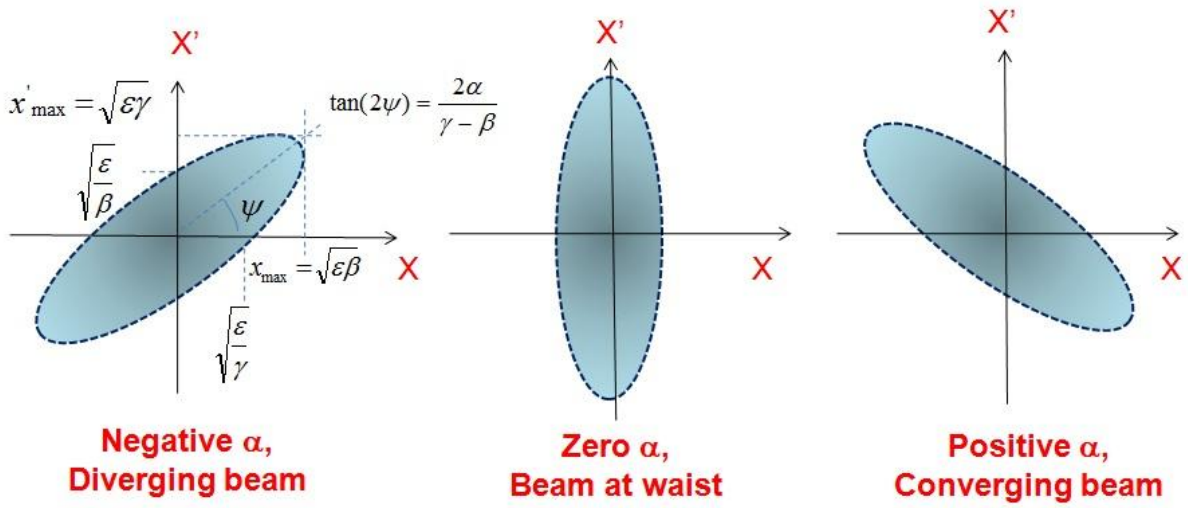

Figure 1.4: *Propagation of the phase space ellipse in an accelerator, Twiss parameters and their correlation with beam size and beam divergence.*

According to the *Liouville's theorem*, phase-space density of the Hamiltonian flow is conserved. Theoretically emittance is the phase space area, and it should also remain conserved. We have also found that area of the ellipse is constant i.e. the emittance is a constant of motion at a particular energy. But, the presence of non-linear forces and other errors in the accelerator causes an apparent growth of the beam emittance (by keeping local density conserved).

During the acceleration when a charge particle passes through the RF-cavity, its longitudinal momentum (p_s) increases, but transverse momentum remains unchanged. Thus the angle $\left(x' = {p_x}/{p_s}\right)$ decreases after each passing through the RF cavity, and it results to beam emittance decreases. This process is known as *adiabatic damping*. Therefore in order to define an emittance which is invariant even during acceleration, *normalized beam emittance* is generally defined by $\epsilon_N = \epsilon\beta\gamma$, where β, γ are the relativistic parameters.

1.3.2 Longitudinal beam dynamics

In RF acceleration, only a very small portion of the RF field cycle is used for particle acceleration, and it produces *bunches* of the charged particles. At each turn, charged particle should reach in the RF at a proper phase with its fields. Similar to transverse beam dynamics, where an ideal charged particle which always follows the design trajectory (i.e. x=0, y=0; x'=0, y'=0) and has the design momentum (i.e. $\delta = {\Delta p}/{p} = 0$), in longitudinal plane a charged particle which always comes at the same phase of RF acceleration cycle is called *synchronous particle*, and that particular phase is known as the *synchronous phase*.

In case of *storage ring* energy of the charged particle remains constant i.e. energy loss as SR (E_{SR}) should be equal to energy gain from the RF ($eV_{RF}\sin(\phi_S) = E_{SR}$), and the synchronous phase will be

$$\phi_S = \sin^{-1}\left(\frac{E_{SR}}{eV_{RF}}\right) \tag{1.9}$$

If the energy loss is higher than the energy gain, then energy of the charged particles will keeps on decreasing, and after few turns it may hit the vacuum chamber. Thus the above relation provides the minimum required RF voltage.

In case of *synchrotrons*, the energy of the charged particles is also increased from the initial (injection energy) to the desired energy level by keeping its orbit constant. Therefore in order to keep the orbit fixed, magnetic fields are also increased in synchronous with the increasing energy. So energy requirement for both SR loss and momentum gain is compensated by RF cavities and the synchronous phase will become

$$\phi_S = \sin^{-1}\left(\frac{E_{SR} + 2\pi e\rho^2 \frac{dB}{dt}}{eV_{RF}}\right) \tag{1.10}$$

where ρ is the bending magnet radius V_{RF} is the RF voltage and B is the magnetic field.

1.3.2.1 Phase focusing

The charge particles are in the form of bunches, and in each bunch, some particles are always deviated from the synchronous phase. Therefore to maintain stability of the beam, there should be some restoring force acting on these deviated particles to bring it back towards the synchronous phase. This is obtained under certain operating conditions and the phenomenon is known as *phase focusing*.

In non-relativistic cases, the velocity of particles (or relativistic factor β) changes during the energy gain from RF cavities. Therefore the revolution time of the particle also changes. So in order to maintain the synchronicity conditions, it is required to increase the frequency of RF in synchronous with the particle energy gain. Whereas for the relativistic

cases, the velocity of particles remains almost constant, and there is no need to change the RF frequency. But the energy loss in the form of SR should be compensated. This energy loss is fulfilled by equal energy gain from the RF cavities to keep the energy of the charged particle a constant in storage rings.

Frequency or phase slip factor (η) give the information about phase difference for an off momentum particle with respect to synchronous particle in one revolution. Mathematically it is written as

$$\eta = \frac{\Delta T_{rev}/T_{rev}}{\delta} \tag{1.11}$$

or

$$\eta = \frac{-\Delta f_{rev}/f_{rev}}{\delta} \tag{1.12}$$

where $T_{rev} = \frac{L}{\beta c}$ is the revolution time of the charged particle, L is the circumference of ring, βc is the velocity of particles, ΔT_{rev} is the change in revolution time for an off momentum particle, and δ is the energy difference with respect to ideal particle. By taking derivative of T_{rev} it becomes

$$\frac{\Delta T_{rev}/T_{rev}}{\delta} = \frac{\Delta L/L}{\delta} - \frac{\Delta \beta/\beta}{\delta} \tag{1.13}$$

By using the definition of momentum compaction factor α, frequency slip factor η, and relativistic relation $\frac{\Delta\beta/\beta}{\delta} = \frac{1}{\gamma^2}$ in the above equation, it becomes

$$\eta = \alpha - \frac{1}{\gamma^2} \tag{1.14}$$

The parameter η governs the actual phase (in RF field) for an off momentum particle, and is a key parameter in longitudinal dynamics. From the definition of η, there are two competitive processes involved during the particle acceleration (in Eq. (1.13)), viz. path length change and velocity change. If the velocity factor is more than the path length factor, η becomes negative i.e. higher energy particles have less revolution time. If the path length factor has greater impact, then η becomes positive and higher energy particles take more time to revolve. When these two processes get equalized, η becomes zero i.e. revolution time does not depends on the momentum deviation (at least in linear domain). The energy at which this happens $\left(\gamma_t = {}^{1}/_{\sqrt{\alpha}}\right)$ is known as g*amma transition.*

In the relativistic domain, the change in particle velocity is almost zero and only path length factor plays a role in defining the frequency slip factor. This is the case for electron synchrotrons ($\eta \approx \alpha$), thus all electron synchrotrons are operated above gamma transition. For proton synchrotron, the injection energy is very low and when beam is accelerated to very high energies, it crosses γ_t. Therefore in order to meet the stability condition, electron machines (working above gamma transition) and proton machines (working below transition) are operated at falling and rising part of the RF cycle respectively.

1.3.2.2 Synchrotron oscillations and momentum acceptance

The change in RF phase in one revolution can be written as

$$\frac{d(\Delta\phi)}{dn} = \omega_{RF}\,\Delta T_{rev} = \omega_{RF}\;T_{rev}\,\eta\,\frac{\Delta p}{p} \tag{1.15}$$

where $\Delta\phi$ is the phase change with respect to synchronous particle, and n is the number of turns. To find how the motion of the charged particle evolves longitudinally with successive turns for a displaced particle ($\Delta\phi \neq 0$ or $\frac{\Delta p}{p} \neq 0$) w.r.t. a synchronous particle (or ϕ_S), the derived equation of motion in longitudinal plane is [68]

$$\frac{d^2(\Delta\phi)}{dn^2} = \frac{2\pi h\eta eV}{\beta^2 E}[\sin(\phi_S + \Delta\phi) - sin(\phi_S)] \tag{1.16}$$

It can be discussed by taking following two cases

Case I: For small amplitudes i.e. $\Delta\phi \ll \phi_S$, Eq. (1.16) becomes

$$\frac{d^2(\Delta\phi)}{dn^2} = \left[\frac{2\pi h\eta eV}{\beta^2 E}\cos\phi_S\right]\Delta\phi \tag{1.17}$$

This is a kind of simple harmonic oscillations in phase ($\Delta\phi$) or energy (ΔE) w.r.t. synchronous phase ϕ_S (or energy E) called *synchrotron oscillation*. The *synchrotron tune* (ν_S) is the number of synchrotron oscillation per turn, and can be written as

$$\nu_S = \sqrt{\frac{2\pi h\eta eV}{\beta^2 E}cos\,\phi_S} \tag{1.18}$$

Case II: For large amplitudes, Eq. (1.16) is very cumbersome to solve analytically, and is solved by numerical techniques. But by coupling the equation in $d(\Delta\phi)/dn$ and $\Delta E/E$, we can get an equation in $\Delta\phi$, $\Delta E/E$ and n. The plot of phase change ($\Delta\phi$) and energy change ($\Delta E/E$) with number of turns (n) will look as shown below in Figure 1.5.

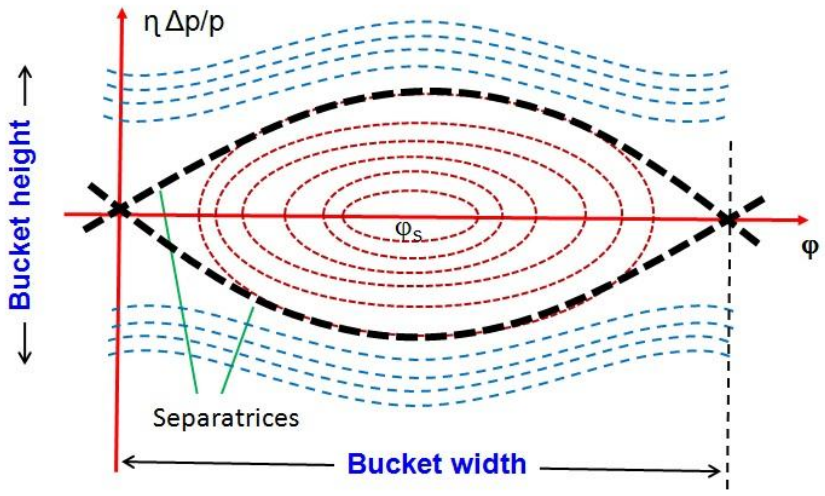

Figure 1.5: *Phase space diagram of the longitudinal beam dynamics with stable and unstable synchrotron oscillations.*

For small amplitudes i.e. small $\Delta\phi$ as well as small $\Delta E/E$ ($\Delta p/p$), we get an ellipse. As the amplitude increases, ellipse becomes distorted and particle starts exhibiting non-periodic motion. Beyond a certain range, the particle motion becomes unbound i.e. unstable. The curve separating the zone of stable and unstable motion is known as s*eperatrix*. The stable zone is also known as *RF bucket* as it is decided by the RF parameters. The area of stable phase space (in analogy to the emittance in transverse phase space) is called *longitudinal emittance*.

In these oscillations, the maximum $\Delta p/p$ for stable oscillations is determined by the RF-bucket i.e. the RF bucket provides the maximum $\Delta p/p$ which can be handled by the machine. In transverse plane, the maximum orbit displacement due to $\Delta p/p$ factor is $\eta\Delta p/p$, and it should be less than the stable aperture of accelerator. Thus aperture also provides the

maximum $\Delta p/p$ which can be handled by the machine. The least of these two $\Delta p/p$ is the *momentum acceptance* of accelerator decided by linear dynamics.

In SRS, two radiation effects (radiation damping and quantum excitation) plays an important role in determining the resultant equilibrium values of transverse beam sizes, beam divergence, beam emittance, energy spread and bunch length [70].

1.4 Optical techniques in beam diagnostics

The electric field $E(t)$ and magnetic field $B(t)$ (i.e. Lienard-Wiechert fields) of a randomly moving charge particle q are given by Ref. [68] as

$$E(t) = \frac{q}{4\pi\,\epsilon_0}\left(\frac{(1-\beta^2)-(n-\beta)}{r^2(1-n.\beta)^3}+\frac{\left[n\times\left[(n-\beta)\times\dot{\beta}\right]\right]}{cr\,(1-n.\beta)^3}\right)_{ret.} \tag{1.19}$$

and

$$B(t) = \frac{[n\times E]}{c} \tag{1.20}$$

where β is the relativistic factor (= v/c) of charge particle, r is the separation between source and observation point, n is the unit vector pointing towards r. First term of the electric field is coulomb field ($\mathbf{E}_C$) also called near-field, and it is proportional to $1/r^2$ i.e. predominant close to the charge. Second term is the radiation field ($\mathbf{E}_R$) also called far-field, and it scales as 1/r. Radiation field reaches large distances from the source and is proportional to both the velocity (β) and acceleration ($d\beta/dt$) of the charge particle [8]. Radiating fields are generated by both longitudinal and transverse acceleration of the charge particle with respect to its

motion. Many properties of radiating fields improve with γ (i.e. Lorentz Factor), and electrons start generating optical radiation at much lower total energies than protons (m_p~ 1837 m_e).

Optical radiations from charge particles are widely used in the beam diagnostics for measuring detailed information on different aspects of charge particle beam. In recent years, the strong developments of optoelectronics components have greatly contributed to the preference of optical beam diagnostics. Although various types of diagnostics devices are installed in the ring (accelerator) for measurement of beam parameters, but there are certain beam parameters (such as beam size, beam emittance, longitudinal distribution and filling pattern) which can be better measured and analysed by optical methods using SR [8][9], optical transition radiation [10][71] and diffraction radiation [12]. These measurement techniques are based on the principle that the emitted radiation "inherits" the information of particle distribution from the electron beam. A broad classification of o*ptical methods* is based on the wavelength (λ) of the observed radiation, viz. x-ray, visible and infra red. An overview of the optical techniques based SR, transition radiation (TR) and diffraction radiation (DR) is discussed here.

1.4.1 Synchrotron radiation

SR is very versatile, efficient and non-destructive tool for characterization of the relativistic charged particle. SR based diagnostics is used for beam dynamic studies related to longitudinal and transverse beam dynamic parameters of charge particles. A brief review of the SR based diagnostic techniques is given in Ref. [9] and Ref. [13].

1.4.1.1 Transverse beam profile measurements

Precise measurement of the particle beam emittance is a very important input to characterize the performance of any accelerator. In most of the accelerators, beam emittance is measured through the transverse beam size [13]. In modern low-emittance rings, it has become possible to reduce vertical emittance to a few pm.rad [14][15]. The corresponding vertical beam size reduces to few microns level in bending magnet sections. Therefore precise measurement of the transverse beam size in new generation SRSs is a challenging task due to their small beam emittance and low beam coupling. Measurement of transverse beam size by visible SR imaging is limited by diffraction [72]. X-rays having lower wavelength can provide better spatial resolution for transverse measurements.

1.4.1.1.1 X-ray imaging methods

In x-rays region, the refractive index ($n = 1 - \delta + i\beta$) value lies close to one for all the materials, and therefore normal transmission lenses as used for visible light imaging do not work in x-rays region. However with the advancement in technology, various x-ray imaging components have been developed. X-ray imaging optics based on *diffraction* by Fresnel zone plates [16], *refraction* by compound refractive lenses [17], *reflection* by Kirkpatrick and Baez optics [18][19], and pinhole camera [9][21] are commonly used for the measurement of transverse beam parameters [22][20].

a) ***Diffractive Optics:***

The Fresnel zone plate (FZP) consists of concentric rings which are transparent and opaque alternatingly [73]. The spacing between the rings is chosen in such a way that the penetrating light waves interfere constructively at the focal point, i.e. the parts of the wavefront which contribute with opposite phase are absorbed. FZP is used as an important diffractive optics in x-ray imaging, particularly in the soft x-rays range.

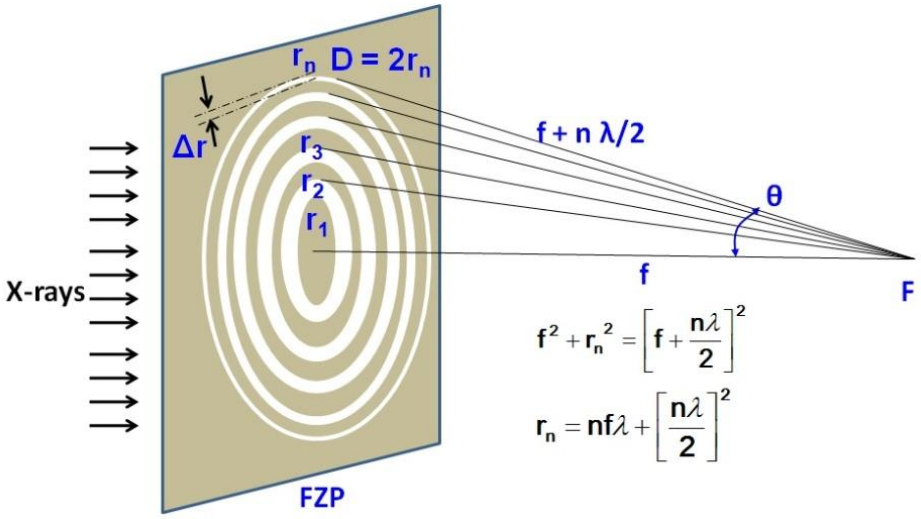

Figure 1.6: *Schematic of the x-rays focusing with Fresnel zone plate.*

The radius of the nth zone is (r_n) is given by Eq. (1.21). All the zones with radii given by following equation will bring incident plane wave (with wavelength λ) to focus at a distance *f* from the lens.

$$r_n{}^2 = n\lambda \left(f + \frac{n\lambda}{4}\right) \tag{1.21}$$

In a diffraction-limited optical system, the spatial resolution (width of the focused beam) is approximately given by

$$\sigma = \frac{\lambda}{2\ (NA)} \tag{1.22}$$

where NA is the numerical aperture of the optical system, generally defined as the *sine* of the half angle of the cone of light that leaves optical element (zone plate) [74]. For a given wavelength (λ) and focal length (*f*), higher resolution requires high NA of the optical system, and thus required more number of zones (N). But as the zone number increase, the width of the n^{th} zone gets smaller. The thinnest zone width is of the outer-most zone (i.e. N^{th} zone), and it becomes the most difficult zone to be fabricated lithographically. So beside wavelength, the width of the outermost zone (Δr) defines the zone plate resolution as $\delta \approx 1.22\ \times \Delta r$ (Rayleigh Criterion) and first order focal length [13][75] is

$$f = \frac{4N\ (\Delta r)^2}{\lambda} \tag{1.23}$$

Number of zones (N) in the FZP has important implications on properties such as resolution, collection efficiency, and source bandwidth requirements. To avoid chromatic blurring, number of zones must be less than inverse relative spectral bandwidth i.e. $N < {}^{\lambda}/_{\Delta\lambda}$.

Beam size monitor based on a single zone plate (of diameter 1.4 mm) is used at Spring-8 diagnostic beamline [76][77]. By using Si (111) reflection in double crystal monochromator, 8.2 keV SR from a bending magnet is focused on the x–rays zooming detector. Theoretical resolution for system is 1.5 μm, and spatial resolution 4.1 μm has been achieved with the total system magnification of 13.7. At ATF (KEK), x-ray imaging optics with two FZPs is used at energy 3.235 keV (Si (220) reflection) to achieve 20 times

magnified beam image [16][78]. The total spatial resolution of this monitor is estimated to be 0.7 μm (rms). By using a fast mechanical shutter with opening times ≤ 1 msec, vertical beam size of 6.4 μm was resolved by removing the effect of beam oscillation (~ 100 Hz). A diffractive optics similar to the zone plate is used at ESRF also [79]

b) Reflective Optics:

Total external reflection of x-rays takes place when the incident radiation hits the surface under gracing incidence. The grazing angle is limited on upper side by the critical angle of total external reflection θ_C given by $\sin(\theta_C) = \sqrt{2\delta}$, where $\delta \approx 10^{-6}$ is the refractive index decrement of the complex index of refraction (n). Due to the very small angle of reflection (< 0.5°) a simple spherical mirror can suffer from astigmatisms.

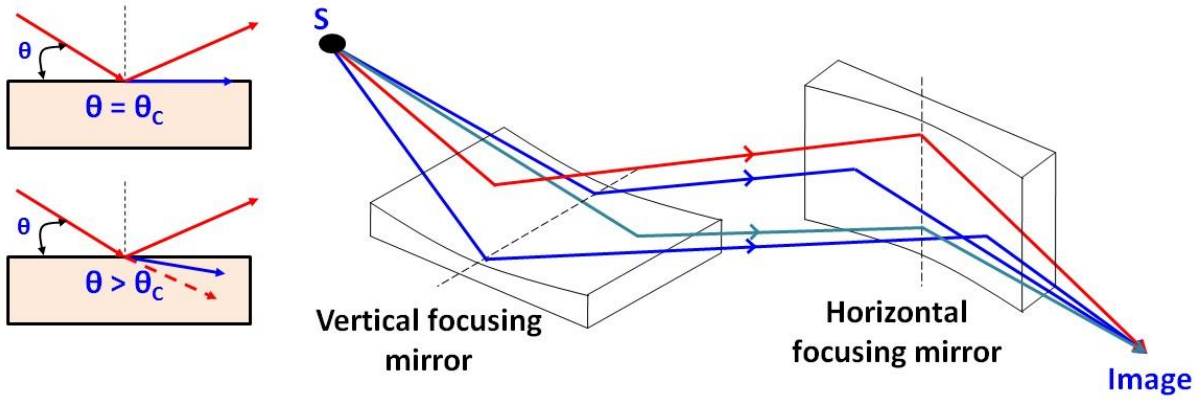

Figure 1.7: *Reflected x-rays propagating along the surface of material (at critical angle), and. beyond critical angle x-rays penetrate into the material (left).The arrangement of the Kirkpatrick-Baez optic for imaging x-rays (right).*

The most common reflective optics with grazing incidence is the Kirkpatrick–Baez (KB) setup [18]. It consists of a pair of consecutive cylindrical or elliptical mirrors and forms a real image. The first reflection focuses to a line, which is focused by the second surface to a

point as shown in Figure 1.7. This arrangement avoids the extreme astigmatism as was suffered from a single mirror [80].

In beam diagnostics, x-rays imaging based on the KB mirror is used for the beam size measurements with a spatial resolution down to ~10 μm and ~ 43 μm at ALS [20] and PLS [81] respectively. Although KB system doesn't have astigmatism as was suffered from a single mirror, but still it is not totally free of geometric aberrations.

c) Refractive Optics

The interaction of x-rays with matter has very weak refraction and strong absorption. For a long time, x-ray lenses were considered as not feasible. Nowadays with the advancement in technology, x-rays focusing by using refraction has become possible. But in order to keep the focal length of x-ray refractive optics at reasonable values, large numbers of individual lenses (N = 10, 20, .., … , 300) are stacked i.e. compound refractive lens (CRL). The focal distance of a CRL composed of an array of *N* holes (in thin lens approx.) is estimated as

$$F \approx {}^{R}/_{2N\delta} \tag{1.24}$$

Where, *R* is the radius of curvature of the focusing surface, δ is the refractive index decrement [82]. Basically there are two types of CRLs for focusing x-rays. One is the saw-tooth, or alligator type, which is truly a spherical aberration-free lens for hard x-rays and are useful for focusing in one-dimension only. Cylindrical CRLs are useful for focusing hard x-rays even in both planes. These are used in many applications related to micro fluorescence and micro diffraction.

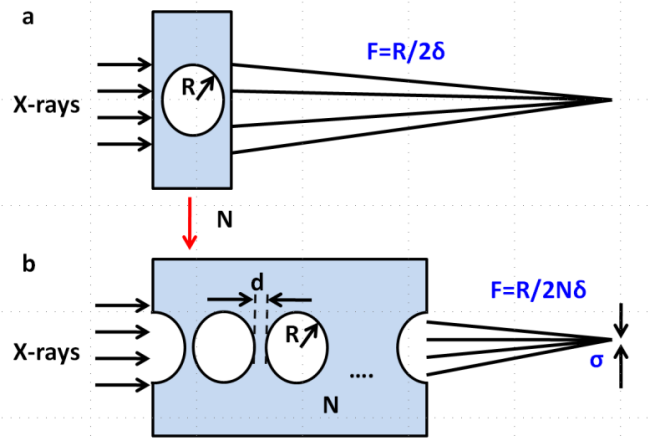

Figure 1.8: *X-rays focusing by single refractive lens and compound refractive lens (CRL).*

In order to optimize the CRLs for higher transmission and lower absorption, CRLs are generally fabricated by using low Z materials such as Al, B, Be etc. The first CRL was fabricated by drilling a number of well aligned holes in Al or Be. The refractive indices decrement for Be and Al at 20 keV photon energy (λ= 0.62 Å) are 8.5×10^{-7} and 1.35×10^{-6} respectively. Therefore by a CRL assembly with N=10, a focal distance of 10 m can be obtained with radii of curvature ~ 170 µm (in Be) or ~ 270 µm (in Al). CRLs can be used in focusing for very wide energy range from 2-150 keV. Beryllium is the material of choice up to ~40 keV, Aluminum is more appropriate for 40-80 keV, and Nickel (Ni) is used beyond these energies. Due to the strong dependence of the refractive index decrement (δ) on the photon energy, a CRL based profile monitor requires a monochromator.

In beam diagnostics, the x-rays imaging system based on the CRL optics is being used at ESRF [83], PETRA III [17] and NSLS [9]. At PETRA III, CRL based emittance monitor with 31 beryllium lenses is used at 20 keV (by a single crystal Si (311) monochromator in Laue geometry). Theoretical resolution of its CRL optics design is ~ 1 µm, and ~ 6 µm has already been achieved.

d) Pinhole based

The x-ray imaging principles discussed so far are based on any focusing element such as FZP, KB or CRL system, but these new x-ray optics/tools could not replace the existing well proven techniques such as pinhole. In pinhole based imaging, only pinhole without any other focusing element is used for forming inverted image of source with infinite depth of focus (focus free imaging). X-ray pinhole camera is widely used because of its simple setup, moderate resolution and high practical reliability.

Circular or rectangular pinhole cameras are successfully used for the measurements of transverse beam profiles and beam sizes (σ_x , σ_y) at various accelerator/SRS. Different types of pinhole/ pinhole arrays are the most common emittance monitors used in diagnostic beamlines at various light sources such as DIAMOND Light Source [21], ESRF [84], Canadian Light Source [85], BESSY II [86][87], ALS [88], NSLS [89], Australian Synchrotron [90][91] and Spring-8 [76]. Pinhole system can be used even outside the vacuum system DIAMOND [21]. The operating experiences of the working x-ray diagnostic beamlines have a spatial resolution of ~15 μm by using pinhole of 15-20 μm diameters

e) In-air x-ray monitor

At few SRSs (such as ESRF [92] and ANKA [93]), in-air x-ray monitors are also used to measure the vertical dimensions of the penetrating hard x-rays from dipole magnets (>150 keV at ESRF and >70 keV at ANKA) [9]. Beam emittance is determined from the measured vertical dimensions and known Twiss parameters and distances.

1.4.1.1.2 Synchrotron radiation interferometer

To overcome the diffraction limits of visible imaging, synchrotron radiation interferometer is a very useful method for the measurement of transverse beam sizes. The theoretical background of this method is described in the framework of wave-optics. It is based on Van Cittert-Zernike (VCZ) theorem which relates transverse source profile to its spatial coherence. The particle beam size can be inferred from the measured fringe contrast [40] [41]. Beam sizes down to few microns can be measured by using visible SR light.

Double slit interferometer technique was applied first time at KEK-PF to measure small beam sizes with a spatial resolution (few tens of microns) which was far better than beam imaging [39]. Two-dimensional SRI with a quad slit (at Spring-8 [94]) or circular pinholes (at ALBA [95]) are used to measure both horizontal and vertical beam sizes. Advanced SRI with Herschelian reflective optics (at KEK-ATF [96]), intensity imbalance design (at Australian Synchrotron [97]), and rotating pinholes design (at ALBA [95][30]) have shown huge diagnostics potential of this technique. Overcoming the effect of dispersion (due to optics), or noise (due to CCD), beam sizes down to few microns have been measured by SRI. It is also implemented for the first time on a proton machine in LHC [98]. Its vertical resolution is also limited by the natural opening angle of SR.

Pi polarization is another useful method for measuring the vertical beam size with a resolution of few microns) SLS [25]). Both SRI and Pi-polarisation are suitable for small beam sizes, but Pi-polarisation is confined to the vertical measurements.

1.4.1.2 Longitudinal beam profile measurements

The length of bunches in any accelerator ranges from few nanoseconds to few femtoseconds depending upon the type of accelerator. It is in the nanoseconds range (in hadron rings), picoseconds range (in lepton ring) and in the range of several femtoseconds (for linac driven FEL with bunch compression) [99]. To cover such a wide range, different measurement techniques are applied, which can briefly be classified into electromagnetic monitors, optical methods, methods based on the bunch frequency spectrum, laser based monitors, and monitors based on RF cavity manipulation. Electromagnetic monitors have bandwidth limitation (typically in the range of several GHz), and these techniques are mainly applied at hadron accelerators. *Optical methods* are widely used, and standard fast measurement instrumentation is easily available at reasonable costs. These are broadly classified into two categories, viz. time-domain techniques and frequency-domain techniques.

a) Time-domain techniques

The duration of the SR light pulse from a single electron is negligible (~10^{-15} s) as compared to typical bunch lengths (10^{-10} to 10^{-12} s) [8]. Therefore, the SR intensity profile vs. time of the SR pulse represents the longitudinal charge distribution along the orbit. Longitudinal profile measurements down to few ps can be done by using standard time-domain techniques [100]. The Streak camera is an ideal instrument to perform single-shot measurements with ps resolution in time domain.

Streak camera works on the principle of conversion temporal information into spatial by applying fast sweep voltage [101]. Light pulses passing through the input slit and optics form its image on the photocathode of the streak tube. The incident photons are converted into electrons according to the temporal profile of the incident light pulse. These electrons are accelerated (by a pair of accelerating mesh) and swept in space by pair of sweep electrodes synchronized to the incident light. In streak tube, these electrons are multiplied several thousands of times on passing through micro-channel plate (MCP), and bombard against the phosphor screen to convert it again into light for measurement. Dynamic observations of the bunch even on a turn-by-turn basis are possible with SC [102][103]. Temporal resolution of SC is also limited [104] by factors such as the initial velocity distribution of the photo electrons from the photo cathode [105], the temporal spread occurring in the deflection field, and the time spread because of space charge effects inside the streak tube [99]. To reduce dispersion of electrons, SC is operated with a narrow-bandwidth optical filter (interference filter) in front of the camera, reflective input optics [97] and at a low incoming intensity level. SC can be used for various longitudinal dynamics studies related to injection optimization, impedance measurements, instability analysis and RF optimsation.

Many times with single shot type measurements, the resolution limit of 200-400 fs [106][107] is not sufficient to resolve beam profiles from fully compressed beams of a FEL. In such cases, sampling techniques can measure average temporal profile by taking samples on successive turns of the bunch. A very stable beam and trigger system is pre requirement for accurate measurements. Measurements of sampling techniques are demonstrated by using fast photodiode and sampling scope ~50 GHz [108][109]. Longitudinal studies by single shot measurements with SC are performed at ELETTRA [110].

Theoretically, the bunch length can also be measured by measuring the fluctuation of the intensity of the incoherent SR [111]. The single-shot spectrum of spontaneous emission from an undulator was measured at the ATF [112], and bunch length of 1-5 ps was extracted from the fluctuations. Similarly the bunch length was measured from the statistical analysis of the turn-by-turn intensity fluctuation at ALS also [113].

b) Frequency-domain techniques

To overcome the temporal resolution limit imposed by a streak camera (in time-domain), diagnostics schemes based on the detection of the bunch frequency spectrum are also applied. As shorter the bunch, broader will be its frequency spectrum, and the bandwidth of the radiation may extend upto THz region for ultra short bunches. Frequency-domain techniques have covered the bunch lengths measurements in femtoseconds range [9].

This method is widely applied in the particle beam diagnostics based on *Coherent Radiation Diagnostics* (CRD) [114]. Radiation is emitted coherently if the wavelength is in the order of the bunch length, and the information about bunch length and shape is encoded in the emission spectrum (which is exploited in CRD).

Independent of the physical process generating the observed radiation (may be SR, TR or DR), the power spectrum is defined as [6][8]:

$$P(\lambda) = P_0(\lambda)\left(N + \underbrace{N\,(N-1)\,f(\lambda)}\right) \tag{1.25}$$

Where $P_0(\lambda)$ the power spectrum of a single particle, N is is the number of particle in the bunch, and $f(\lambda)$is the bunch form factor, which is related to the normalized longitudinal distribution function of the bunch $S(z)$ through its Fourier transform as follows

$$f(\lambda) = \left| \int S(z)\, e^{\frac{2\pi i z}{\lambda}}\, dz \right|^2 \tag{1.26}$$

The form factor $f(\lambda)$ for a gaussian bunch profile with a bunch length $L_b = \sqrt{2\pi}\,\sigma_z$ is [115]:

$$f(\lambda) = e^{-\left(\frac{2\pi\,\sigma_z}{\lambda}\right)^2} \tag{1.27}$$

Similarly form factor $f(\lambda)$ for rectangular bunch profile will be a *sinc* function of $x = \frac{\pi\, L_b}{\lambda}$ as

$$f(\lambda) = \left(\frac{\sin x}{x}\right)^2 \tag{1.28}$$

The two terms in Eq. (1.25) represent the incoherent and coherent emission, and the form factor $f(\lambda)$ can be estimated only for coherent emission. As coherent emission requires the form factor $f(\lambda)$ to extend up to the frequencies where $P_0(\lambda) \neq 0$, therefore only ultra-short bunches emit coherently and the spectral intensity is strongly amplified.

According to Eq. (1.25), the form factor $f(\lambda)$ can be determined from the measurement of the spectral intensity $P(\lambda)$ and with the knowledge of single electron spectrum $P_0(\lambda)$. Inverting the Fourier transform of $f(\lambda)$ results in the reconstructed bunch profile *S*(*z*). As only magnitude of the form factor $|f(\lambda)|$ is determined rather than the complex form factor itself, so this method has phase reconstruction problem. To solve this problem, a minimal phase is re-constructed with the Kramers-Kronig relations [116][117].

The resolution of *CRD* (~ 100 fs) is mainly limited by the uncertainties in the spectral reconstruction.

Coherent Smith-Purcell radiation are used to determine the temporal profile of sub-ps long electron bunches (300-600 fs) at the Facility for Advanced Accelerator Experimental Tests, at SLAC [117]. Coherent SR (CSR) based power detector has been developed at CEBAF [118]. It is used to measure ultra-short electron bunches (~ 0.5 mm) with a resolution of few femtoseconds using GaAs Shottky diode (500 GHz to 3 THz).

The cross-correlation of the SR pulse and the external mode-locked laser pulse is also used for the bunch length measurement at ALS [9]. It is based on the principle that when a short laser pulse interacts with the longer SR pulse in a nonlinear crystal (such as BBO), it generates a signal of high frequency (the sum of the laser and the SR frequencies) corresponding to measurement of their interaction. SR pulse profile is measured by scanning the laser pulse with respect to the SR pulse in time. The overlap time is decided by the laser pulse time, and the time resolution better than few picoseconds is possible by employing laser with ultra short pulses. This technique was also employed for low-alpha experiments at SPEAR-3, and bunch length measurements ~1 ps were tried with a 50 fs mode-locked laser [119].

1.4.2 Transition radiation

Transition radiation (TR) is emitted when a high energy charged particle traverses the boundary between two materials having different dielectric constants [10]. These are emitted

in the both forward and backward direction (reflected) at the interface surface. TR is a surface phenomenon and very thin reflecting screen are used as targets (as an example a silicon wafer with a thin layer of Al or Ag in vacuum). It causes very little effect on particle beam and is used widely as semi destructive diagnostics of charge particle beam. TR in the visible spectral range is called optical transition radiation (OTR).

For an ultra relativistic charge particle crossing an interface from vacuum to metal, the spectral intensity (per unit solid angle) of backward TR in vacuum for the horizontal and vertical directions is given as [120][121][122]

$$\frac{d^2 I_x}{d\Omega\, d\omega} = \frac{\alpha}{\pi^2}\left(\frac{\theta_x}{{\theta_x}^2 + \gamma^{-2}}\right)^2 \frac{1}{(1 - \theta_x\ cot\,\theta_o)^2} \tag{1.29}$$

and

$$\frac{d^2 I_y}{d\Omega\, d\omega} = \frac{\alpha}{\pi^2}\left(\frac{\theta_y}{{\theta_y}^2 + \gamma^{-2}}\right)^2 \tag{1.30}$$

Where α is the fine structure constant, γ is the Lorentz factor, θ_o is the angle between beam trajectory and OTR screen, θ_x and θ_y are the angles between the observed directions and the direction of specular reflection. Theoretically signal for relativistic case $\gamma \gg 1$ is proportional to logarithmic function of energy as $I \propto ln(2\gamma)$; and for a non relativistic particle ($\beta \ll 1$) it is proportional to square of particle velocity i.e. $I \propto \beta^2$. By using Eq. (1.29), theoretically calculated signal within spectral range of 400-600 nm is ~0.014 ph/electron at beam energy of 50 MeV.

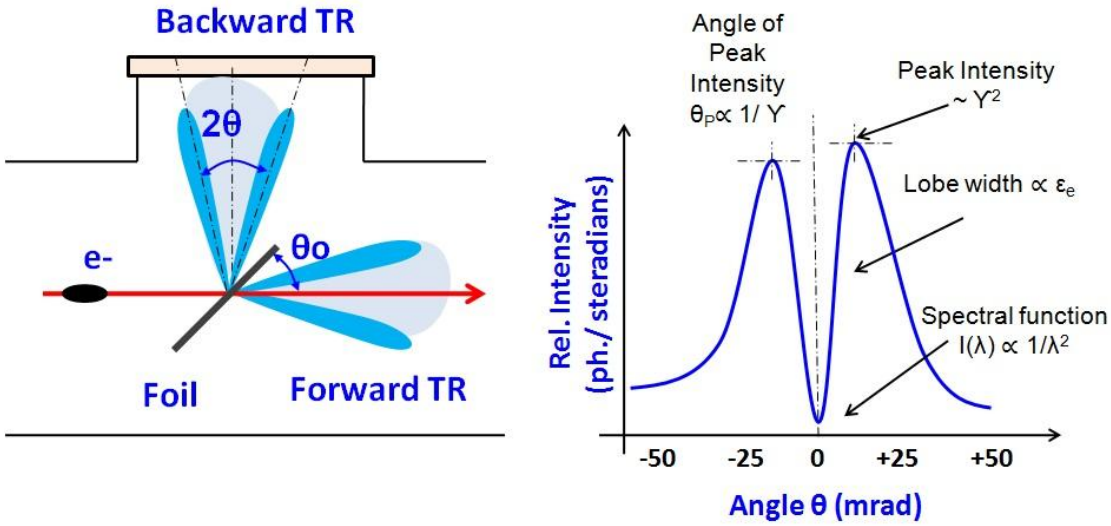

Figure 1.9: *Schematic of the forward and backward OTR signal from a thin metal foil in vacuum (left), and its angular distribution (right).*

TR has number of distinctive features that make it attractive for diagnostics applications in various accelerators. Its main features are directionality, promptness (enabling fast single shot measurements), linearity (neglecting coherent effects), dependence of angular distribution on energy (γ) and ε. OTR emission is instantaneous (typically ~ 100 fs), so this can also be used to extract temporal information (of few-ps) about bunched beam. Beam divergence of a charge particle can be determined from the ratio of the intensity at the peak and at the center of the OTR pattern. The beam energy can also be measured by observing the peak position of the OTR pattern (at $\theta = {}^{1}/_{\gamma}$). Thus the advantage of OTR technique is that it can be used to measure both beam emittance and beam energy by taking only two images, viz. the beam profile at the beam waist (near-field image) and the OTR pattern (far-field image) [123]. It is a surface effect and does not show the type of saturation shown by

fluorescent screens, so quantitative measurements of beam profile is also possible. TR diagnostics is widely used for profile measurements in linear and circular accelerators [71] [124].

In a typical OTR monitor setup, the beam is imaged by using standard lens optics. The recorded intensity profile is a measure of the particle beam spot. The principle achievable resolution of setup is given by $\delta = \frac{1.12\ M\ \lambda}{\theta_A}$ [125]. where λ , θ_A, and M are the wavelength, optics acceptance angle and magnification of the optical system respectively. OTR system has disadvantage of being invasive to beam and weak signal intensity. Therefore for low energy electron beams either it needs low intensity detectors such as ICCD or use luminescent screens. To avert the possibility of screen degradation with high intensity or high brilliant beams, its applicability is usually restricted to single or few bunch operations, and permanent beam operation is not possible. The electron peak current is the most critical parameters for optimizing self-amplified spontaneous emission (SASE) free-electron laser (FEL) performance. It requires precise measurement of the bunch charge and bunch length. OTR with streak camera setup is used for bunch length measurements at the Advanced Photon Source (APS) injector linac, which is used to support SASE-FEL [126].

1.4.3 Diffraction radiation

Diffraction radiation (DR) is produced when a charged particle in uniform motion passes a conducting structure such as an aperture in a metallic foil [12] (i.e. neighborhood of some inhomogeneity). Basically it is produced by the diffraction of the field associated with the beam. DR has many features similar to the TR, but the main difference is that DR is non-

destructive to the beam. Therefore DR can be used for the measurements of intense beams where TR was not possible. Like TR, DR is also produced in the forward and backward direction as shown in Figure 1.10.

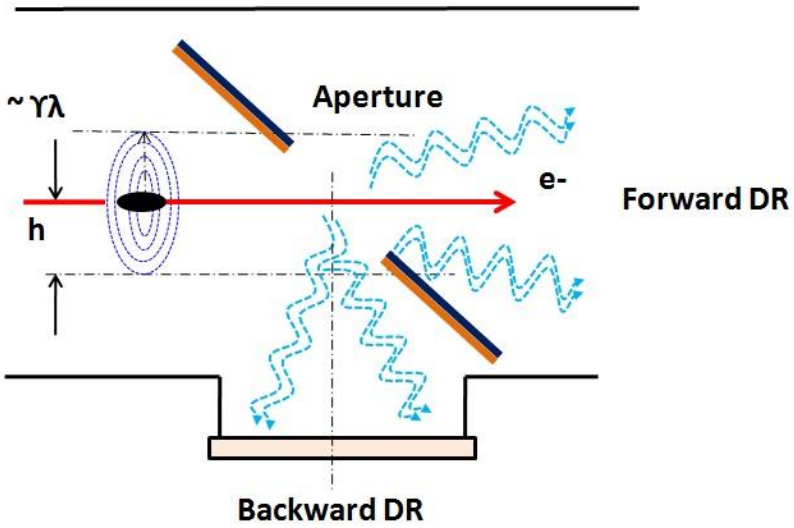

Figure 1.10: *Schematic of the forward and backward DR signal from a metal foil aperture in vacuum.*

The backward DR can be observed by rotating the iris/aperture 45° with respect to the beam trajectory. As the DR generation cause very small perturbation to the beam, therefore it is possible to generate DR signal at several experimental stations along the beam transfer line. Like TR, DR signal is also very weak. ODR interferometry generated at two slits increases the sensitivity of the beam parameter [127]. Accelerators of the next generation or linear colliders (targeted to achieve high luminosity) have beam requirement of extremely low emittance and high current. There is a strong preference for these types of non-invasive beam diagnostics techniques.

1.5 Motivation for work

The prime motivations for pursuing this work are

i. Design and development of diagnostic beamlines at the Indus-2 SRS, which will be used for the measurement of longitudinal and transverse beam parameters.

ii. Studies of longitudinal and transverse beam parameters of the Indus-2 SRS by using the diagnostic beamlines.

iii. Design study of the SR interferometer for measurements of beam sizes with a spatial resolution of few microns during low emittance operation of Indus-2 and for future high brightness SRSs.

1.5.1 Design and development of SR based diagnostics at Indus-2

Main objective of the work is to design and develop SR based diagnostics for the measurement of beam parameters at Indus-2. In view of this objective, literature survey of existing diagnostics schemes was carried out. X-ray diagnostic techniques are mainly classified on the basis of focusing methods, viz. reflection, refraction and diffraction. The choice of technique depends upon requirement of spatial resolution and system dynamic range for beam movement and beam currents. Two diagnostic beamlines, viz. visible diagnostic beamline (V-DBL, BL-23) and X-ray diagnostic beamline (X-DBL, BL-24) have been designed, developed and commissioned at Indus-2 [26][27][28]. These beamlines are used regularly for online measurement of beam parameters at 1 Hz, and measured data is continuously displayed in Indus control room. Beamlines are also used for required measurements during dedicated beam physics studies/experiments.

The X-DBL is installed at BL-24 in Indus-2. It is based on pinhole array assembly, and is used for the measurement of beam size, beam divergence, beam emittance and beam position. Pinhole size and pitch are optimized based on the minimization of spread function and requirement of divergence measurements under various dynamic conditions. Pinhole system provides good spatial resolution (~ 15 μm) for wide range of beam movement and beam currents, which was very much required at the initial stages of Indus-2 operation and optimization. For measurement of photon beam position, a staggered pair blade monitor (SPM) is also installed in parallel to pinhole array at 8 m from the source point [26].

The V-DBL design is based on water cooled primary mirror, which is used to extract visible light from the wide SR spectrum in UHV [35]. The extracted visible light is focused at the detectors (kept in a dark room) by using reflective and refractive optics. The measurement of beam parameters such as bunch length, bunch separation and bunch filling pattern are performed by using streak camera, fast photo receiver and avalanche photodiode. Optimization of angular acceptance and spread function of the V-DBL beamline is carried out by using SR code SPECTRA [128]. Visible diagnostic has immense scope for fast measurements as most of the detectors are available in this spectral range. V-DBL provides online information of the beam parameters even during beam injection in the Indus-2. Details related to design and development of diagnostic beamlines (X-DBL and V-DBL) at Indus-2 is discussed In **Chapter 2**.

1.5.2 Studies of longitudinal and transverse beam parameters

In view of the second objective, studies of longitudinal profile of electron bunch and impedance measurement of Indus-2 SRS were carried out by using streak camera [29] at V-DBL. Transverse measurements related to beam size, beam emittance, beam position, SR position and dispersion were carried out at X-DBL.

The longitudinal profile of electron bunch is analyzed by filling charge in the single bunch (SB) mode of operation at Indus-2. These measurements are carried at injection energy (550 MeV) and at final beam energy (2.5 GeV) by using dual sweep synchroscan streak camera at V-DBL. The affect of wakefield generated interactions between the circulating electrons and the surrounding vacuum chamber are analyzed in terms of measured effects on the longitudinal beam distribution. The equilibrium charge distribution of a bunch is analysed by using solutions of the Haissinski equation [36]. The major factors influencing the bunch lengthening, viz. potential-well distortion and microwave instability are also discussed. Results of longitudinal distribution fitted with the analytical solutions for different longitudinal coupling impedances are also discussed [37][38]. The impedance of the storage ring is obtained from the measured bunch lengthening with different impedance models [31]. The impedance of storage ring obtained by a series R+L impedance model predicts the values of resistance and inductance as 1350 ± 125 Ω and 180 ± 25 nH respectively. These results are also compared with the values obtained from the measured synchronous phase advancing and scaling laws. These studies provide very useful inputs in calculating various thresholds for beam instabilities to beam physicists. These studies are presented in **Chapter 3** [32]. Before doing these studies at Indus-2, we have learned a lot by working on bunch length

measurements at Indus-1 SRS by using fast photo receiver system [33]. Results of these measurements are also discussed briefly at the end of this chapter.

Analysis of transverse beam parameters is presented briefly in **Chapter 4**. Modified theoretical equations for online measurements of source position and emission angle with pinhole array optics are also presented. Results of online measurement are compared with the measurements at an independent x-ray beam position monitor (SPM) installed in the X-DBL. Measured values from both systems found to be within ± 12 μm (or $\pm$ 1.5 μrad) for wide range of beam movements [26]. Results of the experimental measurement of beam dispersion by changing frequency of RF cavity are also discussed. Measurement results of beam position, beam size and beam emittance with natural decay of beam current in Indus-2 are also presented. Measured natural beam sizes in horizontal and vertical plane at the BL-24 source point are 357.2 μm and 47.6 μm respectively. Measurement results during the trial operations of Indus-2 in low emittance mode (~ 45 nm rad) are also discussed [5].

1.5.3 Design study of SR interferometer for beam diagnostics

In view of the third objective, design study of SRI was carried out for beam diagnostics of Indus-2 SRS [34]. The theoretical background of this method is described in the framework of wave-optics. It is based on Van Cittert-Zernike theorem relating transverse source profile to spatial coherence, and the particle beam size can be inferred from fringe contrast [40][41]. Nowadays, many advanced SRSs are opting for the SRI technique (discussed in section 1.4.1.1.2). A quad slit system has been optimized to measure beam sizes in both the planes.

Results of simulation of this SRI system using the SRW code [42] and the visibility analysis of interferogram by horizontal and vertical curve fitting are also presented. Transversal beam size measurements down to few microns can be performed by using SRI. Transverse emittance can also be evaluated from the measured beam size by using known optics (Twiss) parameters of the source point. This work will be useful for measuring very small beam sizes (few microns to tens of micron) during low emittance operations of Indus-2 SRS, and for future high brightness SRSs in India. Even full reconstruction of beam profile under different beam couplings is also possible by rotating double-pinhole mask [95]. Physics design of the SRI for measurement of transverse beam sizes at Indus-2 is described in **Chapter 5**.

Chapter 2 Design and development of diagnostic beamlines

2.1 Diagnostic beamlines

Synchrotron radiation based beam diagnostics is used for the measurement of beam parameters at various accelerators/ synchrotron radiation sources (SRSs). It provides online information of various beam parameters without causing any perturbations to the beam. Two independent diagnostic beamlines have been designed, developed and commissioned at Indus-2 SRS, viz. visible diagnostic beamline and X-ray diagnostic beamline. Former is used for measurement of longitudinal beam parameters and later is used for transverse beam parameters. The measurement of these parameters is helpful for augmenting the performance of Indus-2 SRS.

The design philosophy for Indus-2 diagnostic beamlines has evolved from the study of the design and operating experiences at many other SRS facilities (discussed in Chapter 1). Different types of x-ray imaging techniques have been adopted for measurement of transverse beam parameters [9]. A pinhole forms an inverted image of the source with a suitable magnification factor depending upon the various optical distances. In a pinhole array, in addition to beam size, the intensity variation on either side of the central beam provides the information of beam divergence and hence beams emittance. Different types of pinhole and

pinhole arrays are used for transverse measurements at various light sources such as DIAMOND Light Source [21], ESRF [84], Canadian Light Source [85], BESSY II [86] [87], ALS [88], NSLS [89], Australian Synchrotron [90][91], and Spring-8 [77].

The X-ray diagnostic beamline (X-DBL, BL-24) is installed at 10^{o} port of bending magnet (DP-10) in Indus-2 SRS. It is based on a pinhole array system, and is used to measure transverse beam parameters such as beam size, beam divergence, beam emittance and beam position. For measurement of photon beam position, a staggered pair blade monitor (SPM) is also installed in the beamline at 8 m distance from the source point. Modified algorithm is used for online measurements of source position and emission angle with pinhole array [26].

The visible diagnostic beamline (V-DBL, BL-23), is installed at 5^{o} port of bending magnet (DP-10) in Indus-2 SRS. In this beamline, a water cooled primary mirror is used to extract the visible light from the wide SR spectrum of dipole magnet. The extracted light is focused at various optical detectors placed outside the shielding wall in the dark room. Optical detectors such as dual sweep synchroscan streak camera, fast photo receiver, avalanche photodiode, position sensitive detectors and CCD camera are used for various measurements. BL-23 is used for measurement of bunch length, bunch separation, bunch fill pattern and beam position. Beside regular measurements, these beamlines are very useful for various beam dynamic studies under different operating conditions. In this chapter physics design for development these diagnostic beamlines is presented. Important design parameters of the Indus-2 SRS are discussed in Chapter 1.

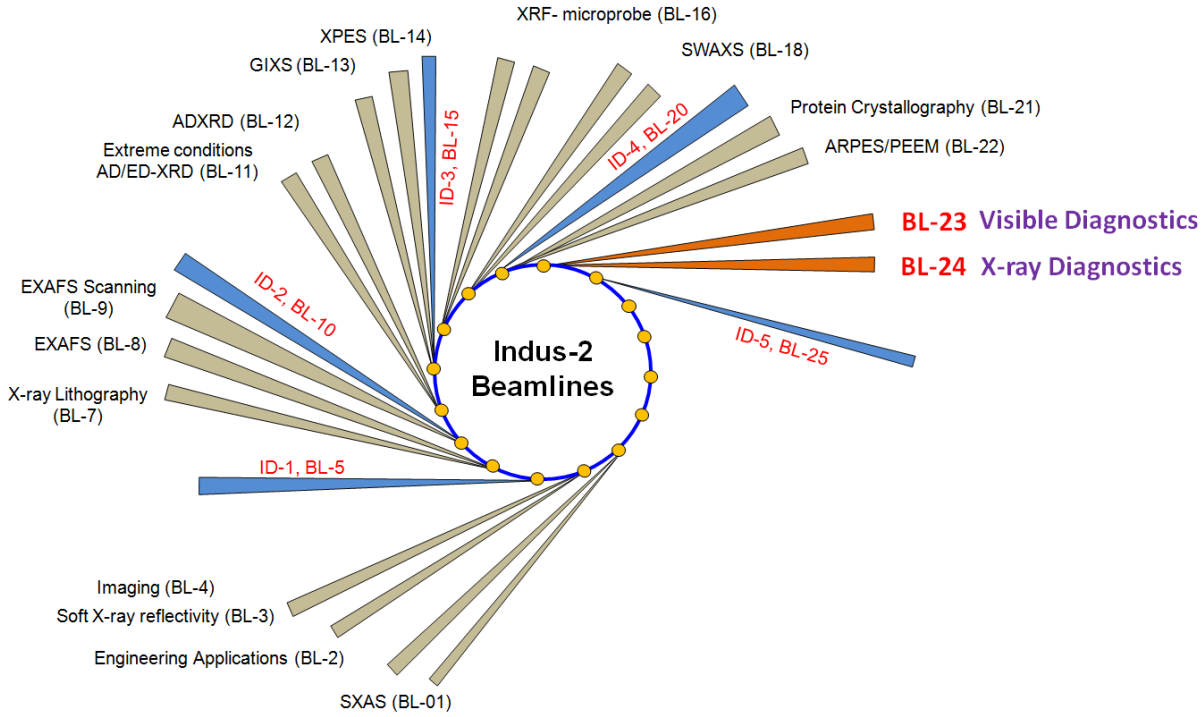

Figure 2.1: *Schematic layout of the Indus-2 beamlines. Diagnostic beamlines V-DBL (BL-23) and X-DBL (BL-24) are also shown along with other user beamlines.*

2.2 X-ray diagnostic beamline (X-DBL)

2.2.1 Beamline configuration

X-DBL based on pinhole array imaging has been designed and developed at Indus-2 SRS. Tungsten pinhole array with 17(H) X 21(V) pinholes of 20 µm diameter each is placed at 8 m from the source point, and its imaging is carried out on a phosphor screen with a magnification factor of 1.2. The phosphor screen converts the x-rays into visible light for measurement with a CCD camera. The beamline is designed to capture more than five fully

resolved pinholes image on the phosphor screen. An additional staggered pair blade monitor (SPM) is also installed inside the pinhole array chamber. It provides the vertical position of photon beam at the location of pinhole array. The schematic of the pinhole array based beam diagnostics employed in X-DBL is shown in Figure 2.2. The design considerations of various sub components used in the beamline are described in the following sub-sections.

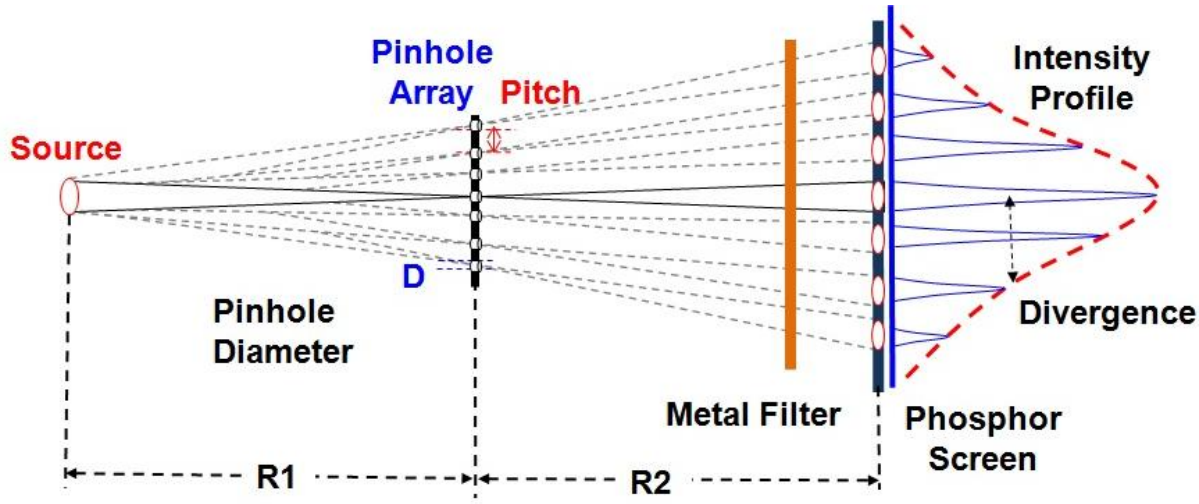

Figure 2.2: *Schematic of the pinhole array based beam diagnostics employed in X-DBL*

2.2.2 Front-end of the beamline

The section which connects a beamline with a storage ring is called front-end (FE). It starts right from a source port and extends upto Beryllium window outside the shielding tunnel. FE acts as an interface between the storage ring and the optical components of the beamline. It consists of a set of ultra high vacuum (UHV) components with associated controls and interlocks. Its main functions are vacuum protection of ring, defining the angular acceptance of beamline, absorption of heat and user safety. Standard FE components used in X-DBL are

collimator, water-cooled shutter, gate valves, fast shutter, safety shutter, fixed mask and delay line chamber [129]. Schematic layout of the FE at X-DBL is shown in Figure 2.3.

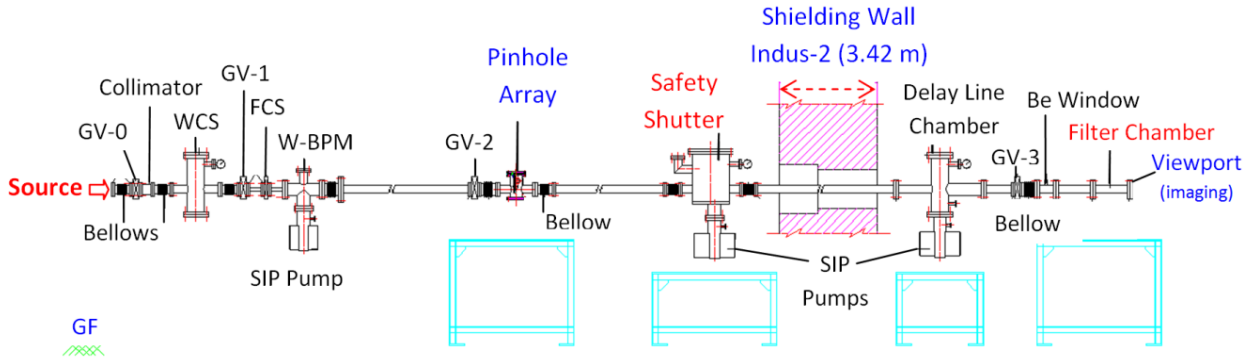

Figure 2.3: *Schematic layout of the front end components at X-DBL in Indus-2.*

2.2.3 Front-end components

a) **Collimator:** It is the first active component to interact with SR beam in the FE, and is used to define downstream angular acceptance of the beamline. It is made of oxygen free high conductivity copper (OFHC) solid block with rectangular tapered hole along its central axis (coinciding with the beam axis). Water cooling arrangement is provided to take high heat load (~300 W, when it selects the SR beam from 22 mrad to 7 mrad horizontal)

b) **Water cooled shutter (WCS):** It is made of a water cooled copper plate tilted along the beam to reduce the thermal power density. Its main function is to completely intercept the x-rays photon beam in its closed position. WCS takes full thermal load of the photon beam (~140 W) for thermal isolation of downstream components.

c) **Gate valve (GV1):** Gate valve is a pneumatically-actuated UHV valve that is used to isolate the storage ring vacuum from any downstream vacuum breach. As GV1 cannot absorb high heat load from the photon beam, so it is interlocked to close only when WCS is closed or when electron beam is not available in the storage ring. Typically its closing time is 1-2 seconds.

d) **Fast shutter (FS):** It is positioned immediately downstream of GV1 and has very fast response time (~ 10 ms). Its main function is to protect the storage ring vacuum from any failure of downstream vacuum. As it cannot absorb high heat load of the SR, so it is also interlocked with the WCS during normal operation.

e) **Safety shutter (SS):** It is a radiation absorber head made up of Densimet (Tungsten alloy). SS is used to absorb BR generated from electron beam scattering in the ring. Pneumatic manipulator provides vertical movements to the absorption head of SS.

f) **Beam Position Monitor (BPM)**: Staggered blade pair monitor (SPM) is used for online measurements of photon beam position. SPM design is based on photo-electron emission principle, and originally developed by Holldack and Peatman [130].

g) **Fixed mask (FM):** It is a water cooled copper (OFHC) plate with a rectangular hole in the centre. It is used for limiting angular width of SR in both horizontal and vertical plane for final application at the beamline. Thus it helps in removing unwanted SR heat load (~120 W) downstream.

h) **Delay line chamber:** It is vacuum protection component of FE. It introduces high resistance path in case of any downstream vacuum failure to protect upstream vacuum.

i) **Be window:** It is used for vacuum isolation and optical transmission of x-rays from vacuum to air.

2.2.4 Pinhole array

2.2.4.1 Imaging with pinhole

The photon beam emittance (ϵ_{Photon}) at the SR source point is a result of the convolution of the electron beam emittance ($\epsilon_{electron}$), with the photon emittance ($\epsilon_{Photon\_Single\_electron}$) generated from the single electron emission. In the pinhole imaging, each x-rays from source point passes through the pinhole and forms an inverted image of the source on the phosphor screen. In terms of phase space, the beam profile seen by the pinhole camera at the source point is the intersection of the pinhole camera acceptance ($y' = {}^{-y}/_{R1}$) and the photon ellipse [131], where R1 is the source to pinhole distance. The phase space ellipses and pinhole acceptance for X-DBL are shown in Figure 2.4**.**

In the horizontal plane, the beam sweeps across the pinhole for all angles limited by horizontal angular acceptance of the beamline. So, the integrated horizontal profile of imaging has dimensions close to the horizontal beam size (see Eq. (A.10) at page A-2). In the vertical plane, the photon ellipse is much larger than that of the electron beam. So, the dimensions of intersected beam profile are close to the electron beam profile for small electron beam emittance, and/or for small pinhole acceptance angle (i.e. R1 large). At lower

slope of the pinhole acceptance, although this difference becomes less but there are practical limitations with long front-end and technical limitation of poor resolution.

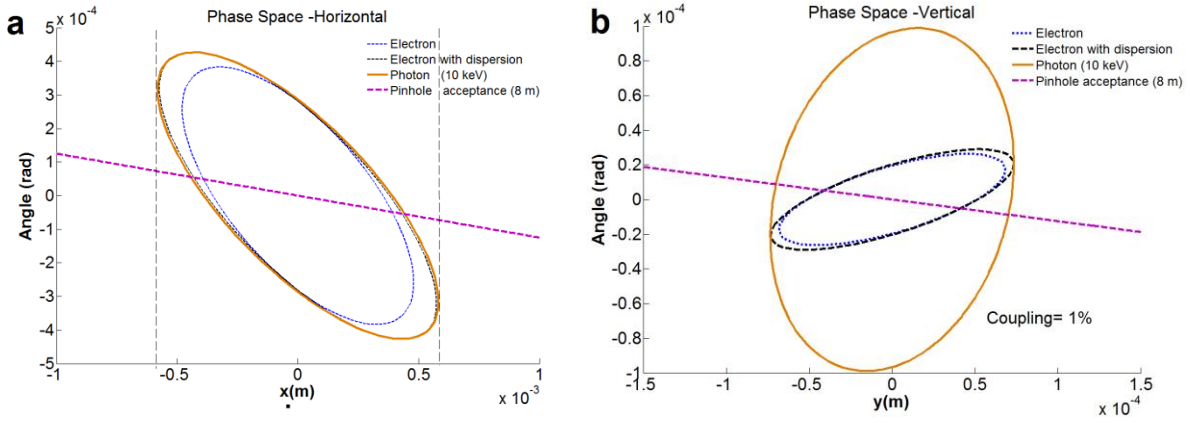

Figure 2.4 : *Representing pinhole imaging in phase space for horizontal plane (a) and for vertical plane (b). Three phase space ellipses correspond to electron emittance, electron emittance with dispersion and photon beam emittance. SR beam sweeps across pinhole acceptance (shown as straight line) in the horizontal plane.*

The X-DBL is designed with optimized pinhole acceptance (0.125 mrad) in the phase space. It also fulfils the space constraints inside the Indus-2 shielding tunnel without any major modification in the front-end. The various parameters of X-DBL source point are given in Table 2.1.

Table 2.1: *Source parameters of the X-DBL (10˚ port of DP-10) in Indus-2.*

Parameter	Value	Parameter	Value	Parameter	Value
$\beta_x(m)$	1.0894	α_x	0.9257	$\sigma_x\ (\mu m)$	427.8
$\beta_y(m)$	4.444	α_y	-1.133	$\sigma_y\ (\mu m)$	82.3
$\eta_x(m)$	0.2097	η'_x	-0.3522	$\sigma_{x'}(\mu\, rad)$	575.4
$\eta_y(m)$	0	η'_y	0	$\sigma_{y'}(\mu\, rad)$	26.37

2.2.4.2 Point spread function of the pinhole

The final image formed by the pinhole camera is the convolution of the source profile, and the contributions of the point spread functions (PSFs) of pinhole, phosphor screen, imaging optics and CCD camera. Consequently, the total convolved PSF of the beamline determines the smallest measurable image size at the beamline. The final measured size ($\sigma_{Measured}$) can be related to the actual beam size (σ_{Actual}) as follows:

$$\sigma_{Measured} = \sqrt{(\sigma_{Actual})^2 + \left(\sigma_{Phosphor}\right)^2 + \left(\sigma_{Zoom\_optics}\right)^2 + (\sigma_{CCD})^2 + (\sigma_{Pin.})^2} \quad (2.1)$$

where $\sigma_{Pin.}$, $\sigma_{Phosphor}$, σ_{Zoom_optics} and σ_{CCD} are the PSF contributions due to pinhole, phosphor screen, zoom optics and CCD camera respectively. The spatial resolution of the pinhole camera ($\sigma_{Pin.}$) is mainly limited by diffraction and geometrical effects [86] [132] as follows:

$$\sigma_{Pin.} = \sqrt{\left(\frac{\sqrt{12}}{4\pi}\frac{\lambda R2}{D}\right)^2 + \left(\frac{D}{\sqrt{12}}\frac{(R2+R1)}{R1}\right)^2} \quad (2.2)$$

where λ is the wavelength, D is the pinhole diameter, $R1$ is the source to pinhole distance and $R2$ is the pinhole to phosphor screen distance. These effects are optimized to get optimum diameter for the best possible resolution ($\sigma_{Pin.\_Min}$) as follows:

$$\left(\frac{d\sigma_{Pin.}}{dD}\right) = 0 \quad (2.3)$$

$$D_{Opt.} = \sqrt{\frac{12}{4\pi}\frac{\lambda R1\, R2}{(R2+R1)}} \tag{2.4}$$

$$\sigma_{Pin.\_Min.} = \sqrt{\frac{\lambda}{2\pi}\frac{R2\,(R2+R1)}{R1}} \tag{2.5}$$

Pinhole is exposed to the white SR beam having photons of all energies coming from the source. Metal filters assembly is used for energy selection, and it acts as a high (energy) pass system. Mostly photon beam of energy range 8-19 keV is used for imaging by pinhole array (see Figure 2.9). Results of variation in width of the pinhole spread function width with pinhole diameter for different photon energies are plotted in Figure 2.5. Pinhole diameter of 15-20 μm has the lowest spread function width for photons in the working energy range.

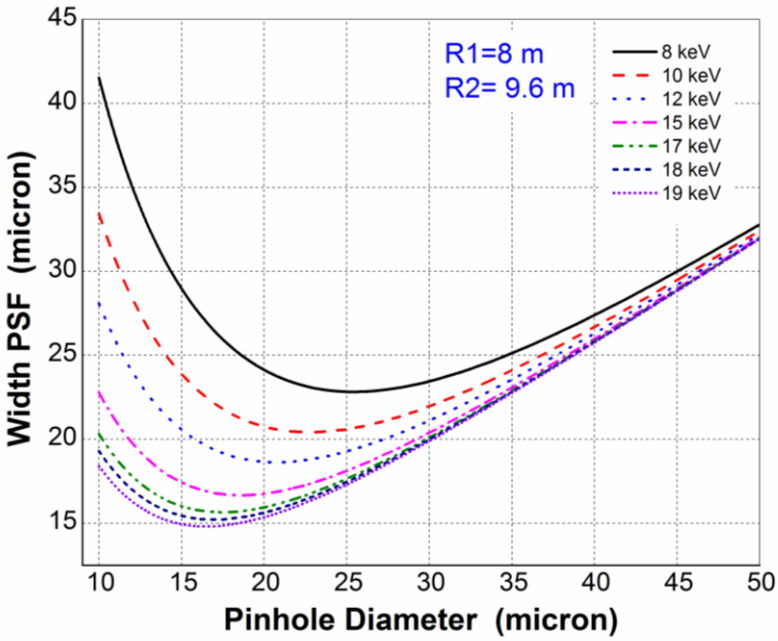

Figure 2.5: *Variation in width of pinhole spread function with pinhole diameter at different photon energies. At 15-20 μm pinhole diameters it has lowest spread function width.*

The pinhole size is also optimized to get sufficient photon flux for imaging at the phosphor screen. In X-DBL, pinholes of ~20 μm diameters are best optimized for the lowest spread function width and detectable transmission of photon flux for imaging at the phosphor screen. SR code SPECTRA 10.0 [128] is used for calculations of flux and power density.

2.2.4.3 Pitch of pinholes in a pinhole array

The quality of information that can be drawn from a pinhole array image is affected by the horizontal and vertical separation between pinhole images and their relative contrast factors. Intensity pattern I(x, y) of the x-rays on the phosphor screen can be calculated using relation as follows [130]

$$I(x,y) = \sum_{i\_Pinholes} g(y)\left(\frac{D}{R1}\right)^2 \left\{ \left[\frac{1}{\sqrt{2\pi}\left(\sigma_H \frac{R2}{R1}\right)} \left(exp\left(\frac{-(x-x_i)^2}{2\left(\sigma_H \frac{R2}{R1}\right)^2} \right) \right) \right] X \left[\frac{1}{\sqrt{2\pi}\left(\sigma_V \frac{R2}{R1}\right)} \left(exp\left(\frac{-(y-y_i)^2}{2\left(\sigma_V \frac{R2}{R1}\right)^2} \right) \right) \right] \right\} \quad (2.6)$$

where σ_V and σ_H are the source size in vertical and horizontal plane respectively; x_i and y_i are the horizontal and vertical position coordinates of any pinhole in the pinhole array. The quantity $(D/R1)^2$ represents the solid angle acceptance of each pinhole, and the vertical angular distribution of SR, g(y) for $\lambda \ll \lambda_C$ is given as

$$g(y) = \left[\frac{I_{Total}}{\sqrt{2\pi}\left(\sigma'_V(R2+R1)\right)}\left(exp\left(\frac{-(y-y')^2}{2\left(\sigma'_V(R2+R1)\right)^2}\right)\right)\right] \quad (2.7)$$

Calculated intensity distributions on the phosphor screen for 8-18 keV are shown in Figure 2.6. A pinhole array with 1 mm pitch gives final image (with more than five vertical points) for the profile measurement even at high energies. Calculated results of the vertical and angular shift of source on intensity distribution are also shown in Figure 2.6.

In X-DBL, 250 μm thick Tungsten pinhole array is sandwiched between the two copper plates (5 mm), and proper water cooling is provided at the base to restrict the thermal deformations. Thermal analysis and design optimization of the system was carried out to keep the maximum steady state temperature (of the pinhole and its support) less than 380 °K. The various design parameters for the pinhole assembly are shown in Table 2.2.

Table 2.2: *Design parameters of the pinhole array assembly for X-DBL.*

Parameter	Specifications
Pinhole diameter (μm)	20
Pinhole array (H X V)	17 X 21
Effective size (mm^2)	16 X 20
Pitch (H & V) (μm)	1000
Thickness (μm)	250
Material	Tungsten
Linear stroke (mm)	±10
Linear resolution (μm)	< 10
Positioning accuracy (μm)	< 30

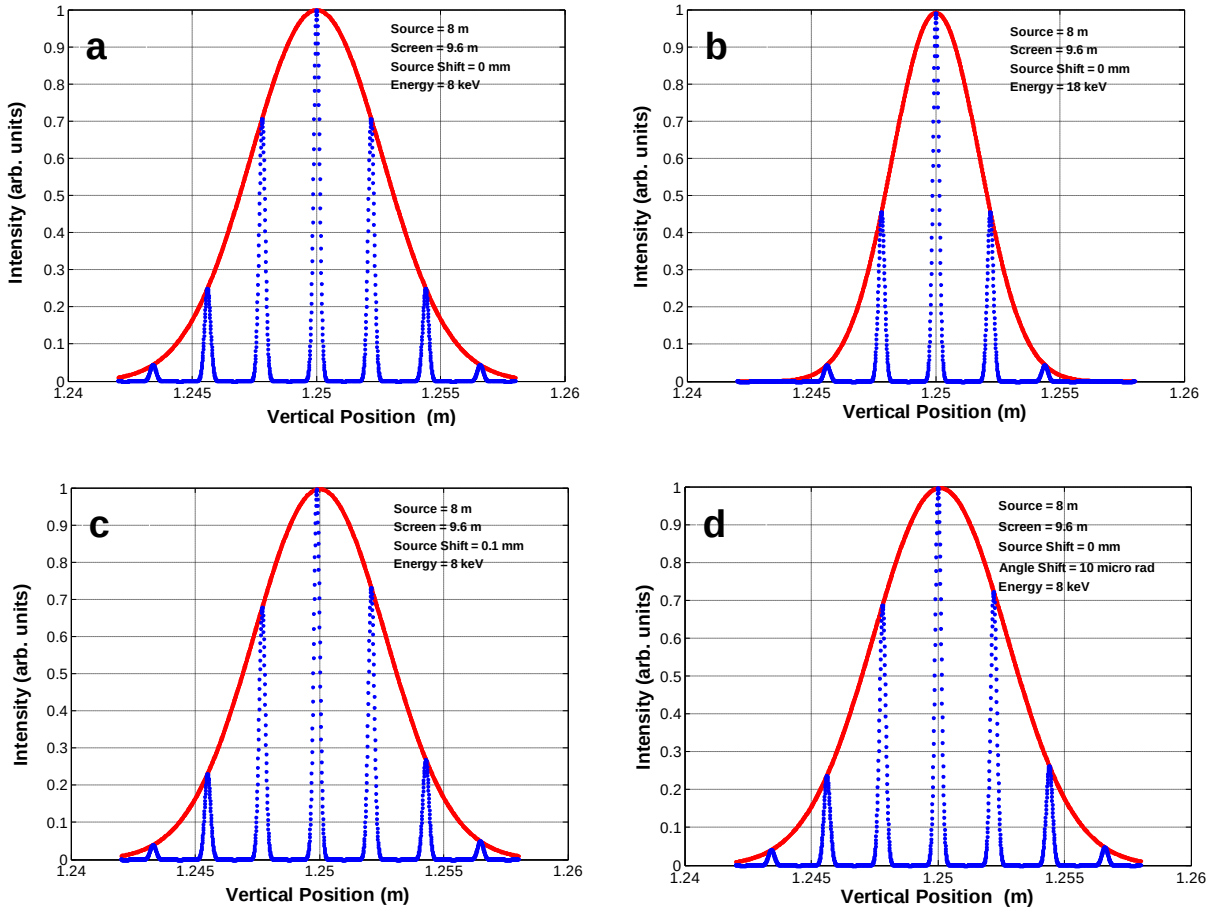

Figure 2.6: *Calculated intensity distribution on the phosphor screen. Pinholes with 1 mm pitch and 20 μm diameter give good contrast factor for seven peaks at 8 keV (a), and five peaks at 18 keV (b). Calculated intensity distributions with 100 μm vertical shift (c), and 10 μrad angular shift of the source point (d), at 8 keV.*

2.2.5 Staggered pair blade monitor (SPM)

The variations in position and emission angle at the source point causes many focusing problems in SR user beamlines. So, the vertical centroid of SR intensity is measured online

by using a staggered pair blade monitor (SPM) [86]. It works on the principle of photoemission from copper blades (OFHC). In a SPM, two set of blade-pairs with the same spacing but staggered with respect to each other are used as shown in Figure 2.7. The position of maximum of the vertical intensity distribution is measured by simultaneously measuring all four photocurrents. In order to distinguish between the source movements and changes in the angle of emission, two such systems are installed in the front-end of diagnostic beamline.

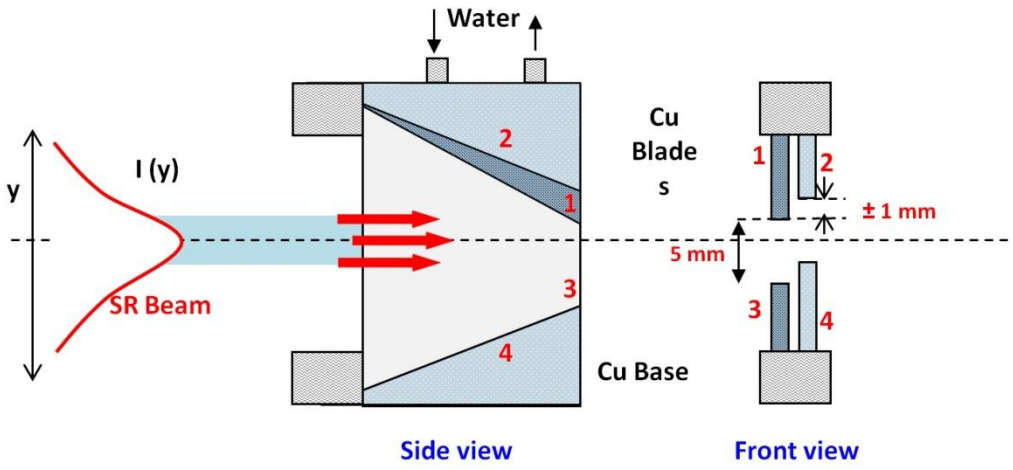

Figure 2.7: *Internal structure of staggered pair blade monitor used at X-DBL*

The asymmetry factors of the photoemission current for two set of blades are $A_{1/3} = (I_1\text{-}I_3)/(I_1+I_3)$ and $A_{2/4} = (I_2\text{-}I_4)/(I_2+I_4)$. The asymmetry results from the photo yield of the copper blades, the size of the blade opening, and the spectral and angular distribution of the radiation. In SPM, internal calibration standard is established by employing two sets of blades, each pair with the same spacing but staggered with respect to each other. For two pairs with positions ± *a* mm above and below the theoretical position of the centre of gravity (of the radiation cone), position 'P' can be given by

$$P = cA_{2/4} - a \tag{2.8}$$

$$P = cA_{1/3} + a \tag{2.9}$$

$$c = {2a}\Big/\left(A_{2/4} - A_{1/3}\right) \tag{2.10}$$

By simultaneously measuring all four photocurrents, one can measure a constant value of *c*. These equations are valid for asymmetry factors between -0.5 and +0.5. SPM system installed at relatively large distance from source can measure very small changes in vertical angle of emission.

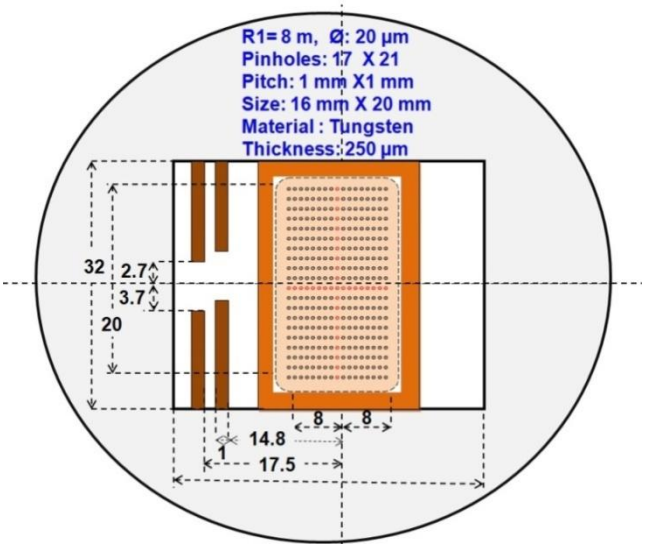

Figure 2.8: *Schematic of the SPM with pinhole array at 8 m from the source in the X-DBL*

In the X-DBL, both pinhole array and the SPM are placed side-by-side at 8 m from the source point as shown in Figure 2.8. For remote alignments, SPM assembly can be moved

with a resolution of 10 μm within a linear stroke of ± 1 mm. The measurements on SPM system are also related to positional shifts measured on the pinhole array system as both are installed on the same dipole magnet. The small changes of few microns in position and angle of the electron beam can also be measured at X-DBL.

2.2.6 Metal filters and phosphor screen

SR spectrum emitted from a dipole magnet has wide spectral range. To improve the spatial resolution, SR photons of higher and lower energies are removed by using energy filters before imaging at the experimental station. A thin metal foil acts as high pass filter for SR photon. Al and Mo metal foils of different thickness (6.5-50 μm) are mounted on remote control actuation mechanism inside the filter chamber. This arrangement can provide nine sets of filter combinations for energy selection in x-rays imaging. Calculated transmitted flux (by using SPECTRA [128] and [133]) on phosphor screen at different energies for different filter combinations in X-DBL is shown in Figure 2.9. Metal filter assembly is integrated with phosphor screen assembly used for conversion of selected x-rays to visible light.

Phosphor selection is based on emission spectrum, conversion efficiency and luminescence decay time of various phosphors used for X-ray diagnostics at other SRSs [134][135]. Relative comparison of these standard phosphors is given in Table 2.3. P-43 is useful for conversion of complete x-rays and UV range below 250 nm, but its decay time is relatively large (few msec). P-43 with grain size of about 1 micron has high conversion efficiency of $7x10^{-3}$ (W/nm)/W, its spectral peak is sharp at 545 nm with 15% conversion efficiency. Conversion efficiency P-46 is lesser than P-43, but its decay time is fast (few

hundred ns). In X-DBL, Aluminium coated Phosphor screens of P-43 and P-46 are used for imaging.

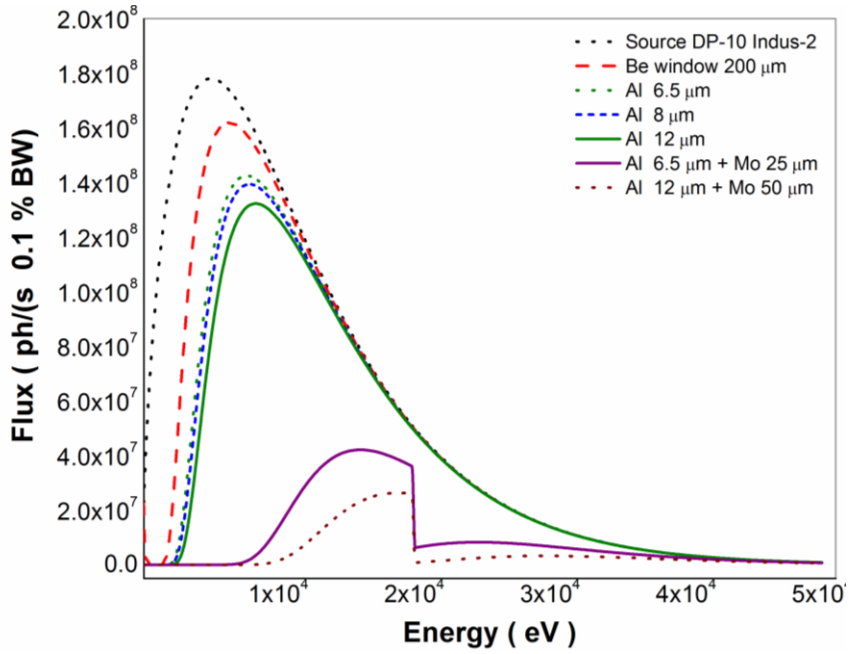

Figure 2.9: *Calculated transmitted flux up to the phosphor screen for different filter combinations in X-DBL.*

Table 2.3: *Relative comparison of the standard phosphors Ref.* [134] [135].

Type	Composition	Light emission				Decay time	
		Range (*nm*)		Peak (*nm*)	Color	From 90% to 10%	From 10 % to 1%
P-43	Gd_2O_2S:Tb	360	680	545	Green	1 ms	1,6 ms
P-46	$Y_3Al_5O_{12}$:Ce	490	620	530	Yellow / Green	300 ns	90 µs
P-47	Y_2SiO_5:Ce, Tb	370	480	400	Blue white	100 ns	2,9 µs
P-20	(Zn, Cd) S: Ag	470	670	550	Yellow Green	4 ms	55ms
P-11	ZnS: Ag	400	550	450	Blue	3 ms	37 ms

2.2.7 Beryllium window

Beryllium window is used for x-rays extraction, vacuum isolation and radiation hardening in the beamlines. Transmission curves of 'Be' window for different thicknesses were plotted using online tool [133]. Beryllium window of 500 µm thickness is used in X-DBL. It has more than 92% transmission for photon energies above 8 keV. It also blocks the effect of unwanted visible light in the imaging system. Transmission curves of the Beryllium window with different thickness are shown in Figure 2.10.

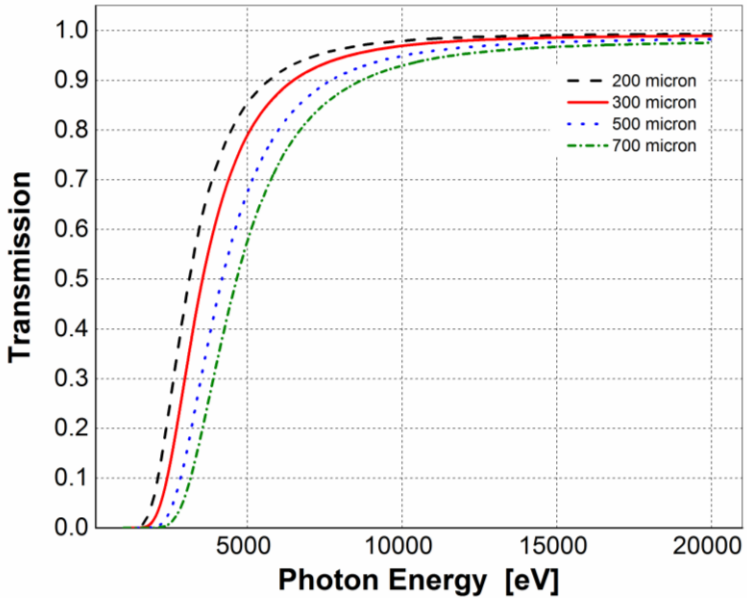

Figure 2.10: *Transmission curves of the Beryllium window with different thickness*

2.2.8 Measurement system

The beam profile on the phosphor screen is capture with a remote controlled zoom lens and a high resolution CCD camera (2456 X 2058 pixels). Zoom optics provides flexibility for imaging from high resolution mode to (where only the central pinhole is visible), to the low

resolution mode (where the whole pinhole matrix becomes visible). Schematic of the image detection system used in X-DBL is shown in Figure 2.11. Snapshot of the GUIs developed for online measurement of beam parameters at X-DBL is shown in Figure 2.12.

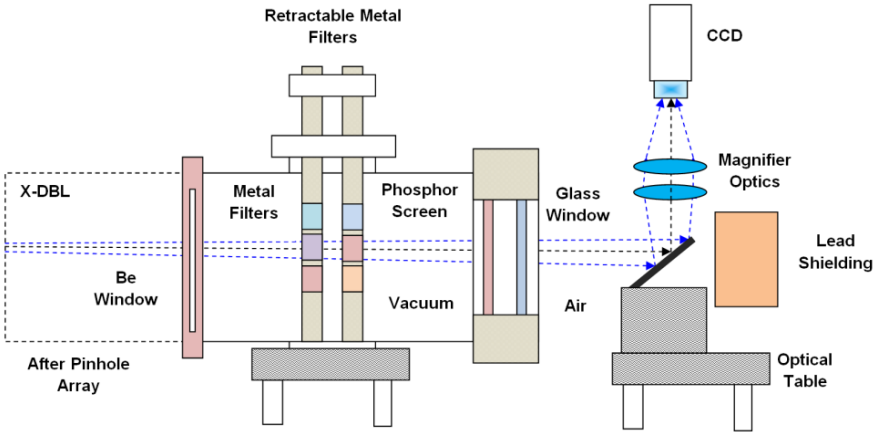

Figure 2.11: *Schematic of the image detection system at X-DBL.*

2.2.9 Measurements at beamline

a) Beam size: The beam spots images on the phosphor screen are captured and processed to get beam size (σ_x , σ_y) and beam centroid in both horizontal and vertical planes as shown in Figure 2.13. Actual beam sizes are calculated by removing the total spread functions of the beamline from the measured values. Beam size measurements under different operating conditions are discussed in Chapter 4.

b) Emittance: Beam emittance is determined by using measured beam size and known Twiss parameters of the source point. Beam size and the beam emittance (ε) are related through beta function, dispersion (η), and momentum spread ($\sigma_\delta = \frac{\Delta p}{p}$) as follows

$$\sigma_x = \sqrt{\in_x \beta_x(s) + \eta(s)^2 \sigma^2_\delta} \tag{2.11}$$

$$\sigma_y = \sqrt{\in_y \beta_y(s)} \tag{2.12}$$

As beta functions of the accelerator are known from the calibrated models (Accelerator Toolbox or LOCO), the emittance can be obtained from the measured beam sizes as

$$\varepsilon_x = \frac{\sigma^2{}_x - \eta(s)^2 \sigma^2{}_\delta}{\beta_x(s)} \text{ and } \varepsilon_y = \frac{\sigma^2{}_y}{\beta_y(s)} \tag{2.13}$$

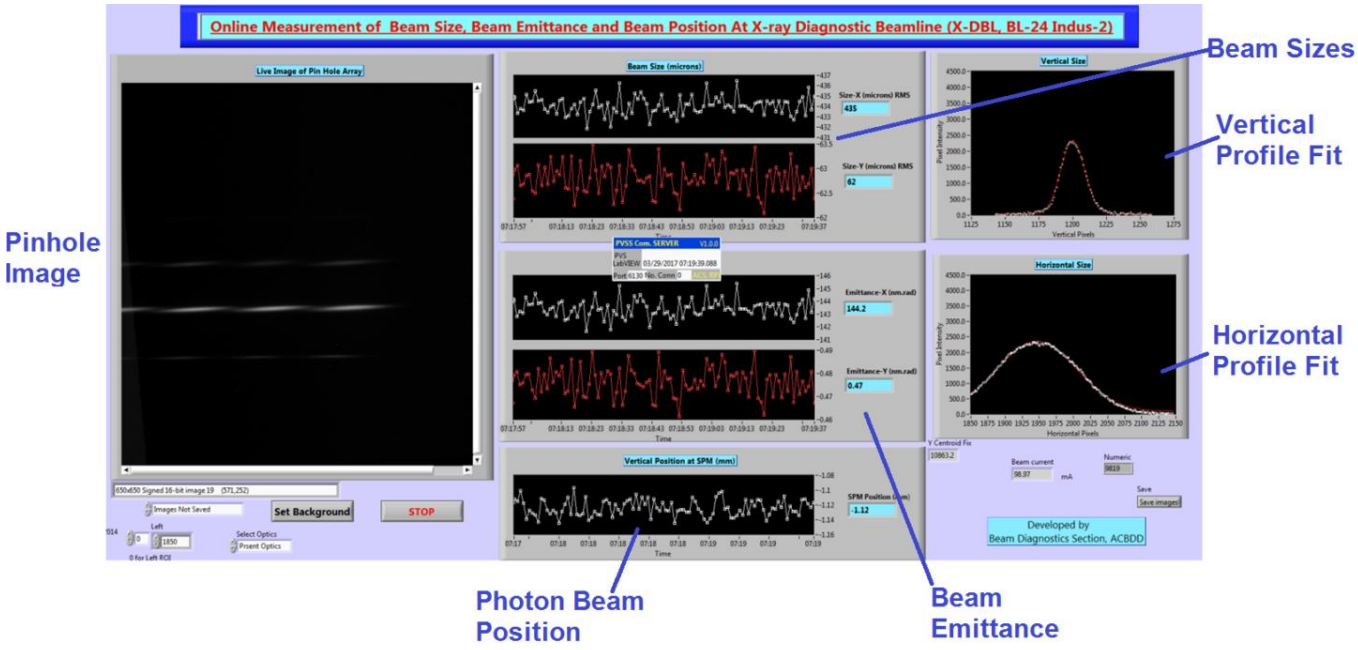

Figure 2.12: *Snapshot of the GUIs developed for online measurement of beam parameters.*

Actually true beam size can be determined from the measured value by subtracting the contributions due to various measurement errors and uncertainties in the Twiss parameters at the source point. In x-ray imaging, spatial measurements have very small diffraction error as compared to the visible. Algorithm for emittance measurement is described in Appendix A [84].

c) Beam stability and beam dispersion: Beam position stability is measured by tracking the centroid of pinhole image at the detector. One significant advantage of the x-ray pinhole camera over the UV/visible imaging is the stability of its final image, since the latter is susceptible to mirror vibrations in long transport line. This feature is used to measure dispersion function at the source point. Generally a set of beam profiles are taken with slightly different RF frequencies, or different beam energies. From the measured displacements of the beam centroid, beam dispersion at the source point can be measured (Ref. Sec. 4.3).

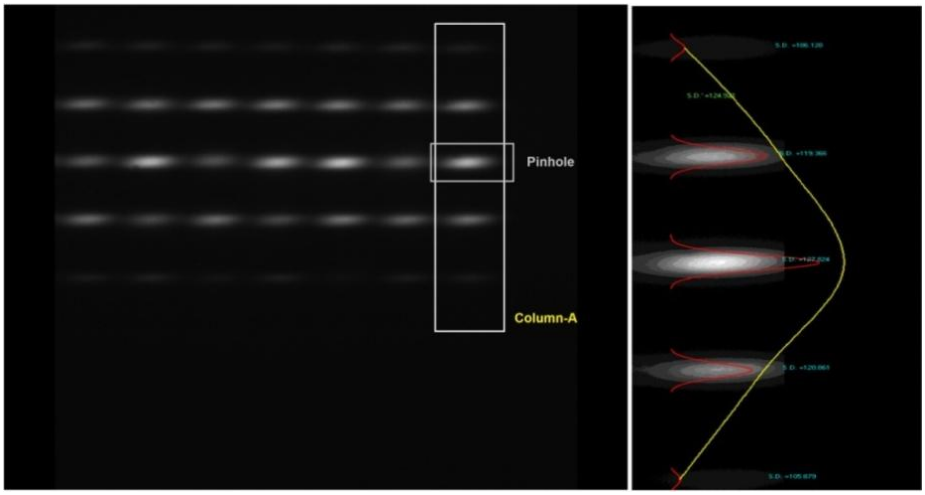

Figure 2.13: *Pinhole array image captured on phosphor screen in the X-DBL at 61 mA beam current. Beam sizes are measured from individual spots, and beam divergence is measured from intensity profile across column-A in the pinhole array image.*

d) Divergence: Beam divergence is measured by Gauss fitting of the intensity distribution of the peaks in vertical column of beam spots. Measurements within a resolution of few micro radians are possible with 500 µm pitch of pinholes.

2.3 Visible diagnostic beamline (V-DBL)

2.3.1 Beamline configuration

The visible diagnostic beamline consists of a water cooled primary mirror in vacuum to extract visible light from the wide SR spectrum. Different type of extraction mirror schemes are used at various visible diagnostic beamlines [102] [136][137] (discussed in section 2.3.3).

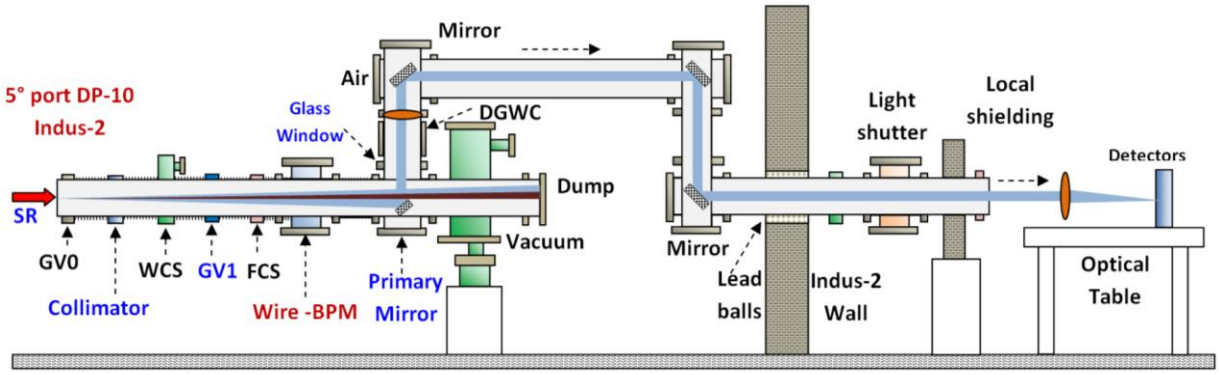

Figure 2.14: *Schematic layout of the visible diagnostic beamline (BL-23) at Indus-2*

In Indus-2, a water cooled copper mirror at 5.5 m from SR source point intercepts only lower half (visible part) of the dipole light. Its total horizontal angular acceptance is ~ 5 mrad. The extracted visible light follows reflective and refractive optics, and focused on optical table in the dark room outside the shielding wall of the Indus-2. Measuring detectors are kept at a distance of ~20 m from the source point in the dark room. Schematic layout of the V-DBL (BL-23) is shown in Figure 2.14. Instrumentation on optical table includes beam profiler, dual sweep synchroscan streak camera, Avalanche photodiode (APD), position sensitive detector (PSD) and fast photo receiver. Beamline is mainly used to measure the

longitudinal beam parameters such as bunch length, bunch separation and bunch filling pattern.

2.3.2 Angular acceptance of the beamline

In the V-DBL, spatial resolution of profile measurement is limited by several factors such as diffraction error, curvature error and depth-of-focus error. Their total contributions can be minimised to some extent by selecting optimum angular acceptance of beamline. The contributions due to each factor and its dependence on angular acceptance of the beamline is discussed below

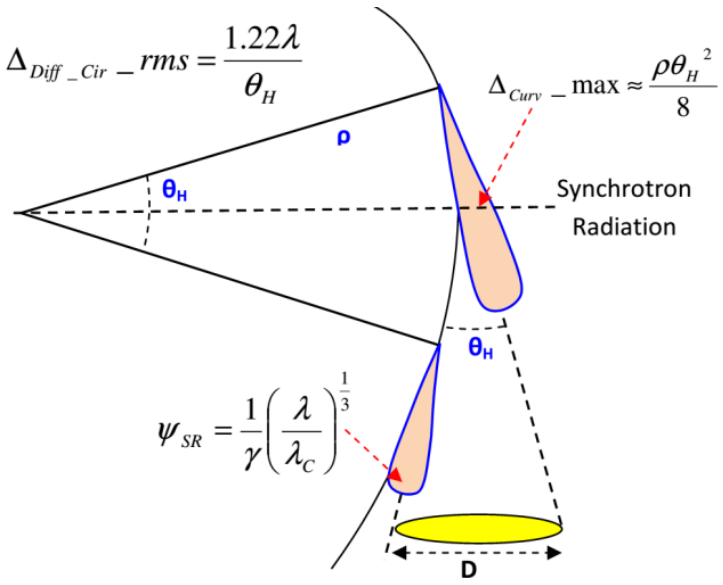

Figure 2.15: *Representation of the contributions due to various errors while imaging the SR fan coming from a dipole magnet at horizontal angular acceptance (θ_H).*

a) Curvature error: It arises due to the curved trajectory of electron beam (source) in dipole magnet. It results in the horizontal broadening of image given by Ref. [137] as

$$\Delta_{Curv\_max.} = \rho - \rho\cos\left(\theta_H/_2\right) \approx \frac{\rho{\theta_H}^2}{8} \tag{2.14}$$

Where ρ and θ_H are the bending radius and horizontal angular acceptance of beamline. Its r.m.s. value can be calculated as follows

$$\Delta_{Curv\_rms} = \sqrt{\frac{1}{\theta_H}\int_{-\theta_H/_2}^{+\theta_H/_2}\frac{\rho x^2}{8}\,dx} \tag{2.15}$$

$$\Delta_{Curv\_rms} = \frac{\Delta_{Curv\_max.}}{\sqrt{5}} \tag{2.16}$$

b) Depth-of-field: As the SR source points are moving electrons, so there is a significant depth-of-field error at the imaging point. This effect is present in both horizontal as well as vertical plane. The dependence of apparent length (*L*) upon angular acceptance of the beamline is as follows.

$$L = \frac{\rho\theta_H}{2}\left(\frac{\theta_H}{2} + \psi_{SR}\right) \tag{2.17}$$

$$\Delta_{Dof\_max.} = \frac{\rho\theta_H(\theta_H + 2\,\psi_{SR})}{4} \tag{2.18}$$

where, $\psi_{SR} \approx 0.45\left(\frac{\lambda}{\rho}\right)^{1/3}$ is the natural opening angle of SR.

c) Diffraction error: As we know that any imaging system that involves apertures, it has inevitable diffraction. Its contribution for a uniformly illuminated slit and circular aperture are $\Delta_{Diff.\_rms.} = \frac{0.5\,\lambda}{\theta_H}$ and $\Delta_{Diff.\_rms.} = \frac{0.6\,\lambda}{\theta_H}$ respectively.

The SR is emitted in narrow cone, and diffraction error limits the ultimate resolution of imaging system. Contrary to the previous two errors (curvature and depth-of-focus error), diffraction error increases with the decrease of aperture (i.e. angular acceptance). SR Hoffmann treated the SR diffraction quantitatively by using Fraunhofer diffraction [72]. The diffraction contribution for σ-mode is given by

$$\Delta_{Diff.\_rms.} = 0.21\ (\lambda^2 \rho\ )^{1/3} \tag{2.19}$$

where ρ and λ are the bending radius and wavelength of light.

d) Chromatic error: Ideally light should be monochromatic for precise optical imaging. But, to good extent chromatic error of visible light is reduced by using optical filters of small bandwidth (10-20 nm).

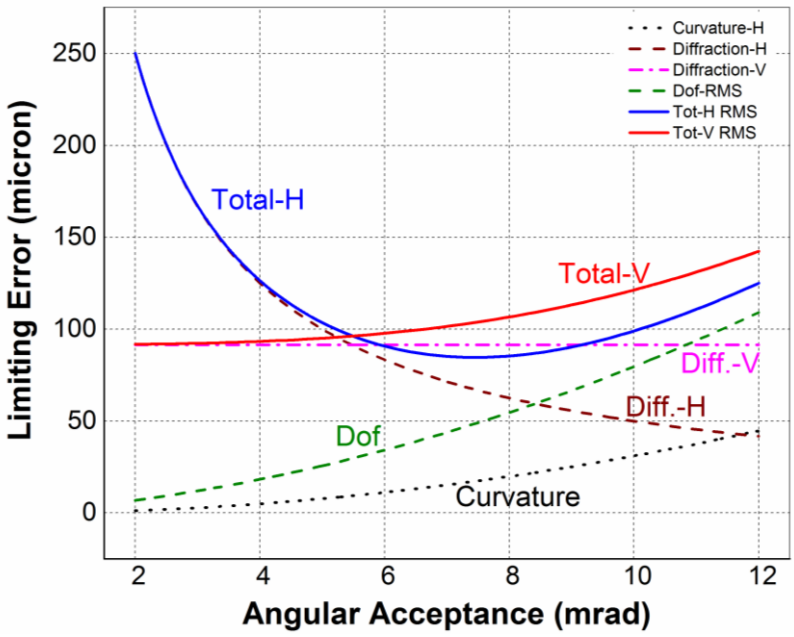

Figure 2.16: *Calculated error contributions at different horizontal angular acceptance in the visible diagnostics.*

e) Total error: These fundamental effects are different in the horizontal and vertical plane. Chromatic and depth of field effect is present in both horizontal and vertical plane. The effect of diffraction and curvature is also different in both the planes. In vertical case, the best resolution is obtained by selecting natural opening angle of the SR. The horizontal angular acceptance is optimized by minimisation of the total effect. Assuming all these beam enlargements as Gaussian distributed and independent, total beam enlargement in the horizontal and vertical planes can be written as

$$\Delta_{Tot.\_H.} = \sqrt{(\Delta_{Curv.})^2 + \left(\Delta_{Dof.}\right)^2 + \left(\Delta_{Diff\_H}\right)^2} \tag{2.20}$$

$$\Delta_{Tot.\_V.} = \sqrt{\left(\Delta_{Dof.}\right)^2 + \left(\Delta_{Diff\_V}\right)^2} \tag{2.21}$$

As the source (electron) here is not a point source, but a Gaussian one, with σ_x and σ_y as the horizontal and vertical sizes respectively, therefore the intensity distribution of the image is also a Gaussian with horizontal and vertical sigma as

$$\sigma_{Image\_x} = \sqrt{(\sigma_x)^2 + \left(\Delta_{Tot.\_H.}\right)^2} \tag{2.22}$$

and

$$\sigma_{Image\_y} = \sqrt{\left(\sigma_y\right)^2 + \left(\Delta_{Tot.\_V.}\right)^2} \tag{2.23}$$

Angular acceptance of the V-DBL is optimized to minimize the effect of these errors and maximize the light output for imaging. Results for angular optimisation are shown in Figure 2.16. Even for optimised angular acceptance ~7 mrad (H), it is mainly dominated by diffraction. Although visible diagnostics has certain diffraction limitations in transverse

measurements but, it is very convenient to use it for longitudinal measurements as a non-destructive diagnostics tool.

2.3.3 Primary mirror

In the visible diagnostics, primary mirror is an essential component to extract visible light out of the vacuum chamber. It is a metallic mirror provided with suitable water cooling mechanism to avert any thermal deformation due to high heat load of the SR. Basically there are three possible options for the primary mirror [137]. First one is to use mirror made of low atomic mass material (like Beryllium). It will be reflective for visible light and transparent to x-rays. The second option is to use a cold finger before the mirror. Cold finger absorbs all the heat load of the central portion of the SR, and the mirror (even without water cooling) reflects visible light. Third option is to use half mirror tilted at 45°, it intercepts lower (or upper) half of the SR fan vertically. To avert thermal effects, mirror is suitably interlocked to remain at least 0.5 mrad away from the central line

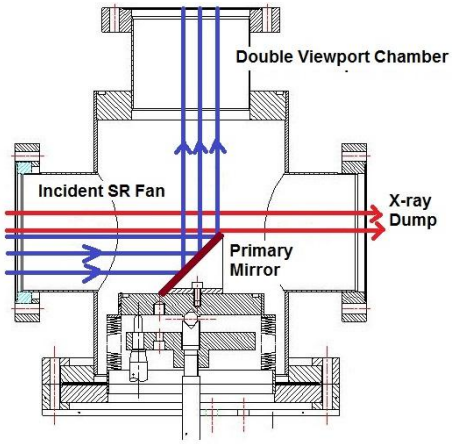

Figure 2.17: *Schematic of water cooled primary mirror at V-DBL*

The photon beam power from the dipole magnet of Indus-2 is ~20 W/mrad at a stored beam current of 200 mA and 2.5 GeV beam energy, and majority of this power falls within the x-rays domain. This high power component is discarded and only visible portion is retained for the visible diagnostics. We are using an approach similar to the split mirror, but with only lower half segment. Thus we are avoiding the complications associated in maintaining co-planar alignment of the two halves and adverse heating problems.

The primary mirror made of copper substrate (80 mm X 50 mm X 10 mm) with 25 μm gold coating is kept at 45° to the horizontal. The mirror can be moved parallel to its surface (45° plane) by stepper motor arrangement, allowing the mirror position to be carefully optimized with respect to the central x-rays core. Optimum water cooling mechanism is provided to avert heating problems. Schematic of water cooled primary mirror at V-DBL is shown in Figure 2.17. Two heat probes extend 1-2 mm away from radiation edge to protect against any thermal overload of the mirror. A temperature rise (exceeding 45 °C) signals the beamline to close water cooled shutter (WCS). The mirror remains typically parked about ~0.5 mrad away from the beam centreline during normal operations.

2.3.4 Power distribution at primary mirror

Angular distribution of the power emitted from dipole magnet (in Watt/mrad^2) is given by Ref. [43] as

$$\frac{dP}{d\Omega} = 5.42\ E^4(GeV)\ B(T)\ I(A)\left[\frac{1}{(1+\gamma^2\psi^2)^{5/2}}\left(1+\frac{5\,\gamma^2\psi^2}{7(1+\gamma^2\psi^2)}\right)\right] \qquad (2.24)$$

where *E*, *I* and *B* are the beam energy (GeV), beam current (A) and strength of magnetic field (T) respectively. Its peak power density (Watt/mrad^2) is

$$\frac{dP}{d\Omega} = 5.42\ \ E^4(GeV)\ B(T)\ I(A) \tag{2.25}$$

By integration Eq. (2.24) over vertical angles gives linear power density (W/mrad Horizontal) as

$$\frac{dP}{d\theta} = 4.22\ \ E^3(GeV)\ B(T)\ I(A) \tag{2.26}$$

Results of the SR power density calculated by using SPECTRA calculation code [128] for V-DBL are shown in Figure 2.18.

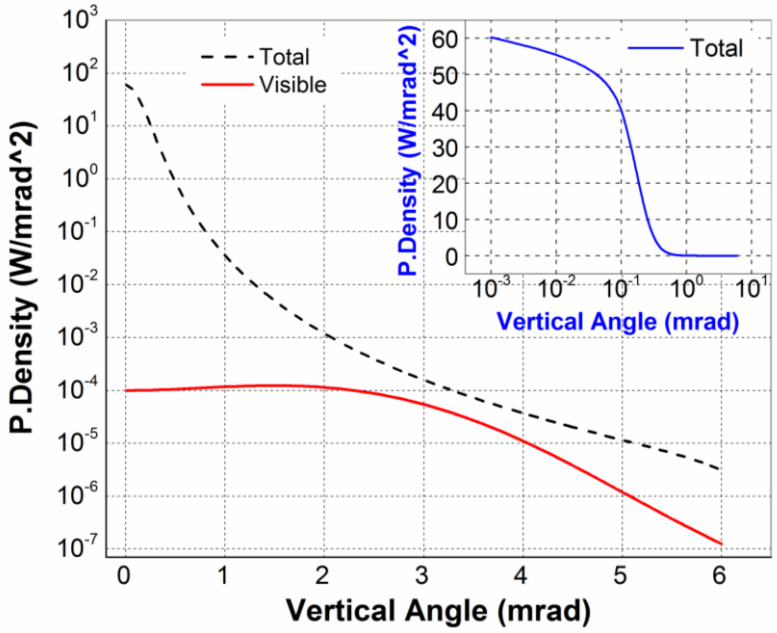

Figure 2.18: *SPECTRA results of angular distribution of total power density and visible power density from dipole magnet of Indus-2. Most of the SR power remains confined within 0.5 mrad vertical angle (inset).*

The calculations of the angular power show that most of the incident SR power is confined within 0.5 mrad (vertical). By positioning primary mirror at ~ 0.5 mrad up or below the centreline, one can avert high heat load of central SR part. Results of incident flux density on the primary mirror for different energies are also shown in Figure 2.19. Flux density at the location of primary mirror is ~10^{11} photons/s/mrad^2/0.1% bandwidth for Indus-2 dipole magnet in visible energy range.

Table 2.4: *Important technical parameters of the V-DBL (BL-23).*

Parameter	**Value**
Energy (*GeV*)	2.5
Beam current (*mA*)	200
Magnetic field of dipole magnet (*T*)	1.5
Bending radius (*m*)	5.5
Critical energy (*keV*)	6.25
Natural opening angle (*mrad*)	0.204
Peak power density (*Watt/mrad*^{2})	60
Linear power density (*W/mrad Hor.*)	~ 20
Total power emitted (*kW*)	~ 125
Total power beyond 0.5 mrad vertical (*Watt/mrad*^{2})	< 2
Angular acceptance of beamline (H) (*mrad*)	5
Distance of primary mirror from source point (*m*)	5
Vertical opening angle of beamline (*mrad*)	~ 5
Peak power density on primary mirror (*Watt/mm*^{2})	3.8
Linear power density on primary mirror (*W/mm Horz.*)	4.0
Calculated visible light power in dark room (*mW*)	< 1

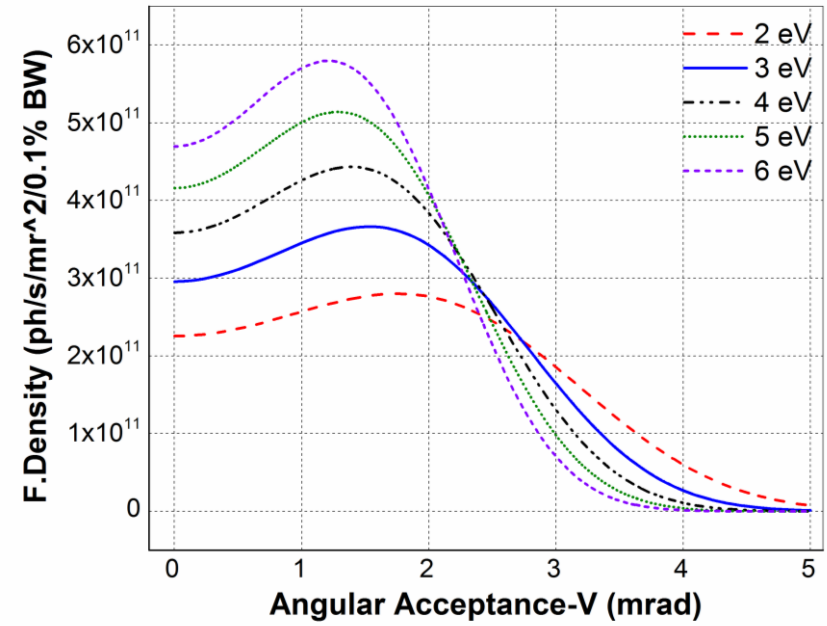

Figure 2.19: *Calculated incident flux density on the primary mirror at different energies*

2.3.5 Ray trace of beamline optics

After the primary mirror, the visible light is extracted out of vacuum through a high-quality Kodial glass window, and then reflected 90^{o} by the secondary optical mirrors. We have kept a vertical offset of ~0.5 m between the two mirrors. It will keep radiation levels inside the adjacent optical hutch well within the safety margins even during beam injection.

Visible light is focused from the source point to the image plane on the optical table (dark room) by a combination of achromatic doublet lenses (f = 5350 mm and diameter = 50 mm). Ray trace of V-DBL was carried out using RayOptik code in MATLAB [138] is shown in Figure 2.20.

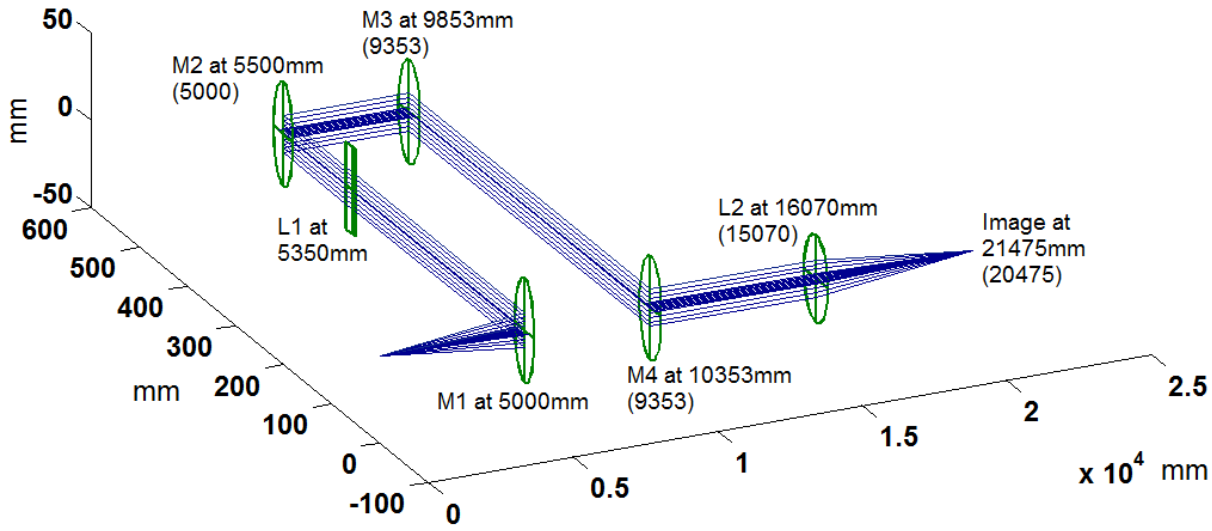

Figure 2.20: *Ray trace of the V-DBL (BL-23) at Indus-2 by using RayOptik.*

2.3.6 Instrumentation for measurements

2.3.6.1 Dual sweep synchroscan streak camera

a) Operation principle: The light pulse to be measured is focused on the photocathode of streak tube (by using input optics), where the incident photons are converted into electrons. These photoelectrons are accelerated by the accelerating mesh and pass through a pair of deflection plates. Electrons get multiplied in a micro-channel plate (MCP), and hit the phosphor screen in the streak tube. These electrons are reconverted into an optical image at the phosphor screen. A voltage ramp (sweep) is applied to the photoelectrons at the instant they pass through the deflection electrodes. Electrons leaving the photocathode at earlier times arrive at the phosphor screen at a position close to the top of the screen, while those electrons that leave the photocathode at later times arrive at a position closer to the bottom of the screen. In this way, streak camera works on transforming the temporal profile of a light

pulse into a spatial profile on a detector (by applying a time-varying deflection). Schematic of streak camera and its operating principle is explained in Figure 2.21.

b) Streak camera at V-DBL: In V-DBL, visible light is focused at the input slit of dual sweep synchroscan streak camera (Model SC-10 Optronis) [29]. Streak camera is equipped with fast vertical synchroscan sweep unit and slow horizontal sweep unit to perform temporal measurements of the beam. Bunch train can be analyzed bunch-by-bunch with synchroscan sweep unit operating at half of Indus-2 RF frequency (505.812 MHz) i.e. even bunches on one sweep and odd ones at the return sweep. The second sweep unit allows the streak camera to measure fast phenomena at relatively slow rate (based on its repeatability). It is possible to look at long term stability of the beam over several milliseconds by using a slow second sweep unit. Schematic of various timing modules used to trigger streak camera system in V-DBL is shown in Figure 2.22.

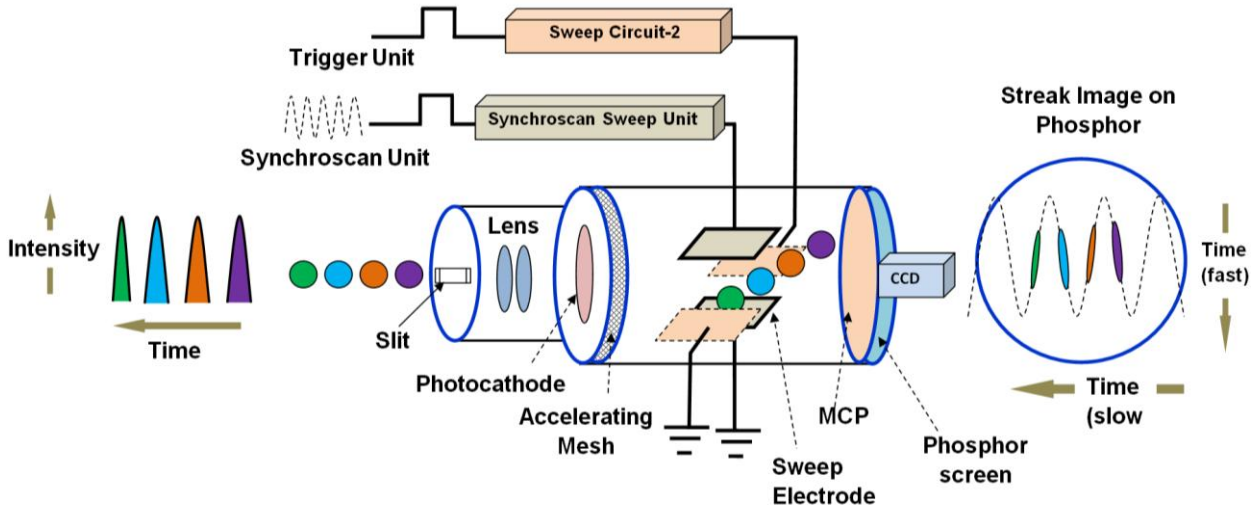

Figure 2.21: *Schematic of the streak camera and its operating principle*

Temporal width of bunches in accelerator/SRS remains few ps to few tens of ps. The temporal resolution of the synchroscan sweep unit is ~3 ps [29], and individual bunches can be clearly resolved and analyzed. The finite temporal resolution of the system is limited by dispersion of the photo-electrons in the streak tube and the jitter of the deflecting voltage. Resolution can be improved by using optical monochromator (< 10 nm bandwidth) and polarisers.

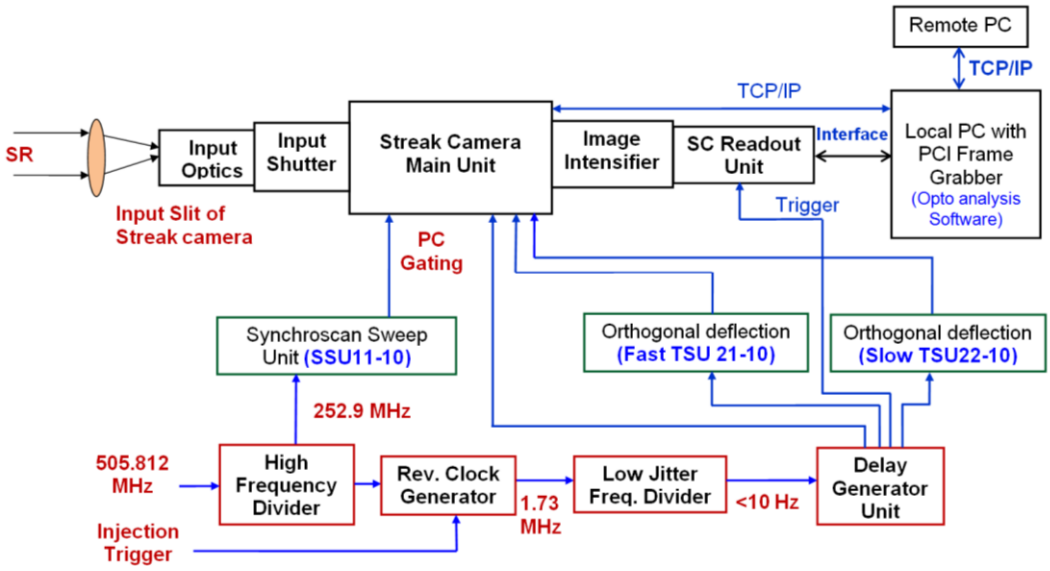

Figure 2.22: *Schematic of the various timing modules used to trigger streak camera*

2.3.6.2 Avalanche photodiode

Avalanche photodiodes have a similar structure to regular photodiodes, but it is operated at much higher reverse bias voltage. This allows each photo-generated carrier to be multiplied by avalanche breakdown and increases the effective responsivity of the device. APD has low capacitance and fast rise time, so it is used to monitor the bunch filling pattern of the SRSs [139][140][141].

2.3.6.3 Beam profiler

Beam profilers/ charge coupled device (CCD) are the most common detector used for measuring beam profiles. It consists of an array of discrete potential wells (pixels) that store accumulated charge. The charge induced by incident photon is read out sequentially [142].

2.3.6.4 Position sensitive detector

Position sensitive detector is an optical position sensor used to measure the position of light spot on the sensor surface [109]. The source position stability can be determined from the measured beam shift and known optics parameters of the beamline.

2.3.7 Measurements at beamline

a) Bunch length: Bunch length, bunch separation and longitudinal dynamics studies of the charge particles are carried by using streak camera system at V-DBL. It can provide temporal resolution down to few picoseconds for bunch length measurement. Typical measured bunch length (RMS) and bunch separation of five consecutive electron bunches are 53±2.5 ps and 1.97±0.026 ns respectively (as shown in Figure 2.23). Bunch length studies to measure longitudinal impedance of Indus-2 are discussed in Chapter 3.

b) Beam profile: Information for beam profile in horizontal and vertical direction is obtained by using CCD or beam profiler. Snap shot of beam profile measured at beam profiler in V-DBL is shown in Figure 2.24.

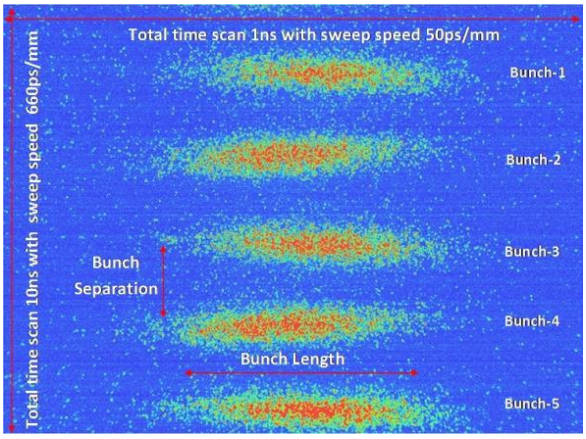

Figure 2.23: *Typical bunch length measured using dual sweep synchroscan streak camera for five consecutive bunches at 75mA beam current in Indus-2.*

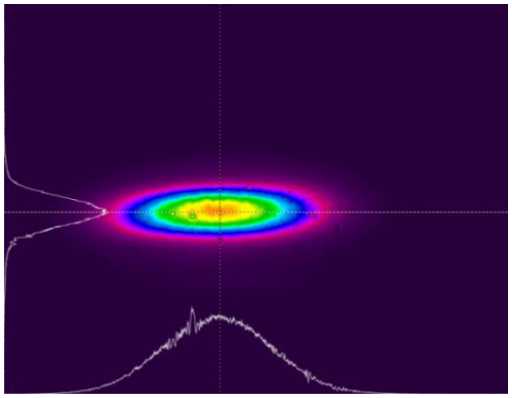

Figure 2.24: *Snap shot of the beam profile measured at beam profiler in the V-DBL*

c) Beam position: Beam position is measured by using position sensitive detectors (PSDs) or CCD camera at the optical table. Linear image sensor and two dimensional sensors can be also be used for measurement of beam position at higher data rate (5-10 MHz) [109].

d) Bunch filling level: Information regarding the number of filled bunch and number of particles in each bunch are called bunch filling pattern and bunch filling level respectively. These measurements were carried out using APD and fast photo receiver [109]. Snap shots of oscilloscope with bunch filling patterns are shown below in Figure 2.25.

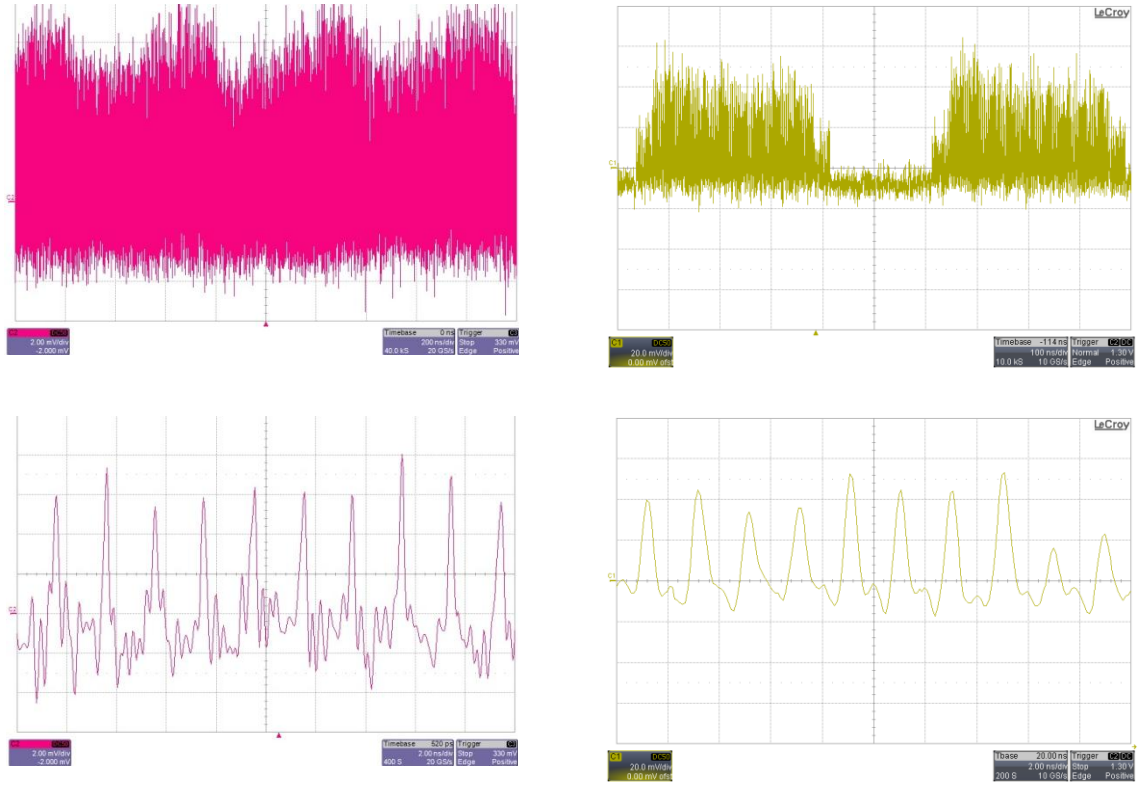

Figure 2.25: *Snap shots of bunch filling patterns captured on oscilloscope, all 291 buckets filled (upper left), 200 filled buckets out of total 291 buckets (upper right), filling level of individual buckets (bottom).*

2.4 Summary and conclusions

Two diagnostic beamlines have been designed, developed and commissioned successfully at Indus-2 SRS, viz. X-ray diagnostic beamline and visible diagnostic beamline. Generally former is used for the transverse measurements whereas latter for the longitudinal measurements. X-DBL (BL-24) is installed at 10^{o} port of the bending magnet (DP-10) in

Indus-2 SRS. Tungsten pinhole array with 17(H) X 21(V) pinholes of 20 µm diameter each is placed at 8 m from the source point, and its imaging is carried out (~ 9.6 m distance) on a phosphor screen with a magnification factor of 1.2. Beamline is designed to capture more than five fully resolved pinholes image on the phosphor screen. An additional staggered pair blade monitor (SPM) is also installed inside the pinhole array chamber. Metal filter assembly have Al and Mo metal foils of different thickness (6.5 to 50 μm) mounted on remote controlled actuation mechanism inside the filter chamber. This arrangement can provide nine sets of filter combinations for the energy selection in x-rays imaging. Aluminium coated Phosphor screens of P-43 and P-46 are used for converting x-rays into visible light for measurements with a CCD camera. Beamline is used to measure transverse beam parameters such as beam size, beam divergence, beam emittance and beam position.

V-DBL (BL-23) is installed at 5^o port of the bending magnet (DP-10) in Indus-2 SRS. A water cooled primary mirror is used to extract visible light from the wide SR spectrum. The extracted light is focused at various optical detectors placed outside the shielding wall of Indus-2 in a dark room. Optical detectors such as dual sweep synchroscan streak camera, fast photo receiver, avalanche photodiode, position sensitive detectors and CCD camera are used for various measurements. V-DBL is used for the measurement of bunch length, bunch separation, bunch fill pattern and beam position. The diagnostic beamlines are useful in beam dynamic studies of charge particle under different operating conditions. Results of longitudinal and transverse measurement done at beamline are discussed in Chapter 3 and Chapter 4. The knowledge of these parameters helps in the stable and smooth operation of the Indus-2 SRS.

Chapter 3 Study of longitudinal profile of electron bunches and impedance measurement

3.1 Introduction

At low beam currents, the motion of a charged particle beam is mainly guided by the magnetic lattice and RF cavities of the accelerator. But in addition to these interactions with the external fields, the beam also interacts with its surrounding vacuum chamber through the electromagnetic fields generated by the beam itself. At high currents, the effects of the beam induced fields become more important and may limit the performance of an accelerator [7] [69].

The various accelerator components such as bellows, injection/extraction septum, RF cavities, BPM, and even a smooth pipe of finite conductivity causes scattering or trapping of the beam-induced fields. These fields can last for long enough to be experienced by a charge particle following the exciting charge, and it can perturb the energy or angle of the following particle's orbit. The dynamics of particle bunches due to their interaction with the environment (of the accelerator) through the beam-induced electromagnetic field is generally described in terms of *collective effects*. Collective instabilities usually limit the performance of an accelerator. The maximum current that can be injected/ stored in an accelerator depends

upon the impedance of accelerator ring. These scattered or trapped fields may also cause heating of the accelerator components.

The electromagnetic interactions of the beam with its surroundings are described as wakefield in the time domain or impedance in the frequency domain. The wake function and impedance are equivalent i.e. the impedance is the Fourier transform of the wake function. The impedance of an accelerator is usually considered to have three major contributions, (i) resistive wall, (ii) several narrow band resonators (modeling cavity-like objects), and (iii) one broad-band resonator (that models the rest of the ring). Both resistive wall and narrow band resonators are usually associated to slowly decaying (high Q) wake fields causing mainly the motion of one bunch to affect subsequent bunches i.e. produce severe *multi bunch effects* (MBE). The broad-band resonator, which models the global effect of all discontinuities in the beam pipe and several non-resonating objects is short range (low Q), mostly affects the particle dynamics within single bunch i.e. *single bunch effects* (SBE) [143].

The impedance of any accelerator/storage ring is a complex quantity with real and imaginary parts. Real part is a resistance and manifests as an extraction of energy from the beam (i.e. energy loss of the bunch). This energy loss is characterized by the loss factor k_l and is expressed as $\Delta E = -k_l q^2$, where q is the bunch charge [144]. The imaginary part does not lead to any net energy loss within the bunch, but it causes energy transfer between the particles within a bunch. Ultimately it also causes bunch lengthening through increase in energy spread of the bunch (deformation of beam profile). Therefore these electromagnetic interactions can deteriorate the quality of stored beam by parasitic energy loss of charge particles, or may make the beam unstable. Further with the increasing requirement for

particle beams with low emittance (in SRSs) and high luminosity (in colliders), it becomes more important to understand these electromagnetic interactions of the beam with vacuum chamber environment for maintaining the quality of the beam.

The major factors influencing the bunch lengthening are potential-well distortion (PWD) and microwave instability. PWD affects the equilibrium charge distribution of a bunch, and the deformed charge distribution inside the bunch can be obtained by solving the Haissinski equation [36]. Numerical and analytical solutions of the PWD equation are given for different longitudinal coupling impedances [145][146][147]. The impedance of storage ring is analyzed by applying these solutions/ impedance models [148][149] on the measured bunch lengthening behaviour. Mostly these studies are performed by filling charge in single bunch mode, where same charge acts as cause as well as probe [150][151].

In Indus-2, longitudinal profiles of electron bunch in single bunch mode were measured at injection energy (550 MeV) and at final beam energy of 2.5 GeV. In this chapter, the behaviour of measured bunch lengthening and phase advancing at streak camera is analyzed. The bunch lengthening and phase advancing is measured by applying asymmetric Gauss fit to the longitudinal profiles captured at streak camera. The effects of wakefield generated interactions between beam and surroundings are analyzed on the longitudinal beam distribution. The inductive and resistive impedance of the ring is obtained by applying theoretical impedance models. These results are also compared with the values obtained from the measured synchronous phase advancing and scaling laws [32]. These studies are very

useful in better understanding and control of these electromagnetic interactions. Main parameters of Indus-2 SRS are discussed in Table 1.1 (Chapter 1).

3.2 Theory of bunch lengthening

The longitudinal distribution of light charge particles is determined by the equilibrium between radiation damping and quantum excitation. Natural bunch length σ_{zo} for a Gaussian distribution is given by Ref. [69] as

$$\sigma_{zo} = \frac{c\,\alpha_p}{2\pi\, f_{S0}}\,\sigma_{\varepsilon o} \tag{3.1}$$

where α_p is the momentum compaction parameter, c is the speed of light, $\sigma_{\varepsilon o}$ is the relative energy spread of the beam and f_{S0} is the synchrotron oscillation frequency. In addition to these factors, bunch length also depends upon peak current of the bunch. The two major effects which change the bunch length are potential well distortion and microwave instability.

3.2.1 Potential-well distortion

As the bunch current increases, the wakefield starts to modify the RF potential in which charge particles sits, and hence distorting the shape of the bunch from a pure Gaussian i.e. called potential-well distortion. PWD effect is present even at very low beam currents. The size of the PWD effect on bunch lengthening depends upon the reactive part of the effective longitudinal coupling impedance given by Zotter's formula [38] as follows

$$\left(\frac{\sigma_z}{\sigma_{zo}}\right)^3 - \left(\frac{\sigma_z}{\sigma_{zo}}\right) - I_{beam}\ \frac{e\ \alpha_p\ Im\left\{\left|\frac{Z_{||}}{n}\right|\right\}_{eff.}}{\sqrt{2\pi}\ E\ {\nu_{so}}^2}\left(\frac{c}{\omega_{rev.}\ \sigma_{zo}}\right)^3 = 0 \tag{3.2}$$

Where I_{beam} is the average beam current, e the electron charge, c the velocity of light, $\omega_{rev.}$ is the revolution frequency, E the beam energy and ν_{so} is the synchrotron tune.

3.2.2 Microwave instability

When the peak bunch current exceeds the stability limit (i.e. threshold) determined by the machine impedance, bunch starts lengthening turbulently until the peak current falls below the threshold level. It causes an increase in the energy spread of the beam, and can also be seen as a sudden increase of the beam size especially in a dispersive region of the lattice. The threshold current (I_{Th}) of MWI is also used to get an estimate of the machine impedance as follows [152]

$$I_{Th} = \frac{\sqrt{2\pi}\ \ {\alpha_p}^2\ \ E\ {\sigma_{\varepsilon o}}^3}{e\ \upsilon_{S0}\ \left|\frac{Z_{||}}{n}\right|_{BB}} \tag{3.3}$$

Where $\left|\frac{Z_{||}}{n}\right|_{BB}$ is the longitudinal broadband impedance, $n = \frac{\omega}{\omega_0}$ is the multiple of revolution frequency, $\sigma_{\varepsilon o}$ is the natural energy spread, α_p is the momentum compaction factor, υ_{S0} is the synchrotron tune, E is the beam energy and e is the electron charge. From Eq. (3.1) and (3.3), it becomes

$$\sigma_z{}^3 = \frac{\alpha_p\ c^2\ R\ \left[\frac{Z_{||}}{n}\right]_{BB}}{\sqrt{2\pi}\left(\frac{E}{e}\right) v_S{}^2\ \omega_o{}^2}\ I_{beam} \tag{3.4}$$

As MWI causes an increase in energy spread (σ_ε) of the beam, therefore horizontal beam size σ_x will also increases as follows

$$\sigma_x{}^2 = \epsilon_x \beta_x + (\eta_x\ \sigma_\varepsilon)^2 \tag{3.5}$$

where ϵ_x is the horizontal emittance, β_x is the horizontal betatron function and η_x is the horizontal dispersion function.

3.2.3 Combined effect of both potential-well distortion and microwave instability

Above the threshold beam current, bunch lengthening is the result of both effects, viz. PWD and MWI. The potential well distortion changes the synchrotron frequency (f_S) and the microwave instability increases the energy spread (σ_ε). So, Eq. (3.1) can be rewritten as

$$\sigma_{zo}\ = \frac{c\ \alpha_p}{2\pi\ f_S}\ \sigma_\varepsilon \tag{3.6}$$

By deriving f_S from the Eqs. (3.1) and (3.2), and σ_ε from the Eqs. (3.1) and (3.3), bunch lengthening due to the combined effect can be written as follows [153]

$$\sigma_z{}^3 = \frac{\alpha_p\ c^2\ R}{\sqrt{2\pi}\left(\frac{E}{e}\right) v_S{}^2\ \omega_o{}^2}\left\{\left[\frac{Z_{||}}{n}\right]_{BB} - Im\left\{\left|\frac{Z_{||}}{n}\right|\right\}_{eff.}\right\} I_{beam} \tag{3.7}$$

where σ_ε , is the natural relative energy spread of the beam, and f_S is the synchrotron oscillation frequency.

3.2.4 Synchronous phase advance

In SRS, in addition to the SR energy loss, various vacuum components in the machine also cause energy loss through their impedance with a specific loss factors associated with each of them. All these loss factors add up and give a total energy loss due to resistive impedance in the machine. These extra energy losses must also be compensated for the bunch stability. Therefore in order to compensate this additional loss, the bunch centroid shifts in the RF phase with the increase of beam current (i.e. phase advancing). Synchronous phase advance of the bunch can be measured to find of the impedance of machine.

The energy loss is directly dependent on charge in the bunch as $\Delta E = -k_l q^2$. In terms of voltage it becomes $\Delta V = -k_l q$ or $\Delta V = -k_l {}^{I_b}/_{f_o}$, where I_b is the bunch current and f_o is the revolution frequency. To compensate this energy loss an equal and opposite voltage shift is experienced by the bunch at the RF cavity. For a small shift, it can be equated as follows [144]:

$$\Delta\hat{V} = V_o \cos(\varphi_S).\Delta\varphi_S \tag{3.8}$$

$$V_o \cos(\varphi_S).\Delta\varphi_S = k_l {}^{I_b}/_{f_o} \tag{3.9}$$

It gives phase and time advancing as $\Delta\varphi_S = \frac{k_l I_b}{V_o \cos(\varphi_S).f_o}$ and $\Delta\tau = \frac{k_l I_b}{\omega_{RF} V_o \cos(\varphi_S).f_o}$ respectively. For Gaussian bunches, measured loss factor (k_l) can be equated with $k_l = \frac{R}{2\sqrt{\pi}\sigma_z}$ to get resistive impedance in the machine.

3.3 Estimation of inductive and resistive impedance

The Haissinski equation [36] is used to describe equilibrium longitudinal particle distribution within a bunch in the presence of an arbitrary longitudinal wakefield. In an electron machine, beam current distribution below the turbulent threshold is given as follows [148]

$$I(t) = K.\exp\left(\frac{-\mathrm{t}^2}{2\,\sigma_{\mathrm{zo}}^2} + \frac{\int_0^{\mathrm{t}} V_{ind.}(t')\,dt'}{V'_{RF}\,\sigma_{\mathrm{zo}}^2}\right) \tag{3.10}$$

σ_{zo} is the natural bunch length, V'_{RF} is the slope of the RF voltage at synchronous phase, and $V_{ind.}$ is the induced voltage due to impedance, and it can by written as

$$V_{ind.} = -\int_0^{\infty} W^{||}(t')\,I(t-t')\,dt' \tag{3.11}$$

where $W^{||}(t)$ is the Green's function of the longitudinal wakefield. Eq. (3.10) gives a particle distribution which is a Gaussian multiplied by a distortion term depending on the wakefield generated by the bunch, which in turn depends on the particle distribution itself. The value of the normalization constant *K* is such that the complete integral of $I(t)$ is equal to the total charge in the bunch Q. By taking logarithmic derivative on both sides of Eq. (3.10), it becomes [148]

$$\frac{\dot{I}(t)}{I} = \frac{-\mathrm{t}}{\sigma_{\mathrm{zo}}^2} + \frac{V_{ind.}}{V'_{RF}\,\sigma_{\mathrm{zo}}^2} \tag{3.12}$$

The effect of PWD can be theoretically estimated by using induced voltages from the vacuum components by taking following cases.

3.3.1 Purely inductive impedance

For purely inductive impedance with constant inductance (L), the induced voltage is

$$V_{ind.} = -L\frac{dI(t)}{dt} \tag{3.13}$$

so Eq. (3.14) becomes

$$\frac{\dot{I}(t)}{I} = \frac{-\mathrm{t}}{\sigma_{\mathrm{zo}}{}^2} + \frac{-L\,\dot{I}(t)}{V'_{RF}\,\sigma_{\mathrm{zo}}^2} \tag{3.14}$$

$$\left(1 + \frac{IL}{V'_{RF}\,\sigma_{\mathrm{zo}}^2}\right)\,\dot{I}(t) = \frac{-\mathrm{It}}{\sigma_{\mathrm{zo}}^2} \tag{3.15}$$

On solving it will become [148]

$$\frac{dy}{dz} = \frac{-zy}{1+y} \tag{3.16}$$

where $y = {LI}/{V'_{RF}\,\sigma_{\mathrm{zo}}^2}$ is the normalized current and $z = {t}/{\sigma_{\mathrm{zo}}}$

$V'_{RF} = \omega_{RF}\,V_{RF}\sqrt{1-\left(\frac{U_{SR}}{V_{RF}}\right)^2}$ where ω_{RF}, V_{RF} and U_{SR} are the RF frequency, peak energy gain from RF and average SR energy loss per turn respectively. The complete integral of y is defined as normalized charge (Γ) as follows

$$\Gamma \equiv \int_{-\infty}^{+\infty} y\;dz = \frac{LQ}{V'_{RF}\,\sigma_{\mathrm{zo}}^3} \tag{3.17}$$

Numerical solution of Eq. (3.16) for various values of normalized charge (Γ) at low beam current are shown in Figure 3.1.The charge distribution for a perfect inductor remains symmetric and bunch length increases with the increase of bunch current.

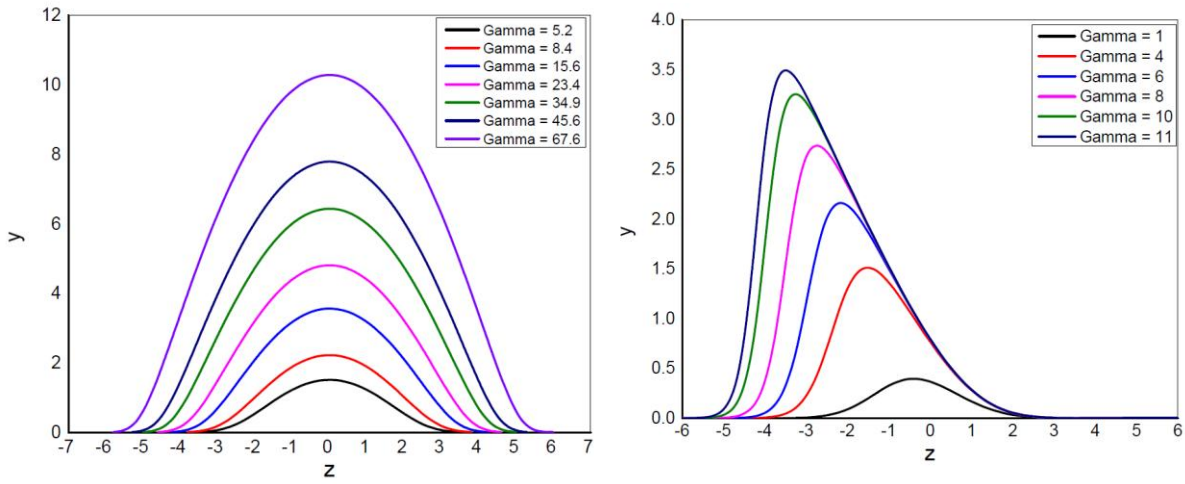

Figure 3.1: *Calculated bunch shapes at different gamma factors corresponding to different bunch currents for pure inductive (left) and for pure resistive impedance model (right).*

3.3.2 Purely resistive impedance

For a purely resistive impedance with a constant resistance (say R), the induce voltage is

$$V_{ind.} = -RI(t) \tag{3.18}$$

So Eq. (3.12) becomes

$$\frac{\dot{I}(t)}{I} = \frac{-\mathrm{t}}{{\sigma_{\mathrm{zo}}}^2} + \frac{-RI(t)}{V'_{RF}\,\sigma_{\mathrm{zo}}^2} \tag{3.19}$$

$$\dot{I}(t) = \frac{-\mathrm{It}}{{\sigma_{\mathrm{zo}}}^2} + \frac{-RI\,I(t)}{V'_{RF}\,\sigma_{\mathrm{zo}}^2} \tag{3.20}$$

On solving it becomes [148]

$$\frac{dy}{dz} = -y(z+y) \tag{3.21}$$

where $y = {RI}/{V'_{RF}\,\sigma_{\mathrm{zo}}}$ and $z = {t}/{\sigma_{\mathrm{zo}}}$.

The complete integral of y is defined as normalized charge (Γ) as follows

$$\Gamma \equiv \int_{-\infty}^{+\infty} y \; dz = \frac{RQ}{V'_{RF}\; \sigma_{zo}^2} \tag{3.22}$$

Calculated bunch shapes for various values of bunch currents for a pure resistive impedance model are shown in Figure 3.1. For pure resistive impedance, the longitudinal charge distribution becomes asymmetric, and distribution centroid is shifted with increasing bunch currents. The bunch lengthening is relatively very slow in resistive machines as compared to inductive one. To measure the bunch lengthening and bunch centroid shift, the measured longitudinal distribution of the bunch is fitted to an asymmetric Gaussian distribution [151] equation given as

$$\mathrm{I(z)} = \mathrm{I_0} + \mathrm{I_1} \exp\left\{\frac{-1}{2}\left(\frac{(\mathrm{z}-\bar{\mathrm{z}})}{[1+\mathrm{sgn}(\mathrm{z}-\bar{\mathrm{z}})\;\mathrm{A}]\sigma_\mathrm{z}}\right)^2\right\} \tag{3.23}$$

where I_0 is the initial base intensity, I_1 is the maximum value of distribution, $\bar{\mathrm{z}}$ is the center of distribution, σ_z is rms bunch length, and A is the asymmetric coefficient.

3.3.3 Series R+L impedance

Let the bunch distribution be

$$\lambda(t) = \frac{\exp\left(\dfrac{-\mathrm{t}^2}{2{\sigma_{\mathrm{zo}}}^2} + \dfrac{\int_0^{\mathrm{t}} V_{ind.}(t')\,dt'}{V'_{RF}\;\sigma_{zo}^2}\right)}{\int_{-\infty}^{+\infty} \exp\left(\dfrac{-\mathrm{t}^2}{2{\sigma_{\mathrm{zo}}}^2} + \dfrac{\int_0^{\mathrm{t}} V_{ind.}(t')\,dt'}{V'_{RF}\;\sigma_{zo}^2}\right) dt} \tag{3.24}$$

$V_{ind.}$ is the induced voltage due to impedance and can be written as

$$V_{ind.}(t) = -\int_0^{\infty} W^{||}(t')\,\lambda(t-t')\,dt' \tag{3.25}$$

where λ is the longitudinal beam distribution, t is the longitudinal position (t<0 means towards the front of bunch), and

$$\int_{-\infty}^{+\infty} \lambda(t)\,dt = 1 \tag{3.26}$$

Table 3.1 : *Numerical solutions for different impedance models* [148]

Impedance model	Induced voltage	Numerical solution	Description
Purely L	$-L\frac{dI(t)}{dt}$	$y' = \frac{-zy}{1+y}$	$z = {}^{t}/_{\sigma_{zo}}$ $y = {}^{LI}/_{V'_{RF}\,\sigma_{zo}^2}$
Purely R	$-R\,I(t)$	$y' = -y(z+y)$	$y = {}^{R\,I}/_{V'_{RF}\,\sigma_{zo}}$
R+ L series	$-eN\left(R\lambda + L\,\dot{\lambda}\right)$	$y' = -y\left(\frac{z+\boldsymbol{r}y}{1+\boldsymbol{l}\,y}\right)$	$y(z) = \lambda\sigma_{zo}$ $\boldsymbol{r} = eNR/V'_{RF}\,\sigma_{zo}^2$ $\boldsymbol{l} = eNL/V'_{RF}\,\sigma_{zo}^3$

By taking the logarithmic derivative on both sides of Eq. (3.24), it becomes

$$\frac{\dot{\lambda}(t)}{\lambda} = \frac{-\mathrm{t}}{{\sigma_{zo}}^2} + \frac{V_{ind.}(t)}{V'_{RF}\,\sigma_{zo}^2} \tag{3.27}$$

With induced voltage $V_{ind.}(t) = -eN\left(R\lambda + L\,\dot{\lambda}\right)$, it will become [148]

$$y' = -y\left(\frac{z + \boldsymbol{r}y}{1 + \boldsymbol{l}\,y}\right) \tag{3.28}$$

where $z = {}^{t}/_{\sigma_{zo}}$, $y(z) = \lambda\sigma_{zo}$, $\boldsymbol{r} = eNR/V'_{RF}\,\sigma_{zo}^2$ and $\boldsymbol{l} = eNL/V'_{RF}\,\sigma_{zo}^3$. To get numerical solution of Eq. (3.28), initial guess values at a distant point ($z=z_0$) are adjusted to fit the solution till it satisfy Eq.(3.26). Curve fit parameters are used to calculate *R* and *L*. Numerical solutions for different impedance models are shown in Table 3.1

3.4 Measurement of longitudinal profiles of bunch in Indus-2

Longitudinal profiles of electron bunch are measured by using dual sweep synchroscan streak camera [29] at V-DBL (BL-23) in Indus-2. Its source point is ~ 20 m away from the detectors in a dipole magnet (5° port of DP-10). The temporal resolution of the system is ~ 3 ps. (system details is provided in the Section 2.3.6.1).

3.4.1 At injection energy

The longitudinal profiles of electrons are captured during injection of beam current upto 11 mA in single bunch mode at injection energy (550 MeV). Profile changes were analysed down to few picoseconds by collecting data of many longitudinal profiles at each beam current. Typical image of the single bunch captured on streak camera is shown in Figure 3.2. The horizontal axis represents bunch length (fast time axis), and the vertical axis represents the longitudinal position of bunch in the direction of beam movement (slow time axis).

In order to get the precise information for the bunch centroid shift, bunch length change and asymmetry factor (bunch shape), the longitudinal distribution measured on streak camera is fitted with asymmetric Gaussian function at each bunch current. Results of measured profiles are also shown in the Figure 3.2. The effect of centroid shift (phase advancing) and bunch lengthening is clearly observed with the increase of beam current.

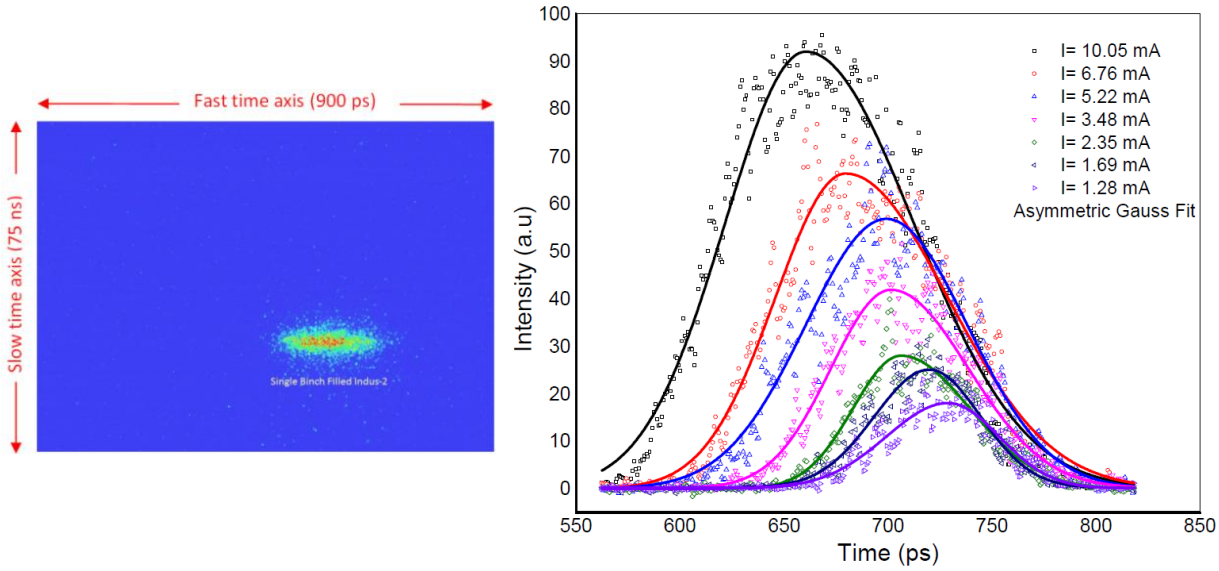

Figure 3.2: *Snapshot of streak camera with single bunch filled in Indus-2 (left). Measured bunch profiles for different beam currents and their asymmetric Gauss fit (solid lines)*

For a purely resistive impedance model, numerically solved solutions of Eq. (3.23) are compared with the measured longitudinal distribution at different beam currents. The correlation between asymmetric coefficients of the longitudinal distribution (A) and beam current (I) is given by linear fitting as $A = 0.053\, I + 0.094$. Resistive value of the vacuum structure is estimated by comparing the measured centroid shift with the calculated values of pure resistive model (shown in Figure 3.3). The estimated resistance contribution (R) using purely resistive impedance model is $1.350 \pm 0.125\ k\Omega$.

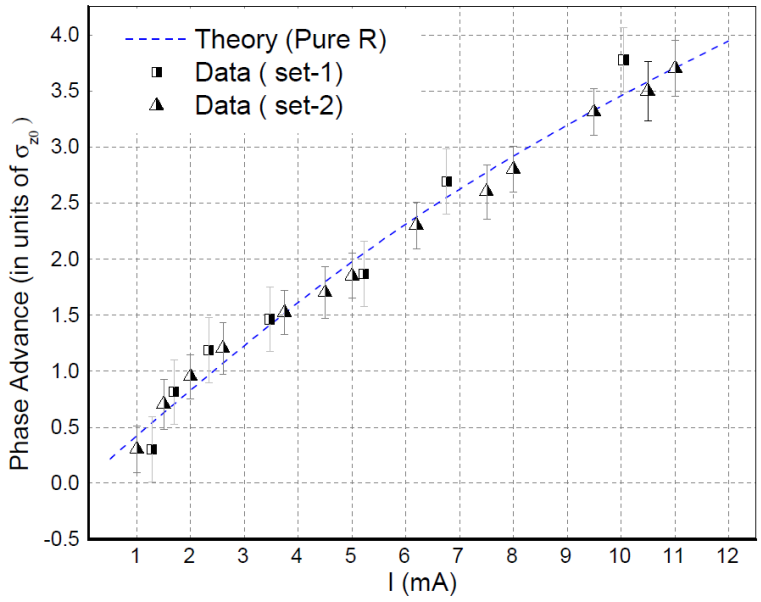

Figure 3.3: *Comparison between the measured centroid shift and those calculated from a pure resistance model (R=1350 Ω at different beam currents).*

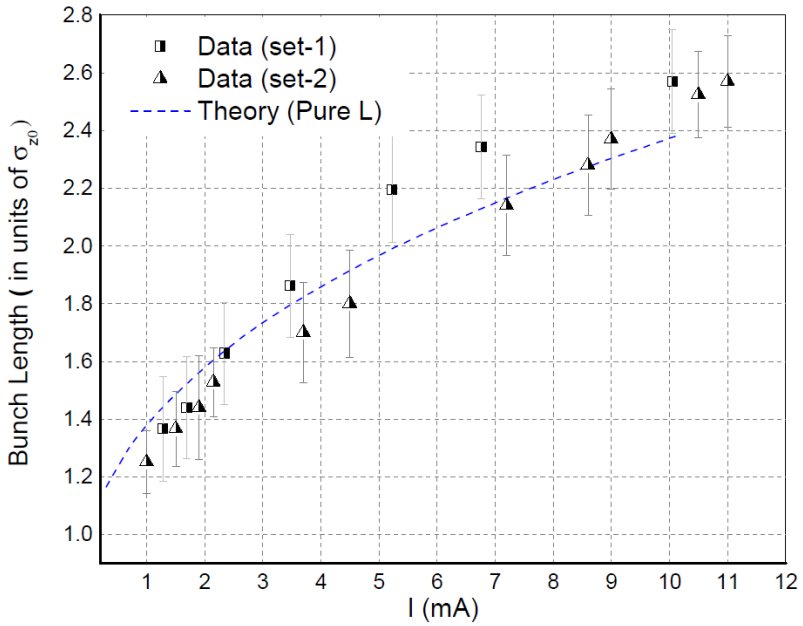

Figure 3.4: *Bunch length measured data and calculated vales for a pure inductance case (L=180 nH) at different beam currents.*

Similarly, for a purely inductive impedance model, numerically solved solutions of Eq. (3.16) are compared with the measured longitudinal distribution at different beam currents. Inductance value of the vacuum structure is estimated by comparing the measured bunch lengthening with the theoretical values of pure inductance model as shown in Figure 3.4. The estimated inductive contribution (L) using purely inductive model is $180 \pm 25\ nH$.

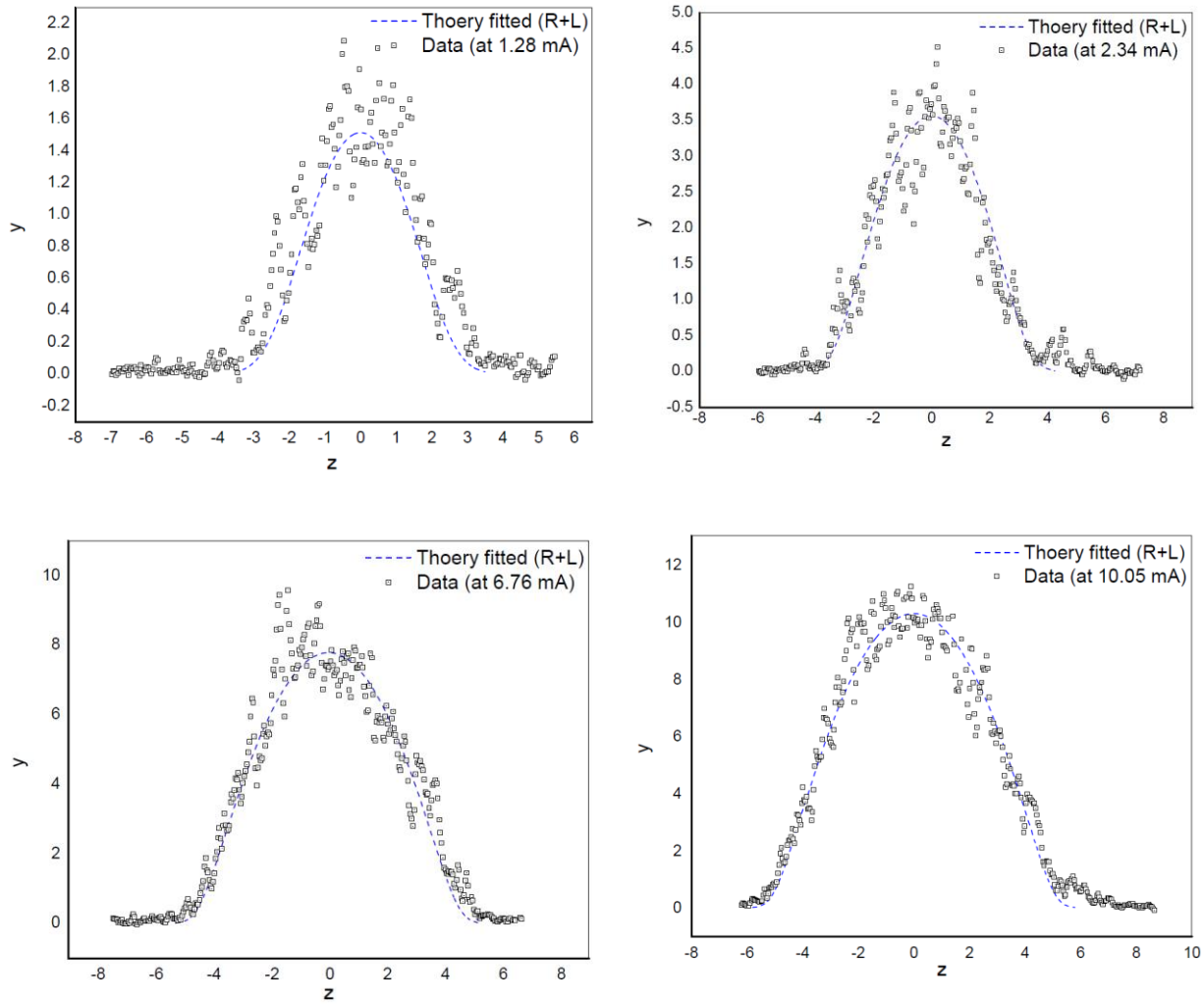

Figure 3.5: *Measured bunch profiles and their asymmetric gauss fit solutions of impedance model (solid lines) (with R= 1350 Ω and L=180 nH) at different beam currents.*

For a series R + L impedance model, Haissinski solution of series R + L impedance model are fitted with the measured bunch distribution at streak camera as shown in Figure 3.5. The resistance *R* and the inductance *L* values are obtained from the fitted ***r*** and ***l*** values at each bunch current. It is observed that the measured data of phase advancing and bunch lengthening is closely matching with estimated values of pure resistive and pure inductive models for all beam currents. But in R + L impedance model, these measured values are closely matching with estimated values only at low beam currents. At high beam currents, measured values are little higher than expected from model as shown in Figure 3.6. This difference may be due to instabilities associated with increase in energy spread and are further analyzed with analytical formulae and scaling laws in this chapter.

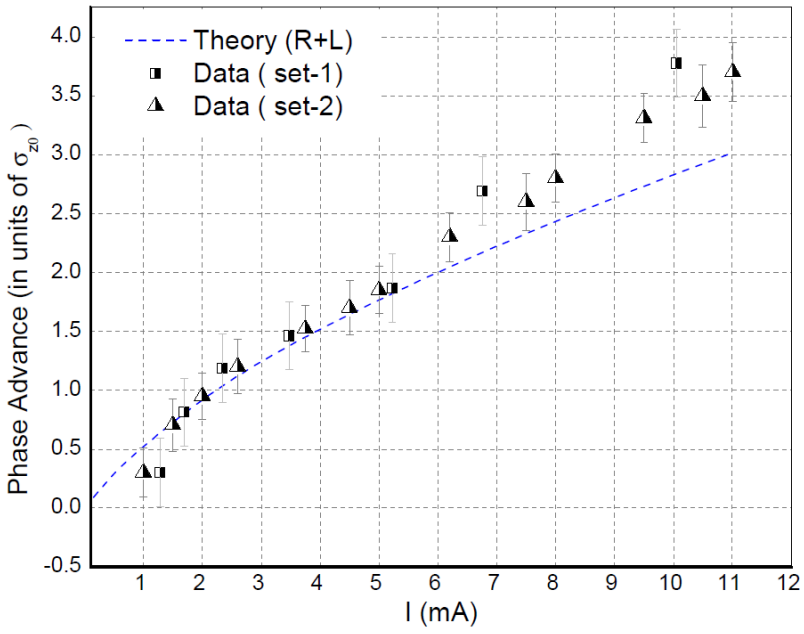

Figure 3.6: *Comparison between the measured data of phase advancing with the values calculated from a series R+L impedance model (with R= 1350 Ω, L= 180 nH).*

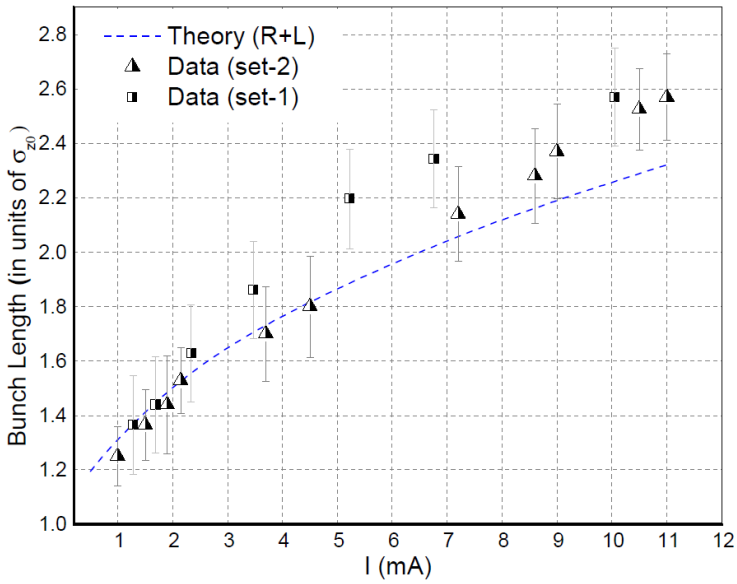

Figure 3.7: *Comparison between the measured data of bunch length with the values calculated from a series R+L impedance model (with R= 1350 Ω, L= 180 nH).*

Resistive impedance (*R*) of Indus-2 SRS is also calculated directly by applying Eq. (3.9) on the measured synchronous phase advancing on the streak camera. The loss factor (k_l) calculated from the measured phase advancing of 5.75 ps / mA is 21.7 V/pc. It gives resistive impedance of 1362 Ω. This value is again close to the value estimated from the impedance model.

3.4.2 During energy ramping

The bunch length measurement were also performed during energy ramping from 550 MeV to 2.5 GeV at ~1 mA beam current in SB mode. These measurements were carried at low beam current to keep the contributions of collective effects as low as possible. Bunch length and synchrotron frequency are measured by using streak camera and spectrum analyzer. The measured trend of bunch length, synchrotron frequency and energy spread during ramping is

shown in Figure 3.8. Measured beam energy spread is very close to theoretical values (Table 1.1) at the present optics settings of Indus-2.

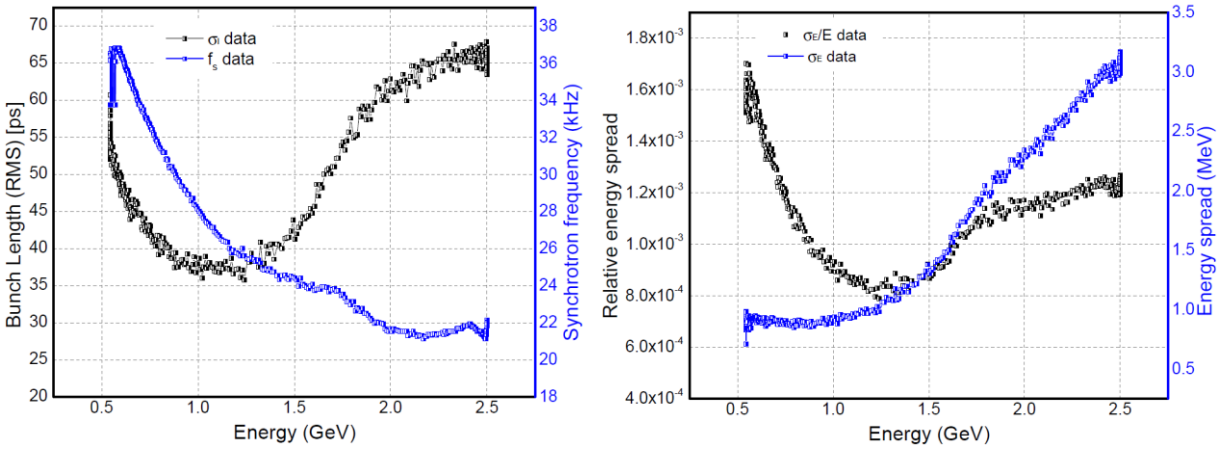

Figure 3.8: *Measured trend of bunch length and synchrotron frequency (left), and relative energy spread (right) during energy ramping from 550 MeV to 2.5 GeV in Indus-2.*

3.4.3 At 2.5 GeV beam energy

Measured longitudinal profiles of charge distribution in single bunch mode during the natural decay of beam current at 2.5 GeV is shown in Figure 3.9 . Measured data of bunch length at different beam currents is fitted with Zotter's PWD formula (Eq. (3.2)) as shown in Figure 3.10. From the fit parameters, the effective longitudinal coupling impedance is measured to be 2.21 Ω. By using $Im\left\{\left|\frac{Z_{\|}}{n}\right|\right\}_{eff.} = \omega_{rev}\, L_{eff}$ for a predominately inductive machine, the effective inductive impedance of machine is found to be ~ 201 nH. This value is close to the inductive contribution estimated using purely inductive model $180 \pm 25\ nH$.

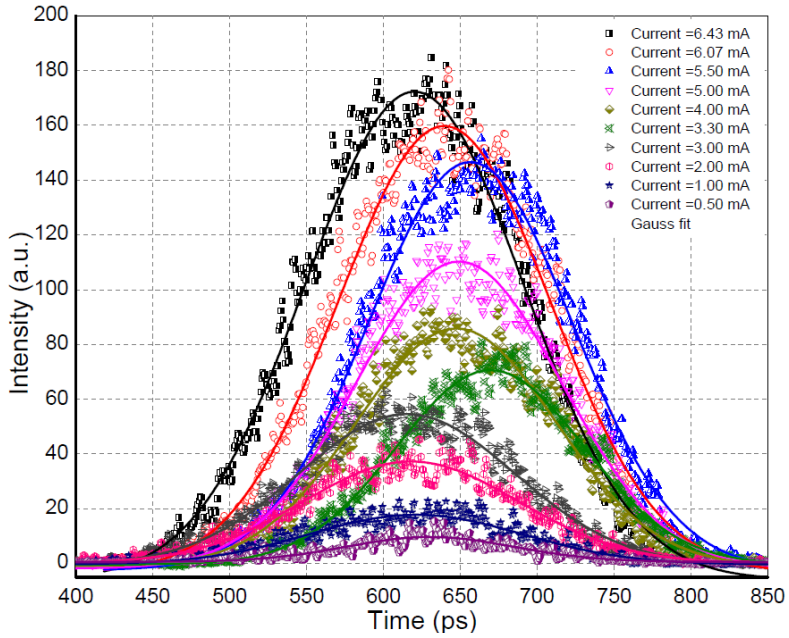

Figure 3.9: *Measured longitudinal profiles for different beam currents and their Gauss fit (solid lines) at 2.5 GeV in Indus-2.*

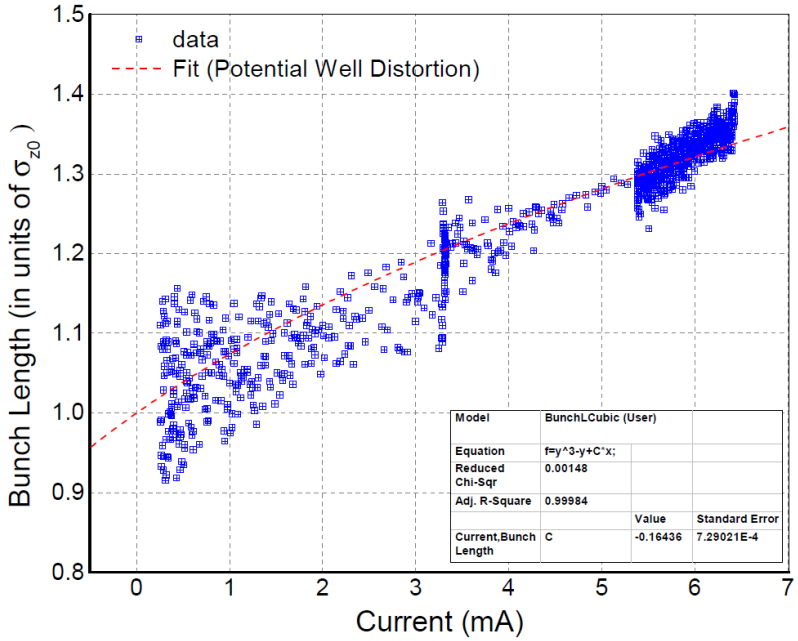

Figure 3.10: *Measured bunch length data and its fit with Zotter's potential-well distortion formula to calculate longitudinal coupling impedance.*

3.5 Scaling laws

Above the microwave threshold, bunch lengthening occurs due to the combination of both PWD and MWI, and it follows the Chao-Gareyte scaling law [145] given by

$$\sigma_z \propto \left(\frac{\alpha\, I_{beam}}{{v_S}^2 E}\right)^{1/(2+a)} \quad for\ I_{beam} > I_{Th} \tag{3.29}$$

where I_{beam} is the average beam current, v_S is the synchrotron tune, and a is the scaling factor.

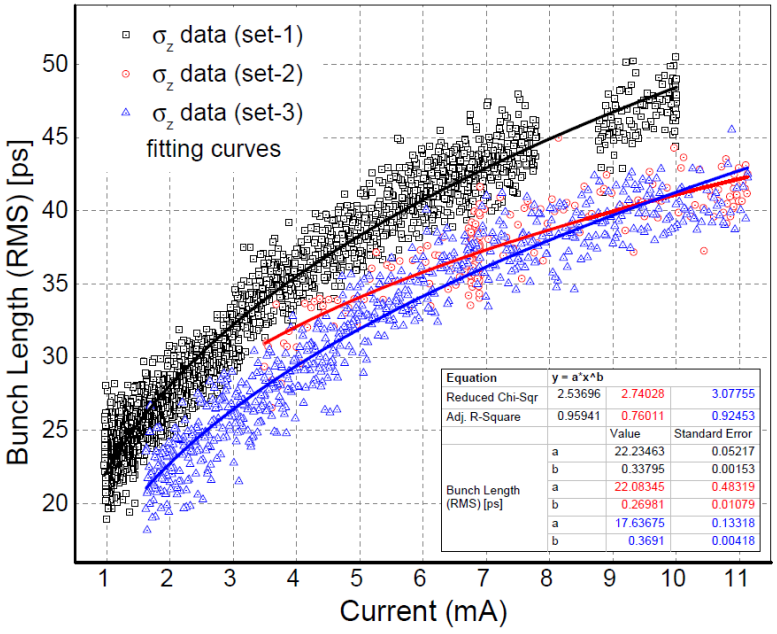

Figure 3.11: *Measured data of bunch lengthening as a function of beam current and scaling law fit at injection energy in Indus-2*

The bunch lengthening only due to microwave instability can be obtained by applying Keil-Schnell criterion [154] as follows

$$\sigma_z{}^3 = \frac{\alpha_p \, c^2 \, R \left|\frac{Z_{||}}{n}\right|_{BB}}{\sqrt{2\pi}\left(\frac{E}{e}\right) v_S{}^2 \, \omega_o{}^2} \, I_{beam} \tag{3.30}$$

In Indus-2, the microwave threshold beam current at injection energy is expected to be << 1 mA. So all these measurement are taken above the threshold value taken at injection energy (550 MeV). We got scaling equation $\sigma_z(mm) = 6.67\, I\,(mA)^{1/3.66}$ by using Chao-Gareyte scaling law as shown in Figure 3.11. The solid lines show the best fit of measured data set (taken at different time) for Chao-Gareyte scaling parameter *a* in the range of 0.7 to 0.96.

The combined vacuum chamber impedance estimated by fitting the measured data with Eq. (3.7) is ~ 0.5 Ω (shown in Figure 3.12). After subtracting the contribution from the effective longitudinal coupling impedance derived from Zotter's formula, it gives a value for the longitudinal broadband impedance of 2.69 Ω.

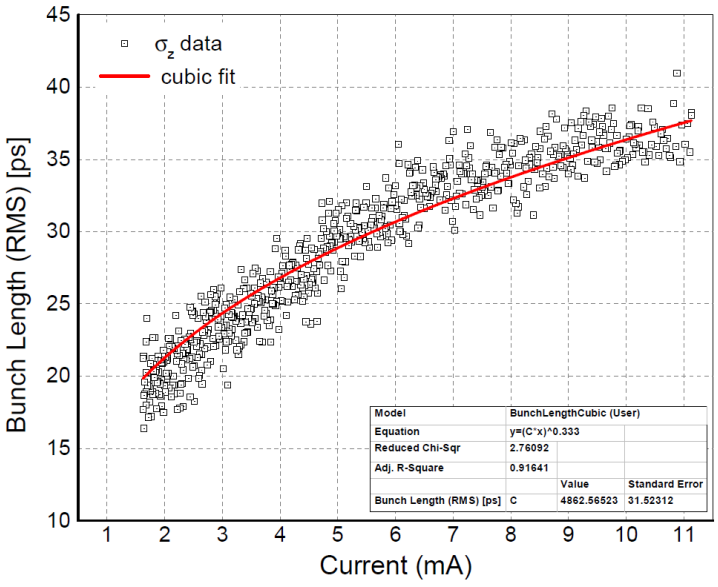

Figure 3.12: *Bunch length data fitted with one-third dependence of beam current to get combined impedance.*

3.6 Measurements at Indus-1 SRS by using fast photodiode

Before doing the studies of longitudinal dynamics at Indus-2 SRS with streak camera system, we have learnt basics of longitudinal measurement system by using fast photo receiver at Indus-1 SRS [33] [155]. Temporal profile of SR emitted from Indus-1 dipole magnet was measured by using fast photodiode and oscilloscope. The bunch length is calculated by gauss fitting of the measured longitudinal profiles. These measurements were carried out at different gap voltage of RF cavity and beam currents. The longitudinal broadband impedance for Indus-1 SRS was estimated using Keil-Schnell criterion and results were compared with theoretical estimated values using ZAP code [156].

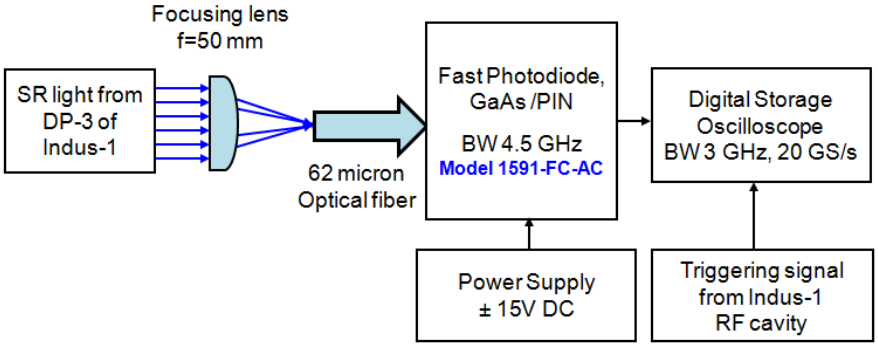

Figure 3.13: *Schematic of the bunch length measurement set up used in Indus-1.*

New Focus made GaAs fast photodiode (model 1591-FC-AC) [109] is used for these measurements. Its 3-dB bandwidth is 4.5 GHz and typical responsivity is 0.4 A/W. Visible light from Indus-1 is just few micro watts or even it goes to few nano watts when worked in 500±10 nm. Input light is focused at small active area of photodiode by using 62.5 µm optical fibre, plano-convex lens and translation stages. The incident light is converted into electrical

signal according to responsivity of detector. The cable contributions are kept low by using small length (24") 40 GHz flex cable for carrying electrical signal from photodiode to oscilloscope for measurements. Schematic of the bunch length measurement set up used in Indus-1 is shown in Figure 3.13.

The measured bunch length has additional contributions due to the instrumental rise time and averaging effect as shown by Eq. (3.31).

$$\sigma_M = \sqrt{(\sigma_A)^2 + (\sigma_{Diode})^2 + (\sigma_{Cable})^2 + \left(\sigma_{Oscilloscope}\right)^2 + \left(\sigma_{fit.}\right)^2} \tag{3.31}$$

Total instrumental rise time (~175ps) is due to the contributions from photodiode, cable and oscilloscope. So, the actual bunch length can be obtained by removing this contribution from the measured values.

3.6.1 Bunch length at different gap voltages of RF cavity

The measurements were performed to find the dependence of the bunch length on gap voltage of RF cavity in Indus-1. Beam current was kept low (~10 mA) to keep the contributions from collective effects as low as possible. To check the system repeatability, these measurements were performed by increasing and decreasing of gap voltage from its nominal operating gap voltage (21 kV). The data of measured bunch length and theoretical calculated values with potential well distortion (PWD) as a function of RF accelerating voltage are plotted in Figure 3.14.

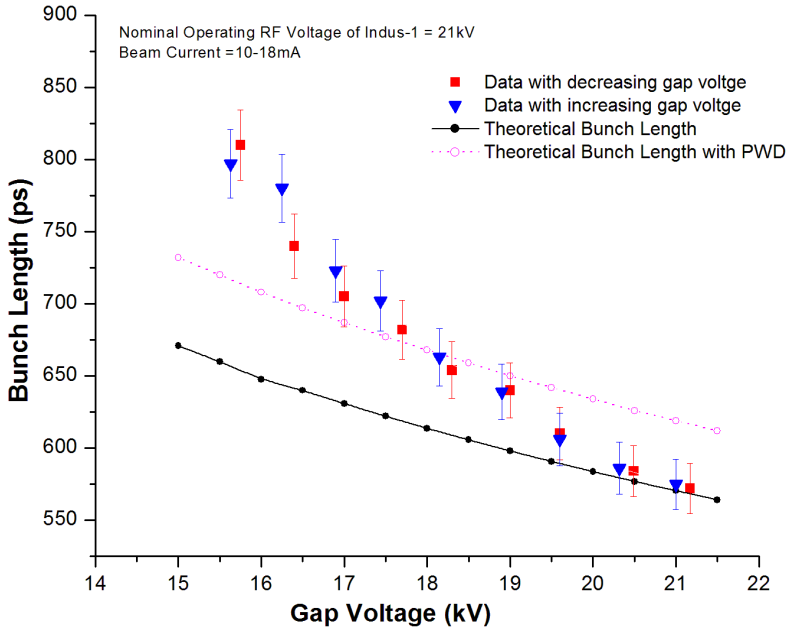

Figure 3.14: *The measured bunch length data is showing good repeatability with decreasing (squares) and increasing (triangles) gap voltage. Theoretical calculated values (solid line) and values calculated with ZAP code for PWD (dotted line) are also shown. Measured values are close to theory near nominal operating voltage of Indus-1 (21 kV).*

Theoretically, the natural bunch length (σ_{zo}) is a function of synchrotron oscillation frequency (f_{S0}), momentum compaction factor (α_p) and beam energy spread ($\sigma_{\varepsilon o}$) as given in Eq. (3.1). Synchrotron oscillation frequency further depends upon the SR loss per turn (U_{SR}), beam energy (E), synchrotron phase $\emptyset_S$ (i.e. $\sin\emptyset_S = \frac{U_{SR}}{eV_{RF}}$), harmonic number ($h$) and gap voltage ($V_{RF}$) across RF cavity as follows

$$f_S = f_0 \sqrt{\frac{\alpha_p\ h\ \cos(\emptyset_S)}{2\pi}\ \frac{eV_{RF}}{E}} \tag{3.32}$$

So by including these contributions in Eq. (3.1), natural bunch length comes out to be inversely proportional to square root of RF cavity gap voltage as shown below

$$\sigma_{zo} = \sigma_{\varepsilon o} \sqrt{\frac{2\pi\, \alpha_p\, h\, c^2}{{\omega_{RF}}^2\, cos(\emptyset_S)}\, \frac{E}{eV_{RF}}} \tag{3.33}$$

The results show that bunch length decrease with the increase of gap voltage of RF cavity. Measured data also shows this theoretical expected trend with good repeatability. At high voltage, measured values are exactly following theory, so these results are useful in study of the bunch lengths with beam current at nominal operating voltage of Indus-1. At low operating voltages the trend is same as expected theoretically and as calculated with ZAP code, but the small systematic difference may be due to low SR signal because of low beam current, bunch distortions, bunch instabilities or change in shape of the bunch that can be studied by using streak camera system.

3.6.2 Bunch length at different beam currents

The bunch length of Indus-1 electron beam was measured for beam current 8 mA to 65 mA in single bunch for few hours. These measurements were taken during different session from the first experiment and at fixed value of nominal operating gap voltage of RF cavity (21 kV). The results are shown in Figure 3.15. Calculated bunch length values with microwave instability (solid line and triangles) and potential well distortion (pentagon) are also compared at different beam current using ZAP code. Results from fitted scaling equation are also shown as dotted line.

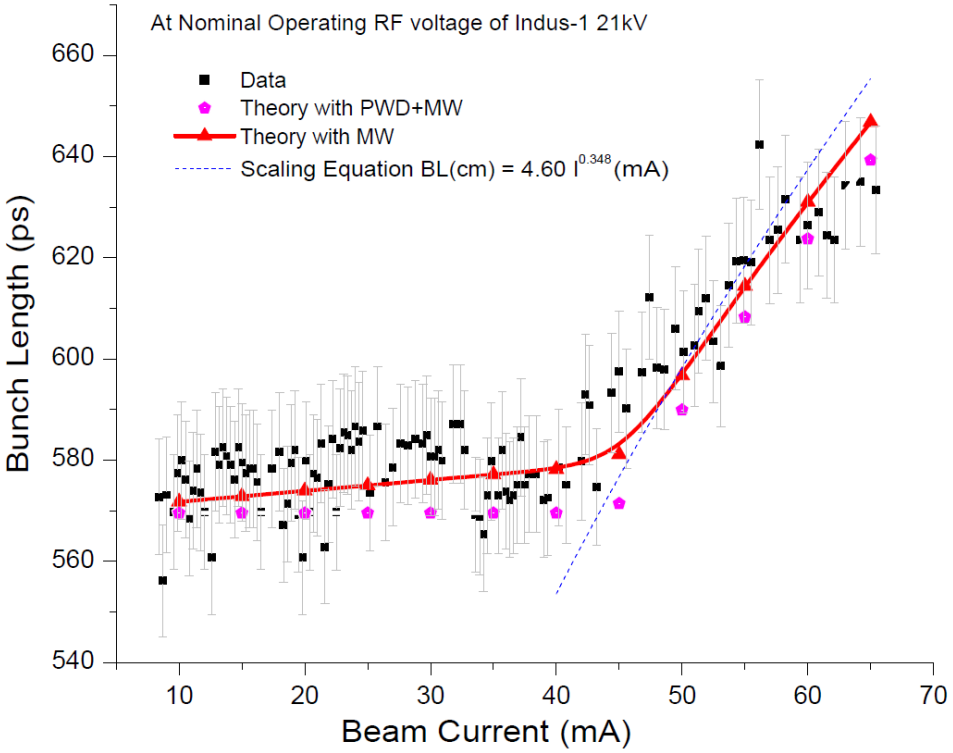

Figure 3.15: *Calculated and measured bunch length values with the increase of beam current at nominal operating gap voltage of RF cavity (21 kV). Results from scaling equation fit are also shown as dotted line.*

These results show that bunch length increases with the increase of beam current. From the theory of collective effects (Section 3.2), if the beam current is less than threshold, the bunch lengthening or shortening is generated only by the potential well distortions. However, when the beam current is more than the threshold beam current, the bunch lengthening is generated by combined actions of the MWI (increases energy spread) and PWD (generates incoherent frequency shift) given by Eq.(3.7). The onset of MWI can give an estimate of the machine impedance. The threshold peak current for the microwave instability is given by Eq. (3.3).

Table 3.2 : *Calculated bunch parameters at different gap voltages using ZAP code*

RMS bunch length (cm)	RF Voltage (kV)	Synchronous phase angle (degree)	Synchrotron tune value	Energy loss DE (RW+BB) ([MeV/q] /turn)	Momentum half height of RF bucket (ΔP/P)	Effective longitudinal impedance (ohm)	Threshold beam current (mA)	Number of particles	Total ring current (mA)
20.142	14.0	164.3	0.00165	$1.54X10^{-4}$	0.00461	49	55.1	$2.18 X10^{-10}$	55.1
19.767	14.5	164.8	0.001681	$1.60 X10^{-4}$	0.00473	49	54.1	$2.14 X10^{-10}$	54.1
19.412	15.0	165.3	0.001712	$1.6 X10^{-4}$	0.00486	49	53.1	$2.10 X10^{-10}$	53.1
19.077	15.5	165.8	0.001742	$1.72 X10^{-4}$	0.00498	49	52.2	$2.06 X10^{-10}$	52.2
18.759	16.0	166.2	0.001772	$1.79 X10^{-4}$	0.00509	49	51.4	$2.03 X10^{-10}$	51.4
18.457	16.5	166.6	0.001801	$1.85 X10^{-4}$	0.00521	49	50.5	$2.00 X10^{-10}$	50.5
18.169	17.0	167.0	0.001829	$1.91 X10^{-4}$	0.00532	49	49.7	$1.96 X10^{-10}$	49.7
17.895	17.5	167.4	0.001857	$1.97 X10^{-4}$	0.00543	49	49.0	$1.93 X10^{-10}$	49.0
17.633	18.0	167.7	0.001885	$2.04 X10^{-4}$	0.00554	49	48.3	$1.91 X10^{-11}$	48.3
17.383	18.5	168.0	0.001912	$2.10 X10^{-4}$	0.00565	49	47.6	$1.88 X10^{-10}$	47.6
17.143	19.0	168.3	0.001939	$2.16 X10^{-4}$	0.00575	49	46.9	$1.85 X10^{-10}$	46.9
16.914	19.5	168.6	0.001965	$2.22 X10^{-4}$	0.00585	49	46.3	$1.83 X10^{-10}$	46.3
16.693	20.0	168.9	0.001991	$2.29 X10^{-4}$	0.00595	49	45.7	$1.80 X10^{-10}$	45.7
16.481	20.5	169.1	0.002017	$2.35 X10^{-4}$	0.00605	49	45.1	$1.78 X10^{-10}$	45.1
16.277	21.0	169.4	0.002042	$2.41 X10^{-4}$	0.00615	49	44.6	$1.76 X10^{-10}$	44.6

At the time of experiments, Indus-1 SRS optics was operating at tune points (v_x,v_y) (1.6008, 1.4674) , with momentum compaction factor (α) 0.285628 and emittance 190 nm.rad. SR loss per turn (U_{SR}) of an electron for Indus-1 is 3.63 *keV* Based on these machine parameters theoretical values for the bunch length are also calculated using Eq. (3.33), and estimation for bunch length at different beam current under MWI and PWD instability was made using ZAP code [156] as shown in Table 3.3. The comparison for measured and calculated values is shown in Figure 3.15. Above threshold current (~41 mA), we obtained fitting equation, which is following the above scaling law at scaling factor a=0.8736 corresponding to Eq. (3.29) as shown by solid line. By using the scaling Eq.(3.30), total longitudinal broad band impedance of Indus-1 comes out to be is 49.04 Ω ± 6%. This value seems to be higher, but this may be due to presence of clearing electrodes, non-uniformities at certain points inside

vacuum chambers structure in this 2nd generation SRS. Ion clearing electrodes are installed to enhance beam life time [54], and presently covers ~ 20% circumference of Indus-1.

3.7 Summary and conclusions

The effect of longitudinal wakefields was investigated by measuring changes in the longitudinal distribution of the beam. Measured longitudinal profiles on the streak camera were fitted with asymmetric Gaussian function to measure the phase advancing and bunch lengthening. In the PWD regime, the impedances were estimated using three kinds of impedance models. The bunch lengthening for a series $R + L$ impedance model showed a good agreement with the results of the bunch lengthening measurements except at higher beam currents. The impedances of storage ring obtained by a series R+L impedance model indicate a resistance (R) of 1350 ± 125 Ω, an inductance (L) of 180 ± 25 nH and broadband impedance ($\left|Z_{||}/n\right|_{BB.}$) of 2.69 Ω. These measurement results are closely matching with the values estimated from synchronous phase advancing, Zotter's formula and scaling law fit. By using Chao-Gareyte scaling law, scaling equation for measured data of bunch length and beam current above the threshold beam current was found to be. $\sigma_z(mm) = 6.67\ I\ (mA)^{1/3.66}$ These studies will be helpful in understanding beam behaviour or various beam instabilities during working with narrow gap insertion devices in future.

In Indus-1, the bunch length measurements were performed by using fast photodiode system. In the first experiment, the results showed that at low beam current, bunch length

increased from 565 ps to 810 ps with the decrease of gap voltage of RF cavity from 21.2 kV to 15.5 kV. These results have shown good repeatability. At high voltage, i.e. near nominal operating voltage of Indus-1 RF cavity, measured values are exactly following theory. And at low RF voltages the trend is same as expected theoretically, but the small systematic difference may be due to low light signal (at low beam current), bunch distortions, bunch instabilities or change in shape of the bunch that can to be studied by using streak camera. In the second experiment, bunch length dependence on beam current was observed. The experimental results showed that bunch length increase with the increase in bunch current, and above a threshold value, it follows Chao-Gareyte scaling law. The longitudinal broadband impedance of Indus-1 storage ring was estimated ~ 49.0 Ω by using Keil-Schnell criterions. This value seems to be higher, but this may be due to presence of clearing electrodes and non-uniformities present at certain points inside vacuum chambers structure. Measurement system with higher temporal resolution was required for further studies to measure the exact contributions from inductance, resistance and capacitance in total impedance budget.

Chapter 4 Measurement of transverse beam parameters

4.1 Introduction

The motion of charge particles in an accelerator is guided by its magnetic lattice and radio frequency (RF) cavities. The electrons confined within bunch execute betatron oscillations about the closed orbit in the transverse planes, and synchrotron oscillations with respect to synchronous phase in the longitudinal plane. The electrons within a bunch are continuously scattered due to elastic and inelastic scattering within same bunch (Touschek scattering) and with the residual atoms present in vacuum chamber [67]. Transverse properties of the beam are affected by these scatterings and various errors present in the machine. Therefore precise measurement of transverse beam parameters is very important for smooth operations and performance enhancement of the SRS. In this chapter, experimental measurements of the source position, angle, dispersion, size, divergence, emittance and natural beam size are discussed. Measurement results of beam sizes during trial experiments for low emittance operation of Indus-2 are also discussed. These measurements have helped us in smooth and stable operation of Indus-2 during various stages of commissioning (storing beam current) [4], life time studies [157], insertion devices testing, low emittance optics testing [5], testing

and optimisation of various feedback systems. Important measurement results are briefly discussed in the following sub sections.

4.2 Source position and emission angle

The variation of source position and emission angle causes SR flux loss or alignment problems at the experimental end of user beamlines. It becomes very critical for long beamlines operating at higher SR energies. Actually, changes in source position and angle shows coupled effects at the measurement detector. Pinhole array is mostly used for the measurement of beam size and emittance, and its use for the measurement of source position and emission angle is less reported. Equations given in [130] are modified to find the exact correlation of source position and angle with intensity and position of various pinhole spots. Measured results for a known shift are closely matching with the theoretical calculated values based on these equations.

Actual behaviour of the source has both position shift and emission angle change. Let us first take the effect of only source position shift. For this case, at the image plane whole pattern moves up/down in a direction opposite to the direction of movement of source point (y_{Source}), but the maxima of the fitted gaussian remains at same position. For second case, if there is change in emission angle only i.e. at fixed source position, there is shift in position of central maxima envelope only, and individual peaks stay fixed. Therefore the vertical position of image from i_{th} pinhole at phosphor screen ($y^{ith}_{Pin._Image}$) can be derived as

$$y^{ith}_{Pin._Image} = \left[\frac{R2+R1}{R1}\right]\left(y^{Centre}_{Pin._Array} + i^{th}\,\Delta\right) - \left[\frac{R2}{R1}\right]y_{Source}\ ; \qquad (4.1)$$

$$\Delta y_{Pin.\_Image}^{ith} = \left[\frac{R2+R1}{R1}\right]\Delta y_{Pin.\_Array}^{Centre} - \left[\frac{R2}{R1}\right]\Delta y_{Source} \; ; \qquad (4.2)$$

$$\forall \; -\left(\frac{n-1}{2}\right) < i^{th} < \left(\frac{n-1}{2}\right)$$

where $R1$ and $R2$ are the distances of pinhole array from the source point and phosphor screen respectively; y_{Source} and $y_{Pin.\_Array}^{Centre}$ are the vertical position of source point and pinhole array centre above the ground level respectively. Δy_{Source} and $\Delta y_{Pin.\_Array}^{Centre}$ are their respective shifts w.r.t. their specified mean positions ; Δ and n are the pitch and number of pinholes in a single column of the pinhole array. Schematic of the vertical position of pinhole image at the phosphor screen from ith pinhole is shown below in Figure 4.1.

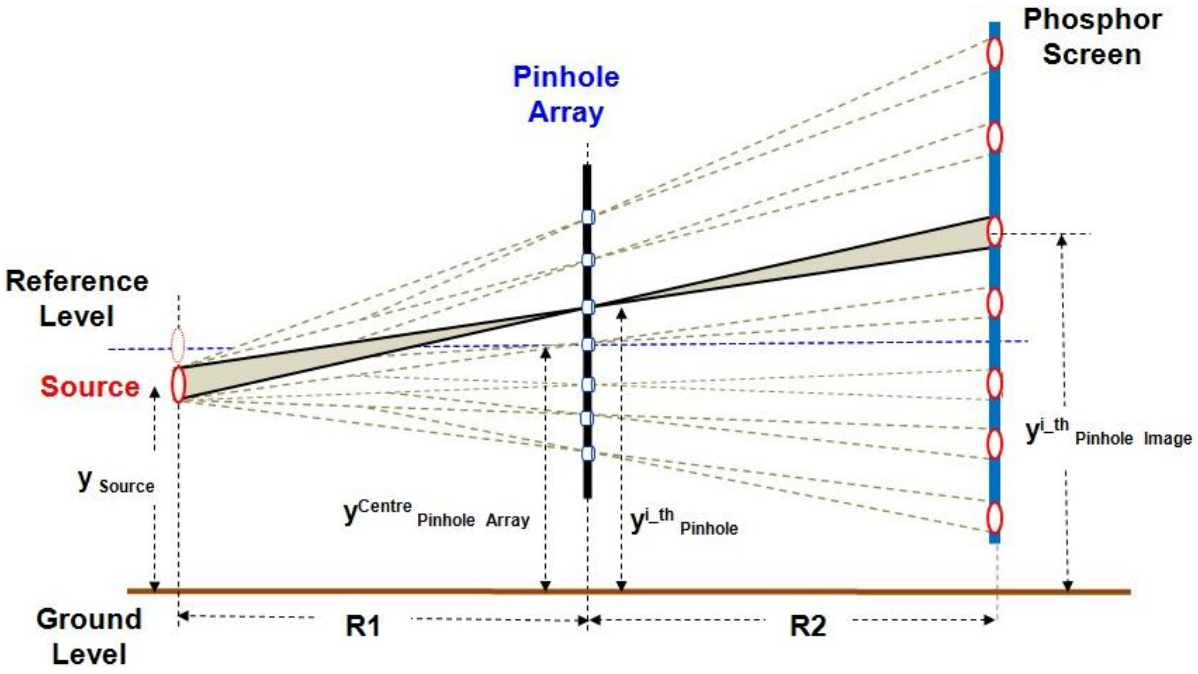

Figure 4.1: *Schematic of the vertical position of pinhole image from ith pinhole at the phosphor screen.*

Now source position can be obtained with higher precision by averaging over the many pinholes for y_{Source} as follows

$$y_{Source} = \frac{1}{n}\sum_{i}\left(\frac{R1}{R2}\right)\left\{\left[y_{Pin.\_Array}^{Centre} + \left(\frac{R2+R1}{R1}\right) i^{th}\,\Delta\right] - y_{Pin.\_Image}^{ith}\right\} \tag{4.3}$$

The maxima position of Gaussian fitting all peaks is very sensitive to angular changes and can be written as follows

$$\Delta y_{Image}^{Peak\_Gaussian} = \begin{cases} \Delta\phi_{V\_Angle}\ (R1+R2) & \text{if } \Delta y_{Source} \ll \dfrac{\Delta}{2} \\ \Delta\phi_{V\_Angle}\ (R1+R2) \pm \Delta y_{Source} & \text{if } \Delta y_{Source} > \dfrac{\Delta}{2} \end{cases} \tag{4.4}$$

By using above equations, both source position and its emission angle can be measured precisely.

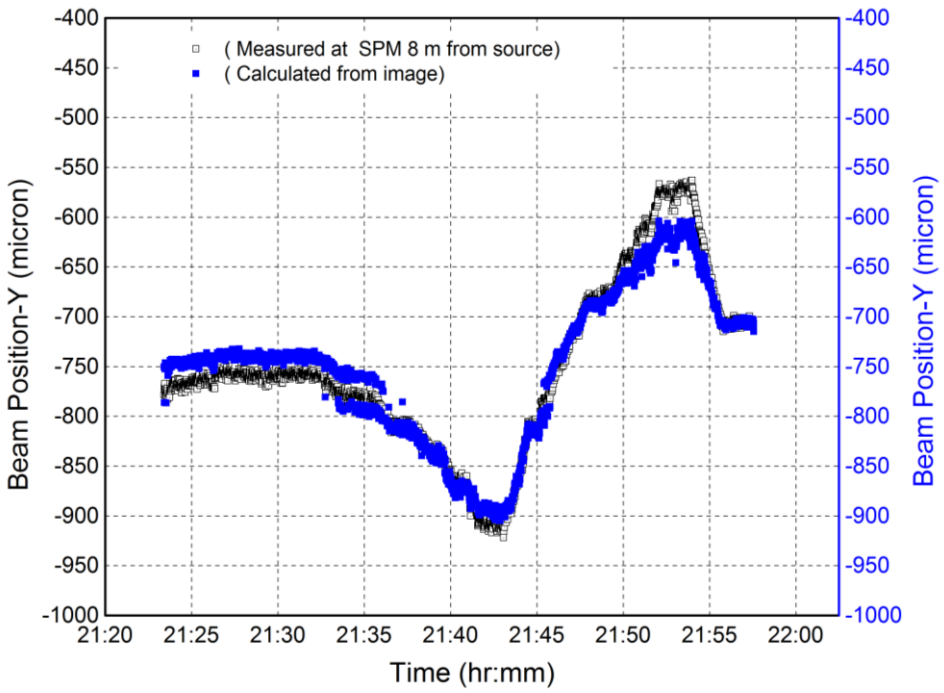

Figure 4.2: *Measured data of the vertical beam position at SPM and from the pinhole images during ±175 µm shift of pinhole array assembly from its mean position.*

To experimentally check the validity of above equations, it can be done by either moving the beam or pinhole system by a known value. In-XDL, SPM and pinhole array are designed in a single assembly unit, which can be moved up and down by using remote actuation mechanism. Pinhole array images are processed to measure the centroid of various pinhole spots captured on the phosphor screen for a known shift of the pinhole array assembly as shown in Figure 4.2.

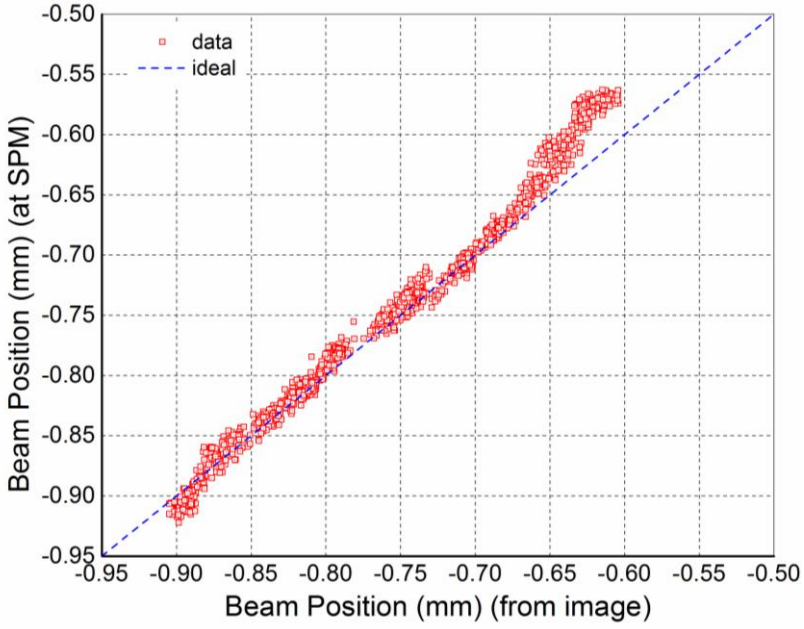

Figure 4.3: *Comparison of the measured vertical position at SPM and from pinhole images using modified equations.*

For a total shift of ± 125 µm from its mean position, measured results are closely matching (± 12 µm) with the theoretical calculated values from pinhole images (Figure 4.3). It was observed that SPM measurements start showing non-linear behaviour beyond a certain range.

Results of the various measured values from pinhole array system at X-DBL are also listed in Table 4.1.

Table 4.1: *Comparison of design and measured values from pinholes image at X-DBL*

Parameter	Design (μm)	Measured (μm)
Pinholes peaks separation on screen.	2200	2200 ± 12
Position shift of i^{th} peak with +100 μm source shift.	-120	-120 ± 2
Position shift of i^{th} peak with +100 μm pinhole shift.	+220	+220 ± 2
Peaks separation with shift of source or pinhole array	2200	2200± 12
Vertical position shift in Gaussian fitted central maxima with +1 μrad change in opening angle.	+17.6	+17.6 ± 8

In X-DBL, photon beam position is monitored online (at 1 Hz) at SPM system. Typical measured data of photon beam position at 8 m from the source during natural decay of beam current is shown in Figure 4.4. Photon beam position has remained within ± 10 μm during the natural decay of beam current from 118 mA to 64 mA in Indus-2.

Typical results of online measured photon beam position for seven days during the natural decays of beam currents with FOFB OFF are shown in Figure 4.5. Its day-to-day position shift has remained within ± 25 μm. Online measured data of photon position is very useful in calibration of various feed-back systems and to study the various possible causes for long term beam drifts.

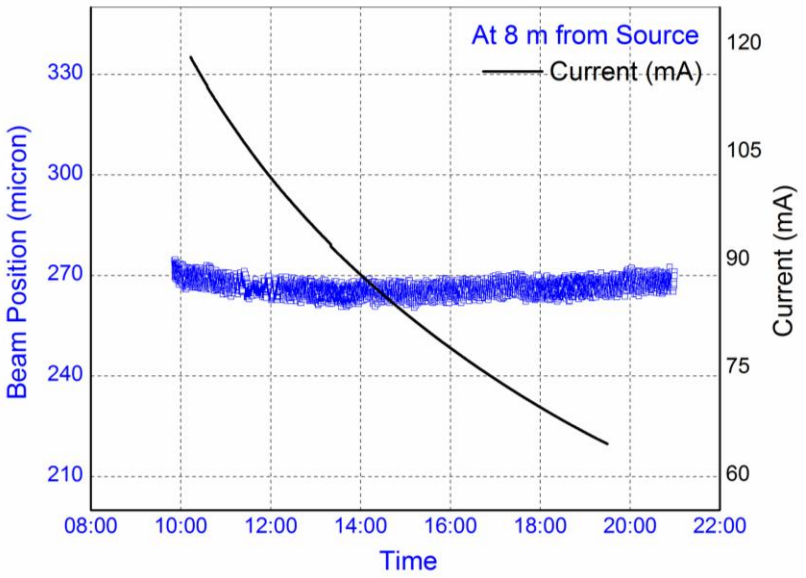

Figure 4.4: *Measured photon beam position at 8 m from the source during the natural decay of beam current from 118 mA to 64 mA in Indus-2.*

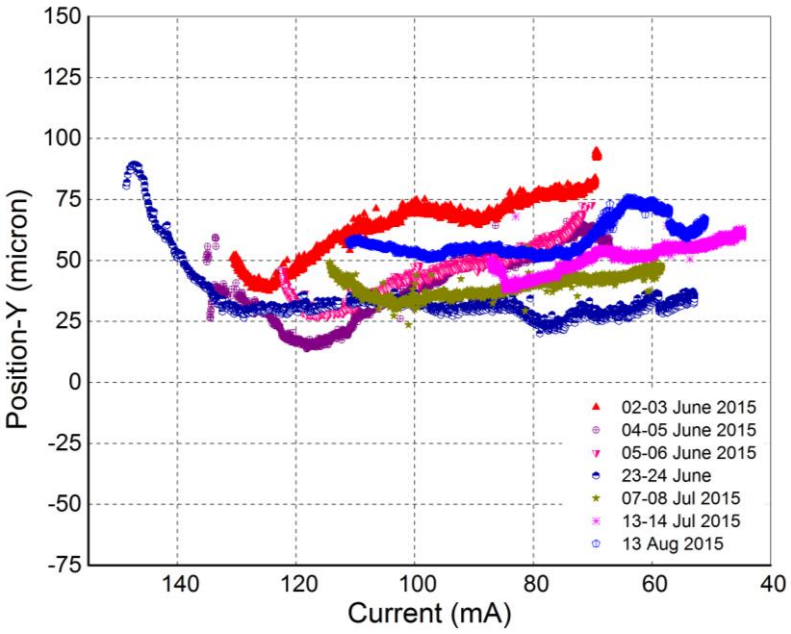

Figure 4.5: *Online measured photon beam positions at 8 m from source for seven days during the natural decay of beam current in Indus-2 (with FOFB OFF).*

4.3 Beam dispersion

One significant advantage of the x-ray pinhole imaging over the visible imaging is the stability of its image, since the latter is susceptible to mirror vibrations in a long transport line. This feature is used to measure dispersion function at the source point. A set of beam profiles are taken with slightly different RF frequencies (i.e. different beam energies), and dispersion at the source point is deduced from the displacement of beam centroid as follows

$$\eta_{i=(x,y)}(s) = -\alpha_C \frac{\Delta_{i=(x,y)}(s)}{\Delta f_{RF}/f_{RF}} \tag{4.5}$$

Where $\alpha_C = 7.3 \times 10^{-3}$ is the momentum compaction factor, $\Delta_{i=(x,y)}$ is the measured change in beam centroid at X-DBL, and $\Delta f_{RF}/f_{RF}$ is the relative change in the RF frequency.

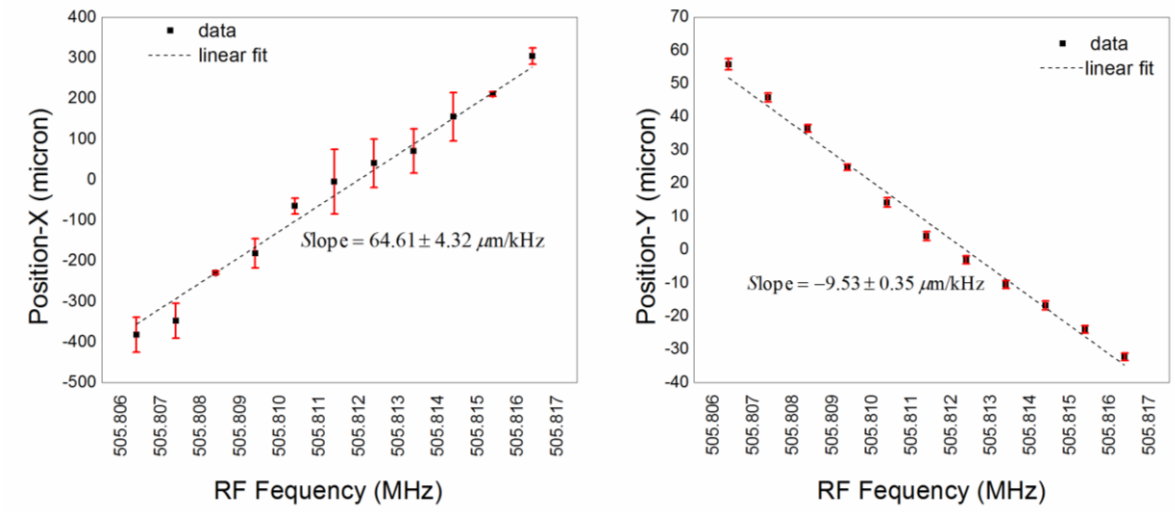

Figure 4.6: *Measured data of the horizontal and vertical beam shifts along with their linear fit during RF frequency change of ± 5 kHz with respect to its normal operating frequency of 505.8114 MHz.*

The horizontal and vertical beam shift of ± 343 µm and ± 44 µm was measured at X-DBL during the RF frequency change of ± 5 kHz with respect to normal operating frequency of 505.8114 MHz (Figure 4.6). By using Eq. (4.5), measured horizontal and vertical dispersions at the X-DBL source point are 0.253 m and 0.0325 m respectively. Ideally vertical dispersion at source point is assumed to be zero, and this measured small dispersion is the spurious dispersion. Precise value of vertical dispersion is very important to find exact beam size at the source point. Measured horizontal dispersion is also closely matching with the theoretical expected values at X-DBL source point (in Chapter 2).

4.4 Beam size, beam divergence and beam emittance

The pinhole beam spots imaged on the phosphor screen are captured and image processed to get beam size (σ_x , σ_y) and beam centroid in both horizontal and vertical planes as shown in Figure 4.7.

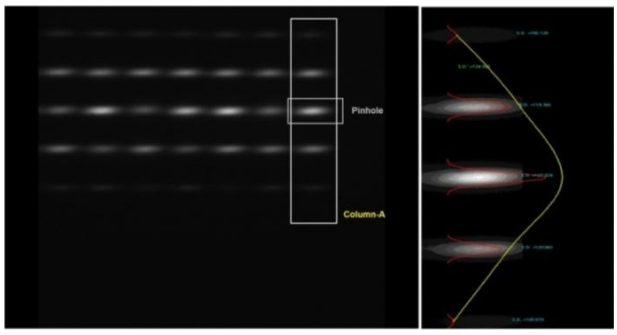

Figure 4.7: *Photograph of the pinhole array image captured on P-43 phosphor screen and measured intensity profile across column-A in the pinhole array image to find beam divergence.*

Actual beam size is calculated by de-convolving of the total spread function (discussed in Chapter 2) from the measured values. Measured horizontal and vertical beam sizes during the natural decay of beam current in Indus-2 are shown in Figure 4.8 . Online measured trend of the horizontal and vertical beam sizes for seven days during the natural decay of beam current in Indus-2 are shown in Figure 4.9 and Figure 4.10 respectively.

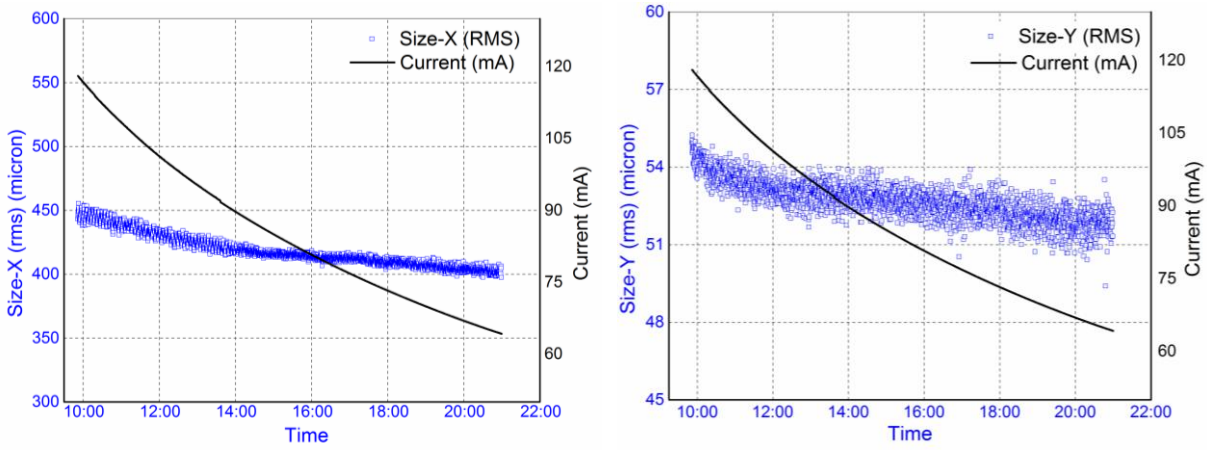

Figure 4.8: *Measured beam size horizontal (left) and vertical (right) during the natural decay of beam current from 118 mA to 64 mA in Indus-2.*

In pinhole array imaging, the beam divergence is measured from the intensity distribution of the pinhole spots in a column of the pinhole array. In order to get exact information of beam divergence, required tunnelling effect of the various pinholes in a column is removed during image processing. Typical measured results for the beam divergence with the beam current for eleven hours are shown in Figure 4.11.

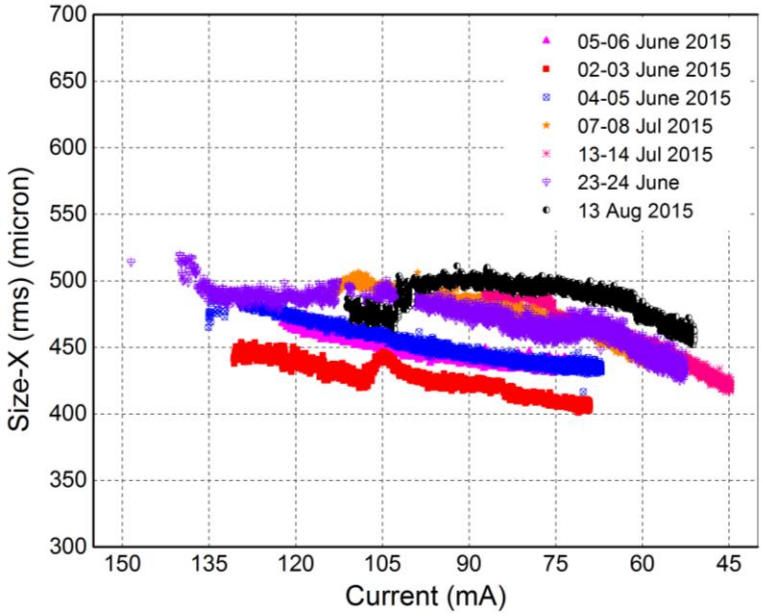

Figure 4.9: *Online measured horizontal beam size data at 1 Hz for seven days during the natural decay of beam current in Indus-2.*

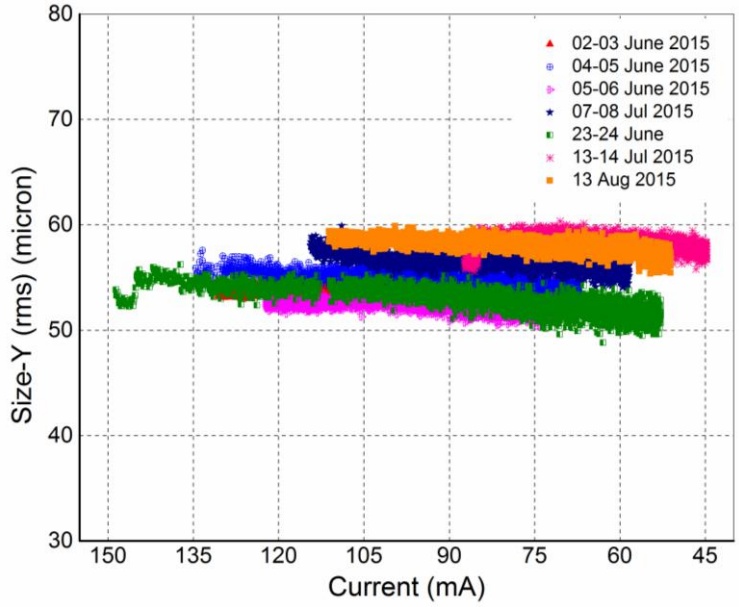

Figure 4.10: *Online measured vertical beam size data at 1 Hz for seven days during the natural decay of beam current in Indus-2.*

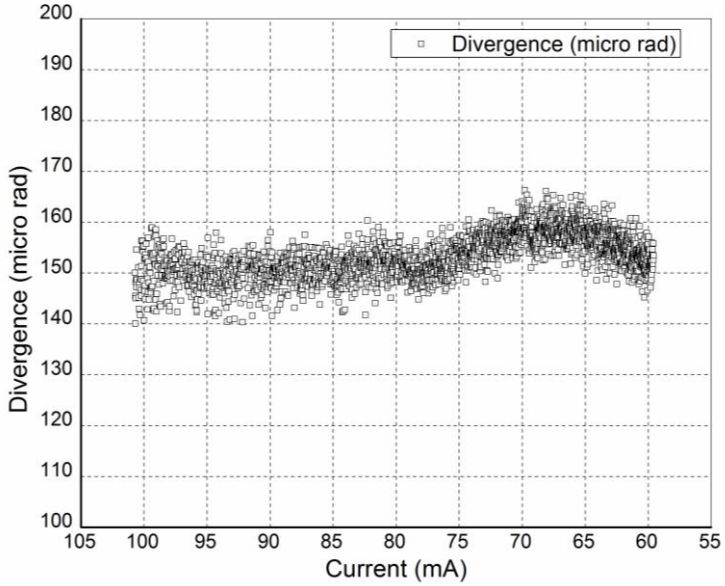

Figure 4.11: *Typical online measured results for beam divergence during the natural decay of beam current for eleven hours.*

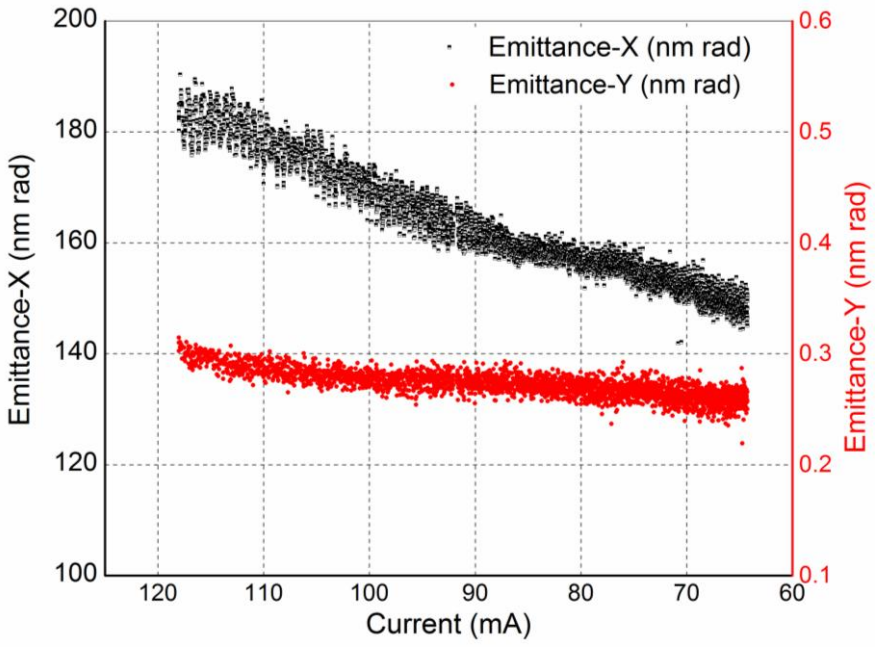

Figure 4.12: *Online measured horizontal and vertical emittance (at 1Hz) during the natural decay of beam current from 118 mA to 64 mA in Indus-2.*

The beam emittance is determined from the measured beam size, beam divergence and known Twiss parameters at the source point. Twiss parameters at the source point are known from the calibrated model fitting with Accelerator Toolbox AT or LOCO. The complete detail for emittance measurement algorithm is given in Appendix A.

4.5 Finding of the natural beam size

In order to get the information of natural beam sizes (at zero current) in Indus-2, beam size was measured as a function of beam current at 2.5 GeV. The variation of horizontal and vertical beam sizes with beam current is shown in Figure 4.13. The natural beam size is obtained from the measured beam size trend. For Indus-2 at 2.5 GeV, natural horizontal for and vertical beam size obtained at BL-24 source point are 357.2 µm and 47.6 µm respectively.

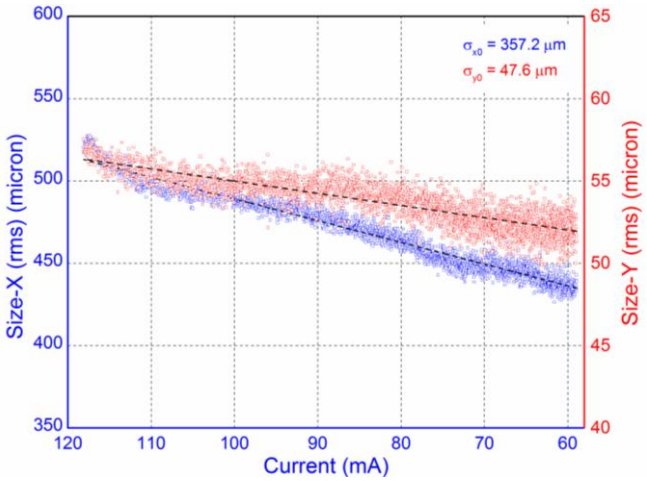

Figure 4.13: *The natural beam sizes obtained from linear relation of beam sizes and beam current are 357.2 µm and 47.6 µm respectively.*

4.6 Beam size during low emittance trial operations of Indus-2

With an aim to get higher photon flux for SR users, trial experiments were performed to operate Indus-2 SRS in lower horizontal beam emittance of ~ 45 nm.rad (i.e. ~1/3rd of the present beam emittance of ~ 135 nm.rad at 100 mA and 2.5 GeV [5]. This will be useful for all user beamlines especially those who require small spot sizes or higher brightness. These trial experiments were performed by beam physicists, and diagnostic beamlines were used for online measurement of the beam size and beam position.

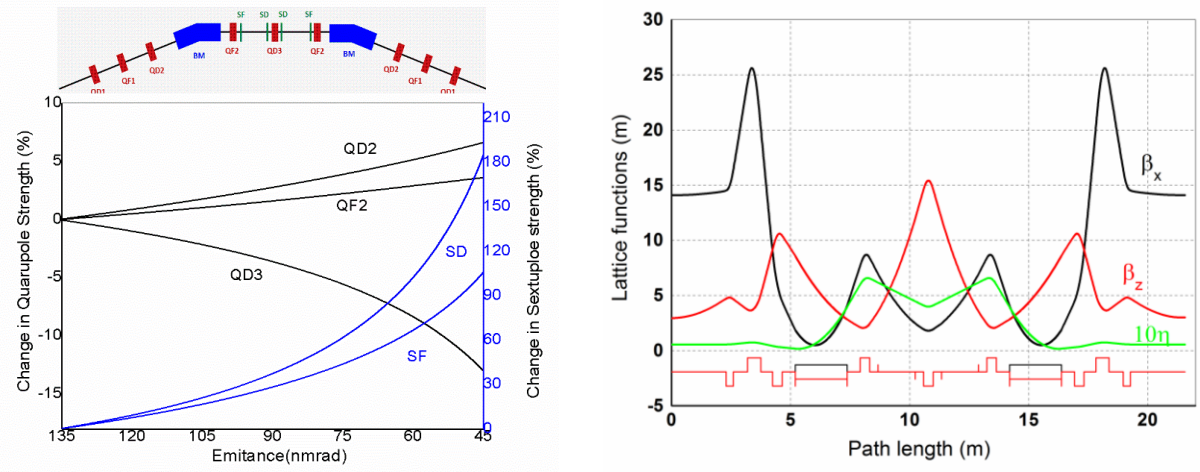

Figure 4.14: *Variation of strengths of various quadrupole and sextupole magnets during switch over to low emittance mode in Indus-2 (left) corresponding lattice functions at low emittance optics (right).*

In low emittance mode, the accelerator becomes more sensitive to the unavoidable field errors leading to the more closed orbit distortions. A suitable procedure was evolved to control the extra beam losses due to this increased sensitivity towards field errors. Moreover at lower beam emittance electron density increases and it leads to beam instability. The

strengths of quadrupole and sextupole magnets were varied during this emittance switch over are shown in Figure 4.14. Slow and fast orbit feedbacks were optimized to control the closed orbit distortion up to the 5 µm (rms) and ±15 µm (peak-peak) over the entire storage ring. Twiss parameters of the low emittance lattice are also shown in Figure 4.14.

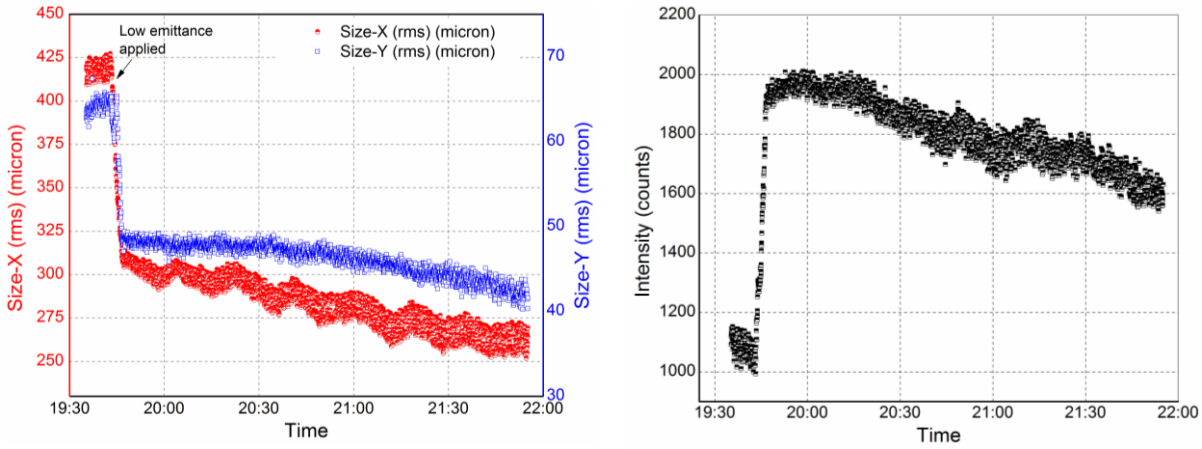

Figure 4.15: *Reduction in horizontal and vertical beam size while low emittance optics is applied (left) increase in SR flux at the detectors in X-DBL (right)*

In this switch over to low emittance mode, beam sizes were measured at X-DBL as shown in Figure 4.15 In the horizontal plane, the electron beam size was reduced from 430 ±20 µm to 310 ± 20 µm which was in agreement with theoretical predictions. During this process, reduction of the vertical beam size from 65 ± 7 µm to 48 ± 7 µm was also observed. The parameters of the bunch-by-bunch feedback were further optimized for arresting beam instabilities in the vertical plane. Peak intensity counts have increased from 1140 counts to 1950 counts. Typical images of the pinhole array before and after applying low emittance optics are shown in Figure 4.16.

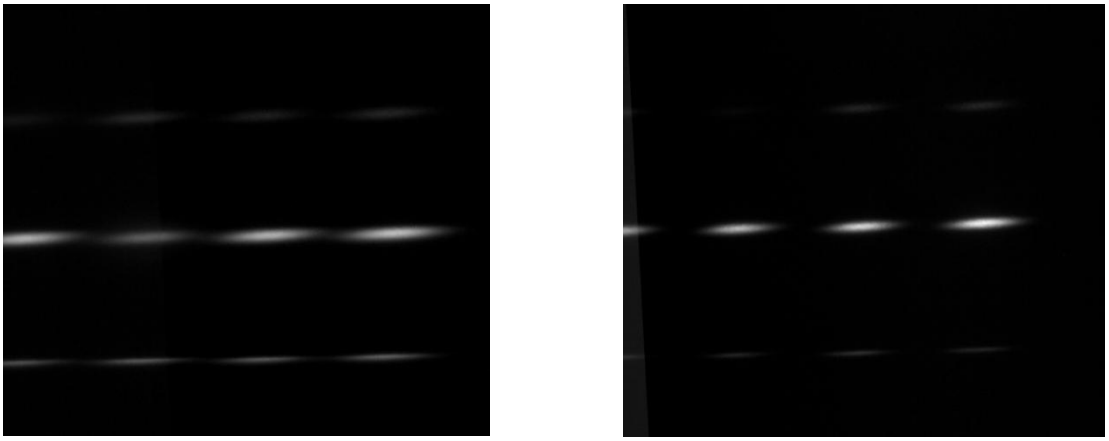

Figure 4.16: *Typical images of the pinhole array before (left) and after (right) applying low emittance optics in Indus-2.*

4.7 Summary and conclusions

Transverse measurements at Indus-2 SRS were carried by using pinhole array system at the X-DBL. Online measurement results (at 1 Hz) of the beam position, beam divergence, beam size and beam emittance were discussed. Modified equations to find the exact correlation of source position and angle from the position and intensity of various pinhole spots were also presented. These equations were tested for the position and angle measurements by known translations of the SPM assembly in vertical plane. The calculated and measured values were matching within ±12 μm (or $\pm$ 1.5 μrad) for a sufficiently wide range of the beam movements (±125μm). The small differences in the beam positions were due to the SPM system limitations. Therefore beside beam size and beam emittance, online information of vertical position and angle can also be measured by using pinhole array. Measured photon

beam position at 8 m from the source point has remained within ± 10 μm for natural decay of beam current in Indus-2.

Experimental measurements of horizontal and vertical dispersions at X-DBL source point (10˚ port DP-10 of Indus-2) were carried out by changing RF frequency (± 5 kHz) with respect to normal operating frequency of 505.8114 MHz. The measured dispersion values (0.253 m, 0.0325 m) are very useful for find the exact beam size at source point. Measured values of the beam size, beam divergence and beam emittance were highly repetitive within their respective measurement ranges. Measured results of the natural horizontal and vertical beam sizes at BL-24 source point are 357.2 µm and 47.6 µm respectively.

Trial experiments to operate the Indus-2 SRS in low horizontal beam emittance mode (~ 45 nm.rad, which is ~1/3rd of the present beam emittance) were carried out at 100 mA and 2.5 GeV. This will be useful for all SR user beamlines especially those who require very small spot sizes (or high brightness). At low emittance optics, beam sizes was reduced from 430 ± 20 µm to 310 ± 20 µm in the horizontal plane, which is also in agreement with theoretical predictions. During this process, vertical beam size was also reduced from 65 ± 7 µm to 48 ± 7 µm, and peak intensity counts increased from 1140 counts to 1950 counts. These measurements were very useful in the optimisation of various feedback systems installed in Indus-2 SRS to arrest various beam instabilities.

Chapter 5 Design study of synchrotron radiation interferometer for beam diagnostics

5.1 Introduction

In order to achieve a higher brightness of the SR beam modern SRS facilities are designed to have beam emittance of a few nm.rad or even less [1]. Precise measurement and control of the particle beam emittance is an important requirement to characterize the performance of any accelerator or SRS. Beam emittance is not a direct measurable parameter, and most of the accelerators monitor it through the transverse beam size. The particle beam emittance is then inferred from the knowledge of the Twiss parameters [67]. The transverse beam size is generally measured by using SR diagnostic techniques [13]. X-rays imaging techniques based on Kirkpatrick-Baez optics [18][20], Fresnel zone plate [77], compound refractive lens [17], and pinhole [84][26] are discussed in Chapter 1. All these techniques are non-destructive to the beam and are useful in online measurements. Although it can provide spatial resolution down to few microns, but their response time is limited by response of phosphors used to convert x-rays into visible (~ few μs) [135][134], so fast spatial measurements (~ few ns) are not possible.

Telescopic imaging by visible SR light is another important beam diagnostics technique, but its spatial resolution is mainly limited by diffraction [72]. For the measurement

of small transverse beam sizes, synchrotron radiation interferometer (SRI) is a very useful method. At KEK-PF, double SRI was applied for the first time to measure small beam sizes with a spatial resolution of few tens of microns [39]. The theoretical background of this method is described in the framework of wave-optics. It is based on Van Cittert-Zernike (VCZ) theorem which relates transverse source profile to its spatial coherence. The particle beam size can be inferred from the measured fringe contrast [40][41]. Beam sizes down to few microns can be measured by using visible SR light. Two-dimensional SRI with a quad slit (at Spring-8 [94]) or circular pinholes (at ALBA [95]) are used to measure horizontal and vertical beam sizes. Advanced SRI with Herschelian reflective optics (at KEK-ATF [96]), intensity imbalance design (at Australian Synchrotron [97]), and rotating pinholes design (at ALBA [95][30]) have shown huge diagnostics potential of this technique. Beam sizes down to few microns have been measured by overcoming the effect of dispersion (due to optics), or noise (due to CCD). SRI is implemented for the first time on a proton machine at LHC [98].

In this chapter, design study for the proposed double-slit SRI at V-DBL (BL-23) in Indus-2 is described. A quad slit SRI has been optimized to measure the beam sizes in both the planes[34]. SRI system is simulated by using Synchrotron Radiation Workshop (SRW) code [42], and visibility analysis of interferogram was carried by horizontal and vertical curve fittings in MATLAB [138]. This work will be used for measuring very small beam sizes (few tens of microns) during low emittance operations of Indus-2, and for the future high brightness SRSs in India. Even full reconstruction of the transverse beam shape is also possible by using rotating pinholes. This technique also provides the possibility of bunch resolved measurement with detector gating, which is useful for studies related to injection dynamics, intra beam scattering and transverse instabilities.

5.2 Coherence and interference

The electric field $E(x, y, z, t)$ due to an electromagnetic wave at any point in space is represented by amplitude and phase. Coherence theory is the study of correlations that exist between different parts of these light fields. In *temporal coherence*, the focus is on the correlation between the fields at different times, $E_1(x, y, z, t_1)$ and $E_1(x, y, z, t_2)$ at same spatial point. In *spatial coherence*, the focus is on the correlations between fields at different spatial locations, $E_1(x_1, y_1, z_1, t)$ and $E_2(x_2, y_2, z_2, t)$ at same time. The maximum length of the wave train on which any two points can be correlated is called *coherence length* [158].

Wave oscillations for visible light (~10^{15} Hz) are too fast to resolve directly, so interference techniques are used to study optical coherence. In interference, light from different times or places in the light field are superimposed at a detection point. If the two fields have a high degree of coherence, they interfere consistently i.e. constructively or destructively at the detection point. If the two fields are not coherent, the interference at the detection point rapidly fluctuates between constructive and destructive interference, and the time-averaged signal does not show any interference fringe. The wave fronts in a laser beam shows effects similar to those emanating from a single point source i.e. high degree of spatial coherence. Similarly there is high degree of temporal coherence arising from the lasers mono chromaticity. Two familiar instruments used to measure temporal coherence and spatial coherence are the Michelson interferometer, and Young's two-slit interferometer respectively [159].

According to the principle of superposition, the net complex amplitude is the sum of all component fields i.e. $E(x,y,z,t) = \sum_i E_i(x,y,z,t)$. Resultant field intensity is the time average of the modulus squared of the total complex amplitude.

$$I(x,y,z,t) = \langle |E(x,y,z,t)|^2 \rangle \tag{5.1}$$

where $< >$ indicates a time average (i.e. $< >_t$) over a period much longer than $1/\nu$. For two interfering waves E_1 and E_2, this result simplifies to

$$I(x,y,z,t) = \langle |E_1|^2 \rangle + \langle |E_2|^2 \rangle + \langle E_1 . E^*{}_2 \rangle + \langle E^*{}_1 . E_2 \rangle \tag{5.2}$$

$$I(x,y,z,t) = I_1 + I_2 + \underbrace{\langle E_1 . E^*{}_2 \rangle + \langle E^*{}_1 . E_2 \rangle} \tag{5.3}$$

where I_1 and I_2 are the intensities at the observation point from each beam individually. Third term contains the effect of interference called cross term or interference term. This general result can be simplified by assuming linearly polarized monochromatic waves of the form

$$E_i(x,y,z,t) = \boldsymbol{A}_i(x,y,z,t)\, e^{j\left(\omega t - \emptyset(x,y,z,t)\right)} \tag{5.4}$$

where both amplitude (**A)** and phase $(\emptyset)$ are functions of the spatial coordinates and time. The resulting expression of intensity pattern becomes

$$I(x,y,z,t) = I_1 + I_2 + \underbrace{2\,(\boldsymbol{A_1}.\boldsymbol{A_2})\,\cos[(\omega_1 - \omega_2)t - (\emptyset_{\boldsymbol{1}} - \emptyset_{\boldsymbol{2}})]} \tag{5.5}$$

We can draw two important conclusions from the above interference term. First, there will be no visible interference effect if the two interfering waves are orthogonally polarized i.e. dot product term will be zero. Second, if the frequencies of the two waves are different, the interference effects will be modulated at a temporal beat frequency equal to the difference frequency [160].

5.2.1 Mutual coherence function and degree of coherence

In the double slit system, instantaneous electric field for any point 'Q' on the screen is given by the principle of superposition as

$$E_{total}\,(r_1,\, r_2, t,\, t_1,\, t_2) = \sqrt{K_1}\,E(r_1, t + t_1) + \sqrt{K_2}\,E(r_2, t + t_2) \tag{5.6}$$

where K_1 and K_1 are the slit transmission constants of pinholes (P_1 and P_2), t_1 and t_2 are the transit time required for optical waves to travel from pinholes P_1 and P_2 to the point 'Q' on the observation screen; r_1 and r_2 are the respective position of pinholes with respect to centreline.

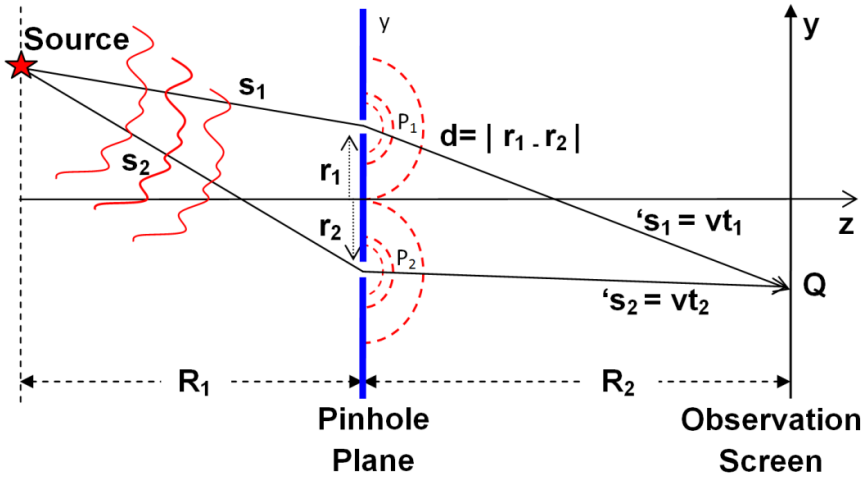

Figure 5.1: *Schematic of double slit interferometer for a point source.*

Irradiance of the interference pattern on the observation screen will be

$$I(r_1,\, r_2;\, t_1,\, t_2)$$

$$\approx K_1\,\langle|E(r_1, t + t_1)|^2\rangle + K_2\langle|E(r_2, t + t_2)|^2\rangle + \underline{\sqrt{K_1K_2}\;Re[\langle E(r_1, t + t_1)\,E^*(r_2, t + t_2)\rangle]} \tag{5.7}$$

where first two terms are the intensities at the observation point from each pinhole individually. Third term (or interference term) is also called *mutual coherence function* (Γ) (MCF). Basically MCF is a statistical property, representing the temporal correlation of the electric field at two positions in space with respect to time.

$$\Gamma(r_1, r_2; t_1, t_2) = \langle E(r_1, t + t_1)\, E^*(r_2, t + t_2)\rangle \tag{5.8}$$

For a case of stationary fields, statistics of the optical field depends only on time difference $\boldsymbol{\tau}$

$$\Gamma(r_1, r_2; \Delta t) = \langle E(r_1, t)\, E^*(r_2, t + \Delta t)\rangle \tag{5.9}$$

here $\Delta t = t_1 - t_2 = \tau\ (say)$.

$$\boldsymbol{\Gamma(r_1, r_2; \tau) = \langle E(r_1, t)\, E^*(r_2, t + \tau)\rangle} \tag{5.10}$$

Normalized MCF is called *complex degree of coherence* or simply degree of coherence. Generally it is a complex and periodic function of τ.

$$\gamma_{12}(r_1, r_2; \tau) = \frac{\sqrt{K_1 K_2}}{\sqrt{I_1 I_2}}\, \Gamma(r_1, r_2; \tau) \tag{5.11}$$

where I_1 and I_2 are the irradiances at the observation point (Q) from each pinhole independently. Based on $|\gamma_{12}|$,light can be classified into full coherent, partially coherent and fully incoherent as follows

$$\begin{cases} |\gamma_{12}(r_1, r_2; \tau)| = 1 & \text{Fully coherent} \\ 0 < |\gamma_{12}(r_1, r_2; \tau)| < 1 & \text{Partially coherent} \\ |\gamma_{12}(r_1, r_2; \tau)| = 0 & \text{Fully Incoherent} \end{cases} \tag{5.12}$$

By using Eq. (5.11) in Eq. (5.7) for the simplest case

$$I_P = I_1 + I_2 + 2\sqrt{I_1 I_2}\ Re[\gamma_{12}(r_1, r_2; \Delta t)] \tag{5.13}$$

Maximum and minimum value of irradiance at point (Q) can be summarised as

$$I_{P\ Max.,\ Min.} = I_1 + I_2 \pm 2\sqrt{I_1 I_2}\ |\gamma_{12}(r_1, r_2; \tau)| \tag{5.14}$$

Visibility

$$V = \frac{I_{P\_Max.} - I_{P\_Min.}}{I_{P\_Max.} + I_{P\_Min.}} \tag{5.15}$$

$$V = \frac{2\sqrt{I_1 I_2}}{I_1 + I_2}\ |\gamma_{12}(r_1, r_2; \tau)| \tag{5.16}$$

5.2.2 Spatial coherence of an extended source

An extended continuous source is basically an ensemble of incoherent point sources, and it resultant intensity can be obtained by adding irradiance from individual point source. The interference fringe pattern (at any point Q on screen) due to a point source (P) with radiance $a^2(y_S) = {a_0}^2\delta(y_S - y_{S0})$ on the source plane (Figure 5.2) can be written as [158]

$$I(Q;\ y_S) = K_1 a^2(y_S) + K_2 a^2(y_S) + \sqrt{K_1 K_2}\ a^2(y_S)\ \cos[k(OPD_O - OPD_S)] \tag{5.17}$$

where $k = \frac{2\pi}{\bar{\lambda}}$, $\bar{\lambda}$ is average wavelentgth of quasimonochromatic source, $OPD_O\left(= \frac{d}{R_2} y_0\right)$ and $OPD_S\left(= \frac{d}{R_1} y_S\right)$ are the respective optical path differences.

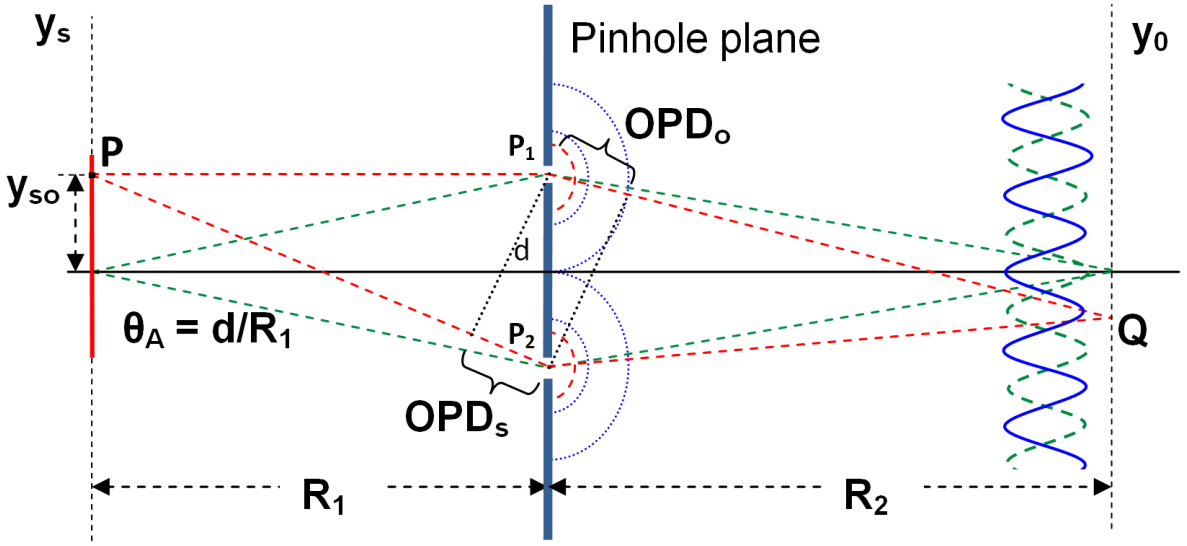

Figure 5.2: *Schematic of double slit interferometer for an extended source.*

Integrating Eq. (5.17) over a one dimensional continuous source distribution

$$I(Q) = \int_{Source} \{K_1 a^2(y_S) + K_2 a^2(y_S) + \sqrt{K_1 K_2}\, a^2(y_S)\, cos[k(OPD_O - OPD_S)]\} dy_S \tag{5.18}$$

$$= \int_{Source} \left\{(K_1 + K_2) a^2(y_S) + \sqrt{K_1 K_2}\; a^2(y_S)\, cos\left[k\left(\frac{d}{R_2} y_0 - \frac{d}{R_1} y_S\right)\right]\right\} dy_S \tag{5.19}$$

$$= (K_1 + K_2)\, I_L + 2\sqrt{K_1 K_2}\; Re\left\{ e^{jk \frac{d}{R_2} y_0} . \int_{Source} a^2(y_S)\, e^{-j\, k\, \theta_A\, y_S}\; dy_S \right\} \tag{5.20}$$

where $I_L = \int_{Source}\; a^2(y_S)\; dy_S$ and $\theta_A = \frac{d}{R_1}$ are the source radiance and angular subtense of the pinholes as seen from the source. By taking last term as $\mathcal{F}\{a^2(v)\}_{\left(\frac{\theta_A}{\lambda}\right)}$ i.e. Fourier transform of the source irradiance distribution, it becomes

$$= (K_1 + K_2)\, I_L + 2\sqrt{K_1 K_2}\; Re\left\{ e^{jk\ OPD_O} . \underbrace{\boldsymbol{\mathcal{F}}\{a^2(v)\}_{\left(\frac{\theta_A}{\bar{\lambda}}\right)}} \right\} \tag{5.21}$$

$$I(Q) = (K_1 + K_2)\, I_L + 2\sqrt{K_1 K_2}\;\; I_L\;\; \gamma_{12}\left(\frac{\theta_A}{\bar{\lambda}}\right) cos\left[k\,\frac{d}{R_2} y_0 + \beta_{12}\left(\frac{\theta_A}{\bar{\lambda}}\right)\right] \tag{5.22}$$

where $\gamma_{12}\left(\frac{\theta_A}{\bar{\lambda}}\right) = \frac{\left|\boldsymbol{\mathcal{F}}\{a^2(v)\}_{\left(\frac{\theta_A}{\bar{\lambda}}\right)}\right|}{I_L}$ and $\beta_{12}\left(\frac{\theta_A}{\bar{\lambda}}\right) = arg\left\{ \boldsymbol{\mathcal{F}}\{a^2(v)\}_{\left(\frac{\theta_A}{\bar{\lambda}}\right)} \right\}$ are the normalised amplitude and phase of Fourier transform of source irradiance distribution. First term is also called *degree of spatial coherence* (γ_{12}).

$$I(Q) = (K_1 + K_2)\, I_L \left\{1 + \frac{2\sqrt{K_1 K_2}}{(K_1 + K_2)}\;\; \gamma_{12}\left(\frac{\theta_A}{\bar{\lambda}}\right) cos\left[k\,\frac{d}{R_2} y_0 + \beta_{12}\left(\frac{\theta_A}{\bar{\lambda}}\right)\right]\right\} \tag{5.23}$$

$$I(Q) = (K_1 + K_2)\, I_L \left\{1 + V\; cos\left[k\,\frac{d}{R_2} y_0 + \beta_{12}\left(\frac{\theta_A}{\bar{\lambda}}\right)\right]\right\} \tag{5.24}$$

where $\frac{2\sqrt{K_1 K_2}}{(K_1+K_2)}\;\; \gamma_{12}\left(\frac{\theta_A}{\bar{\lambda}}\right)$ term is also called *fringe visibility* (V). We may note that the fringe visibility is not a function of position (Q) i.e. independent of optical path difference in observation space. Secondly, fringe spacing for an extended source $\left(= \frac{\bar{\lambda}\, R_2}{d}\right)$ is identical to fringe spacing of interference pattern resulting from an individual point source.

5.3 Theoretical framework of beam size measurement by SRI

SRI is a wave-front-division type interferometer using polarized quasi-monochromatic SR produced from the charge particles. The beam size is measured from the visibility of the interferogram, which indicates the complex degree of spatial coherence of the photons. Schematic of the beam size measurement system is shown in Figure 5.3.

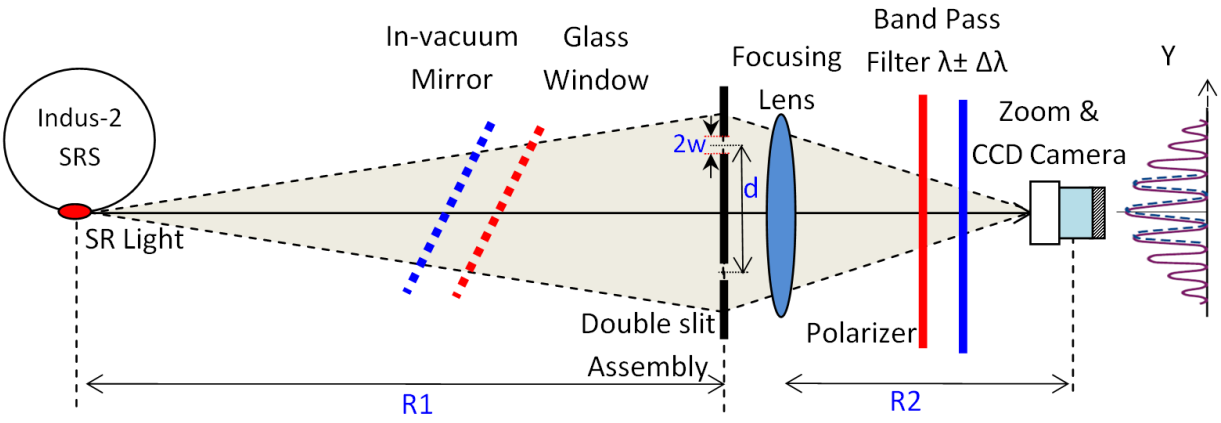

Figure 5.3: *Schematic of SR interferometer for beam size measurement at Indus-2.*

Intensity profile of a double-slit interferogram produced by an incoherent light source illuminating slits with equal intensity (I_o), (with no diffraction effects) can be given by expressed as [94][161][162]

$$I(y) = 2I_0\left[1 + |\gamma|\ \ cos\left(2\pi f_y\, y\right)\right] \tag{5.25}$$

where y is the vertical position, $f_y = {d_V}/{\bar{\lambda}\, R_1}$ is the spatial frequency (units m^{-1}), d_V is the vertical slit separation, $\bar{\lambda}$ is the wavelength, R_1 is the distance from source to double slit assembly and $|\gamma|$ is the visibility of the interference pattern.

As we know that a single monochromatic plane-wave produces the interference pattern with full-contrast i.e. $|\gamma|$ =1 for all d_V. But, for a distributed source, the electromagnetic fields can be taken as a linear combination of many plane waves. The differential path length from each elemental radiator $(d\sigma)$ at the source to slits 1 and 2 varies with position of the radiator element. As a result, each elemental fringe pattern has a different relative phase shift, and the net interference pattern will lose its contrast i.e. $|\gamma| < 1$. This is the basis for measurement of stellar diameters by Michelson; and for monitoring size of SR source by Mitsuhashi [39].

According to Van Cittert-Zernike theorem [40][41], the complex degree of spatial coherence (γ) from an extended, distant, incoherent source is proportional to Fourier transform of the normalized source intensity distribution I(y)

$$\gamma(f_y) = \int I(y)\, e^{-i2\pi f_y\, y}\, dy \tag{5.26}$$

The derivation of the VCZ theorem to above simplified form is based on few assumptions for source and measurement setup (Appendix B). Source is assumed to be distant, incoherent, quasi monochromatic, two dimensional with very small angular size; and the medium is also assumed to be homogeneous. These assumptions may not be true for all kind of sources. In SRS, source size is very small (σ ~ 50-300 μm) and for a measurement system at few meters, it could be taken as distant source. It can also be treated as quasi monochromatic by selecting narrowband (Δλ ~10 nm at 545 nm). In SR source medium is also vacuum (i.e. homogeneous), so the required conditions for the measurement of SR

source size by using VCZ theorem are satisfied. Measurement of SR source size by using VCZ theorem is similar to measuring the angular dimensions of distant stars by Michelson.

From Eq. (5.26), the normalized degree of coherence in the interference pattern for a one dimensional Gaussian source (with σ_y rms size) becomes

$$\gamma(f_y) = I_0 \int e^{-\frac{y^2}{2\,{\sigma_y}^2}}\; e^{-i2\pi f_y\, y}\, dy \tag{5.27}$$

$$\gamma(f_y) = I_0\, e^{-2\,\pi^2\,{f_y}^2{\sigma_y}^2} \tag{5.28}$$

Three cases are taken to understand different measurement setups. **Case-I:** If slit separation (d) is fixed (i.e. at fixed spatial frequency f_y), for a measured fringe contrast of γ_d , Eq. (5.28) gives source size as

$$\sigma_y = \frac{1}{\pi\, f_y}\sqrt{\frac{1}{2}\, ln\frac{1}{\gamma_d}} \;\text{ or }\; \sigma_y = \frac{\lambda\, R_1}{\pi\, d_V}\sqrt{\frac{1}{2}\, ln\frac{1}{\gamma_d}} \tag{5.29}$$

This result enables for fast on-line beam size measurements with a fixed slit separation (d_V).

Case-II: If slit separation is scanned through a range of optimized values (i.e. spatial frequency f_y is changed), measured fringe contrast fit to a Gaussian profile as

$$\gamma(f_y) = Ke^{-\frac{{f_y}^2}{2{\sigma_\gamma}^2}} \tag{5.30}$$

where K be a constant of proportionality and σ_γ is the rms width of the contrast curve. Comparing Eq. (5.28) and Eq. (5.30) yields the identity

$$\sigma_y{}^2\,\sigma_\gamma{}^2 = \frac{1}{4\pi^2} \quad \text{or} \quad \sigma_y\,\sigma_\gamma = \frac{1}{2\pi} \tag{5.31}$$

Case-III: When slit assembly is rotated with respect to vertical axis. VCZ theorem for a two dimension source can be expressed as

$$\gamma(f_x\,,\,f_y) = \int\int I(x,y)\,e^{-i2\pi\,(f_x\,x\,+\,f_y\,y)}\,dx\,dy \tag{5.32}$$

where the configuration space axes (x, y) and spatial frequencies (f_x, f_y) are referenced in the x-y cartesian coordinate system. Therefore for a bi-Gaussian beam profile with distribution as

$$I(x,y) = I_0\,e^{-}\left(\frac{x^2}{2\sigma_x{}^2} + \frac{y^2}{2\sigma_y{}^2}\right) \tag{5.33}$$

Normalized degree of coherence will become

$$\gamma(f_x,f_y) = Ke^{-\left(\frac{f_x{}^2}{2\sigma_{\gamma x}{}^2} + \frac{f_y{}^2}{2\sigma_{\gamma y}{}^2}\right)} \tag{5.34}$$

when slit assembly (at experimental end) is rotated by angle θ with respect to x-axis, the coherence function will become [162]

$$\gamma(f_x,f_y,\theta) = Ke^{-\left\{\frac{\left(\frac{d}{\lambda\,R_1}\cos\,\theta\right)^2}{2\sigma_{\gamma x}{}^2} + \frac{\left(\frac{d}{\lambda\,R_1}\sin\,\theta\right)^2}{2\sigma_{\gamma y}{}^2}\right\}} \tag{5.35}$$

The standard SRI using double aperture/pinholes provides the beam size projection in a given direction. So, the beam shape is not fully characterized and the information about possible

transverse beam tilts is not determined. A rotating double-pinhole mask can be used to fully reconstruct the transverse beam profile under different beam couplings [95][30].

5.4 Upgrade of visible diagnostics at Indus-2 SRS

V-DBL (BL-23) is used for the measurement of longitudinal beam parameters of Indus-2 SRS. In the present scheme of the V-DBL, a water cooled primary mirror at 5 m from the source point (dipole magnet) is used to extract visible light from the wide SR spectrum. This light is focused outside the Indus-2 tunnel in dark room by using optical chicane of four plane optical mirrors (at 45°) and lenses [35]. Optical detectors such as streak camera, fast photo receiver, avalanche photodiode and CCD camera are used for the measurements in the dark room. To improve the spatial resolution of beamline, it is planned to include SRI in BL-23. Schematic of the proposed upgradation of V-DBL to include SRI is shown in Figure 5.4.

In this new scheme, wave front distortion will be reduced by extracting visible light outside the Indus-2 tunnel with single water cooled mirror. The distance from the SR source point to the extraction mirror located outside the Indus-2 tunnel is ~15 m. To reduce wave front distortion, primary mirror and optics have flatness better than $\lambda/10$. The SRI system consists of a slit assembly, lenses (50 mm, f = 500 mm), a band pass filter (545 ± 10 nm), a magnification lens to widen the interference pattern, a polarizer to select the σ-polarization and π-polarization, and optical detectors to record the interferogram.

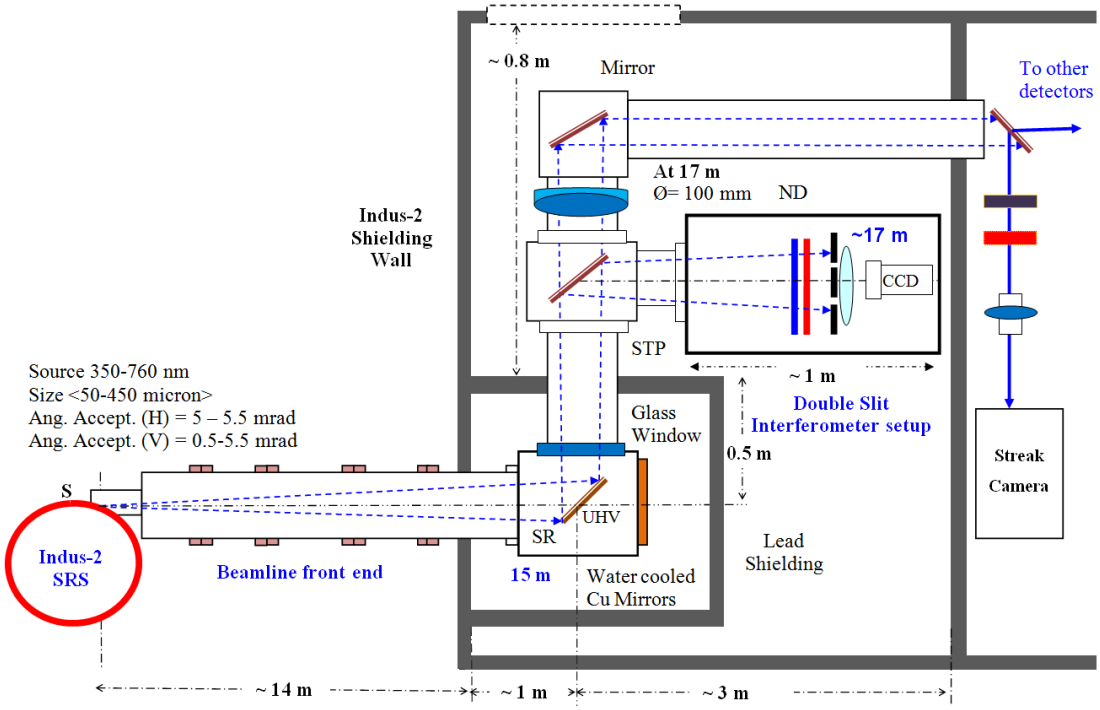

Figure 5.4: *Schematic of the proposed upgradation of V-DBL to include SRI at Indus-2.*

5.5 Design parameters

To optimize the SRI system, the effect of various input variables at final measurement is estimated. The intensity of the interferogram pattern as a function of the position (y) is [161][96]

$$I(y) = I_0\, sinc^2\left(\frac{2\pi\, w_V}{\lambda R_2} y + \emptyset\right)\left[1 + |\gamma_y| \cos\left(\frac{2\pi\, d_V}{\lambda R_2} y + \psi\right)\right] \tag{5.36}$$

where R_2, w_V and λ are the distance from the slit to detector, half aperture size of vertical slit and the wavelength of light respectively. ψ and $\emptyset$ denotes the phase and offset of the

interferogram respectively. γ_y is the complex degree of spatial coherence i.e. Fourier transform of the source spatial distribution profile. Similarly the intensity profile of a two dimensional interference pattern from a quad slits can be expressed as

$$I(x,y) = I_0\, sinc^2\left(\frac{2\pi\, w_H}{\lambda R_2}x + \emptyset\right)\left[1 + |\gamma_x|\cos\left(\frac{2\pi\, d_H}{\lambda R_2}x + \psi\right)\right] \times \quad sinc^2\left(\frac{2\pi\, w_V}{\lambda R_2}y + \emptyset\right)\left[1 + |\gamma_y|\, cos\left(\frac{2\pi\, d_V}{\lambda R_2}y + \psi\right)\right] \tag{5.37}$$

where w_H (w_V) and d_H (d_V) are the slit half width and slit separation in horizontal (vertical) plane respectively. The beam size information is encoded in the form of modulation depth in the interferogram. Smaller the beam size, deeper is the modulation depth. The relationships between the source size σ_x and σ_y, and the visibilities $|\gamma_x|$ and $|\gamma_y|$ for fixed slit can be expressed as

$$\sigma_x = \frac{\lambda R_1}{\pi\, d_H}\sqrt{\frac{1}{2}\ln\frac{1}{|\gamma_x|}} \text{ and } \sigma_y = \frac{\lambda R_1}{\pi\, d_V}\sqrt{\frac{1}{2}\ln\frac{1}{|\gamma_y|}} \tag{5.38}$$

5.5.1 Slit separation and visibility

To find out the optimised slit separation, visibility curves are analyzed by using Eq. (5.38) at a slit width of 2 mm, at 17 m from source point with visible light (545 nm). Visibility decreases with the increase of slit separation and with beam size as shown in Figure 5.5. For a smaller beam size, higher can be the slit separation. But in SR, slit separation is also limited by angular acceptance of beamline and narrow collimation of SR in vertical plane. Further,

we will see in next section that slit separation are also related to error in beam size measurement through visibility.

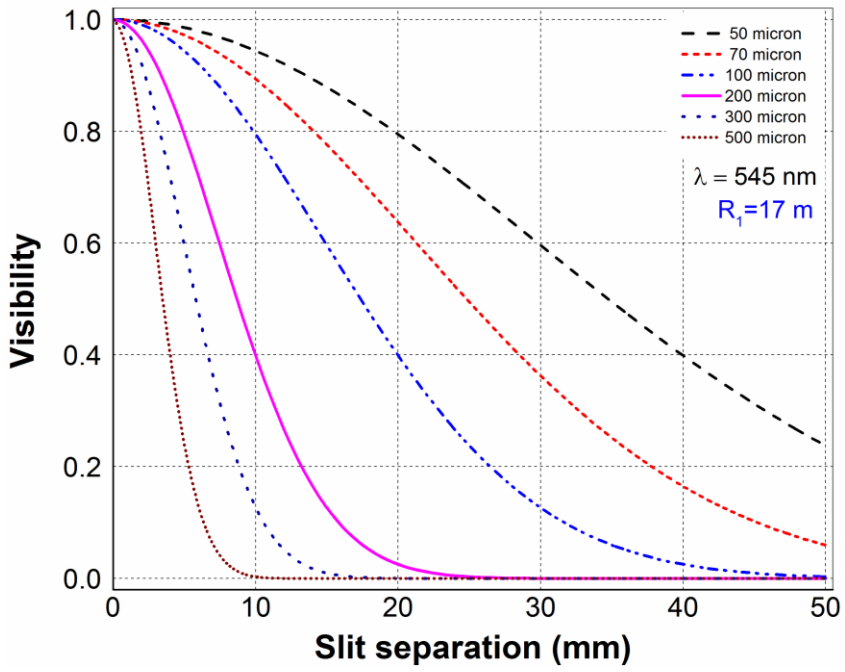

Figure 5.5: *SRI visibility curves for various source sizes at 17 m from the source point.*

5.5.2 Intensity imbalance

The visibility of an interference fringes is related to the complex degree of coherence ($|\gamma|$) by a factor involving the intensity of each beam I_1 and I_2 given by

$$V_y = \frac{2\sqrt{I_1 I_2}}{I_1 + I_2} \; |\gamma_y| \tag{5.39}$$

Mostly one can assume $I_1 \approx I_2$ and take $V_y = |\gamma_y|$. In SRS, if the radiation produced by each electron is considered as a spherical wave, the intensity of the light will be uniformly

distributed in all the directions, and $V_y = |\gamma_y|$. But because of intensity imbalance at the slits [97], true beam size can be determined by correcting the measured visibility to the complex degree of coherence using the imbalance ratio $\rho = \frac{I_2}{I_1}$ and then computing the beam size from Eq. (5.38) as follows

$$|\gamma_y| = \frac{(1+\rho)}{2\sqrt{\rho}} V_y \tag{5.40}$$

Theoretically calculated effect of the intensity imbalance on coherence and beam size measurement error is shown in Figure 5.6. It is observed that the visibility change and beam size error is less than 0.5 % for an intensity imbalance up to 17 % for these optimized parameters.

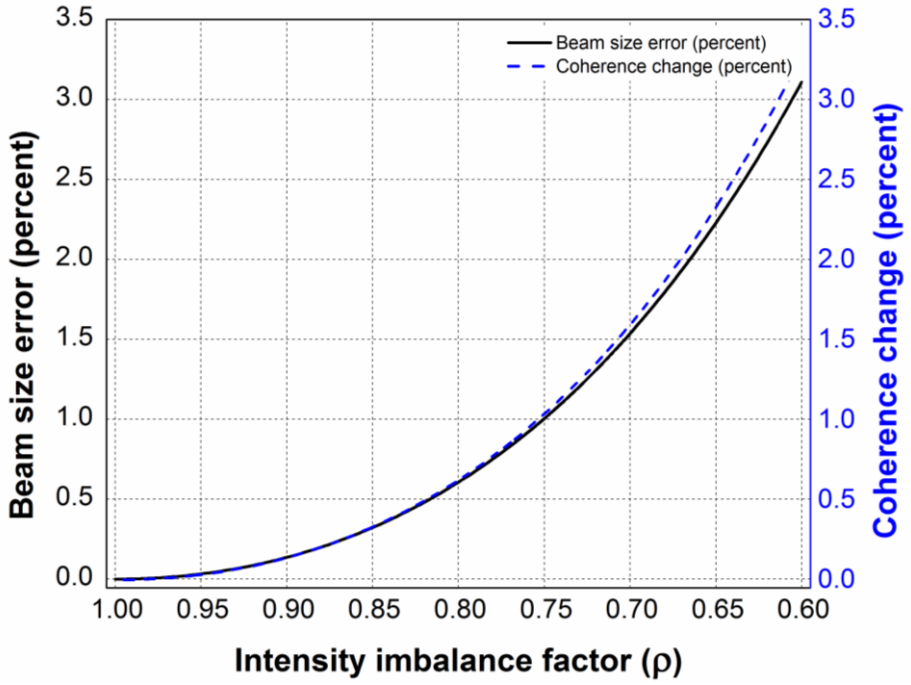

Figure 5.6: *Calculated effect of intensity imbalance factor (ρ) on coherence and beam size measurement for V-DBL.*

5.5.3 Error in beam size measurement

From Eq. (5.36), the intensity of the interferogram pattern for a Gaussian beam can be written as the function of the position *y* as

$$I(y) = I_0\, sinc^2\left(\frac{2\pi\, w_V}{\lambda R_2} y + \emptyset\right)\left[1 + \; e^{-2\left(\frac{\pi\, d\, \sigma_y}{\lambda R_1}\right)^2} \cos\left(\frac{2\pi\, d_V}{\lambda R_2} y + \psi\right)\right] \tag{5.41}$$

$$I_{Max} = I_0\, sinc^2\left(\frac{2\pi\, w_V}{\lambda R_2} y + \emptyset\right)\left[1 + \; e^{-2\left(\frac{\pi\, d\, \sigma_y}{\lambda R_1}\right)^2}\right] \tag{5.42}$$

$$I_{Min} = I_0\, sinc^2\left(\frac{2\pi\, w_V}{\lambda R_2} y + \emptyset\right)\left[1 - \; e^{-2\left(\frac{\pi\, d\, \sigma_y}{\lambda R_1}\right)^2}\right] \tag{5.43}$$

By using

$$\frac{I_{Max.} + I_{Min.}}{2} = I_0\, sinc^2\left(\frac{2\pi\, w_V}{\lambda R_2} y + \emptyset\right) = I_{Av}\,(say) \tag{5.44}$$

Eq. (5.41) will become

$$I(y) = I_{Av}\; \left[1 + \; e^{-2\left(\frac{\pi\, d\, \sigma_y}{\lambda R_1}\right)^2} \cos\left(\frac{2\pi\, d_V}{\lambda R_2} y + \psi\right)\right] \tag{5.45}$$

Differentiating Eq. (5.45)

$$dI = I_{Av}\; \left[-\; e^{-2\left(\frac{\pi\, d\, \sigma_y}{\lambda R_1}\right)^2} 2\left(\frac{\pi\, d\, \sigma_y}{\lambda R_1}\right)^2 \; \frac{2d\, \sigma_y}{\sigma_y}\right] * \cos\left(\frac{2\pi\, d_V}{\lambda R_2} y + \psi\right) \tag{5.46}$$

Now visibility can be expressed as

$$V = \frac{I_{Max.} - I_{Min.}}{I_{Max.} - I_{Min.}} = e^{-2\left(\frac{\pi\ d\ \sigma_y}{\lambda R_1}\right)^2} \tag{5.47}$$

$$ln(V) = -2\left(\frac{\pi\ d\ \sigma_y}{\lambda R_1}\right)^2 \tag{5.48}$$

Combining Eq. (5.48) and Eq. (5.47) in Eq. (5.46) to get

$$\frac{dI}{I_{Av}} = \left[V \quad ln(V) \quad \frac{2\ d\ \sigma_y}{\sigma_y}\right] * \cos\left(\frac{2\pi\ d_V}{\lambda R_2} y + \psi\right) \tag{5.49}$$

So, for a detector which can detect minimum relative change in intensity $\left(\frac{dI}{I_{Av}}\right)$, there will be relative size error in measurements as

$$\frac{d\ \sigma_y}{\sigma_y} = \frac{\frac{dI}{I_{Av}}}{-2V \quad ln(V)} \tag{5.50}$$

The error in beam size measurement at various visibilities of interferogram was calculated by using Eq. (5.50), and results are shown in Figure 5.7. It was found that relative size error increases at the extremes of visibility (0 and 1). For a reasonable value of detector sensitivity $^{dI}/_{I} \sim 0.5\ \%$, it remains less than 2 % for wide range of visibility. The error in measured beam size is almost insensitive to intensity errors in the visibility range of 0.2 to 0.6.

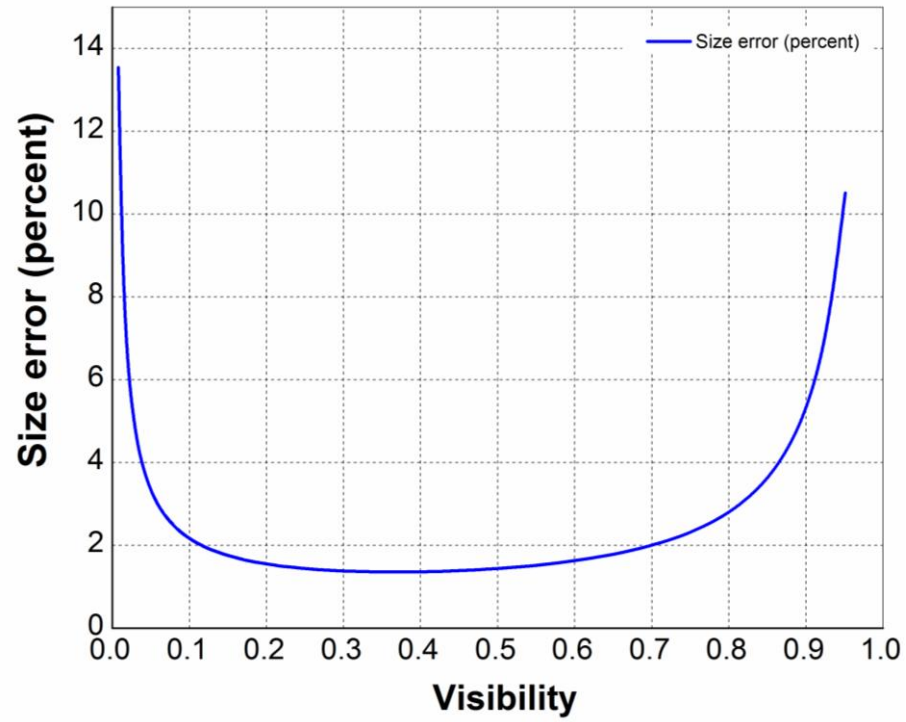

Figure 5.7: *Variation of beam size measurement error w.r.t. visibility of interferogram.*

In SRI design, slit separation (*d*) is optimized to keep visibility V~ 0.5 for specified range of beam sizes. So, it needs high slit separation for better resolution, which is further limited due to opening angle of SR. Final resolution and accuracy of system depends upon suitable optimization of these design parameters and sensitivity (relative intensity change) of measuring detectors.

5.5.4 Beam shift

In accelerators, it has been observed that a turn-by-turn beam motion of few tens of microns generally remains in both horizontal and vertical planes. This beam jitter generates a phase shift in the interference patterns that leads to reduction in the visibility, and results in an

overestimation of the measured beam sizes. When the beam is off the nominal orbit, the phase error is

$$\Delta\emptyset = \frac{2\pi\, d_H}{\lambda R_1}\, \Delta x_{beam} \tag{5.51}$$

where Δx_{beam} is the beam offset from the orbit. If the beam moves horizontally from $-\Delta x$ to Δx, the phase of the interference pattern will change from $-\Delta\emptyset$ to $\Delta\emptyset$. By integrating the interference intensities over this phase shift, average visibility is found to be [31][163]

$$\bar{V}_x = \mathrm{sinc}(\Delta\emptyset)\, V_x \tag{5.52}$$

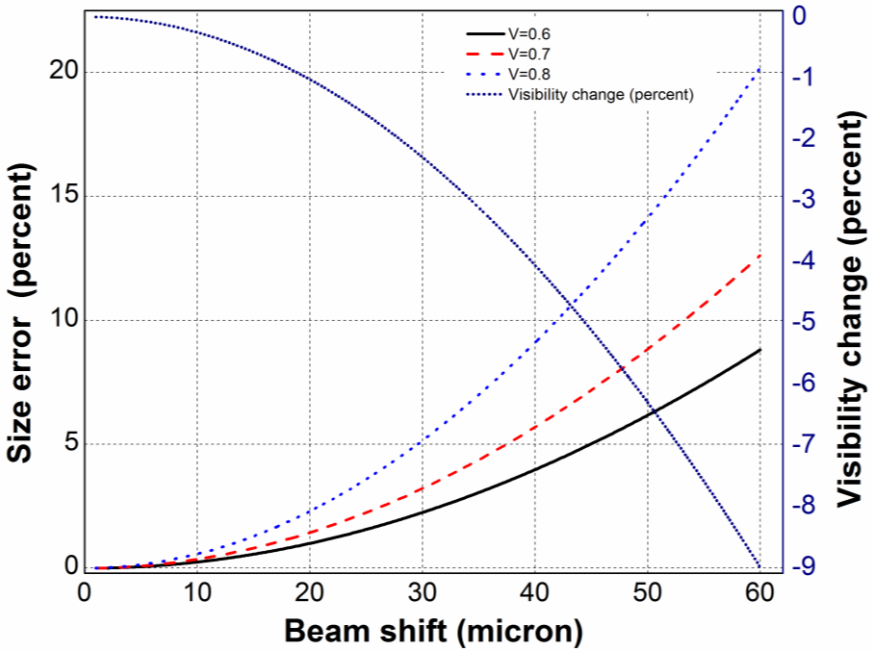

Figure 5.8: *Calculated effect of beam shift on visibility and beam size measurement error*

Using above equation, the effect of beam shift was calculated and results are shown in Figure 5.8. For a beam shift of ~ 30 μm, there is $\Delta\emptyset$=0.3 and $\bar{V}_x \sim 0.98\, V_x$. This reduction in visibility (~ 2 %) corresponds to an error less than 2 % (i.e. 1~2 μm) in the measurement of beam size.

5.5.5 Polarization

The horizontal and vertical polarization of the SR leads to interference fringe shift by π rad in phase. In SRI, using both polarizations of SR results a loss of the visibility and an overestimation of the beam size. Typical image of total spectral flux of visible light (at 1.58 eV) and contributions from different polarizations as simulated in SRW are shown in Figure 5.9. Optical polarizer mounted on a motorized rotating stage is scanned to identify the nominal angle position for selecting mainly horizontal polarization (which is more intense than vertical).

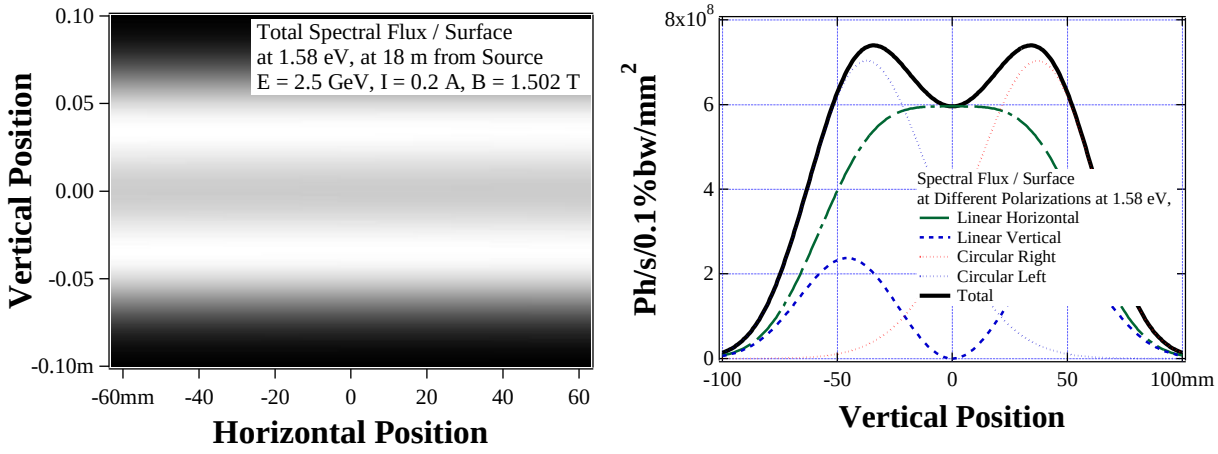

Figure 5.9: *Typical SRW simulated image of total spectral flux of visible light (at 1.58 eV) at 18 m from source point (left) and contributions from different polarizations (right).*

5.5.6 The effect of multiple wavelengths

For a point source with two wavelengths λ_a and λ_b , the resultant intensity will be sum of the irradiance patterns from individual wavelength [158]. If $K_1 = K_2 = 1$, for an experimental

setup discussed in section (5.2.2), resultant intensity from addition of field components will become

$$I(x) \approx \langle |E_{Tot.}|^2 \rangle = 2A^2 \left[1 + |\gamma_x| \cos\left(\frac{2\pi}{\bar{\lambda}} OPD\right) * \cos\left(\frac{2\pi}{\lambda_{eq.}} OPD\right)\right] \quad (5.53)$$

Where A is the amplitude of each component wave at the observation point y_0 on the screen, OPD=$d\ \sin\theta \sim \frac{d\ y_0}{R_2}$ is the optical path difference, $\bar{\lambda} = \frac{\lambda_a + \lambda_b}{2}$ is the average wave length and $\lambda_{eq.} = \frac{\lambda_a \lambda_b}{|\lambda_a + \lambda_b|}$ is the equivalent wavelength. The cosine terms on the right side of Eq. (5.53) indicates a slow modulation corresponding to $\lambda_{eq.}$. The higher frequency occurs with a period $OPD = \bar{\lambda}$.

Theoretical interferogram and its vertical intensity profile showing reduction in visibility due to the effect of two interfering wavelength 545 nm and 565 nm are shown in Figure 5.10. Optimized design parameters of SRI are specified in Table 5.1

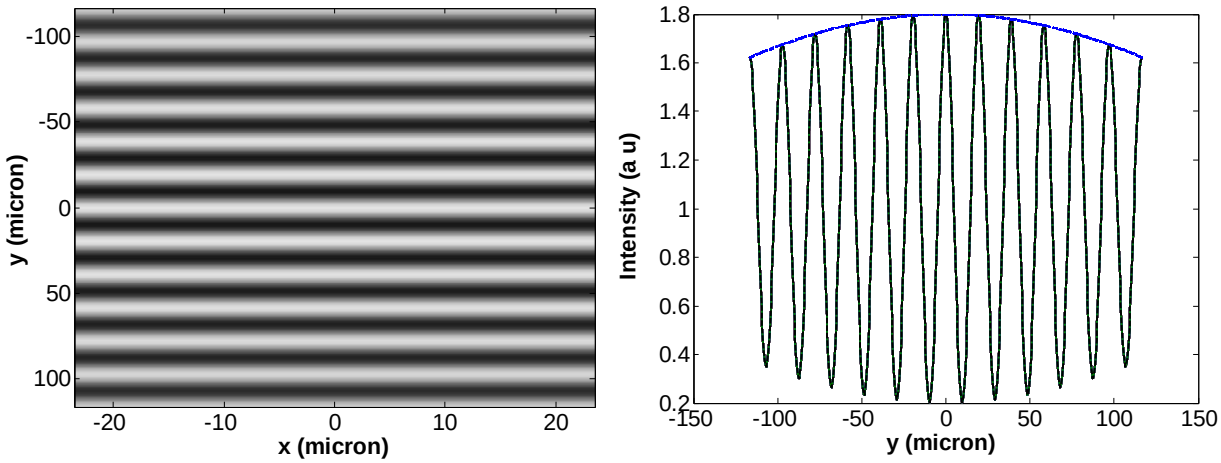

Figure 5.10: *Theoretical interferogram and its vertical intensity profile showing reduce in visibility due effect of two interfering wavelengths 545 nm and 565 nm.*

Table 5.1: *Basic design parameters of the SRI setup at Indus-2*

Beam energy (*GeV*)	2.5
Current (*A*)	0.2
Beam vertical position (*mm*)	0.0001
Beam vertical angle (*mrad*)	0.0
Energy spread	0.00091
Horizontal emittance (*nm.rad*)	60
Beam vertical emittance (*nm.rad*)	1.1
Source to slit distance (*m*)	17
SR energy at 545nm (*eV*)	2.227
Slit size (*mm*)	2 X 2
Slit separation (d) (*mm*)	5, 15
Slit vertical centre (*mm*)	0, 25.5
Peak flux (point source) (*ph/s/0.1% BW/mm^2*)	16 X 10^{10}
Peak flux (extend source) (*ph/s/0.1% BW/mm^2*)	8 X 10^{10}

5.5.7 Vibrations

In the visible diagnostics most of the beamline remains in the air. So, air turbulence generates vibration in the optical components, and causes rigid displacement of the centroid of the image. These vibrations cause changes in the interferogram characteristics (visibility) and may lead to wrong estimation of beam size.

To some extent it can be reduced by decreasing the integration time of the CCD camera during the image acquisition, but this decreases the quantity of light reaching the

CCD sensor and the interferogram might be not clear enough for the measurement. To overcome this problem, dedicated algorithms can be implemented to improve the dynamic range of the measurements. It is also possible to measure the spectrum of the vibration by measuring the displacement of the interferogram centroid with a fast acquisition camera or position sensitive detectors. The FFT of the displacement in the both horizontal and vertical directions with respect to time will measure problematic/ major peaks of vibrations (~10-14 Hz) [164]. Optimized design parameters of SRI are specified in Table 5.1.

5.6 Simulation in SRW and profile fitting

SRI setup with above design parameters was simulated by using SRW code [42] for V-DBL in Indus-2. Typical pictures of simulated SR intensity (at 545 nm) just before and after the interferometer slits at 17 m from the source point are shown in Figure 5.11 and Figure 5.12.

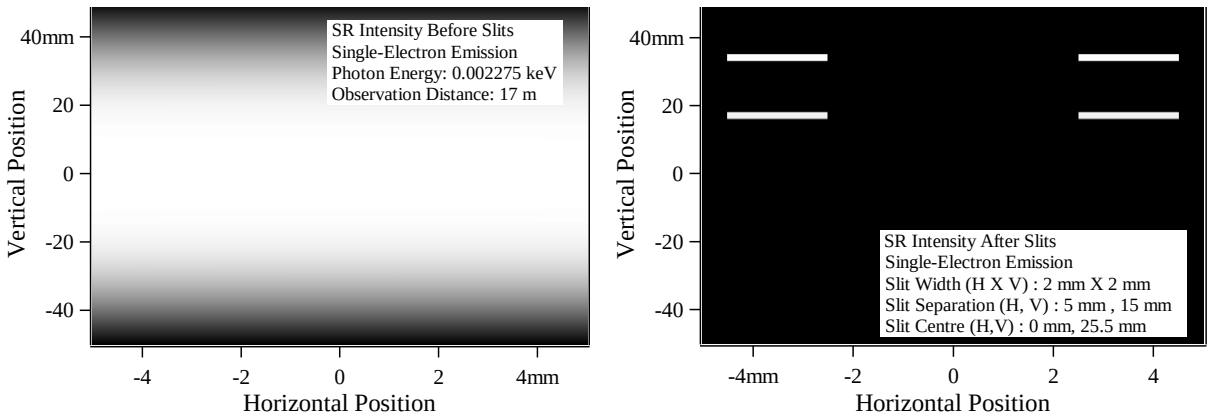

Figure 5.11: *SR intensity (at 545 nm) just before (left) and after (right) interferometer slits at 17 m from the source point in Indus-2.*

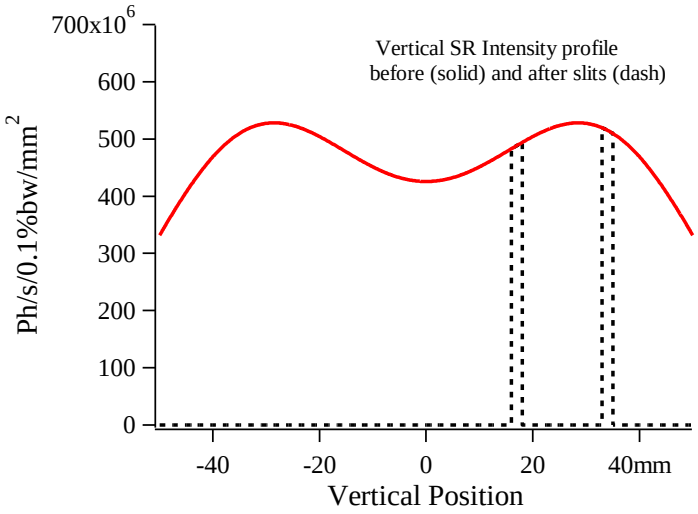

Figure 5.12: *SR intensity before and after SRI slits at 17 m from the source point.*

Two dimensional interference patterns with a slit width of 2 mm and beam emittance of 60 nm rad for point source and finite size source are shown in Figure 5.13. The horizontal and vertical separations between the slits are 5 mm and 15 mm respectively.

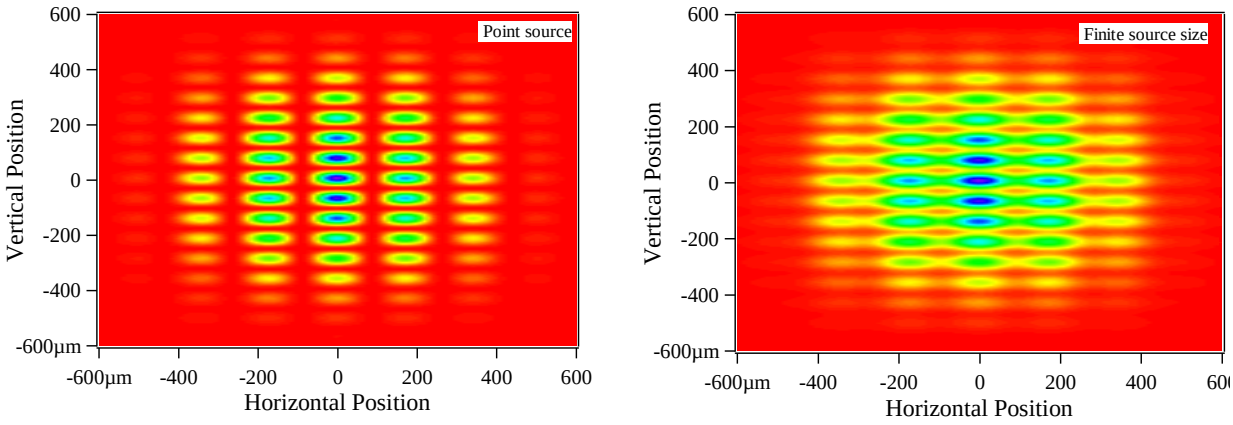

Figure 5.13: *Typical image of simulated interferogram for a point source (left) and for finite source size (right) of Indus-2 beam.*

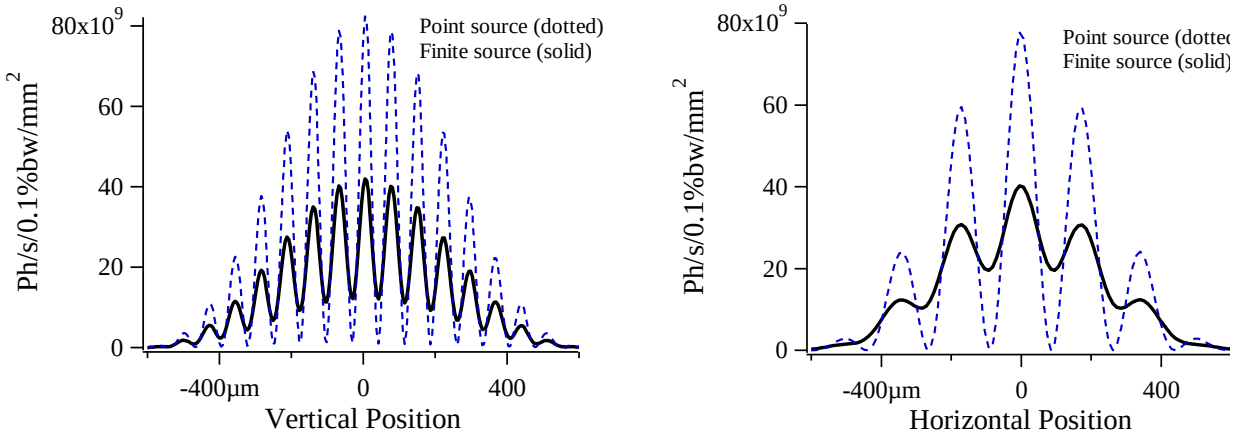

Figure 5.14: *Comparison of simulated intensity profiles for point source and for finite source size in the vertical plane (left) and horizontal plane (right).*

The comparison of simulated intensity profiles for point source and for finite size source in the vertical plane and horizontal plane are shown in Figure 5.14. To fit the horizontal and vertical intensity profiles obtained with SRW, image processing is done in MATLAB [138] (Appendix C). Fit parameters from image processing are useful to check that information inscribed in the interferogram is closely matching with the system design information.

The effect of slit separation variation was also analyzed. Typical SRW simulated interferogram for vertical slit separation of (a) 12 mm (b) 15 mm (c) 20 mm , and (d) 28 mm at 60 nm.rad beam emittance and 100 mA beam current are shown in Figure 5.15. Corresponding vertical and horizontal intensity profiles are shown in Figure 5.16 and Figure 5.17 respectively. Results of fit parameters show that horizontal and vertical beam size are 282 ±3 microns and 66 ± 2 micron respectively (Table 5.2). Plots of horizontal and vertical fit for 25 mm slit separation are shown in Figure 5.18**.** Similarly simulations were done at various beam currents ranging from 30 mA to 200 mA with Indus-2 parameters. Obtained

interferogram were image processed to find consistency in the visibility values. This analysis will be useful in beam size measurement at different beam currents

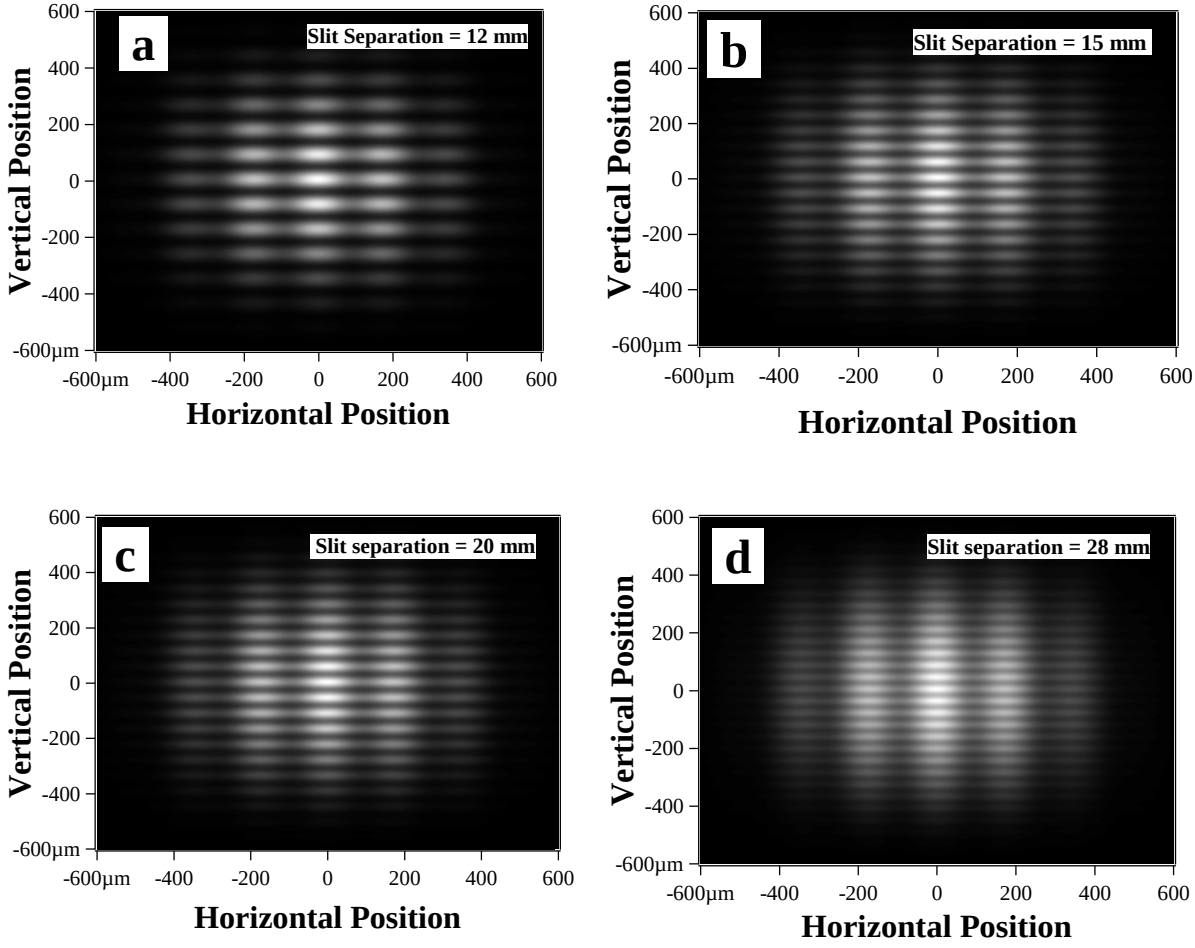

Figure 5.15: *Typical SRW simulated interferogram at 60 nm.rad beam emittance and 100 mA beam current for slit separation of (a) 12 mm (b) 15 mm (c) 20 mm, and (d) 28 mm.*

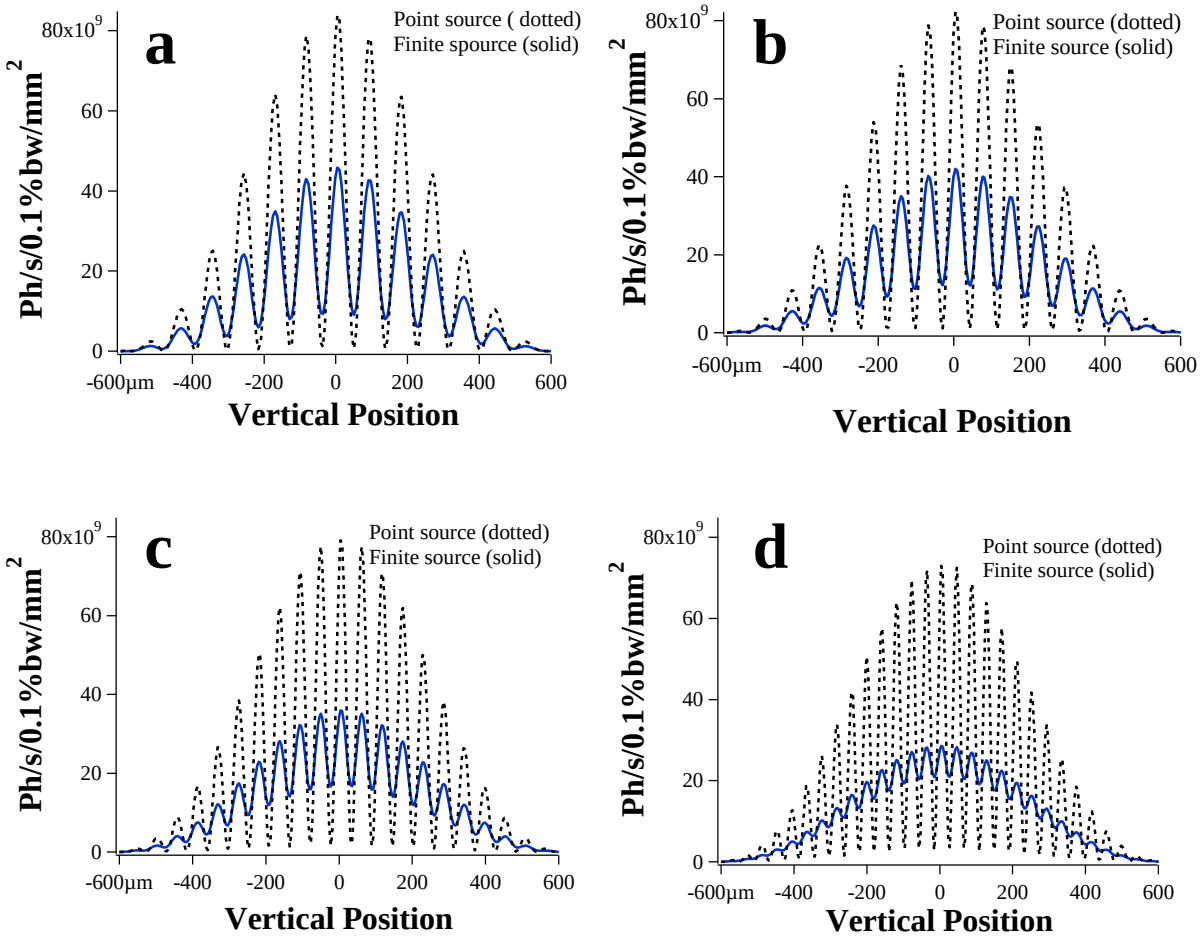

Figure 5.16: *Vertical intensity profiles of SRW simulated interferogram at 60 nm.rad beam emittance and 100 mA beam current at slit separation of (a) 12 mm (b) 15 mm (c) 20 mm, and (d) 28 mm.*

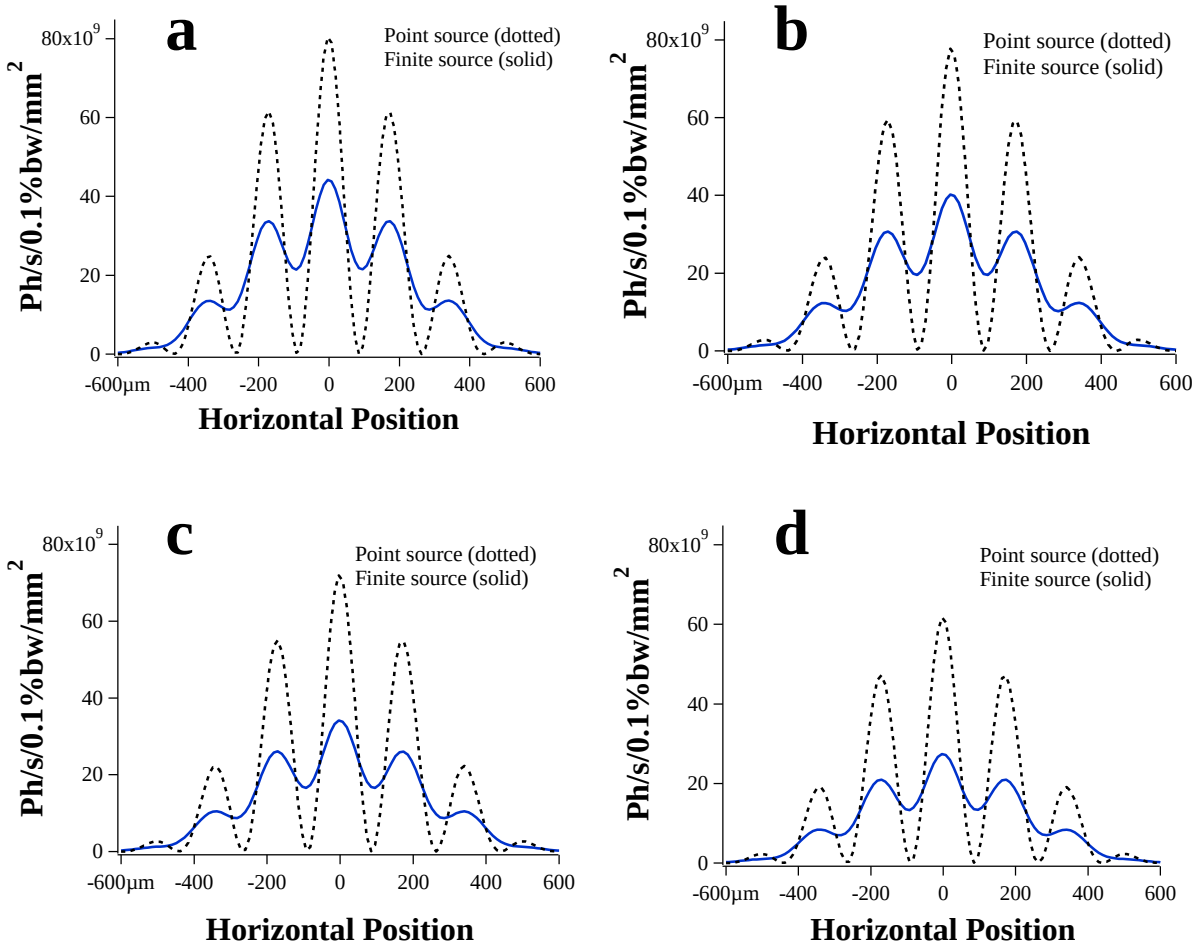

Figure 5.17: *Horizontal intensity profiles of SRW simulated interferogram at 60 nm.rad beam emittance and 100 mA beam current at vertical slit separation of (a) 12 mm (b) 15 mm (c) 20 mm, and (d) 28 mm.*

Table 5.2: *Fit parameters obtained from image processing of various interferogram*

	Slit separation (d_H, d_V) (*mm*).	a_1	a_2	a_3	a_4	a_5	a_6	Beam size (*microns*)
		Mean	Mean	Mean	Mean	Mean	Mean	
Horizontal profile	5, 12	0.7584	-0.03	-0.03	0.3421	0.196	0.201	284.8
	5, 15	0.7461	0.0316	0	0.3553	0.198	0.003	279.7
	5, 20	0.7488	0.0234	0	0.3469	-0.152	-0.029	283.0
	5, 25	0.7529	-0.023	0	0.3445	0.152	0.021	283.9
	5, 28	0.7547	-0.03	0	0.3425	-0.196	0.002	284.7
Vertical profile	5, 12	0.583	0.0313	0.0072	0.7288	0.4168	0.092	64.4
	5, 15	0.643	0.031	0.0144	0.5808	0.5113	0.2115	67.6
	5, 20	0.728	0.0239	0	0.3901	0.5057	-0.052	66.7
	5, 25	0.8172	0.0242	0.0135	0.2391	0.6214	0.2292	65.8
	5, 28	0.8682	0.0307	0.0137	0.1648	0.8931	0.2757	65.9

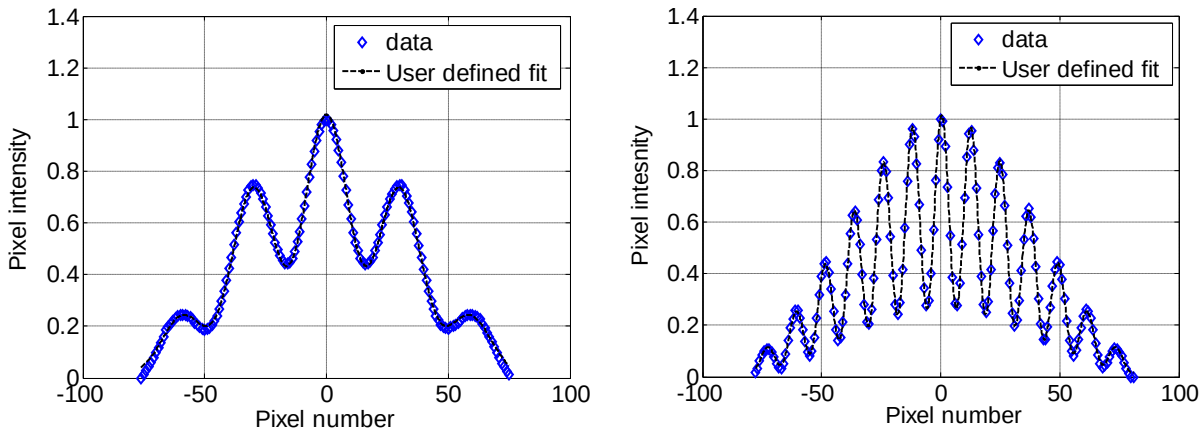

Figure 5.18: *Plots showing data and corresponding fit for horizontal (left) and vertical (right) profiles at slit separation (d_V) of 25 mm*

5.7 Practical issues and circular pinhole in SRI diagnostics

Refractive optical elements (lenses) cause dispersion errors, and results in a significant blurring of the interferogram. Recently this issue was addressed by using reflective Herschelian optics [96] and beam sizes down to 4 µm was measured.

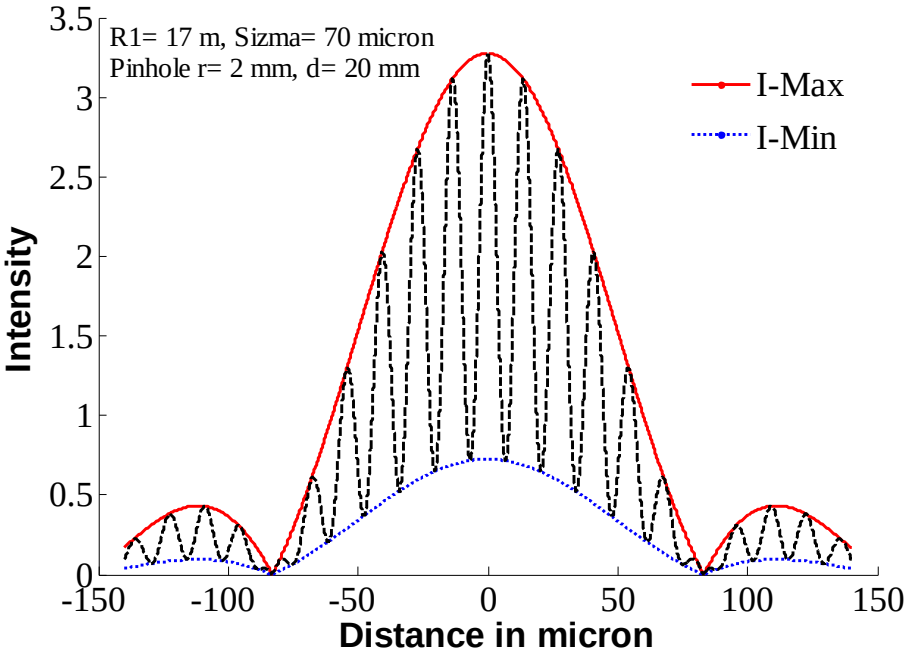

Figure 5.19: *Interferogram with 2 mm radius pinholes separated by 20 mm at 17 m from source*

The footprint of the SR light reaching in dark room is affected by Fraunhofer diffraction due to the horizontal and vertical cuts by the light extraction system (mirror) in the beamline. Long rectangular slits of SRI causes the selection of a large number of Fraunhofer fringes. The relative phase of these fringes is not necessarily the same and this leads to modification in the interferogram, which ultimately causes a loss of contrast. A solution to

this problem was found by using pinholes instead of slits [95]. Pinholes are easy to align as compared to slits, and it also allows selecting more uniform zones of the SR footprint.

The overall envelope of the interferogram is a function (Fourier transform) of the shape of the aperture generating the interference. Now, if pinholes are used rather than slits, it will become a Bessel function of the first type J_1 and the formula for the interferogram becomes [95] [161]

$$I(x) = I_0 \left\{ \frac{J_1\left(\frac{2\pi\, r_H}{\lambda f} x + \emptyset\right)}{\left(\frac{2\pi\, r_H}{\lambda f} x + \emptyset\right)} \right\}^2 \left[1 + |\gamma_x| \cos\left(\frac{2\pi\, d_H}{\lambda f} x + \psi\right)\right] \tag{5.54}$$

Where I_0 is the intensity of the interferogram, r_H is the pinhole radius, f is the focal distance of the optical system used, λ is the radiation wavelength, V_x is the visibility and d_H is the distance between the pinhole centers. Interferogram with 2 mm radius pinholes separated by 20 mm at 17 m from source is shown in Figure 5.19. In SRI, even full reconstruction of spatial beam profile can also be done by selecting pinholes on rotating translation stage [95].

5.8 Summary and conclusions

Presently pinhole array system is used for the measurement of beam size, beam emittance and photon beam position in Indus-2 SRS. Pinhole system with 20 micron diameter has a spatial resolution of 15-20 micron. Now with the increasing requirement for higher brightness at user beamlines, beam emittance of source is reduced. So there is a strong requirement of measuring system with spatial resolution of few microns. It is proposed to upgrade V-DBL (BL-23) by including SRI.

In this thesis work, various design parameters for proposed double-slit SRI at V-DBL were optimized. A quad slit SRI system was optimized to measure beam sizes in both the planes. Design of SRI system was simulated by using SRW code, and visibility analysis of interferogram was carried by horizontal and vertical curve fittings in MATLAB. This work will be used for measuring very small beam sizes (few tens of microns) during low emittance operations of Indus-2, and for future high brightness SRS facilities. Even full reconstruction of the transverse beam shape is also possible by using rotating pinholes in SRI. This technique also provides the possibility of bunch resolved measurement with detector gating, which is useful for studies related to injection dynamics, intra beam scattering and transverse instabilities. Applicability range of SRI technique can be further enhanced by incorporating few changes in optics, slit design and image processing methods.

Chapter 6 Conclusions

6.1 Summary of the research work

This thesis deals with the design and development of SR based diagnostics, and measurement of Indus-2 SRS beam parameters. Literature survey of the existing diagnostic schemes was carried out for design and development of SR based diagnostics at Indus-2. X-ray diagnostic techniques are classified on the basis of focusing methods, viz. reflection, refraction and diffraction. The choice of any technique depends upon the requirement of spatial resolution, dynamic range for beam position shift and signal strength (beam current). Based on these studies, two diagnostic beamlines, viz. visible diagnostic beamline (V-DBL, BL-23) and X-ray diagnostic beamline (X-DBL, BL-24) have been designed, developed and commissioned at the Indus-2 SRS [26]. These beamlines are used regularly for the measurement of beam parameters such as beam size, beam emittance, beam position, bunch length, bunch separation and bunch fill pattern. Measured beam parameters are continuously displayed in the Indus control room. Diagnostic beamlines are also used for beam parameter measurements during dedicated beam physics experiments for smooth operation and performance enhancement.

X-DBL is based on pinhole array imaging and is used to measure beam size, beam divergence, beam emittance and beam position. In our design, pinhole assembly is installed

inside the front end of the beamline, and beam imaging is carried out outside the Indus-2 tunnel in a lead shielded hutch. Size of the pinhole (~ 20 μm) and pitch (~ 1mm) are optimized based on minimization of spread functions and requirement of divergence measurements under various dynamic conditions. Pinhole system provides good spatial resolution (~ 15 μm) for wide range of beam movement and beam currents, which was very much required at the initial stages for operation and optimization of any SRS. In our design, a staggered pair blade monitor (SPM) is also installed in parallel to the pinhole array for measurement of photon beam position at 8 m from the source point.

V-DBL design is based on water cooled primary mirror, which is used to extract the visible light from wide SR spectrum. The extracted light is focused at the detectors kept in the dark room (~20 m away from the source). Measurement of beam parameters such as bunch length, bunch separation and bunch filling pattern are performed by using streak camera, fast photo receiver and avalanche photodiode. V-DBL provides information about longitudinal beam parameters even during the beam injection. Optimization of angular acceptance (~7 mrad) and spread function of V-DBL beamline is carried out using SR calculation code SPECTRA [128]. Visible diagnostics has immense scope for fast measurements as most of the available detectors are in this spectral range.

Studies of longitudinal profile of electron bunch and impedance measurement of Indus-2 SRS were carried out by using dual sweep synchroscan streak camera at V-DBL [32]. The longitudinal profile of electron bunch is analyzed in a single bunch mode. The effects of wakefield generated interactions between the circulating electrons and the surrounding vacuum chamber were analyzed in terms of the measured effects on longitudinal

beam distribution. The equilibrium charge distribution of a bunch was analysed by using solutions of the Haissinski equation. The major factors influencing the bunch lengthening, potential-well distortion and microwave instability were also analysed. The impedance of the Indus-2 ring was obtained from the measured bunch lengthening with different impedance models. The impedance of storage ring obtained by a series R+L impedance model predicts the values of resistance and inductance as1350 ± 125 Ω and180 ± 25 nH respectively. These results are also compared with the values obtained from the measured synchronous phase advancing and scaling laws. These studies provide very useful inputs for calculating various thresholds of beam instabilities. Bunch length measurements at Indus-1 storage ring were performed by using fast photo receiver system. Results of the measurements at different RF voltage and beam currents were also discussed. The longitudinal broadband impedance of Indus-1 storage ring was estimated ~ 49.0 Ω by using Keil-Schnell criterions [33].

Transverse measurement related to beam size, beam emittance, beam position, photon beam position, and beam dispersion at source point were carried out at X-DBL. Modified theoretical equations for online measurements of the source position and emission angle with pinhole array optics were also discussed. Results of online measurement were compared with the measurements at an independent x-ray beam position monitor (SPM) installed in the X-DBL. Measured values from both systems were found to be within ± 12 μm (or $\pm$ 1.5 μrad) for sufficiently wide range of beam movements [26]. Results of experimental measurement of beam dispersion (0.253 m (H), 0.0325 m (V)) by changing frequency of RF cavity were also discussed. Measurement results of beam position, beam size and beam emittance with natural

decay of beam current in Indus-2 are presented. At 2.5 GeV, natural horizontal and vertical beam sizes at the BL-24 source point are 357.2 μm and 47.6 μm respectively. Measurement results of beam size during the trial operations of Indus-2 in low emittance mode (~ 45 nm rad) were also discussed [5].

Design study of synchrotron radiation interferometer was carried for beam diagnostics of Indus-2 [34]. Nowadays, SRI is being used in many advanced SRS. It is based on Van Cittert-Zernike theorem relating transverse source profile to spatial coherence, and the particle beam size can be inferred from the fringe contrast. A quad slit system was optimized to measure the beam size in both planes. Results of simulation of this SRI system using the SRW code [42] and the visibility analysis of interferogram by horizontal and vertical curve fitting in MATLAB were also presented. By using SRI, transversal beam sizes down to few microns can be measured. Transverse emittance can also be evaluated from the measured beam size by using known optics (Twiss) parameters of the source point. Even full reconstruction of beam profile under different beam couplings is possible by rotating double-pinhole mask [95]. This work will be useful for measuring very small beam sizes (few microns to tens of micron) during low emittance operations of Indus-2 SRS, and for future high brightness SRSs in India.

6.2 Outlook and Perspective

The results presented on the development of SR based diagnostics at Indus-2 SRS forms an important basis for the future work in this field. There are few limitations that need to be addressed for effective utilization of the developed system. There is scope for including fast

phosphors for better temporal measurements (less than ns) in x-ray diagnostics. It can be used for beam dynamic studies related to bunch-by-bunch measurements even during beam injection (for top-up machines). With the advancement of technology in basic research, the demand for high brightness (SR beam) has been increasing steadily. To meet this requirement, advanced SRS facilities are being designed to keep the beam emittance low i.e. few pm.rad. The measurement of these beam sizes of the order of few microns is a challenging task, and advanced x-ray optics such as Fresnel zone plate, compound refractive lens, KB optics etc can also be incorporated for high spatial resolution measurements.

Visible diagnostics has a major challenge due to weak signal of visible light (typically less than 1 mW) in the wide SR fan. Further a large part of this light is lost during multiple reflections, refractions and absorptions in the lengthy optics. Effective signal at the measurement detector can be increased by incorporating advanced designs of primary mirrors and lesser number of optics elements. SR interferometer can be used to overcome the spatial resolution limitation (due to diffraction) of visible light, and beam size down to few microns can be measured. Visible diagnostics have a huge potential in beam measurements as most of the fast detectors are available in this spectral range. System like time correlated single photon counting (TCSPC) [140] can be used for controlled filling of selected bunches or uniform filling (or in top-up mode) of SRS. Studies related to impedance measurements can be further extended for analysis of various beam instabilities especially during passage of beam through narrow insertion device chambers. SRS operation in low alpha mode can fulfil user's requirement of ultra short light pulses. Longitudinal measurements related to low alpha

experiments can also be performed by using fast detectors or measurement in the frequency domain with visible diagnostics [165][166].

REFERENCES

[1] R.P. Walker, "Overview of Synchrotron Radiation and Free Electron Laser Projects," in *6th European Particle Accelerator Conf. (EPAC'98)*, Stockholm, Sweden, Jun. 1998, 1998, pp. 133-137.

[2] M. Cornacchia and H. Winick, SLAC-PUB-5164, 1990.

[3] http://www.rrcat.gov.in/technology/accel/indus2.html.

[4] A.D. Ghodke, Riyasat Husain, Pradeep Kumar, S. Yadav, and T.A. Puntambekar, *Rev. Sci. Instrum.*, vol. 83, p. 103303, 2012.

[5] A.A. Fakhri, P. Kant, A.D. Ghodke, and G. Singh, *Rev. Sci. Instrum.*, vol. 86, 2015.

[6] H. Widemann, *Particle Accelerator Physics*. Berlin , Heidelberg: Springer, 1993.

[7] A.W. Chao, *Physics of collective beam instabilities in high energy accelerators*. New York: John Wiley & Sons Inc., 1993.

[8] M. Ferianis, "Optical Techniques in Beam Diagnostics," in *Proc. of 6th European Particle Accelerator Conf. (EPAC'98)*, Stockholm, Sweden, 1998, pp. 159-163.

[9] S. Takano, "Beam Diagnostics with Synchrotron Radiation in Light Sources," in *Proc. of IPAC'10*, Kyoto, Japan, 2010, pp. 2392-2396.

[10] I. Frank and V. Ginzburg, "J. Phys. USSR," vol. 9, p. 363, 1945.

[11] L. Wartski, PhD Thesis, Univ. De Paris-Sud, centre d'Orsay, 1976.

[12] D. Rule, R.B. Fiorito, and W.D. Kimura, in *Proceedings of BIW '96*, Argonne, 1996.

[13] G. Kube, "Review of Synchrotron Radiation based Diagnostics for Transverse Profile Measurements," in *Proc. of DIPAC'07*, Venice, Italy, 2007, pp. 6-10.

[14] ESRF. [Online]. http://www.esrf.eu

[15] J. Breunlin, A. Andersson, N. Milas, and Á. Saá Hernán, *Nucl. Instrum. Methods Phys. Res. A*, vol. 803, p. 55, 2015.

[16] H. Sakai, M. Fujisawa, K. Iida, I. Ito, H. Kudo, N. Nakamura, K. Shinoe, T. Tanaka, *Phys. Rev. ST Accel. Beams*, vol. 10, p. 042801, 2007.

[17] G. Kube, J. Gonschior, U. Hahn, P. Ilinski, G. Priebe, H. Schulte-Schrepping, Ch. Wiebers, S. Weisse, C.G. Schroer, "PETRA III Diagnostics Beamline for Emittance Measurements," in *Proc. 1st Int. Particle Accelerator Conf. IPAC'10*, Kyoto, Japan, 2010, pp. 909-911.

[18] P. Kirkpatrick and A.V. Baez, *Journal of the Optical Society of America*, vol. 38, p. 766, 1948.

[19] R.C.C. Perera, M.E. Melczer, A. Warwick, A. Jackson, and B.M. Kincaid, *Rev. Sci. Instrum.*, vol. 63, p. 541, 1992.

[20] T.R. Renner, H.A. Padmore, and R. Keller, *Rev. Sci. Instrum.*, vol. 67, p. 3368, 1996.

[21] Cyrille Thomas, Guenther Rehm, Ian Martin, and Riccardo Bartolini, *Phys. Rev. ST Accel. Beams*, vol. 13, p. 022805, 2010.

[22] L. Yong-Bin, H. Guo-Qing, Z. Man-Zhou, C. Zhi-Chu, C. Jie, Y. Kai-Rong, *Chinese Physics C*, vol. 36, p. 80, 2012.

[23] Dechong Zhu, Jianshe Cao, Jie Chen, Yanfeng Sui, and Junhui Yue, "Beam Profile Measurement Using Kirkpatrick Baez Mirror Optics at Shanghai Synchrotron Radiation Facility," in *Proceedings of. IPAC'16*, Busan, Korea, 2016, pp. 167-171.

[24] T. Mitsuhashi, "Spatial Coherency of the Synchrotron Radiation at the Visible Light Region and its Application for the Electron Beam Profile Measurement," in *Proc. of PAC'97*, vol. 1, Vancouver, B.C., Canada, 1997, pp. 766-768.

[25] A. Andersson, M. Boege, V. Schlott, A. Streun, and A. Ludeke, *Nucl. Instrum. Methods Phys. Res. A* , vol. 591, p. 437 , 2008.

[26] Akash Deep Garg, A.K. Karnewar, A. Ojha, B.B. Shrivastava, A.C. Holikatti, T.A. Puntambekar, C.P. Navathe, *Nucl. Instrum. Methods Phys. Res. A*, vol. 754, p. 15, 2014.

[27] A. Ojha, Akash Deep Garg, A.K. Karnewar, A.C. Holikatti, B.B. Shrivastava, T.A. Puntambekar, C.P. Navathe, in *Proceedings of Indian Particle Accelerator Conference (InPAC-2013)*, VECC, Kolkata, India, 2013.

[28] B.B. Shrivastava, A.C. Holikatti, A. Ojha, A.D. Garg, A K. Karnewar, B.B. Sonawane, M. Chauhan, H.T. Satyawan, T.A. Puntambekar, and C.P. Navathe, in *Proceedings of Indian Particle Accelerator Conference (InPAC-2013)*, VECC, Kolkata, India, 2013.

[29] Optronis streak camera. [Online]. http://www.optronis.com/de/home.html

[30] L. Torino and U. Iriso, "Beam Shape Reconstruction Using Synchrotron Radiation Interferometry," in *in Proc. 5th Int. Beam Instrumentation Conf. (IBIC'16)*, Barcelona, Spain, 2016, pp. 589-592.

[31] S.T. Wang, R. Holtzapple, and D.L. Rubin, *Nucl. Instrum. Methods Phys. Res. A*, vol. 847, p. 34, 2017.

[32] Akash Deep Garg, S. Yadav, M. Kumar, B.B. Shrivastava, A. Ojha, T.A. Puntambekar, *Nucl. Instrum. Methods Phys. Res. A*, vol. 814, p. 66, 2016.

[33] Akash Deep Garg, R.K. Nathwani, A.C. Holikatti, A.K. Karnewar, Y. Tyagi, S. Yadav, T.A. Puntambekar, C.P. Navathe, *Rev. Sci. Instrum.*, vol. 83, p. 113304, 2012.

[34] Akash Deep Garg, M.H. Modi, and T.A. Puntambekar, *Nucl. Instrum. Methods Phys. Res. A*, vol. 902, p. 164, 2018.

[35] V-DBL. [Online]. http://www.rrcat.gov.in/technology/accel/srul/beamlines/visible_diag_beam.html

[36] J. Haissinski, *Nuovo Cimento*, vol. 18, p. 72, 1973.

[37] B.W. Zotter and W. Bruno, CERN Report CERN- SL/AP 90-115, 1990.

[38] B. Zotter, CERN Report SPS/81-14 , 1981.

[39] T. Mitsuhashi, *Proc. of the Joint US–CERN–Japan–Russia School on Particle Accelerators*. Montreux and Geneva, Switzerland: World Scientific, 1998.

[40] P.H. Van Cittert, *Physica*, vol. 1, p. 2001, 1934.

[41] F. Zernike, *Physica*, vol. 5, p. 785, 1938.

[42] O. Chubar and P. Elleaume, "Accurate and Efficient Computation of Synchrotron Radiation in the Near Field Region," in *Proceedings of the EPAC'98*, Stockholm, Sweden, 1998.

[43] CERN. Geneva. CERN Accelerator School, "CAS - CERN Accelerator School : Synchrotron Radiation and Free Electron Lasers," Grenoble, France, 10.5170/CERN-1998-004, 1996.

[44] Gianluca Geloni, Vitali Kocharyan, and Evgen Saldin, "Brightness of synchrotron radiation from undulatators and bending magnets," *J. Synchrotron Rad.*, vol. 22, pp. 288–316, 2015.

[45] H. Winick, *Synchrotron Radiation Research.*: Plenum Press, 1980, ch. 2.

[46] A. Hofmann, "Physics Reports," 64:253, 1980.

[47] S.L. Hulbert and G.P. Williams, *Handbook of Optics, Synchrotron Radiation Surces*. New York: National Synchrotron Light Source Brookhaven National Laboratory Upton, vol. Chapter 32, www.digitalengineeringlibrary.com.

[48] *X-ray Data Booklet*. Berkeley, CA: Lawrence Berkeley national Lab. Univ. of California, 2009.

[49] H. Winick, *Journal of Synchrotron radiation*, vol. 5, pp. 168-175, 1998.

[50] Herman Winick, "Fourth Generation Light Sources," in *Proc. of the 1997 Particle Accelerator Conference*, Vancouver, BC, Canada, 1997, pp. 37-41.

[51] I. Ben-Zvi, "The 300 mA SRF ERL," in *Workshop to Explore Physics Opportunities with Intense, Polarized Electron Beams Up to 300 MeV*, Cambridge, MA, 2013.

[52] M. Cornacchia, SLAC Pub 7433, 1997.

[53] D.D. Bhawalkar, G. Singh, and R. V. Nandedkar, "Synchrotron radiation sources Indus-1 and Indus-2," *PRAMANA Journal of Physics*, vol. 50, no. 6, pp. 467-484, june 1998.

[54] A.D. Ghodke, D. Angal-Kalinin, and A. Banerjee, "Staus of Indus-1 Synchrotron Radiation Source," in *Proc. 2nd Asian Particle Accelerator Conf. (APAC'01)*, Beijing, China, 2001.

[55] G. Singh, G.K. Sahoo, D. Angal, Beni Singh, A.D. Ghodke, P. Kant, *Indian Journal of Pure and Applied Physics*, vol. 35, pp. 183-192, 1997.

[56] [Online]. http://www.rrcat.gov.in/technology/accel/isrf_index.html#

[57] V.C. Sahani, "Commissioning of the Indus-2 Storage Ring," in *Proc. 4th Asian Particle Accelerator Conf. (APAC'07)*, Indore, India, 2007, pp. 61-65.

[58] S.K. Deb, G. Singh, and P.D. Gupta, "Indus-2 Synchrotron Radiation Source: current status and utilization," *J. Phys. : Conf. Ser.*, vol. 425 , no. 072009, 2013.

[59] P.A. Naik, "Accelerator activities at Raja Ramanna Centre for Advanced Technology," in *Proc. of the eighth DAE-BRNS Indian particle accelerator conference*, vol. 49, Raja Ramanna Centre for Advanced Technology, Indore (India), 2018.

[60] A.K. Sinha, Archna Sagdeo, Pooja Gupta, Anuj Upadhyay, Ashok Kumar, M.N. Singh, R.K. Gupta, S.R. Kane, A. Verma, and S.K Deb, "Angle Dispersive X-ray Diffraction Beamline on Indus-2 Synchrotron Radiation Source: Commissioning and First

Results," *J.Phys. : Conf Ser*, vol. 425, no. 072017, 2013.

[61] M.K. Tiwari, S.R. Kane, A.K. Sinha, C.K. Garg, A.K. Singh, P. PGupta, S.R. Garg, G.S. Lodha, S.K. Deb, "A microprobe-XRF Beamline on Indus-2 Synchrotron Light Source," *J.Phys.: Conf. Ser.*, vol. 425, no. 072020, 2013.

[62] M.H. Modi, R K. Gupta, S.R. Kane, V. Prasad, C.K. Garg, P. Yadav, V.K. Raghuvanshi, Amol Singh, Mangalika Sinha, "A soft x-ray reflectivity beamline for 100-1500 eV energy range at Indus-2 synchrotron radiation source," in *AIP Conference Proceedings*, vol. 2054, 060022, 2019.

[63] V.P. Dhamgaye, B. Gowri Sankar, C.K. Garg, and G.S. Lodha, "Commissioning of soft and deep X-ray lithography beamline on Indus-2," in *AIP Conference Proceedings*, vol. 1447 Issue 1, pp. 527-528.

[64] V.P. Dhamgaye and G.S. Lodha, "Fabrication of compound refractive lens using soft and deep X-ray lithography beamline on Indus-2," in *AIP Conference Proceedings*, vol. 1447 Issue 1, 2012, p. 525.

[65] [Online]. http://www.rrcat.gov.in/technology/accel/srul/beamlines/index.html

[66] [Online]. http://www.rrcat.gov.in/technology/accel/indus/index.html

[67] H. Wiedemann, *Particle Accelerator Physics*. Berlin : Springer, 2007.

[68] A. Hofmann, CERN Accelerator School on SR and FEL , 1989.

[69] Mathew Sands, SLAC, SLAC- 121 UC-28 (ACC), 1970.

[70] H. Wiedemann, *Synchrotron Radiation*. Berlin: Springer, 2002.

[71] L. Wartski, Universite de Paris Sud, Centre d'Orsay, Doctoral Thesis 1976.

[72] A. Hofmann, "Diagnostics with synchrotron radiation," CERN, CERN 98-04, 1998.

[73] [Online]. http://xdb.lbl.gov/Section4/Sec_4-4.html

[74] Zone plates. [Online]. http://zoneplate.lbl.gov/theory

[75] D. Attwood, *Soft X-rays and Extreme Ultaviolet Radiation: Principles and Applications*.: Cambridge University Press, 1999.

[76] S. Takano, M. Masaki, and H. Ohkuma, "The X-Ray Beam Imager for Transversal Profiling of Low-Emittance Electron Beam at the SPring-8," in *Proc. 7th European Workshop on Beam Diagnostics and Instrumentation for Particle Accelerators*

(DIPAC'05), Lyon, France, 2005, p. 241.

[77] S. Takano, M. Masaki, and H. Ohkuma, *Nucl. Instrum. Meth. Phys. Res. A*, vol. 556, p. 357, 2006.

[78] H. Sakai et al., "Operation of the Opposite-Field Septum Magnet for the J-PARC Main-Ring Injection," in *Proc. 10th European Particle Accelerator Conf. (EPAC'06)*, Edinburgh, Scotland, 2006, p. 2784.

[79] Ya. Hartmann et al., *Rev. Sci. Instrum.*, vol. 66, p. 1978, 1995.

[80] Christian Morawe and Markus Osterhoff, *X-Ray Optics and Instrumentation*, vol. 2010, p. 479631, 2010.

[81] Jung-Yun Huang, Dong K. Seon, In-Soo Ko, and Tae-Yeon Lee, "Beam Studies in Diagnostic Beamline at PLS," in *Proc. 18th Particle Accelerator Conf. (PAC'99)*, New York, NY, USA, 1999, p. 2131.

[82] B. Lengeler et al., *J. Synchrotron Rad.*, vol. 6, p. 1153, 1999.

[83] O. Chubar, M. Drakopoulos, F. Guenzler, B. Lengeler, C. Schroer, A. Snigirev, I. Snigireva, T. Weitkamp, "Electron Beam Size and Profile Measurements with Refractive X-Ray Lenses," in *Proc. 7th European Particle Accelerator Conf. (EPAC'00)*, Vienna, Austria, 2000, pp. 1824-1826.

[84] P. Elleaume, C. Fortgang, C. Penel, and E. Tarazona, *J. Synchrotron Rad.*, vol. 2, p. 209, 1995.

[85] J.C. Bergstrom and J.M. Vogt, *Nucl. Instrum. Meth. Phys. Res. A*, vol. 587, p. 441, 2008.

[86] W.B. Peatman and K. Holldack, *Journal of Synchrotron Radiation*, vol. 5, p. 639, 1998.

[87] K. Holldack et al., *Nucl. Instrum. Meth. Phys. Res. A* , vol. 467, p. 235, 2001.

[88] F. Sannibale et al., "Commissioning of BL 7.2, the New Diagnostic Beamline at the ALS," in *Proc. 9th European Particle Accelerator Conf. (EPAC'04)*, Lucerne, Switzerland, 2004, p. 783.

[89] I. Pinayev, "Evaluation of Pinhole Camera Resolution for NSLS-II Storage Ring," in *Proc. 13th Beam Instrumentation Workshop (BIW'08)*, Lake Tahoe, CA, USA, 2008, pp. 270-273.

[90] M.J. Boland, R.T. Dowd, G. LeBlanc, M.J. Spencer, Y.E. Tan, A. Walsh, "X-ray and Optical Diagnostic Beamlines at the Australian Synchrotron Storage Ring," in *Proc. 10th European Particle Accelerator Conf. (EPAC'06)*, Edinburgh, UK, 2006, p. 3263.

[91] G. LeBlanc, J.C. Bergstrom, M.J. Boland, and R.T. Dowd et al., "Measurements using the X-Ray and Optical Diagnostic Beamlines at the Australian Synchrotron," in *in Proc. APAC'07*, Indore, India, 2007, pp. 407-409.

[92] K.B. Scheidt, "Measurement of Vertical Emittance with a system of Six -In-Air-X-Ray-Projection Monitors at the ESRF", in , , May 2007, paper , pp.," in *Proc. 8th European Workshop on Beam Diagnostics and Instrumentation for Particle Accelerators (DIPAC'07)*, Venice, Italy, 2007, pp. 72-74.

[93] A.S. M¨uller, I. Birkel, E. Huttel, K.B. Scheidt, and P. Wesolowski, "Precise Measurements of the Vertical Beam Size in the ANKA Storage Ring with an In-air X-ray Detector," in *Proc. 10th European Particle Accelerator Conf. (EPAC'06)*, Edinburgh, UK, 2006, p. 1073.

[94] M. Masaki and S. Takano, *J. Synch. Rad.*, vol. 10, p. 295, 2003.

[95] L. Torino and U. Iriso, *Phys. Rev. ST Accel. Beams*, vol. 19, p. 122801, 2016.

[96] T. Naito and T. Mitsuhashi, *Phys. Rev. ST Accel. Beams*, vol. 9, p. 122802, 2006.

[97] M.J. Boland, T. Mitsuhashi, T. Naito, and K.P. Wooten, "Intensity Imbalance Optical Interferometer Beam Size Monitor," in *Proc. 1st Int. Beam Instrumentation Conf. (IBIC'12)*, Tsukuba, Japan, 2012, pp. 566-570.

[98] G. Trad, E. Bravin, A. Goldblatt, S. Mazzoni, F. Roncarolo, T.M. Mitsuhashi, "Beam Size Measurements Using Interferometry at LHC," in *in Proc. 5th Int. Beam Instrumentation Conf. (IBIC'16)*, Barcelona, Spain, pp. 583-588.

[99] G. Kube, *Book on Particle beam diagnostics and control*. DESY Hamburg, Germany.

[100] E. Rossa, *Opt. Engineering*, vol. 34, p. 2353, Aug. 1995.

[101] [Online]. https://www.hamamatsu.com/

[102] K. Scheidt, "Dual Streak Camera at the ESRF," in *Proc. 5th European Particle Accelerator Conf. (EPAC'96)*, Sitges, Spain, 1996.

[103] A. Fisher et al., "Streak Camera Measurements of the PEP-2 High Energy Ring," in *Proc. of BIW '98*, Stanford, 1998, p. 471.

[104] T. Watanabe et al., *Nucl. Instr. and Meth. A*, vol. 480, p. 315, 2002.

[105] K. Kinoshita et al., *Rev. Sci. Instrum.*, vol. 58, p. 932, 1987.

[106] [Online]. https://www.hamamatsu.com/resources/pdf/sys/SHSS0022E_FESCA-100.pdf

[107] M. Uesaka et al., *Nucl. Instr. and Meth. A*, vol. 406, p. 371, 1998.

[108] Tektronix 11801A sampling scope - 50 Ghz head. [Online]. https://www.tek.com

[109] New Focus Inc. Santa Clara (CA) USA. [Online]. https://www.newport.com/b/new-focus

[110] M. Ferianis, "The ELETTRA Streak Camera: System Set-Up and First Results," in *Proc. 4th European Workshop on Beam Diagnostics and Instrumentation for Particle Accelerators (DIPAC'99)*, Chester, UK, 1995, pp. 72-76.

[111] M.S. Zolotorev and G.V. Stupakov, SLAC, SLAC-PUB-7132, 1996.

[112] P. Catravas et al., *Phys. Rev. Lett.*, vol. 82, p. 5261, 1999.

[113] F. Sannibale et al., *Phys. Rev. ST Accel. Beams*, vol. 12, p. 032801, 2009.

[114] O. Grimm, "Coherent Radiation Diagnostics for Short Bunches," in *Proc. 22nd Particle Accelerator Conf. (PAC'07)*, Albuquerque, NM, USA, 2007, pp. 2653-2657.

[115] Chitrlada Settakorn, Michael Hernandez, Kristina Woods, and Helmut Wiedemann, "FEMTOSECOND ELECTRON BUNCHES," in *Proc. 1st Asian Particle Accelerator Conf. (APAC'98)*, Tsukuba, Japan, 1998.

[116] O. Grimm and P. Schm, TESLA-FEL Report 2006-03 2006.

[117] H. L. Andrews and F. Bakkali Taheri et. al., *Phys. Rev. ST Accel. Beams*, vol. 17, p. 052802, 2014.

[118] D.X. Wang et al., *App. Phys. Lett.*, vol. 70(4), p. 529, 1997.

[119] J.W. Corbett, "Injected Beam Dynamics in SPEAR3," in *Proc. 1st Int. Particle Accelerator Conf. (IPAC'10)*, Kyoto, Japan, 2010.

[120] V.L. Ginzburg and V.N. Tsytovich, "Transition Radiation and Transition Scattering," Adam Higler, New York, 1990.

[121] G.M. Garibyan, *Sov. Phys. JETP*, vol. 6, p. 1079, 1958.

[122] A.P. Potylisyn, *Nucl. Instrum. Methods B*, vol. 145, p. 169, 1998.

[123] F. Sakamoto, H Iijima, K. Dobashi, T. Imai, T. Ueda, T. Watanabe, M. Uesaka, *J. Appl. Phys.*, vol. 44, p. 1485, 2005.

[124] L. Wartski et al., *J. Appl. Phys.*, vol. 46, p. 3644, 1975.

[125] G. Kube, TESLA-FEL Report 2008-01 2008.

[126] A.H. Lumpkin, B.X. Yang, W.J. Berg, J.W. Lewellen, N.S. Sereno, U. Happek, *Nucl. Instrum. and Meth. A*, vol. 445, pp. 356-361, 2000.

[127] E. Chiadroni, M. Castellano, A. Cianchi, K. Honkavaara, and G. Kube, "Optical Diffraction Radiation Interferometry as Electron Transverse Diagnostics," in *Proc. 9th European Workshop on Beam Diagnostics and Instrumentation for Particle Accelerators (DIPAC'09)*, Basel, Switzerland, 2009, pp. 151-154.

[128] SPECTRA Code. [Online]. http://spectrax.org/php/download.php?code=spectra

[129] V.K. Raghuvanshi, V.P. Dhamgaye, A.K. Sinha, and R.V. Nandedkar, in *International conference on synchrotron radiation instrumentation*, vol. 879 (1), Daegu, Republic of Korea, 2006.

[130] K. Holldack and W.B. Peatman, Berlin, BESSY Technical Report TB-AS3/96, 1996.

[131] C. Limborg, J. Safranek, and P. Stefan, "A Pinhole Camera for SPEAR 2," in *Proc. 7th European Particle Accelerator Conf. (EPAC'00)*, Vienna, Austria, 2000, p. 1774.

[132] F. Sannibale, D. Baum, K. Holldack, N. Kelez, and T. Scarvie, "A Second Beam-Diagnostic Beamline for the Advanced Light Source," in *Proc. 20th Particle Accelerator Conf. (PAC'03)*, Portland, OR, USA, 2003, pp. 2527-2529.

[133] [Online]. http://henke.lbl.gov/optical_constants

[134] Proxivision. [Online]. https://www.proxivision.de/

[135] Phosphor Technology. [Online]. http://www.phosphor-technology.com/

[136] J.C. Bergstrom and J.M. Vogt, *Nucl. Instrum. Meth. Phys. Res. A*, vol. 562, pp. 495-512, 2006.

[137] Weixing Cheng, "Synchrotron Light Monitor System for NSLS-II," in *Proc. 14th Beam Instrumentation Workshop (BIW'10)*, Santa Fe, NM, USA, 2010, pp. 478-482.

[138] MATLAB. [Online]. https://in.mathworks.com/

[139] V. Schlott, M. Dach, C. David, B. Kalantari, M. Pedrozzi, A. Streun, in *Proceedings of EPAC'04*, Lucerne, Switzerland , 2004, pp. 2526-2528.

[140] Picoquant. [Online]. https://www.picoquant.com/images/uploads/page/files/7253/technote_tcspc.pdf

[141] D.J. Peake, M.J. Boland, G.S. LeBlanc, and R.P. Rassool, *Nucl. Instrum. Methods Phys. Res. A*, vol. 589, p. 143, 2008.

[142] Ophir. [Online]. https://www.ophiropt.com/laser--measurement/beam-profilers

[143] G. Rumolo and M. Munoz, "A study of collective single bunch phenomena in the ALBA ring," ALBA Project Document No. AAD-SR-BD-AN-0050 2005.

[144] R.T. Dowd and M.J. Boland et al., "Measurements of Impedance and Beam Instabilities at the Australian Synchrotron," in *Proc. 22nd Particle Accelerator Conf. (PAC'07)*, Albuquerque, New Mexico, USA, 2007, pp. 3859-3861.

[145] W. Chao and J. Gareyte, *Particle Accelerators*, vol. 25, p. 229, 1990.

[146] K. Bane et al., SLAC-PUB-8846, 2001.

[147] Victor Smaluk et al., "Beam based model of broad-band impedance of the Diamond Light Source," *Physical Review Special Topics - Accelerators and Beams*, vol. 18, p. 064401, 2015.

[148] Joung-Moo Ko, Suk-Min Chung, Eun-San Kim, Chong-Do Park, and Takashi Naito, *Japanese Journal of Applied Physics 1A*, vol. 44, p. 438, 2005.

[149] K. Bane and R. Ruth, SLAC-PUB-4905 , 1989.

[150] K. Bane, K. Oide, and M. Zobov, SLAC-PUB-11007, 2005.

[151] R. Holtzapple, M. Billing, D. Hartill, M. Stedinger, and B. Podobedov:, *Phys. Rev. ST Accel. Beams*, vol. 3, p. 034401, 2000.

[152] H. Winick:, *Synchrotron Radiation Source*.: World Scientific, 1994.

[153] J.A. Clarke, "Bunch Lengthening Thresholds on the Daresbury SRS," IEEE (1996), 1996.

[154] E. Keil and W. Schnell, CERN Internal Report CERN-TH-RF/69-48, 1969.

[155] D. Angal-Kalnin, D.D. Bhawalkar, A.A. Fakhri, A.D. Ghodke, P. Kant, P. Kumar, P.K. Nema, A.S. Raja Rao, B. Singh, G. Singh et al., "Commissioning of the Indus-1 Storage Ring," in *Proc. 7th European Particle Accelerator Conf. (EPAC'00)*, Vienna, Austria, 2000, pp. 687-689.

[156] M.S. Zisman, S. Chattopadhyay, and J.J. Bisognano, ZAP User's Manual LBL-21270, 1986.

[157] Pradeep Kumar, A.D. Ghodke, and G. Singh, *PRAMANA - Journal of physics*, vol. 80, no. 5, pp. 855-871, 2013.

[158] T.D. Milster and N.A. Beaudry, *Coherence and fringe localisation*., 2006, ch. 5, http://optics.hanyang.ac.kr.

[159] A.A. Michelson and F.G. Pease, "Measurement of the diameter of α-Orionis with the interferometer," *Astrophysical Journal*, pp. 249-258, 1921.

[160] J.E. Greivenkamp, *The Handbook of Optics, Vol I*, 3rd ed.: M. Bass, Ed. (McGraw Hill, 2009), 2009, ch. 2, pp. 2.3-2.42.

[161] M. Born and E. Wolf, *Principles of Optics*. New York: Pergamon Press Ltd., 1980.

[162] C.L. Li, Y.H. Xu, M.J. Boland, T. Mitsuhashi, W.J. Zhang, M. Grinberg, J. Corbett, "Double-slit Interferometer Measurements at SPEAR3," in *Proc. 7th Int. Particle Accelerator Conf. (IPAC'16)*, Busan, Korea, 2016, pp. 368-370.

[163] S.T. Wang, D.L. Rubin, J. Conway, M. Palmer, D. Hartill, R. Campbell, R. Holtzapple, *Nucl. Instrum. Methods Phys. Res. A*, vol. 703, p. 80, 2013.

[164] L. Torino and U. Iriso, "Limitations and Solutions of Beam Size Measurements via Interferometry at ALBA," in *Proc. 4th Int. Beam Instrumentation Conf. (IBIC'15)*, Melbourne, Australia, 2015, pp. 428-432.

[165] I.P.S. Martin, G. Rehm, C. Thomas, and R. Bartolini, *Phys. Rev. ST Accel. Beams*, vol. 14, p. 040705, 2011.

[166] C.H. Chen, C.Y. Liao, J.Y. Chen, F.H. Tseng, C.C. Kuo, H.J. Tsai et al., "Bunch Length Measurements with a Streak Camera in Low Alpha Lattice Operation at the TPS," in *Proc. 9th Int. Particle Accelerator Conf. (IPAC'18)*, Vancouver, Canada, 2018, pp. 2316-2319.

Appendix A **Algorithm for emittance measurement with pinhole array**

A.1 Emittance measurement

a) At source point

The distribution of the photon ellipse at the source point can be represented as [84]

$$f_{Source\ (y,y')} = \frac{1}{2\pi\ \epsilon_{Photon}}\ exp\left(\frac{-\left(\gamma_{Photon}\ y^2 + 2\alpha_{Photon}\ yy' + \beta_{Photon}\ y'^2\right)}{2\varepsilon_{Photon}}\right) \quad \text{(A.1)}$$

with

$$\epsilon_{\mathrm{Photon}} = K\epsilon \quad \text{(A.2)}$$

$$\alpha_{Photon} = \frac{\alpha - \frac{\eta\eta'\ \sigma_{e\delta}{}^2}{\epsilon}}{K} \quad \text{(A.3)}$$

$$\beta_{\mathrm{Photon}} = \frac{\beta + \frac{\eta^2\ \sigma_{e\delta}{}^2}{\epsilon}}{\mathrm{K}} \quad \text{(A.4)}$$

$$\gamma_{\mathrm{Photon}} = \frac{\gamma + \frac{\eta'^2\sigma_{e\delta}{}^2 + \sigma_r'^2}{\epsilon}}{\mathrm{K}} \quad \text{(A.5)}$$

$$\sigma_{\mathrm{r}}' = \frac{0.565}{\gamma}\left(\frac{\mathrm{E_C}}{\mathrm{E}}\right)^{0.425} \quad \text{(A.6)}$$

and

$$K = \sqrt{1 + \frac{\sigma_{e\delta}{}^2\left(\gamma\,\eta^2 + 2\alpha\,\eta\,\eta' + \beta\,\eta'^2\right)}{\epsilon} + \frac{\beta\sigma_r'^2}{\epsilon} + \frac{\eta^2\ \sigma_{e\delta}{}^2\sigma_r'^2}{\epsilon^2}} \quad \text{(A.7)}$$

Various terms in the constant *K* represents different physical contributions to emittance at source point. First term represents the on-energy electrons in a storage ring, second term represents the contributions due to energy spread and dispersion, third and fourth terms represents the additional contributions due to photon opening angle.

b) At pinhole array

The photon ellipse from source point to pinhole array can be propagated by using translation $y = y + R1\, y^{'}$ and $y^{'} = y^{'}$ as follows:

$$f_{\text{Pinhole}\ (y, y^{'})} = \frac{1}{2\pi\, \varepsilon_{\text{Photon}}} \exp\left(\frac{-\left(\gamma_{\text{Photon}}\ (y + R1\, y^{'})^2 + 2\alpha_{\text{Photon}}\ (y + R1\, y^{'})y^{'} + \beta_{\text{Photon}}\ y^{'2}\right)}{2\varepsilon_{\text{Photon}}}\right) \quad \text{(A.8)}$$

c) At phosphor screen

Case-1: For measurement of horizontal profile: In horizontal plane, photon ellipse sweeps across the pinhole acceptance. So effective horizontal beam profile can be calculated by integrating the changing profiles over all angles

$$\int_{-\infty}^{+\infty} f_{Source\ (x, x^{'})}\ dx_o^{'} \quad \text{(A.9)}$$

$$\int_{-\infty}^{+\infty} exp\left(\frac{-\left(\gamma_{Photon}\, x^2 + 2\alpha_{Photon}\ xx^{'}(x, x_o^{'}) + \beta_{Photon}\ x^{'2}(x, x_o^{'})\right)}{2\epsilon_{Photon}}\right) dx_o^{'} \quad \text{(A.10)}$$

Using pinhole acceptance $x^{'}(x, x_o^{'}) = x_o^{'} - \frac{x}{R1}$ gives above equation as $\exp\left(\frac{-x^2}{2\,(\beta\varepsilon + \eta^2\, \sigma_{e\delta}{}^2)}\right)$

So, the integrated profile seen by the pinhole camera has beam size almost equal to the electron beam size as

$$\sigma_{x_{Measured}} \approx \sqrt{\beta\varepsilon + \eta^2\, \sigma_{e\delta}{}^2} = \sigma_{x\_electron} \quad \text{(A.11)}$$

Case-2: For measurement of vertical profile: The beam profile at the source point seen by the pinhole is the intersection of the pinhole acceptance $y' = \frac{-y}{R1}$ and the photon ellipse. Phosphor screen is located at distance R2 from the pinhole array. Let $\sigma_{Image\ \_Screen}$ be the r.m.s size of the photon beam at the screen. Then $\sigma_{Image\ \_Screen}$ will be equal to the r.m.s. divergence (can be taken from equation by setting y=0) of the beam at the centre of pinhole multiplied by R2, if we just neglect the contributions due to geometric, diffraction, broadening due to screen and camera in $\sigma_{Image\ \_Screen}$.

$$\sigma_{Image\ \_Screen} = R2 \sqrt{\frac{\varepsilon_{Photon}}{\beta_{Photon} + 2\alpha_{Photon}\ R1 + \gamma_{Photon}\ (R1)^2}} \tag{A.12}$$

By solving, it gives a quadratic equation in emittance as follows

$$\varepsilon^2 + P\varepsilon + Q = 0 \tag{A.13}$$

$$P = -\sigma^2{}_{Image\ \_Scr.} \left(\gamma - \frac{2\alpha}{R1} + \frac{\beta}{(R1)^2}\right) + {\sigma_{e\delta}}^2 \left(\gamma\, \eta^2 + 2\alpha\, \eta\, \eta' + \beta\, \eta'^2\right) + \beta {\sigma'_r}^2 \tag{A.14}$$

$$Q = -\sigma^2{}_{Image\ \_Screen} \left({\sigma'_r}^2 + {\sigma_{e\delta}}^2 \left(\eta' + \frac{\eta}{R1}\right)^2\right) + \eta^2\, {\sigma_{e\delta}}^2\, {\sigma'_r}^2 \tag{A.15}$$

Emittance can be calculated from the above quadratic equation as

$$\varepsilon = \left[\frac{(C - A) + \sqrt{(C - A)^2 - 4(B - D)}}{2}\right] \tag{A.16}$$

where A, B, C and D can be calculated as follows

$$A = {\sigma_{e\delta}}^2 \left(\gamma\, \eta^2 + 2\alpha\, \eta\, \eta' + \beta\, \eta'^2\right) + \beta {\sigma'_r}^2 \tag{A.17}$$

$$B = {\sigma_{e\delta}}^2\, \eta^2\, {\sigma'_r}^2 \tag{A.18}$$

$$C = \left(\frac{\sigma_{Image\_Screen}}{R2}\right)^2 (\gamma R1^2 + 2\alpha R1 + \beta) \quad (A.19)$$

$$D = \left(\frac{\sigma_{Image\_Screen}}{R2}\right)^2 \left[(\eta - \eta' R1)^2 {\sigma_{e\delta}}^2 + R1^2 {\sigma_r'}^2\right] \quad (A.20)$$

A.2 Accuracy in emittance measurement

The final measured emittance with the pinhole array depends upon various input parameters i.e. $\varepsilon(\alpha, \beta, \gamma, \eta, \eta', \sigma_{e\delta}, \sigma'_r, \sigma_{Image\_Screen}, R1, R2)$. So, the final experimental error in the emittance measurement depends upon the uncertainty contributions from all input values. The sensitivity of emittance was theoretically calculated for the X-DBL input parameters by using

$$\Delta\varepsilon = \sqrt{\sum_i \left(\frac{\partial\varepsilon}{\partial x_i}\right)^2 (\Delta x_i)^2} \quad (A.21)$$

The propagating affect of major error sources in emittance calculation are described in Table A.1. These are assumed to be originated from the imprecise knowledge of 10% (although high) in each input parameters. The measured emittance remains most sensitive to beta function and measured size uncertainties.

Table A.1. *Propagating effects of major sources of error in emittance calculation*

10% error in input parameter	Percentage error in (ε_y)	Percentage error in (ε_x)
α	0.11	0.22
β	9.9	10.17
η	1.9	4.7
σ_r'	0.75	0.88
$\sigma_{e\delta}$	1.56	4.6
σ_{Image_Screen}	18.1	5
Total	19.8	13.27

Appendix B **Van Cittert-Zernike Theorem**

B.1 Van Cittert-Zernike theorem

The Van Cittert-Zernike theorem (named after physicists Pieter Hendrik van Cittert and Frits Zernike) is a formula in coherence theory that states that under certain conditions fringe visibility from an extended, distant, incoherent source is proportional to Fourier transform of the source spatial distribution. This implies that the wave front from an incoherent source will appear mostly coherent at large distances.

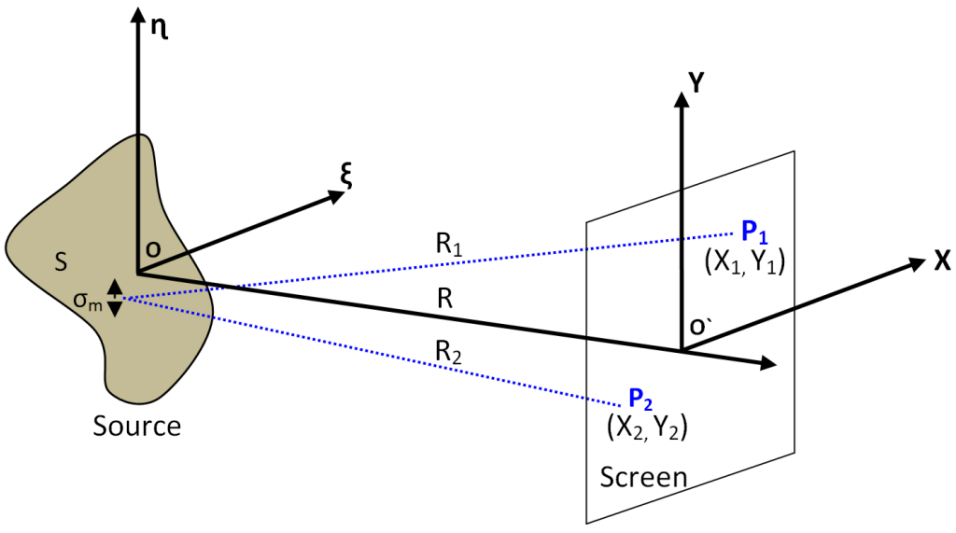

Fig. B.1: *Schematic for the VCZ theorem with an extended quasi monochromatic source illuminating screen*

Let an extended (σ) quasi monochromatic source (S) at (ξ, η) coordinates illuminates a screen at O' [161]. Assume the source to be divided into elements $d\sigma_1$, $d\sigma_2$... centred on points S_1, S_2.... of linear dimensions very small compared to mean wavelength $\bar{\lambda}$. If $V_{m1}(t)$ and $V_{m2}(t)$ are the complex disturbances at point P_1 (X_1, Y_1) and P_2 (X_2, Y_2) due to element $d\sigma_m$, the total disturbance at these points will be

$$V_1(t) = \sum_m V_{m1}(t) \qquad V_2(t) = \sum_m V_{m2}(t) \tag{B.1}$$

Now we will calculate mutual intensity J_{12} and complex degree of coherence γ_{12} for points P_1 and P_2 on the screen.

$$J(P_1, P_2) = \langle |V_1(t)\, V^*{}_2(t)| \rangle \tag{B.2}$$

$$= \sum_m \langle |V_{m1}(t)\, V^*{}_{m2}(t)| \rangle + \sum_{m \neq n} \sum \langle |V_{m1}(t)\, V^*{}_{n2}(t)| \rangle \tag{B.3}$$

Light vibrations arising from different elements of the source may be assumed to be statistically independent i.e. mutually incoherent, and of zero mean value. So

$$\langle |V_{m1}(t)\, V^*{}_{n2}(t)| \rangle = \langle |V_{m1}(t)\,| \rangle \langle |\, V^*{}_{n2}(t)| \rangle = 0 \quad \text{when } m \neq n \tag{B.4}$$

If R_{m1} and R_{m2} are the distances of P_1 and P_2 from the source element $d\sigma_m$, then

$$V_{m1}(t) = A_m \left(t - \frac{R_{m1}}{v}\right) \frac{e^{-j2\pi\bar{\nu}\left(t - \frac{R_{m1}}{v}\right)}}{R_{m1}} \tag{B.5}$$

$$V_{m2}(t) = A_m \left(t - \frac{R_{m2}}{v}\right) \frac{e^{-j2\pi\bar{\nu}\left(t - \frac{R_{m2}}{v}\right)}}{R_{m2}} \tag{B.6}$$

where v is the velocity of light in the medium, $|\boldsymbol{A_m}|$ and $\mathbf{arg}\ \boldsymbol{A_m}$ characterizes the strength and phase of radiation from the m^{th} element.

$$\langle |V_{m1}(t)\, V^{*}{}_{m2}(t)| \rangle = \langle A_m\,(t)\;\; A^{*}{}_m \left(t - \frac{R_{m2} - R_{m1}}{v}\right) \rangle \;\; \frac{e^{-j\,2\pi\bar{\nu}\left(\frac{R_{m2}-R_{m1}}{v}\right)}}{R_{m1}\, R_{m2}} \tag{B.7}$$

If the path difference $R_{m2} - R_{m1}$ is taken very small as compared to the coherence length of the light, we may neglect the retardation $\frac{R_{m2}-R_{m1}}{v}$ in the arguments of $A^{*}{}_m$. It becomes

$$J(P_1, P_2) = \langle A_m\,(t)\;\; A^{*}{}_m\,(t) \rangle \; \frac{e^{-j\,2\pi\bar{\nu}\left(\frac{R_{m2}-R_{m1}}{v}\right)}}{R_{m1}\, R_{m2}} \tag{B.8}$$

The quantity $\langle A_m\,(t)\;\; A^{*}{}_m\,(t) \rangle$ characterizes the intensity from the source element $d\sigma_m$. Practically for a continuous source with $I(S)$ intensity per unit area, it becomes

$$J(P_1, P_2) = \int_{\sigma} I(S) \; \frac{e^{-jk\,(R_2 - R_1)}}{R_1\, R_2}\, dS \tag{B.9}$$

where $k = {2\pi\bar{\nu}}/{v}$ is the wave number of the medium, now the complex degree of coherence can be written as

$$\gamma_{(P_1,P_2)} = \frac{1}{\sqrt{I(P_1)}\sqrt{I(P_2)}} \int_{\sigma} I(S) \; \frac{e^{-j\,\bar{k}\,(R_2 - R_1)}}{R_1\, R_2}\, dS \tag{B.10}$$

Where

$$\sqrt{I(P_1)} = J(P_1, P_1) = \int_{\sigma} \frac{I(S)}{{R_1}^2}\, dS \text{ and } \sqrt{I(P_2)} = J(P_2, P_2) = \int_{\sigma} \frac{I(S)}{{R_2}^2}\, dS \tag{B.11}$$

are the intensities at P_1 and P_2. Results of Eq. (B.10) are similar to diffraction pattern arising from diffraction of a spherical wave on an aperture in an opaque screen by Huygen-Fresnel principle. So, the complex degree of coherence, which describes the correlation of vibrations

at points P_1 and P_2 on screen illuminated by an extended quasi monochromatic source is equal to the normalized complex amplitude of diffraction pattern.

In most applications the intensity $I(S)$ may be assumed to be independent of the position of S on the surface (uniform intensity). The corresponding diffraction problem is then that of a diffraction of a spherical wave of uniform amplitude by an aperture of the same size and shape as the source.

Now solving and substituting for $R_1 - R_2$

$$R_1{}^2 = (X_1 - \xi)^2 + (Y_1 - \eta)^2 + R^2 \tag{B.12}$$

$$R_1 \sim R + \frac{(X_1 - \xi)^2 + (Y_1 - \eta)^2}{2R} \tag{B.13}$$

$$R_1 - R_2 \sim \frac{\left(X_1{}^2 + Y_1{}^2\right) - \left(X_2{}^2 + Y_2{}^2\right)}{2R} - \frac{(X_1 - X_2)\xi + (Y_1 - Y_2)\eta}{R} \tag{B.14}$$

Now put $\frac{(X_1 - X_2)}{R} = p$, $\frac{(Y_1 - Y_2)}{R} = q$ and $\psi = \frac{\bar{k}\left[\left(X_1{}^2 + Y_1{}^2\right) - \left(X_2{}^2 + Y_2{}^2\right)\right]}{2R}$ as phase difference between P_1 and P_2 .So Eq. (B.10) reduces to

$$\gamma_{(P_1,P_2)} = \frac{e^{j\psi} \iint_\sigma I(\xi,\eta)\ e^{-j\bar{k}(p\xi + q\eta)}\ d\xi\ d\eta}{\iint_\sigma I(\xi,\eta)\, d\xi\ d\eta} \tag{B.15}$$

So, if the linear dimensions of the source and the distance between P_1 and P_2 on the screen are small as compared to the distance of these points from the source, the degree of coherence γ_{12} is equal to the absolute value of the normalized Fourier transform of the intensity function $I(\xi,\eta)$ of the source. So VCZ theorem for spatial coherence relates the mutual coherence function of the field from an incoherent source to the diffraction pattern for an aperture of the same dimensions as the source.

B.2 Assumptions of the VCZ theorem

The VCZ theorem is based on few assumptions such as

a) Incoherence of the source

b) Distance to the source is much greater than the size of the observation area

c) Angular size of the source is assumed to be small

d) Source is assumed to be quasi monochromatic

e) Source is assumed to be two dimensional

f) Medium is assumed to be homogeneous.

These assumptions may not be true for all kind of sources, but these are approximately true for nearly all astronomical sources [40][41].

a) Incoherence of the source: A spatially coherent source does not obey the VCZ theorem. In that case, when we calculate the mutual coherence function for an extended coherent source, we would not be able to simply integrate over the intensity function of the source, i.e. the presence of non-zero cross terms ($m \neq n$) would give the mutual coherence function a complex form (not simple form). This assumption holds for most astronomical sources except Pulsars and masers which exhibit coherence.

b) Distance to the source: In the proof of the theorem it was assumed that the distance to the source is much greater than the size of the observation area i.e. source is observed in the far field region.

c) Angular size of the source: The derivation of the theorem was simplified with assumption that angular source size be small. But for a large source, we cannot neglect few

terms, and the VCZ theorem no longer holds. As an example, angular subtense of most of the astronomical sources remains very small in the sky (typically much less than a degree), so above assumption is easily fulfilled in the domain of radio astronomy.

d) Quasi-monochromatic waves: Theorem assumes that the source is quasi-monochromatic. That is, if the source emits light over a range of frequencies $\Delta\upsilon$, with mean frequency $\bar{\upsilon}$, then it should satisfy $\frac{\Delta\upsilon}{\bar{\upsilon}} \ll 1$. Moreover, the bandwidth of source must be narrow enough. Without this assumption, one cannot neglect retardation term $\frac{R_{m2}-R_{m1}}{v}$ compared to t in its derivation.

e) Two-dimensional source: The VCZ theorem assumes that source in a two-dimensional plane, but actually sources remain three-dimensional. To a good extent, angular distribution of any astronomical source can be taken same in the far field region, and three-dimensional structure can be projected upon a two-dimensional plane. Therefore it may be applied to measurements of astronomical sources, but we cannot determine structure along the line of sight with such measurements.

f) Homogeneity of the medium: Theorem assumes that the medium between the source and the imaging plane is homogeneous. In the case of a heterogeneous medium, light from one region of the source will be differentially refracted relative to other regions of the source due to the difference in light travel time through the medium. So, in that case one must use a generalization of the VCZ theorem, called Hopkins's formula.

B.3 Using VCZ theorem for finding spatial coherence

According to VCZ theorem, if a quasi monochromatic source is at a considerable distance from the aperture plane (R1), and pinhole separation (d) is small, fringe visibility (V) from an extended source is proportional to Fourier transform of the source spatial distribution. The transform variable is the angular separation of the aperture-plane sampling points divided by the wavelength.

$$V = \frac{2\sqrt{K_1 K_2}}{K_1 + K_2} \left| \frac{\boldsymbol{\mathcal{F}}_{\left(\frac{\theta_A}{\bar{\lambda}}\right)}[a^2(y_S)]}{I_L} \right| \tag{B.16}$$

$$V = \frac{2\sqrt{K_1 K_2}}{K_1 + K_2} \gamma_{12}\left(\frac{\theta_A}{\bar{\lambda}}\right) \tag{B.17}$$

here second term i.e. normalized FT of the source irradiance distribution and is called degree of spatial coherence (γ_{12}). It can be used to find spatial coherence of source as follows

a) Spatial coherence for a one dimensional source: Let irradiance of one dimensional source of length (L) is $a^2(y_S) = rect\left(\frac{y_S}{L}\right)$. Its degree of coherence will be

$$\gamma_{12}\left(\frac{\theta_A}{\bar{\lambda}}\right) = \left| sinc\left(\frac{L\,\theta_A}{\bar{\lambda}}\right) \right| \tag{B.18}$$

Visibility will be

$$V = \frac{2\sqrt{K_1 K_2}}{K_1 + K_2} \gamma_{12}\left(\frac{\theta_A}{\bar{\lambda}}\right) \tag{B.19}$$

In order to increase the visibility, θ_A or L must be reduced, or $\bar{\lambda}$ must be increased.

b) Spatial coherence for a Gaussian source: Let a one dimensional Gaussian source with radiance $a^2(y_S) = e^{-\frac{{y_S}^2}{2{\sigma_y}^2}}$, where σ_y is the rms source size. Then the normalized degree of coherence in the interference pattern is

$$\gamma_{12}\left(\frac{\theta_A}{\bar{\lambda}}\right) = I_0 \int e^{-\frac{{y_S}^2}{2{\sigma_y}^2}}\, e^{-i2\pi\frac{\theta_A}{\bar{\lambda}}y_S}\, dy_S \tag{B.20}$$

$$\gamma_{12}\left(\frac{\theta_A}{\bar{\lambda}}\right) = I_0\, e^{-2\,\pi^2\left(\frac{\theta_A}{\bar{\lambda}}\right)^2{\sigma_y}^2} \tag{B.21}$$

c) Spatial coherence length for a uniform circular source: Degree of coherence for a uniform circular source of radius (r_s) can be calculated as

$$\gamma(r) = \frac{2\,J_1\left(\frac{\pi\, r_s\, \alpha}{\lambda}\right)}{\frac{\pi\, r_s\, \alpha}{\lambda}} = \frac{2\,J_1(\vartheta)}{\vartheta} \tag{B.22}$$

where J_1 being the Bessel function of the first kind and first order, r is the distance of observation point from centre of screen (at R_1 distance from source), $\vartheta = \frac{\pi\, r_s\, \alpha}{\lambda}$. and $\alpha = \frac{r}{R_1}$.

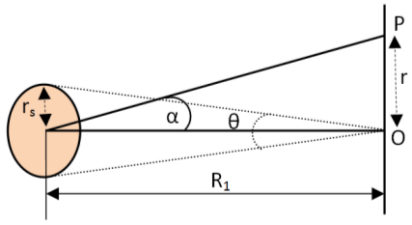

Fig. B.2: *Coherence from a circular source*

$$r_C = \frac{1.22\lambda}{\left({r_s}/{R_1}\right)}$$

It will have its first zero, when $r = 1.22\pi$ (Fraunhofer diffraction from a circular aperture). The first illuminated circular region (from 0 to 1.22π in the plot of the intensity) is called Airy disk. After airy disk there are a series of concentric bright rings which constitute the Airy pattern.

Appendix C **Measuring visibility from synchrotron radiation interferogram**

The intensity of the interferogram in one dimensional case can be described by the Eq. (5.36)

$$I(y) = I_0\, sinc^2\left(\frac{2\pi\, w_V}{\lambda R_2} y + \emptyset\right)\left[1 + V_y \cos\left(\frac{2\pi\, d_V}{\lambda R_2} y + \psi\right)\right] \tag{C.22}$$

where w_V is the slit width, d_V is the vertical slit separation, R_2 is the slit to screen distance (or focal length of lens), λ is the wavelength of quasi-monochromatic light, y is the displacement at screen plane, and V_y is the visibility of the fringes.

Visibility can be derived from the Fourier transform of the normalized source spatial distribution. For a Gaussian source it will be Eq. (5.28)

$$V_y = e^{-2\left(\frac{\pi\, d_V\ \sigma_V}{\lambda R_1}\right)^2} \tag{C.23}$$

where R_1 is the distance from source to slit assembly, σ_V is the vertical beam size (RMS) of Gaussian SR source.

In this work our first objective is to write a program which can best fit data generated with the SR interferometer i.e. interferogram. The second objective is to use the fitting function/program to determine the effect of various design parameters optimization.

The individual constants at each parameter of equation were consolidated into one parameter (say a_1, a_2, a_3…etc.) as follows

$$I(y) = a_1 \left[\frac{\sin\,(a_2 y - a_3)}{(a_2 y - a_3)}\right]^2 [1 + a_4 \cos\,(a_5 y - a_6)] \tag{C.24}$$

Here parameter (a_3) takes into account the shift of interference pattern to some point other than at zero. Similarly parameter (a_6) is introduced to take into account phase shift. This phase shift (offset) may come due to slight misalignment of the light source, slit assembly, lens etc.

The program is written in MATLAB [138]. It gives the horizontal and vertical profile at the selected point on the given image of the interferometer. These data points of profile are fitted with the given equation. The "best fit" parameters (a_1, a_2, a_3…etc.) are displayed. These fit parameters can be used to find beam size and other design parameters of SRI setup.